11-2

SANDIA REPORT

SAND95–0857 • UC–814
Unlimited Release
Printed September 1995

Yucca Mountain Site Characterization Project

Unsaturated-Zone Fast-Path Flow Calculations for Yucca Mountain Groundwater Travel Time Analyses (GWTT-94)

B. W. Arnold, S. J. Altman, T. H. Robey, R. W. Barnard, T. J. Brown

Prepared by
Sandia National Laboratories
Albuquerque, New Mexico 87185 and Livermore, California 94550
for the United States Department of Energy
under Contract DE-AC04-94AL85000

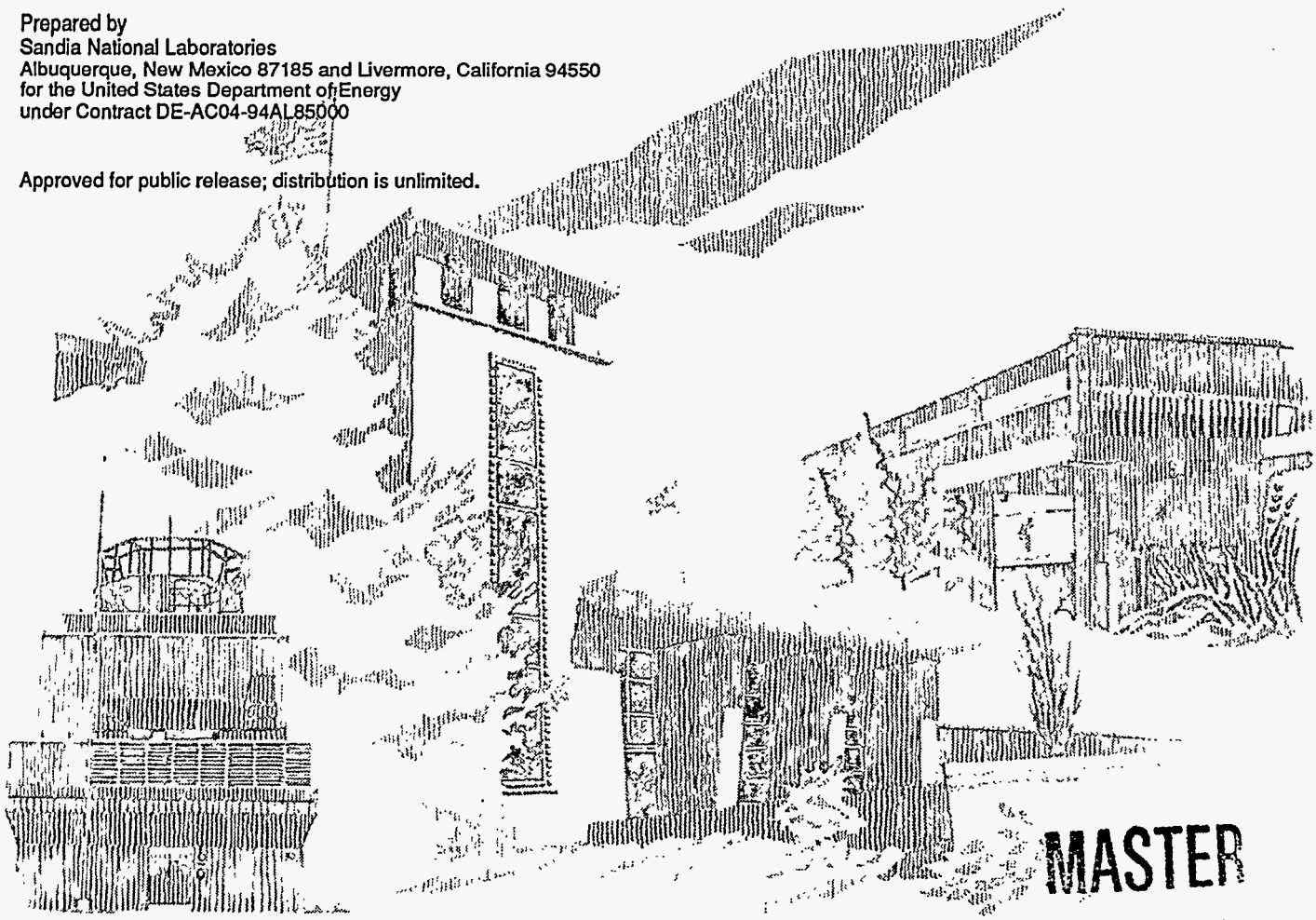

"Prepared by Yucca Mountain Site Characterization Project (YMSCP) participants as part of the Civilian Radioactive Waste Management Program (CRWM). The YMSCP is managed by the Yucca Mountain Project Office of the U.S. Department of Energy, DOE Field Office, Nevada (DOE/NV). YMSCP work is sponsored by the Office of Geologic Repositories (OGR) of the DOE Office of Civilian Radioactive Waste Management (OCRWM)."

Issued by Sandia National Laboratories, operated for the United States Department of Energy by Sandia Corporation.

Available to DOE and DOE contractors from
Office of Scientific and Technical Information
PO Box 62
Oak Ridge, TN 37831

Prices available from (615) 576-8401, FTS 626-8401

Available to the public from
National Technical Information Service
US Department of Commerce
5285 Port Royal Rd
Springfield, VA 22161

NTIS price codes
Printed copy: A20
Microfiche copy: A01

SAND95-0857
Unlimited Release
Printed August 1995

Distribution Category
UC-814

UNSATURATED-ZONE FAST-PATH FLOW CALCULATIONS FOR YUCCA MOUNTAIN GROUNDWATER TRAVEL TIME ANALYSES (GWTT-94)

B.W. Arnold, S.J. Altman, T.H. Robey†, R.W.Barnard, T.J. Brown
Sandia National Laboratories
Albuquerque, NM 87185

†Spectra Research Institute
Albuquerque, NM 87102

Abstract

Evaluation of groundwater travel time (GWTT) is required as part of the investigation of the suitability of Yucca Mountain as a potential high-level nuclear-waste repository site. The Nuclear Regulatory Commission's GWTT regulation is considered to be a measure of the intrinsic ability of the site to contain radionuclide releases from the repository. The work reported here is the first step in a program to provide an estimate of GWTT at the Yucca Mountain site in support of the DOE's Technical Site Suitability and as a component of a license application.

Preliminary estimation of the GWTT distribution in the unsaturated zone was accomplished using a numerical model of the physical processes of groundwater flow in the fractured, porous medium of the bedrock. Based on prior investigations of groundwater flow at the site, fractures are thought to provide the fastest paths for groundwater flow; conditions that lead to flow in fractures were investigated and simulated. Uncertainty in the geologic interpretation of Yucca Mountain was incorporated through the use of geostatistical simulations, while variability of hydrogeologic parameters within each unit was accounted for by the random sampling of parameter probability density functions. The composite-porosity formulation of groundwater flow was employed to simulate flow in both the matrix and fracture domains. In this conceptualization, the occurrence of locally saturated conditions within the unsaturated zone is responsible for the initiation of fast-path flow through fractures.

The results of the GWTT-94 study show that heterogeneity in the hydraulic properties of the model domain is an important factor in simulating local regions of high groundwater saturation. Capillary-pressure conditions at the surface boundary influence the extent of the local saturation simulated. Regions of local saturation, though limited in extent, were

predicted by simulations to occur primarily beneath the outcrop of the Paintbrush Tuff nonwelded interval and near the basal vitrophyre of the Topopah Spring member, in most realizations of the system. In the particle-tracking simulations, particles which remained in matrix-flow conditions moved very small distances over the duration of the simulation; only when particles move advectively at fracture-flow velocities are they likely to exit the system. Within 1000 years of release at the horizon of the potential repository, 0-3% of the particles were simulated to experience movement at fracture flow velocities, in 8 of 9 realizations of the system.

This work was supported by the United States Department of Energy under Contract DE-AC04-94AL85000, and was performed under WBS 1.2.5.4.4

The data in this report were developed subject to the controls in QAGR 042, Revision 0, PCA 2.0, Task 2.1, and was done under Work Agreement WA-0132, Revision 0. The data are not to be used for licensing.

Acknowledgments

The authors would like to thank all those individuals who contributed to the success of this effort. We acknowledge the contributions of Christopher Rautman and Sean McKenna (Sandia National Laboratories Geohydrology Department), and Marc Cromer (Spectra Research Institute) for their assistance in developing the geostatistical simulations. Sharon Shannon (SNL YMP System Performance Assessment Department) produced many of the graphics used in the figures. Lee Skinner and Nalini Zieman (Spectra Research Institute) did most of the coding of the particle tracker under a tight delivery schedule. Al Schenker and David Guerin (Los Alamos Technical Associates) provided access to the hydrologic data through the Performance Assessment Working Database. Clifford Ho (SNL Geohydrology Department) and Steven Sobolik (SNL YMP Performance Assessment Applications Department) provided technical review of this document and many helpful comments. Holly Dockery (SNL YMP System Performance Assessment Department) ably managed the entire effort and completed the management review.

CONTENTS

Figures

Tables

Acronyms

CDF	Cumulative distribution function
DOE	US Department of Energy
ESF	Exploratort Studies Facility
FY	Fiscal year
GWTT	Groundwater Travel Time
HLW	High level waste
IGF	Incomplete gamma function
NTS	Nevada Test Site
NRC	Nuclear Regulatory Commission
PAWDS	Performance-Assessment working data sets
PDF	Probability density function
PET	Potential evapotranspiration
SGS	Sequential Gaussion simulation
SIS	Sequential indicator simulation
SZ	Saturated Zone
TSS	Technical Site Suitability
UZ	Unsaturated Zone

Executive Summary

Introduction

Yucca Mountain is being investigated by the US Department of Energy (DOE) as a potential site for a high-level nuclear-waste repository. Yucca Mountain is located about 120 km northwest of Las Vegas, Nevada, at the Nevada Test Site. One of the reasons Yucca Mountain is being investigated as a potential repository site is because the thick sequence of unsaturated rock is expected to impede releases of radionuclides. Because groundwater flow is perhaps the most important mechanism for transport of radionuclides from the repository, characterization of groundwater movement in the unsaturated zone (UZ) under arid conditions is of considerable importance to an evaluation of the ability of the site to isolate waste.

This document reports on the fiscal year (FY) 1994 groundwater travel time (GWTT) investigations for the DOE's Yucca Mountain Site Characterization Project. GWTT is a component of the characterization of Yucca Mountain being performed for the DOE's Technical Site Suitability (TSS) assessment. The TSS assessment will include an evaluation of the site in the context of DOE's Postclosure Geohydrology guideline given in 10 CFR 960.4-2-1 (d). In addition, the licensing process will consider the Nuclear Regulatory Commission's (NRC) GWTT Performance Requirement given in 10 CFR 60.113(a)(2). Both these regulations state, in effect, that the ... *pre-waste-emplacement groundwater travel time shall not be less than 1,000 years from the edge of the disturbed zone to the accessible environment.* The focus of the GWTT effort is thus to characterize the nature of groundwater flow at the site with respect to compliance with the above-mentioned regulations.

Because there may be relatively few direct observations of site data or features at Yucca Mountain that could assist in estimates of GWTT (such as the groundwater-age studies), an evaluation of travel times requires numerical modeling of groundwater-flow processes and simulations of the long-term effects of these processes. Considerable modeling of groundwater-flow has been done previously for performance-assessment analyses and prior GWTT calculations, so the general implications of alternative conceptual models are understood. Previous modeling has shown that in the UZ, groundwater that flows only in the rock matrix moves sufficiently slowly that it would take many tens of thousands of years to go from the location of the potential repository to the water table. In contrast, both field evidence and modeling have shown that groundwater that moves in fractures in the rock can travel at much faster rates — it is able to move this distance in perhaps tens to hundreds of years. Models of groundwater flow have shown that the degree of saturation in the rock is a major factor controlling the extent to which water flows in the rock matrix or in the rock fractures. One of the differences among the conceptual models describing groundwater flow in the UZ is the degree of rock-matrix saturation necessary to initiate flow through fractures (fracture flow). The GWTT-94 work builds on the prior efforts by investigating credible mechanisms that can produce the localized matrix saturation necessary to initiate fracture flow for one of the conceptual models.

The conceptual model of groundwater flow used for GWTT-94 imposes the greatest restrictions on the degree of matrix saturation necessary before fracture flow can occur. In this model, the matrix must be essentially fully saturated before fracture flow can occur. Although the rock mass at Yucca Mountain may be subdivided into layers based on the gross similarity of lithology, the heterogeneous nature of the rock also induces variation of hydrologic properties within each layer. It is this layered, heterogeneous rock structure that has been modeled to investigate the hypothesis that regions of localized saturation will form. Since Yucca Mountain is considered to be generally unsaturated, it is expected that the regions of saturation are quite localized and continuous regions of saturation from the repository horizon to the water table are unlikely to occur. As a result of this restrictive requirement for propagation of fracture flow, the main emphasis of the GWTT-94 work has been on the initiation of fracture flow through the simulation of localized saturated regions. Work is still to be done on understanding how flow in fractures may be sustained once it has begun.

The GWTT-94 work only modeled groundwater flow in the unsaturated zone. A complete GWTT evaluation must also consider groundwater flow through the saturated zone to the accessible environment. In addition, the regulations specify that the disturbed zone also be included in the definition of potential GWTT pathways. Because these factors were not considered for these analyses, this work is not presented as an assessment of site compliance with regulatory requirements. This study does, however, represent a major step toward a compliance-analysis model. Future work will include enhancements to the numerical model, implementation of alternative conceptual models, and inclusion of the remaining factors required for a complete GWTT analysis.

Conceptual Model

The conceptual model of hydrologic processes and conditions in the UZ at Yucca Mountain forms the basis for numerical simulations of groundwater flow and GWTT calculations in this study. This conceptual model is based on current understanding of unsaturated flow in fractured porous media and on data on the geology and existing groundwater flow conditions at the site. Because site-specific data are sparse and uncertain, the conceptual model encompasses a range of possible geologic alternatives and flow conditions.

Conceptual models of large-scale UZ flow processes have evolved as site characterization at Yucca Mountain proceeds and continue to undergo refinement with the acquisition of additional data. Initial models of flow in the UZ assumed that flow occurs primarily through the rock matrix at relatively low velocities. Alternatively, other researchers have proposed that the principal mode of groundwater flow is in saturated fractures at relatively high velocities. The unsaturated-matrix and the saturated-fracture conceptual models represent extremes and do not account for the interaction of flow between the rock matrix and fractures. A third conceptualization, as used in this study, acknowledges the role of both matrix and fracture flow processes, with local hydrologic conditions determining the dominant flow process. Two possible modes of initiating and sustaining groundwater flow in fractures are transient, nonequilibrium flow in response to surface infiltration processes and steady-state flow associated with zones of locally high saturation (perched water). Because observations in boreholes indicate the presence of perched water in some places in the

stratigraphic interval between the repository and the water table, it is the later mode which is considered in the research presented here.

The conceptual model of UZ flow processes used in this study employs the composite-porosity formulation in which the properties of both the matrix and the fractures are combined into a single continuum. In this model, fracture-dominated flow conditions occur only when the matrix is nearly saturated. This approach allows the simulation of a steady-state UZ flow field in which matrix flow dominates in drier regions of the flow field and fracture flow dominates in nearly saturated regions. Heterogeneity of material properties results in the development of locally saturated zones within the medium. These zones of local saturation are the areas in which fast-path fracture flow is initiated.

Parameter Development

Numerical modeling of groundwater flow in the UZ for the 1994 analyses used the hydrogeologic parameters that have been derived from available data. Because of uncertainty in both the geology and the hydrogeologic parameters, a probabilistic approach has been adopted in this study. Uncertainty in the geologic interpretation of Yucca Mountain was incorporated through the use of geostatistical simulations to produce multiple, equally likely realizations of the hydrostratigraphic units. Also, variability of parameters within each hydrostratigraphic unit was accounted for by the derivation of parameter probability density functions (PDFs), from which values were randomly drawn for individual locations in the system. Three realizations along each of three cross-sections were generated, for a total of nine realizations of the model domain.

The hydrological parameters porosity, average pore size, standard deviation of pore size, Brooks-Corey constant, and saturated hydraulic conductivity were required input for the flow simulations. Porosity data were obtained from cores, and these data were used to derive saturated hydraulic conductivity values, moisture retention curves, and relative permeability curves by regression relationships. Due to the lack of fracture property data, fracture porosity was randomly drawn from the PDF of fracture porosity for each unit and the other fracture parameters obtained in a similar manner as for the matrix properties.

Flow Model

Numerical modeling of groundwater flow within the cross-sections generated by geostatistical simulation was performed to calculate a fluid-velocity field for flow analyses. The numerical solution of steady-state unsaturated flow was calculated by the finite-element method using the dual-variable approach as implemented by the computer code, DUAL. The size and shape of individual elements in the finite-element technique may vary within the problem domain, making it well suited to problems with heterogeneous material properties and irregular boundaries. The dual-variable approach differs from standard finite-element methods in that the effects on flow of contrasting material properties are preserved with relatively coarser numerical grids.

Because of computational limitations, the numerical grid used for the flow model was much coarser than that used at the geostatistical simulation scale. A unique grid was developed for each realization by using an adaptive numerical gridding algorithm that adjusted the boundaries of an initially uniform grid in such a way as to minimize variation of porosity within each grid element. Properties assigned to an individual element of the flow grid were derived by averaging the properties associated with the geostatistical-scale nodes within that element to achieve parameter values consistent with the flow-element scale.

The boundary conditions applied to numerical simulations of flow in the UZ were both specified flux and specified pressure. The faults, which were the lateral boundaries of the three cross-sections, were specified as no-flow boundaries. The lower boundary was the water table and had a specified pressure head equal to 0.0 m. The upper boundary conditions were specified-pressure values drawn from PDFs of capillary pressure developed for the three outcropping hydrogeologic units.

The results of the flow simulations showed zones of relatively higher saturation beneath the outcrop of the nonwelded Paintbrush interval and near the horizon of the Topopah Spring Member basal vitrophyre. High saturations in a broad zone were observed in a single flow simulation with relatively "wet" upper boundary conditions. Dominant groundwater fluxes were vertical in the flow simulations, in contrast to site-scale flow modeling that has predicted significant lateral flow along the dip of stratigraphic units. Some lateral flow was observed above the Topopah Spring Member basal vitrophyre.

Particle Tracking

The language of the GWTT regulations has been interpreted by the DOE and the NRC to mean that the results of GWTT analyses will be evaluated as distributions of travel times, rather than as single values (DOE, 1984; NRC, 1983). To generate these distributions, individual water "particles" are tracked as they travel in the flow field calculated by the flow simulations. Their varying arrival times at the boundary of the UZ are presented as distributions. The distributions can then be evaluated in terms of their means and variances, and the percentage of particles that arrive in less than 1,000 years.

A particle tracking procedure that simulates the movement of individual water particles by advection and molecular diffusion within the two-dimensional steady-state groundwater velocity field calculated by the flow code provides the means to determine a distribution of particle travel times. Advection occurs at either matrix- or fracture-flow velocities, depending on the local saturation determined by the flow model. If the fracture pore velocity is greater than the matrix pore velocity at the particle location, then the particle is moved at the fracture-flow velocity. Because of the relatively high fracture velocities and large time steps, particles in fractures were moved large distances without reimbibition into the matrix. In most of the simulations, particles were transported to the water table in a single time step following transfer to the fracture-flow domain. While reimbibition into the matrix would be expected in zones of lower saturation after the initiation of fracture flow in the unsaturated zone, this process was generally excluded from the particle

tracking scheme due to the large time steps. Therefore, the distance which particles traveled under fracture-flow conditions was probably overestimated, yielding an underestimate of the water particle transit-time distribution. An underestimate of the travel time distribution is a conservative bounding approximation.

In most of the realizations, the particles that exited the system originated from the western part of the potential repository, beneath the outcrop of the nonwelded Paintbrush interval. The position of the Topopah Spring member basal vitrophyre relative to the elevation of the western part of the potential repository had a significant effect on the number of particles exiting the system during the simulation. The closeness of the initial particle positions to the zones of high saturation at the basal vitrophyre was a controlling feature of the GWTT calculated by the model.

In eight of the nine realizations, 0% to 3% of the particles exited the UZ within 1,000 years of the beginning of the simulation. In the single realization in which relatively high saturations were simulated due to relatively "wet" upper boundary conditions, 35% of the particles were transported from the UZ within 1,000 years.

Sensitivity Analyses

Sensitivity analyses of the numerical model were performed to determine which hydrologic parameters exerted the greatest control over the simulation results. Identification of sensitive parameters, as determined in this study, allows for refinement of future numerical modeling efforts with regard to these parameters. Sensitivity analyses were also performed to test the numerical capabilities and limitations of the flow simulation code.

Inclusion of intra-unit heterogeneities is critical to modeling groundwater fast-path flow. Comparison of flow simulations show that average saturations are higher in a heterogeneous realization of the UZ domain than in a homogeneous realization. In addition, zones of high local saturation, which play an important role in the initiation of fast fracture flow, are more widespread in the heterogeneous simulation than in the homogeneous one. The use of a uniformly thick nonwelded Paintbrush unit, in comparison to the variably thick geostatistically simulated unit, result in higher saturations, but the contrasts are not as great as in the heterogeneous versus homogeneous cases.

Infiltration rates, saturations, and groundwater fluxes in simulations of steady-state flow in the UZ system are very sensitive to capillary pressure boundary conditions and porosity at the upper surface of the model. Additional constraints on the magnitude and distribution of capillary pressure at the surface boundary of the model would lead to a significant refinement to the flow model.

Alteration of the numerical grid indicated that the results of the numerical flow model are relatively insensitive to the number of elements used in the calculation and to the shape of the grid at unit contacts. This result suggests that the grid used on this study was not too coarse to calculate an accurate flow field for fast-path flow determinations.

Summary

Given the limited scope of these analyses, some important conclusions have been drawn:

- Local saturation of the matrix and the consequent initiation of fracture flow can occur due to the heterogeneous distribution of hydraulic properties within hydrogeologic units.

- The infiltration rate at the outcrops of the units has a strong influence on matrix saturation, and consequently on fracture flow.

- Enhanced infiltration at the outcrop of the high-porosity nonwelded Paintbrush interval can result in higher saturation and increased probability of fracture flow in regions deep beneath the outcrop.

- In most realizations of the UZ model domain, the extent of localized matrix saturation was quite limited. Generally, a maximum of 3% of the water particles at the repository horizon were exposed to such saturated conditions.

- To more accurately determine GWTT distributions in future investigations, alternative conceptual models for groundwater flow must be implemented. Such numerical models simulate matrix and fracture flow independently, and permit reimbibition of water from fracture flow into the matrix.

Numerical simulations of groundwater flow in the UZ for GWTT-94 analyses indicate that water particles that remain in matrix-flow conditions move very small distances over the 600,000-year duration of the simulations. Only when water particles move at fracture-flow velocities are they likely to move to the water table, indicating the importance of understanding the mechanisms causing locally saturated conditions that initiate fracture flow. The factors that cause locally saturated conditions that result in shorter travel times are: heterogeneous rock material properties, infiltration rate at the outcrop of the nonwelded Paintbrush interval, capillary pressure conditions at the upper boundary, and low values of porosity in the Topopah Spring Member basal vitrophyre. Little lateral groundwater movement was simulated by the model, precluding the development of high local saturation values along the Ghost Dance fault at the boundary of the model. Material heterogeneities may have a strong influence on the flow system to minimize lateral flow toward the fault.

Sensitivity analyses demonstrate that intra-unit heterogeneities of porosity are critical to modeling groundwater-flow fast-paths because they concentrate flow, forming areas of higher saturation. These zones of high local saturation result in the initiation of fracture flow.

Refinements to the model codes are needed to simulate fracture heterogeneities and more accurately portray the interaction of flow in fractures and the matrix. The location of the potential repository disturbed zone needs to be included in the model. Understanding infiltration into and flow within the nonwelded Paintbrush interval will increase confidence in predictions of UZ flow behavior. More detailed and accurate data about infiltration and capillary pressure along the nonwelded Paintbrush interval outcrop are needed.

Improvements will be included for the modeling to be done for 1995 GWTT calculations. Additional cross-sections will be selected. Matrix porosity and saturated hydraulic conductivity will be cosimulated in the geostatistical simulation procedure. A dual-permeability formulation of the numerical flow model will be used, allowing for independently modeled flow in the fracture and matrix domains, as well as flow between fractures and matrix.

This page intentionally left blank.

Chapter 1
Introduction

This document reports on the fiscal year (FY) 1994 Groundwater Travel Time (GWTT) investigations for the US Department of Energy (DOE) Yucca Mountain Site-Characterization Project. The Yucca Mountain Site-Characterization Project is an effort by the DOE to evaluate Yucca Mountain, Nevada, as a potential repository for high-level nuclear waste. Yucca Mountain is located approximately 120 km northwest of Las Vegas, NV, adjacent to the DOE's Nevada Test Site (NTS) (Figure 1-1).

The location and geologic features of the Yucca Mountain site are an important factor in its consideration as a potential repository site. The site is composed of thick sequences of unsaturated rock that are expected to present barriers to the release of radionuclides. Since groundwater flow is expected to be one of the most important mechanisms for the transport of radionuclides from the repository, the characterization of groundwater flow in the unsaturated zone (UZ) is of great importance in an evaluation of the suitability of the site.

The US Nuclear Regulatory Commission (NRC) is responsible for licensing any nuclear-waste repository. Among their considerations are the reasonable assurance that construction, operation, and closure of the repository will not endanger public health and safety. The US Environmental Protection Agency (EPA) has responsibility for establishing regulations for performance of the repository system (i.e., the combination of the engineered components and natural barriers), and the NRC has established subsystem requirements for suitability specifically related to groundwater flow. The NRC will evaluate any license application against the total-system and subsystem requirements. Prior to a license application before the NRC, the DOE is conducting a Technical Site Suitability (TSS) assessment for use in preparing a recommendation to the President regarding the suitability of the Yucca Mountain site. The DOE has established its own qualifying and disqualifying conditions for any potential nuclear-waste repository site. Among them are hydrologic disqualifying conditions related to groundwater travel time. GWTT is therefore one of the site conditions that must be evaluated as part of the TSS assessment. The focus of the GWTT effort is to characterize the nature of groundwater flow at the site with respect to compliance with the NRC and the DOE regulations.

1.1 Regulatory Issues

One of the major components of the TSS assessment is an evaluation of the site in terms of both the NRC GWTT Performance Requirement given in 10 CFR 60.113(a)(2) [NRC, 1983] and the DOE GWTT Disqualifying Condition (contained in the DOE Postclosure Geohydrology guideline in 10 CFR 960.4-2-1 (d) [DOE, 1984]). The Performance Requirement states that "...*pre-waste-emplacement groundwater travel time along the fastest path of likely radionuclide travel from the disturbed zone to the accessible environment shall be at least 1,000 years....*" The Dis-

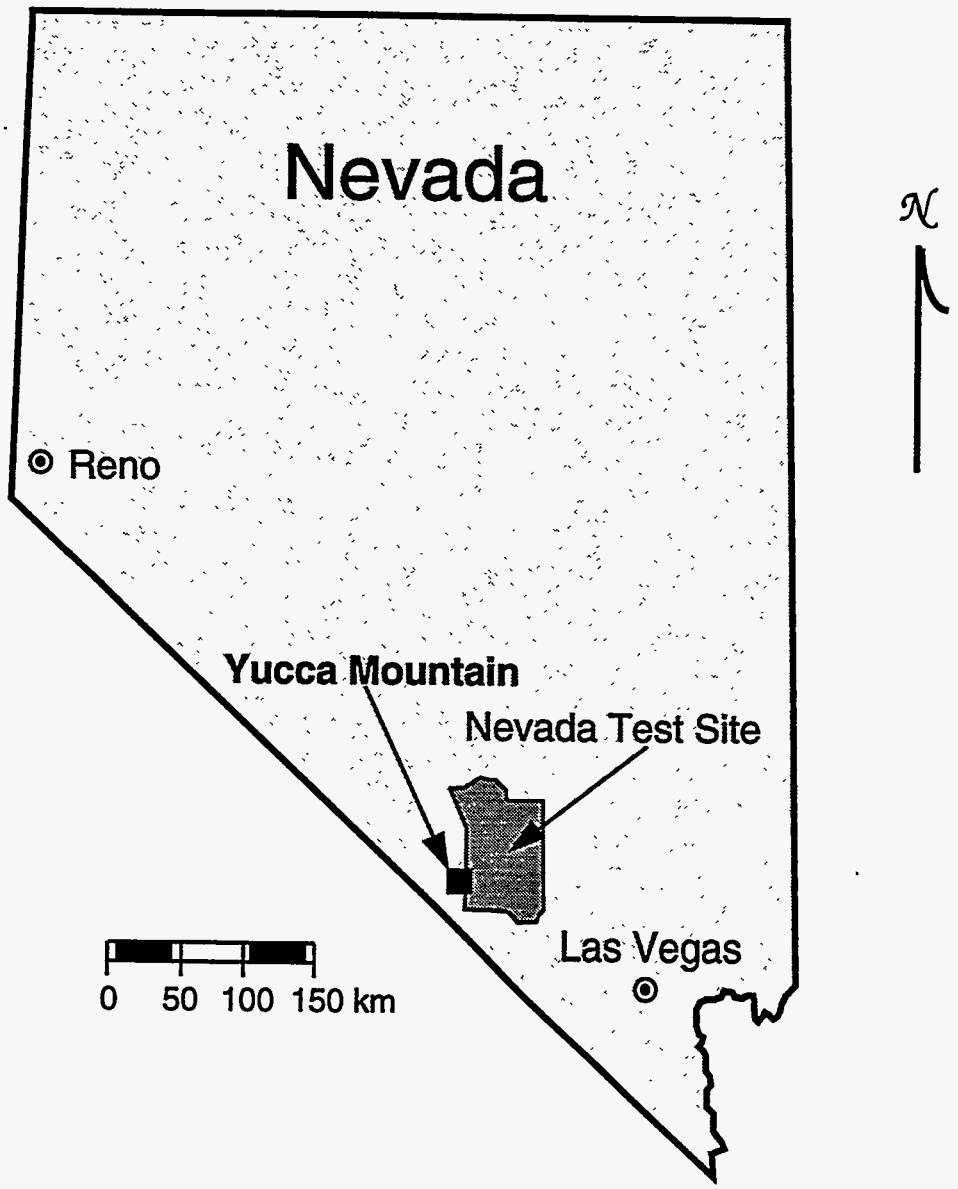

Figure 1-1. Location of the Yucca Mountain Site adjacent to the Nevada Test Site in southern Nevada.

qualifying Condition is that "*A site shall be disqualified if the pre-waste-emplacement groundwater travel time from the disturbed zone to the accessible environment is expected to be less than 1,000 years along any pathway of likely and significant radionuclide travel.*" The use of the word *likely* has been interpreted by DOE and NRC (NRC, 1989) to mean that the GWTT must be construed as a distribution, rather than a single value. Such distributions may result from differences in travel times along paths at various locations at the site and variations in hydraulic conductivity among the paths, or from differences attributable to conceptual and computational models of groundwater flow. The inclusion of the word *significant* in the Disqualifying Condition is taken by DOE to mean that the distributions must be evaluated to see if the fastest paths can contribute to radionuclide releases that exceed the release criteria. The disturbed zone has been defined by the NRC to include "*...that portion of the controlled area the physical or chemical properties of which have changed as a result of underground ... construction or heat generated ... such that the resultant change of properties may have a significant effect on the performance of the geologic repository.*"

The DOE approach to addressing both the NRC and the DOE regulations for GWTT is based on evaluating the likelihood and significance of distributions of travel times. It is expected that the GWTT evaluation process will be iterative, with successive work building on the models and results developed previously. The 1994 GWTT model is the first implementation of the DOE approach.

1.2 Previous GWTT Modeling Work

Several evaluations of the GWTT characteristics of Yucca Mountain have been made in the past (e.g., Lin et al., 1986; Kaplan, 1993). Lin et al. (1986) used a Monte Carlo analysis on a non-mechanistic model of groundwater flow through the unsaturated zone (i.e., $t=l/v$, where v is a function of the groundwater infiltration rate) to develop distributions over approximately 960 vertical columns covering the potential repository area. This work found that the mean of the GWTT distribution in the unsaturated zone was over 40,000 years, and less than 1% of the GWTT distribution was travel times of less than 10,000 years. Kaplan (1993) used a one-dimensional flow code to model unsaturated-zone flow; the emphasis of this work was to sample a range of hydrologic parameter values using Monte Carlo techniques. These results showed a sensitivity of the GWTT distributions to fracture conductivity in some of the units.

In the most recent total system performance assessment (TSPA) analyses (Wilson et al., 1994), a modeling domain and hydrologic-parameter working data set have been developed that have been adapted to the 1994 work. The geostatistical simulation methods used for the fast-path flow analyses were first applied to the TSPA modeling domain, and the parameter probability density functions (PDFs) were developed as part of the performance-assessment working data sets (PAWDS)[1]. The DUAL flow code used for this analysis was first applied to Yucca Mountain

1. Schenker, A.R., D.C. Guerin, T.H. Robey, C.A. Rautman, and R.W. Barnard (in review). *Stochastic Hydrogeologic Units and Hydrogeologic Properties Development.* SAND94-0244. Albuquerque, NM: Sandia National Laboratories.

groundwater-flow problems in an INTRAVAL exercise (Robey, 1994) that also included the geostatistical simulations with data from the PAWDS.

1.3 Analysis Method

The first step in the GWTT evaluation process is to select an appropriate conceptual model (or models) of the hydrogeologic regime of the Yucca Mountain site, which then becomes the basis for a numerical flow model. Since the data available for the site are not comprehensive, the data requirements of the flow model have been met by statistically generating three-dimensional realizations of the geometry of the hydrostratigraphic units. The flow model then simulates groundwater-velocity fields and saturations on the model domain. The language of the GWTT regulations has been interpreted to mean that the results of GWTT analyses will be evaluated as distributions of travel times. To generate these distributions, individual water "particles" are tracked as they travel on the flow field calculated by the flow simulations. Their varying arrival times at the water table are presented as distributions. Finally, the results of the modeling process were further investigated by sensitivity analyses.

The 1,000-year regulatory time limit for GWTT is a relatively short time period in contrast to the EPA radionuclide-containment regulations. Consequently, the existence of rapid groundwater flow paths are important for the GWTT evaluation. If unsaturated-zone groundwater flow at Yucca Mountain (Chapter 2) is assumed to be matrix-dominated, water may take tens to hundreds of thousands of years to move from the potential repository horizon to the water table (e.g., Prindle and Hopkins, 1990; Barnard et al., 1992; Eslinger et al., 1993; Wilson et al., 1994). However, if flow occurs in fractures, the water can move that same distance in just a few years (e.g., Wilson et al., 1994; Buscheck and Nitao, 1988). Consequently, it is the mechanisms and conditions associated with fast-path flow through fractures that are being investigated and simulated in this study.

The conceptual model employed in this study considers that fast-path flow is primarily controlled by the degree of saturation of the rock. The degree of rock saturation necessary for initiation of fracture flow is dependent on the conceptual models for groundwater flow; such models can generally be divided into continuum and discrete models. For this study, an equivalent-continuum approach in which both matrix and fracture flow can be described by a single hydraulic conductivity curve (the composite-porosity model) was selected. Unlike other conceptual models that may not have a strong coupling between matrix and fracture saturations, and may predict that fracture flow will occur at less-than-saturated matrix conditions, the composite-porosity model requires that the matrix be nearly saturated before significant fracture flow will occur. This work has used a method for simulating locally saturated regions by modeling a domain with heterogeneous hydraulic properties and by applying a spatially variable infiltration rate along the surface boundary.

A steady-state groundwater flow field is calculated for the heterogeneous model domain. Because the transient nature of infiltration tends to be dampened with depth, a steady-state representation of groundwater flow is used. At locations where local saturation has developed, fracture flow can initiate. Once initiated, propagation of fracture flow is similarly dependent on the conceptual model for groundwater flow. Because the composite-porosity model requires that the ma-

trix be saturated before fracture flow can propagate, a model domain with isolated zones of high saturation would not support long-distance fracture flow. However, in this study, the composite-porosity saturation requirements were not enforced to conservatively model fracture-flow propagation.

An overview of the analytical strategy in this study is shown in the flow chart of Figure 1-2. Three two-dimensional cross-sections through the unsaturated zone of the Yucca Mountain site using geostatistical simulation methods were generated (Figure 1-3); on each of these cross-sections, three alternative realizations of the porosity distributions were produced. Relevant parameters were stochastically assigned along the cross-sections based on estimates of the distributions of these parameters within each unit. The two-dimensional problem domain was discretized into quadrilateral elements using an adaptive gridding method. Effective hydraulic parameters were assigned to each element by an upscaling process that averaged parameter values from the smaller geostatistical scale. Boundary conditions were imposed on the resulting domain and the steady-state solution for unsaturated flow was calculated using the dual mixed-finite-element method. Particle tracking simulation based on the numerical solution of the flow field was used to calculate the travel times of individual water particles from the potential repository horizon to the water table. The resulting distribution of groundwater travel time is influenced by both: 1) the spatial variability of flow within individual realizations of the system and 2) the variabilities and uncertainties of the hydrostratigraphic units and the hydraulic parameters.

1.4 Caveats

Because of the limited goals and simplifying assumptions of the 1994 work, the results obtained are not to be considered as GWTT determinations suitable for comparison to the regulations. However, the results will be compared to the requirements and used as guidance for further analysis and for prioritizing site-characterization activities. The sensitivities of the results to model-domain parameters and the flow model will be evaluated as a guidance for site characterization activities, and for use in subsequent iterations.

A complete GWTT evaluation must include unsaturated-zone flow, saturated-zone flow, a definition of the disturbed zone, the interactions among these elements, and evaluation of the distributions of GWTT. The 1994 work addresses only portions of the flow components. However, the model-development process and sensitivity analyses identified several factors that strongly affect fracture flow of groundwater at the site. Therefore, the results of this study can provide the basis for future investigations and modeling activities.

1.5 Data Sources and Participants

An effort was made to incorporate the most current hydrologic and physical data available. The data set is an enhancement of that used for the recent TSPA-93 analyses (Wilson et al., 1994; Schenker et al.[1]). Some aspects of the data development have gone beyond the previous TSPA work, including refinements of the geostatistical simulations and scaling of parameters.

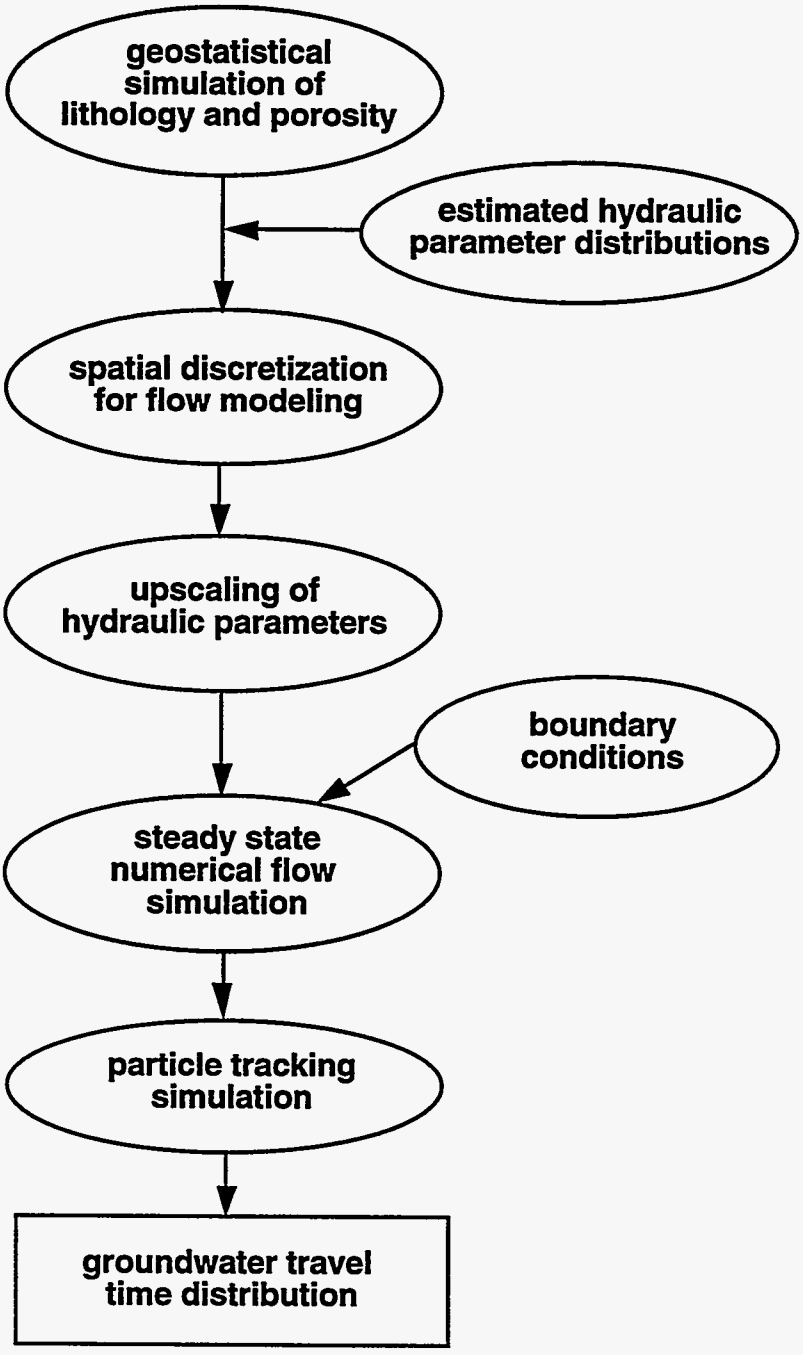

Figure 1-2. Flow chart of the groundwater travel time calculation. Note that multiple realizations of the domain, flow simulations, and particle-tracking simulations were used to calculate a combined groundwater travel time distribution.

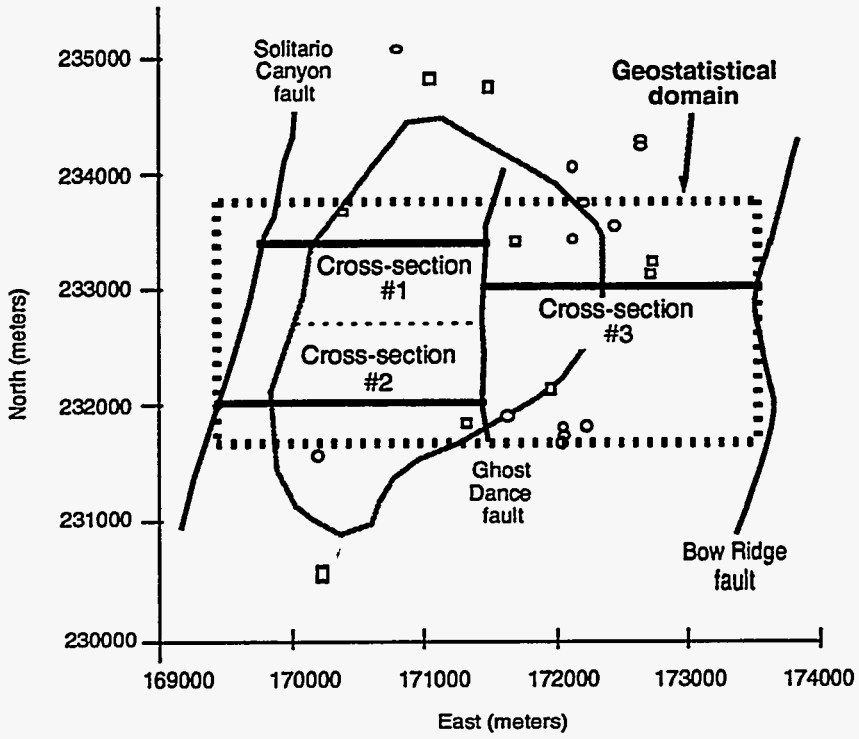

Figure 1-3. Location of cross-sections. Circles and squares show the locations of drillholes used as sources of conditioning data for geostatistical indicator simulations.

This effort has benefited from the contributions of numerous people. The GWTT Working Group established by DOE (E. Smistad (DOE), J. Duguid (Intera), L. Berkowitz (TRW), and R. Barnard (SNL)) has established the overall strategy for addressing the GWTT issue. Data provided by the USGS (A. Flint), and interpreted by LBL (G. Bodvarsson) have been incorporated into the models. Geostatistical modeling and scaling have been provided by C. Rautman and S. McKenna of SNL.

This page intentionally left blank.

Chapter 2
Conceptual Model

Once the purpose of conducting a groundwater modeling project has been established, it is essential to produce a conceptual model of the system before undergoing the numerical modeling procedure.(Anderson and Woessner, 1992). A conceptual model should include as much as is known about the hydrostratigraphic units and system boundaries as field data permit. The purpose of this chapter is to introduce the conceptual model used for the 1994 GWTT calculations. A conceptual model of the hydrogeologic conditions at Yucca Mountain is based on the general understanding of unsaturated and saturated flow in fractured porous media as well as data on the geology and existing flow conditions at the potential site. Since site-specific hydrologic data are sparse, geographically uneven, and uncertain, the conceptual model must take into account all the reasonably possible flow conditions. This conceptual model provides the basis for construction of numerical models of the site and the sensitivity analysis of those models.

This chapter contains a description of site hydrology, including the general geology of the site, surface conditions, and description of unsaturated and saturated hydrologic conditions. Chapter 3, Parameter Development, should be referred to for more detailed information on the hydrogeologic parameters. A history and description of conceptual models of the Yucca Mountain area is presented in Section 2.2. Linking the various conceptual models to possible numerical implementations is explained in Section 2.3. Finally, Section 2.4 provides a description of the conceptual model as implemented for the 1994 calculations.

2.1 Yucca Mountain Site Hydrologic System

2.1.1 Geology

Yucca Mountain is part of the southwestern Nevada volcanic field in the southern Basin-and Range physiographic province. The rock units of the region include Paleozoic sedimentary and metasedimentary rocks, several late Mesozoic quartz monzonitic and granodioritic intrusions, Cenozoic silicic and basaltic volcanic sequences, and recent alluvial deposits (e.g., Carr, 1988). The rock units underlying the site are the Miocene silicic ash-flow and air-fall tuffs erupted from the Timber Mountain-Oasis Valley caldera complex, immediately north of the potential repository site (e.g., Byers et al., 1989). The basement is formed by Paleozoic carbonate rocks which generally lie far beneath the water table. Within the volcanic sequence, the individual Member-level stratigraphic units correspond to major volcanic eruptive events. The tabular sheets of alternating welded and nonwelded tuffs are relatively uniform in thickness, typically several hundreds of meters thick. While all units are not completely continuous throughout the Nevada Test Site (NTS) region, there is a high degree of predictability of the geometry of the units due to an understanding of their formation. The major welded ash-flow tuffs are usually separated by

thinner intervals of nonwelded or poorly welded ash flows, air-fall tuffs, and reworked tuffaceous materials. A description of the hydrogeologic units of importance for this study is included in Table 2-1. The relative stratigraphic positions of the thicker units along with the approximate location of the potential repository are shown in Figure 2-1. The potential repository horizon is within the Topopah Spring Member of the Paintbrush Tuff (TSw). Surficial exposures at Yucca Mountain include the welded ash-flow tuffs belonging to the Tiva Canyon Member of the Paintbrush Tuff (TCw), Paintbrush nonwelded interval (PTn) and the TSw along Solitario Canyon on the western side of Yucca Mountain.

Table 2-1. Hydrogeologic units at the Yucca Mountain Site.

Unit ID	Hydrogeologic Unit	Description
TCw	Tiva Canyon welded	Moderately to densely welded, devitrified ash-flow tuffs belonging to the Tiva Canyon member of the Paintbrush Tuff.
PTn	Paintbrush nonwelded interval	Nonwelded to partially welded, vitric and locally devitrified tuffs belonging to the lowermost Tiva Canyon member, Yucca Mountain member, Pah Canyon member and uppermost Topopah Spring member of the Paintbrush Tuff; also includes air-fall tuffs, "bedded tuffs", and intercalated reworked tuffaceous sediments.
TSw	Topopah Spring Welded	Moderately to densely welded, devitrified ash-flow tuffs including the upper vitrophyre belonging to the Topopah Spring Member of the Paintbrush Tuff.
TSbv	Topopah Spring basal vitrophyre	Densely welded basal vitrophyre belonging to the Topopah Spring Member of the Paintbrush Tuff.
CHnv	Calico Hills vitric	Lowermost nonwelded to partially welded part of the Topopah Spring lying underneath the basal vitrophyre and nonwelded to partially welded, vitric and locally argillic ash-flow, bedded, and reworked tuffs of the tuffaceous beds of the Calico Hills.
CHnz	Calico Hills zeolitic	Nonwelded and partially welded zeolitic tuffs of the tuffaceous beds of the Calico Hills and the bedded tuffs overlying the Prow Pass Member.
PPn	Prow Pass nonwelded	Nonwelded and partially welded ash-flow tuffs belonging to the Prow Pass Member of the Crater Flat Tuff.
PPw	Prow Pass Welded	Moderately welded ash-flow tuffs belonging to the Prow pass Member of the Crater Flat Tuff.
BFw	Bullfrog welded	Moderately welded ash-flow tuffs belonging to the Bullfrog Member of the Crater Flat Tuff
BFn	Bullfrog nonwelded	Nonwelded to partially welded ash-flow tuffs belonging to the Bullfrog Member of the Crate Flat Tuff.

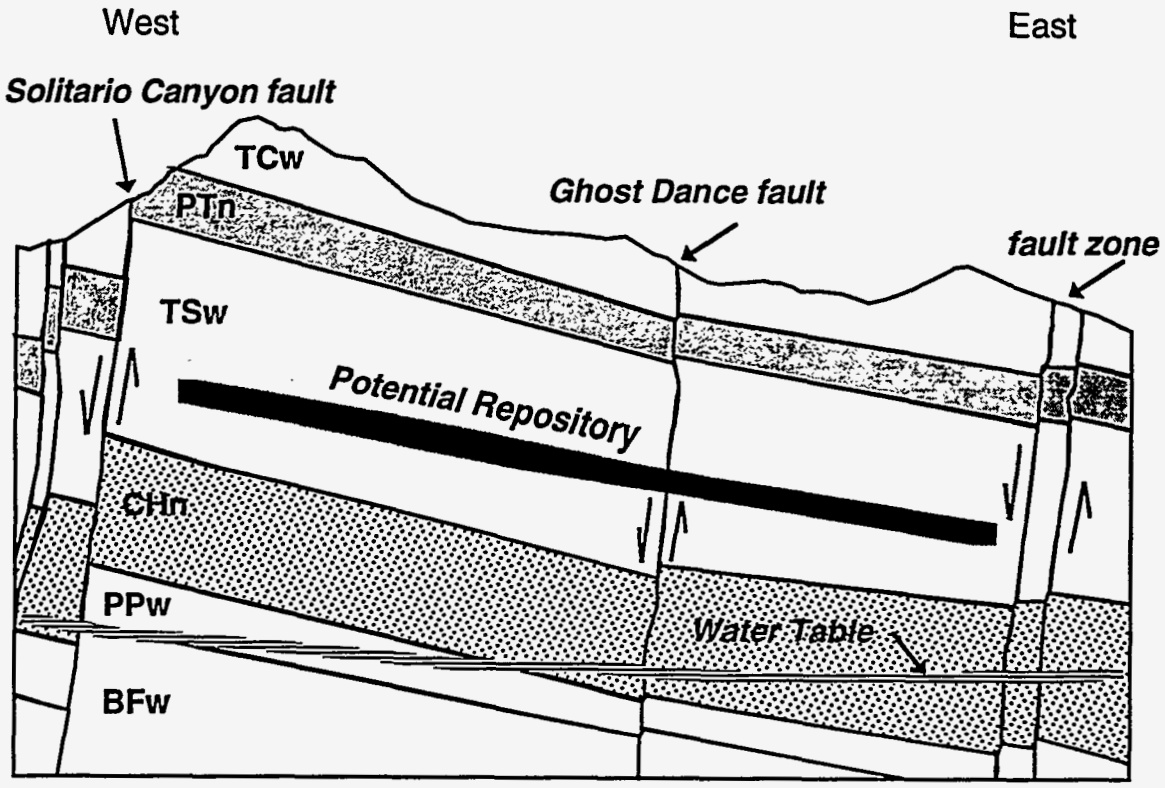

Figure 2-1. Schematic cross-section of the potential Yucca Mountain repository region.

The tuffs have been gently tilted toward the east by generally north-trending Basin and Range block faulting. Yucca Mountain itself consists of a large, relatively unfaulted block (e.g., Scott, 1990). The main block of Yucca Mountain is bordered to the west by Solitario Canyon fault, a major normal fault with more than 300 m displacement at the southern end of Yucca Mountain, and on the east by the Bow Ridge fault, a more diffuse zone of normal faulting (Figures 2-1 and 1-3). The repository block is transected by the north-trending Ghost Dance fault. The displacement on the Ghost Dance fault is 30 m down on the west side near the southern edge of the potential repository area with displacement decreasing to the north. Near the northeastern edge of the potential repository area the fault changes into a zone of highly fractured and brecciated rock (Scott and Bonk, 1984). Recent, more detailed structural mapping of the Ghost Dance fault has discovered the presence of several additional dominantly north trending sub-parallel faults on both sides of the Ghost Dance fault with offsets 3 to 6 m down to the west (Spengler et al., 1993). Another, newly mapped, near-vertical, northwest-trending structural zone within the repository is the Sundance Fault system (Spengler et al., 1994). Mapping of this system is preliminary, so relative age relationship of the Sundance fault system to the Ghost Dance fault remains unresolved. In summary, in the region of the repository both north trending, dip-slip faults (e.g. the Solitario Canyon, Ghost Dance, and Bow Ridge faults) and northwest trending strike-slip faults with potential wide zones of fractures (e.g. the Sundance fault) are recognized.

Fractures are found in all lithologic units at the site. The existing fractures generally can be divided into two groups: tectonic fractures and cooling fractures. Tectonic fractures may cross cooling unit contacts, whereas cooling fractures are confined to individual intervals corresponding to a cooling event. In general, the densely welded tuffs are highly fractured, while fractures in the nonwelded units are less frequent. For example, expected fracture frequency values for the non-welded units range from 1.0 to 1.4/m, whereas the range of expected fracture frequency for the welded units is 1.0 to 4.5/m. There are, however, variations in fracture density within and between lithologic units due to the differences in the mechanical properties and cooling history of the rocks, as well as the location of the unit relative to faults and the ground surface. Generally, higher fracture frequencies are observed near faults. In contrast to this observation, very few fractures were observed close to the Bow Ridge fault in the Exploratory Studies Facility (ESF). This is thought to occur because the fault itself is taking up the stress. Measurements of fracture aperture are minimal, but expected aperture ranges derived from measured fracture frequencies and air permeability, using the parallel plate theory (Snow, 1970) range from 4.3 μm to 2,380 μm. Fracture dip for the welded tuffs can generally be categorized into two groups; the majority of fractures are nearly vertical and a secondary group exists of nearly horizontal fractures (DOE, 1993).

On the ground surface of most of the Yucca Mountain area, a layer of alluvium covers the volcanic rocks. The thickness of the alluvium varies, tending to be thickest in washes and channel bottoms where surface runoff accumulates and thin to non-existent on ridge tops and steeper side slopes. Thicker alluvial deposits also exist on top of terraces of the side slopes. Existing soils on the ridge tops are fairly well developed and thin calcium carbonate layers are occasionally present within the soils. In contrast, channel soils have varying degrees of calcium carbonate cementation, which is often extensive (Flint et al., 1994).

2.1.2 Surface Hydrology

The average annual precipitation has been estimated to be 17 cm in the vicinity of the potential repository (Hevesi et al., 1992). Two types of storm events typically occur at the mountain: 1) regional, low-intensity winter storms which tend to last 1 to 2 days and with precipitation occurring as snow at higher elevations, and 2) more localized summer monsoon storms which tend to be of shorter duration but higher intensity (Hevesi and Flint, 1993). The winter storms generally occur from November to April, whereas the summer monsoon season is typically from July to August. There is generally more precipitation during the winter storms with a total precipitation measured from January 17, 1990 through October 11, 1993 of 58 cm for the winter storms, and 9.6 cm for the summer storms (Hevesi et al., 1994a). The spatial distribution of precipitation at the site is not well known and has only been monitored since 1990 (Hevesi et al., 1994b).

Once precipitation has reached the ground surface it has several potential fates: redistribution as runoff, reintroduction to the atmosphere through evapotranspiration, and infiltration into the groundwater system. All of these paths must be evaluated in order to determine an accurate flux of water into the unsaturated zone. The greatest amount of runoff is

likely to occur in summer months due to the high intensity of the monsoon storms. The amount of runoff from a basin depends on the surface area of the drainage basin and the amount of the precipitation that becomes runoff. The areas with the steepest slopes will usually have a higher percentage of runoff than areas with more level terrain. Runoff tends to be concentrated in the washes. The unsaturated hydraulic conductivity of the sediments or rocks at the surface will also influence whether the water will infiltrate the ground surface or flow as runoff.

Water can be subject to evaporation or transpiration either on the ground surface or in the shallow alluvium or bedrock. Evapotranspiration is greatest during the summer months due to increased plant activity and solar radiation. Calculated potential evapotranspiration (PET) in the Yucca Mountain area using the Priestly-Taylor equation ranged from approximately 0 mm/day to 5 mm/day (Hevesi and Flint, 1993). However, the calculations of PET do not take into account the episodic nature of precipitation, timing and form of precipitation, or limitations on the evapotranspiration rate caused by the hydraulic conductivity of the sediments. The spatial distribution of evapotranspiration is a function of the amount of solar radiation received, relative humidity, wind speeds, and the type and density of vegetation. The amount of radiant energy received is lower on north-facing slopes and in shaded areas than on exposed or level areas or slopes facing south, east, or west. The depth to which evapotranspiration influences the groundwater is unknown. Seasonal wetting and drying of the alluvium was measured to a maximum depth of 2.5 m in three boreholes over the period from January, 1990 through October, 1993 (Hevesi et al., 1994a).

Shallow boreholes, "neutron holes", have been drilled throughout the Yucca Mountain area to obtain water-content profiles using a neutron-backscatter moisture probe. These boreholes are not present on steep sideslopes where access by a drilling rig is limited. Monthly water-content data have been obtained in 34 of these boreholes (with depths ranging from 6 to 19 m) at 0.1-m depth intervals in order to evaluate shallow infiltration at different topographic regions at the site (Flint et al., 1994). Net infiltration was determined from these data by evaluating the depth of the wetting front below the zone influenced by evapotranspiration. Conceptual models of relative infiltration have been developed based on these studies (Flint et al., 1994) (see section 2.2.1). Present-day flux into Yucca Mountain has been estimated for each of the exposed units based on the relative saturation of the unit at a steady state depth, the moisture retention functions of that unit and the estimated relative permeability using Darcy's Law (Table 2-2) (Flint and Flint, 1994). Fluxes into the mountain actually vary significantly within a unit depending on the locations of the outcrop and the thickness of the alluvium overlying the tuff.

2.1.3 Subsurface Hydrology

The hydrologic conditions controlling subsurface, unsaturated flow include: amount, timing and distribution of precipitation, evapotranspiration, and runoff, surface water-groundwater interactions, water distribution in the unsaturated zone, fracture-matrix fluid interactions, and capillary pressure gradients. The geologic conditions controlling subsurface flow include: distribution, interconnection and aperture of fractures and pores, and distribution and hydraulic characteristics of fault zones.

Table 2-2. Estimates of Average Present-Day Flux into Yucca Mountain (Flint and Flint, 1994).

Surface Unit	Present Day Flux (mm/year)	Surface Unit	Present Day Flux (mm/year)
Tiva Canyon- caprock	0.04	PTn	13.40
Tiva Canyon- moderately welded	0.22	Rainier Mesa - partially welded	0.60
Tiva Canyon- welded	0.02	TSw	0.08

2.1.3.1 Unsaturated zone

Subsurface hydrology in the unsaturated zone (UZ) has been observed through the drilling of boreholes and examination of the hydrologic properties of the boring cores. Measurements of hydrologic parameters such as bulk density, porosity, particle density and *in situ* saturation, gravimetric water content, and saturated hydraulic conductivity have been made on core samples in most of the geologic units. In addition, testing in the boreholes, such as air-permeability tests of the fracture permeability (LeCain and Walker, 1994) and measurements of *in-situ* temperature, pneumatic pressure and water potential (Kume and Rousseau, 1994) are being conducted. Additional hydrogeologic parameters have been measured along transects of outcrops (Flint et al.[2]; Istok et al., 1994). Measured matrix saturations vary from unit to unit, tending to be lower in the higher porosity units such as the PTn (Figure 2-2).

Perched water has been observed in several of the drillholes (Table 2-3). There is some question as to whether the perched water found in borings drilled in Drillhole Wash is natural or drilling fluid that was lost during the drilling of USW G-1. UZ-1 was drilled in 1983 and there is not as much documentation for the hole. Drilling stopped when the perched water was found at 387 m. It is believed that this water was in the Calico Hills, but this is not certain. Recently (March 1995), what is thought to be perched water was found in boring SD-7. The water was encountered at 480 m below the ground surface, 59 m below the top of the Calico Hills. Investigations are presently taking place on the water encountered in SD-7 (pump tests, geochemical and isotopic analyses).

2. Flint, L.E., A.L. Flint, C.A. Rautman and J.D. Istok, (in review), *Physical and Hydrologic Properties of Rock Outcrop Samples at Yucca Mountain, Nevada.* Open-File Report 95-280. Denver, CO: U.S. Geological Survey.

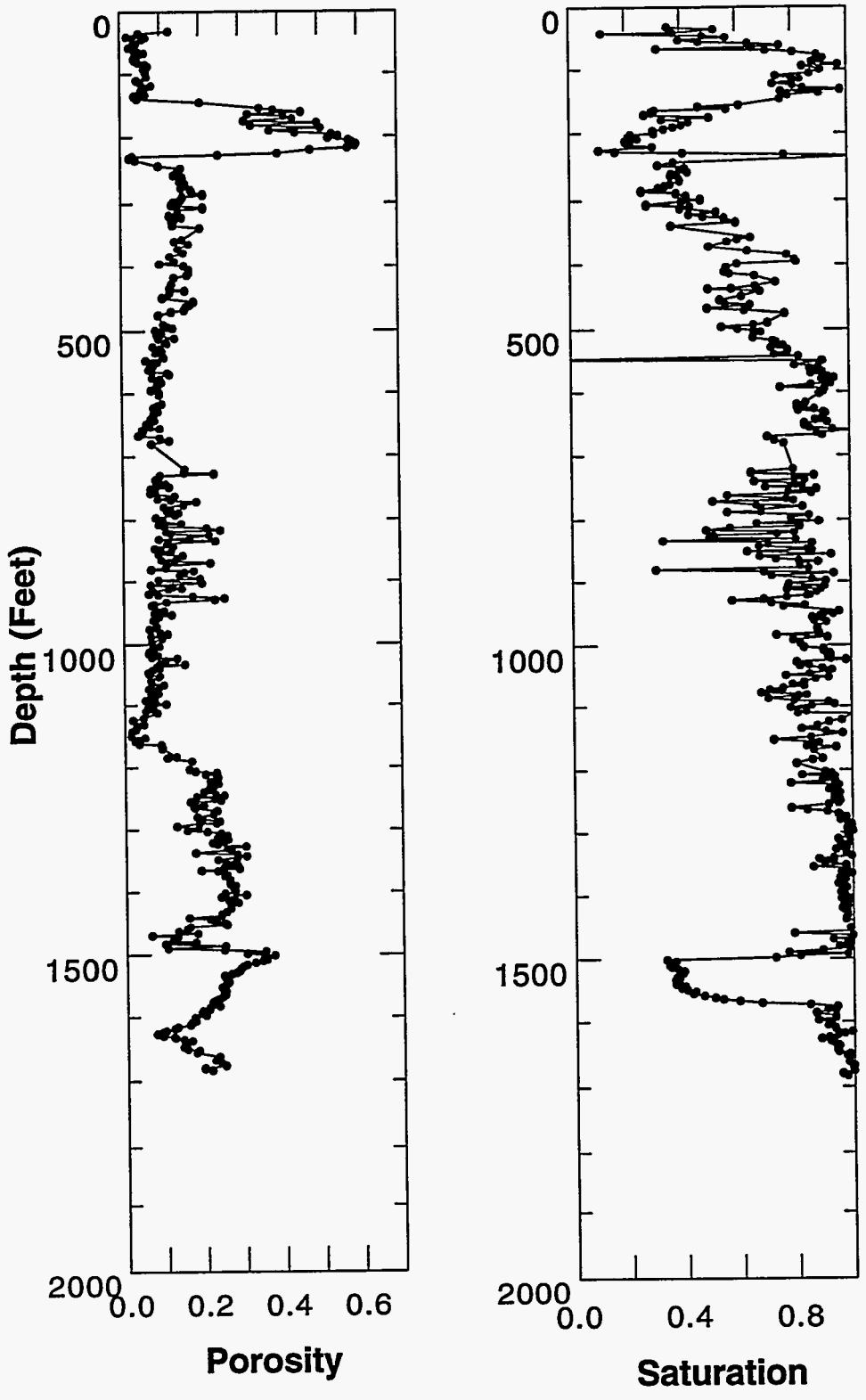

Figure 2-2. Example distribution of porosity and liquid saturation in the UZ at Yucca Mountain as observed in drill hole UZ-16.

Table 2-3. Occurrences of Perched Water in Boreholes.

Boring	Depth to Perched Water (m)	Elevation of Perched Water (m)	Unit in which Perched water was Encountered	Polymer Drilling Fluid from USW G-1?
UZ-14	384.6	956	Basal portion of the Topopah Spring Tuff non-lithophysal unit. Water appeared to be perched on clay layer developed on top of the welded basal vitrophyre of the Topopah.	traces
NRG-7/7A	460.2	822.1	Non-welded base of the Topopah Spring Tuff. The water was perched on top of the Calico Hills Tuff.	Yes
SD-9*	452.3	843.1	Calico Hills, 15 feet below the upper contact of the Calico Hills with the Topopah Spring Tuff.	Yes
UZ-1	387	962.0	Calico Hills?	Yes

* - SD-9 is located in Coyote Wash (south of Drillhole Wash)

2.1.3.2 Saturated Zone

Groundwater flow in the saturated zone under Yucca Mountain occurs in the Cenozoic volcanic rocks and the underlying Paleozoic sedimentary strata. The Paleozoic strata beneath Yucca Mountain are part of the regionally extensive carbonate aquifer of the south-central Great Basin (Winograd and Thordarson, 1975). At the present time, direct observation of the saturated zone is limited to 30 drill holes. Depth to the water table varies from approximately 275 m in valley floors to about 750 m at ridgetops in the vicinity of the site (Czarnecki and Luckey, 1989). The general configuration of the water table indicates groundwater flow from the northwest to the southeast at the site. The magnitude of the horizontal hydraulic gradient, as indicated by the potentiometric surface, varies dramatically across the site (Robison, 1984). Beneath most of the potential repository and to the south and east, the hydraulic gradient is very small (about 0.0001). Directly to the north of the repository, the water-table elevation increases by approximately 300 m, defining a region with a large hydraulic gradient (>0.15). Another significant step in the water table occurs to the west of the potential repository, where the horizontal hydraulic gradient is >0.03. Anomalously low heat flow measurements and variations in temperature at the water table (Sass et al., 1988) indicate the possibility of significant vertical flow of groundwater at the site.

2.2 Conceptual Models of the Hydrogeologic System

The location and orientation of paths of significant groundwater flow depend on the distribution of relevant hydraulic properties, the boundary conditions of flow, and the nature of flow processes. All of these factors are dependent on both the geology of the site (lithology, topography, and geologic structure) and the existing hydrologic conditions. Analysis of fast-path flow in the UZ is particularly sensitive to the conceptualization of flow processes.

2.2.1 Unsaturated Flow

2.2.1.1 Boundary Conditions

Alternative conceptual models of UZ flow used in recent performance assessments are consistent in that infiltration at the ground surface is the primary source of groundwater in the UZ flow system. However, the magnitude and distribution of infiltration vary among different conceptual models. Montazer and Wilson (1985) believed that infiltration occurs episodically during large precipitation events and is focused in fractures in the TCw. They further proposed that runoff which is concentrated in washes leads to increased infiltration in these areas. Flint et al. (1994) asserted that infiltration is higher on sideslopes and ridge tops because of lower evapotranspiration due to the presence of clay soils and bedrock fractures, whereas infiltration is lower in active channels and terraces due to greater evapotranspiration of moisture stored in relatively thick alluvium. Because of differences in solar radiation and evapotranspiration between south-facing slopes and north-facing slopes, increased infiltration on north-facing slopes has been proposed. Variations in infiltration depending on outcropping bedrock unit were proposed by Flint and Flint (1994) (see Table 2-2).

Shallow infiltration is a transient process due to seasonal variations in precipitation and the episodic nature of recharge events. The depth at which transient infiltration is "averaged" into net infiltration depends on the conceptualization of shallow infiltration processes and on the conceptual model of fracture-matrix flow interaction processes at greater depths. The depth to which evapotranspiration-induced flow will occur is unknown. The choice of a steady-state or transient conceptual model of flow is partially dependent on the conceptualization of infiltration processes.

Major dip-slip faults have been invoked as lateral boundaries to groundwater flow in the UZ in conceptual models of the flow system either because flow was assumed to be primarily vertical or because the faults were assumed to be barriers to lateral flow (Montazer and Wilson, 1985; Wang and Narasimhan, 1985, 1986, 1988). The actual influence of faults on the groundwater flow system is uncertain. Faulting produces uneven, offset, and discontinuous boundaries between lithologic units. The juxtaposition of units with different hydraulic properties may either impede or focus groundwater flow. The hydraulic properties of the brecciated zones and the potential effect on groundwater flow is unknown. The brecciated zones may create either a barrier to unsaturated groundwater flow or a path of preferential saturated groundwater flow, depending on the persis-

tence of large pore spaces with depth. Clay-rich fault gouge may impede lateral unsaturated groundwater flow by reducing porosity and hydraulic conductivity. However, if there is lateral flow in the unsaturated zone toward the fault, the increase in water content around the fault may cause the zone to become a preferential flow path. All of these factors may lead to the downward diversion of any lateral groundwater flow at fault zones.

The lower boundary of the UZ flow system is the water table, with pressure equal to atmospheric pressure. Because the low rate of infiltration in the local UZ flow system can be assumed to have little influence on the elevation of the water table and because the location of the water table has been directly measured in drill holes, the water table serves as the constant-pressure lower boundary in all of the conceptual models presented here.

2.2.1.2 Flow Processes

Groundwater flow in the UZ can occur as flow in the matrix and as flow in fractures (Figure 2-3). The nature of the interaction of flow between matrix and fractures has important implications in the conceptualization of the flow system. Figure 2-4 depicts some of the possible simplified modeling scenarios based on alternative conceptual models. The first set of scenarios assumes that the system can be represented using a steady-state flow simulation. The simplest assumes that flow occurs exclusively in the matrix (scenario A); fractures do not participate in the flow process, but may act to impede unsaturated flow in the matrix. Conversely, another highly simplified representation of the system assumes that the most significant flow path is through the fractures (scenario B) (see also Figure 2-3). To sustain steady-state fracture flow in an unsaturated system, either the unsaturated flow occurs as movement of a thin film along the fracture surface, or the fracture must remain fully saturated. A more general conceptual model of the UZ flow process is that flow occurs in both the matrix and the fractures (scenario C), being dominated by flow in either the matrix or the fractures depending on the local hydrologic conditions. In a locally saturated area there can be flow from the matrix to the fractures (see Figure 2-3). The transient-flow scenario recognizes the episodic nature of infiltration events and includes the propagation of saturated flow pulses from the surface in fractures. The significance of transient flow to the analysis of fast-flow paths in groundwater travel time depends on the depth to which saturated pulses penetrate before imbibition into the matrix. The possible numerical formulations, as explained in Section 2-3, corresponding to each of the conceptual modeling scenarios are also shown in Figure 2-4.

The earliest models of the Yucca Mountain site included only the conceptual models of unsaturated groundwater flow. Montazer and Wilson (1985), Wang and Narasimhan (1985, 1986) and Sinnock et al. (1984) proposed different conceptual models of the unsaturated flow system. These models were developed in an attempt to visualize the large-scale flow system at the site and the potential changes in the hydrology due to the presence of an HLW repository. Montazer and Wilson (1985) believed that infiltration occurring during large precipitation events is focused in fractures in the TCw and diverted laterally by the PTn. Lateral flow continues until it reaches a fault, where the water moves downward. They speculated that perched water zones occur at these fault boundaries. Wang and Narasimhan's conceptual model had transient flow occurring primarily in fractures with dissipation of the transient pulse by the nonwelded Paintbrush tuff. In this model, flow is primarily vertical, with some lateral diversion of flow due to inclined hydrologic units

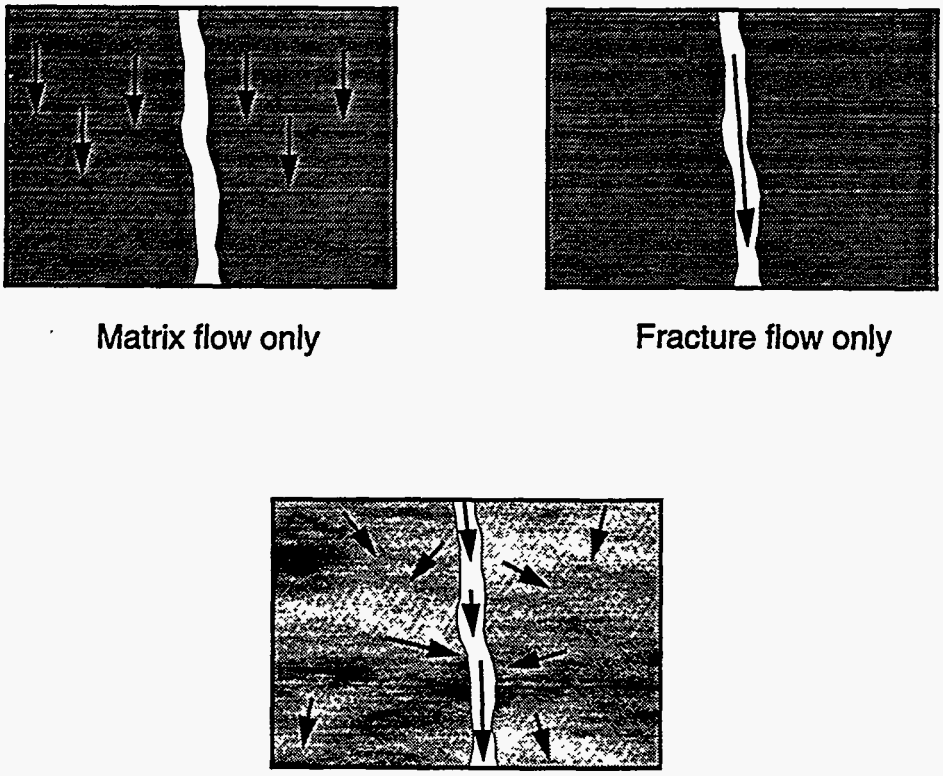

Figure 2-3. Alternative conceptualizations of flow in fractured porous media.

(Wang and Narasimhan, 1985, 1986, 1988). In their model, Sinnock et al. (1984) assumed the unsaturated flow at the site is one-dimensional, transient, and occurring only in the matrix.

Previous research efforts have shown that the conceptual model of flow processes influences numerical modeling results. The initial numerical models of the UZ were based on the assumption that flow would occur primarily in the matrix and that fractures would tend to act as flow barriers (Kaplan, 1993; Dudley et al., 1988; Bloomsburg et al., 1989; Lin and Tierney, 1986). Calculations made using these models indicated that, in the absence of preferential flow paths, the site probably meets the GWTT criteria. The observations of flowing fractures and perched water zones prompted researchers to use existing saturated fracture-flow models to analyze flow in the UZ (Wilson et al., 1994). These models indicated that if sustained saturated fracture flow occurs, the GWTT will be less than 1,000 years. The unsaturated matrix and saturated fracture flow conceptual models represent extremes, not the actual conditions. Nitao and Buscheck's (1991) saturated fracture-flow model required a continuously ponded source of water at the ground surface, while the TSPA Weeps model (e.g. Barnard et al., 1992) used a constant-flux boundary condition to maintain the flow system. These conditions do not occur at the site.

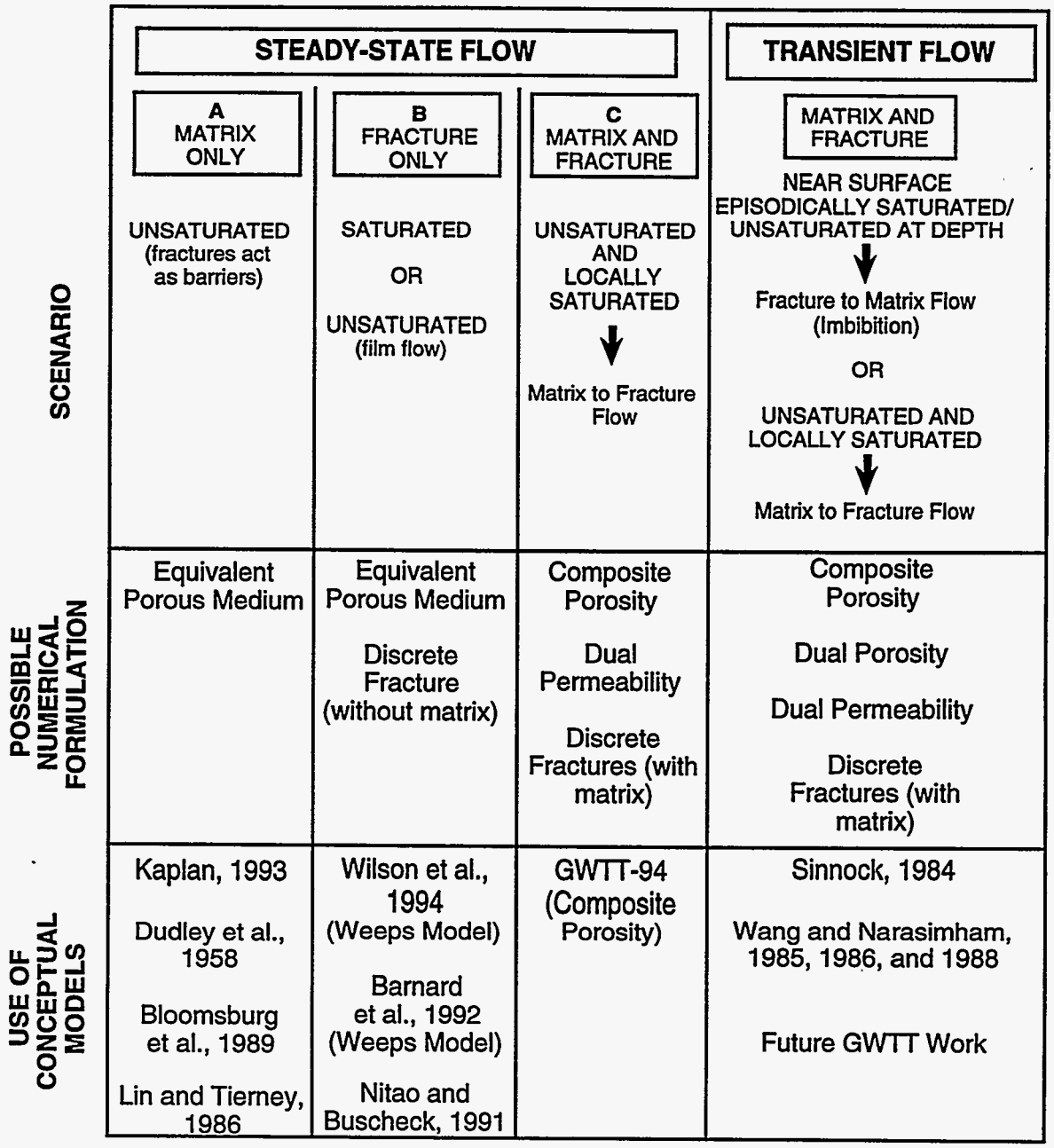

Figure 2-4. Possible modeling scenarios for groundwater flow in the UZ.

2.2.2 Saturated Zone

The conceptual model of groundwater flow in the saturated zone (SZ) within both the volcanic units and the Paleozoic carbonate aquifer is that flow occurs predominantly in the fracture network. The fastest paths to the accessible environment occur in the areas with the optimum combination of steep gradient and fracture conductivity. These fast SZ paths may or may not be in hydraulic connection to the fastest UZ paths. Factors that influence the connection of the fast paths in the two systems include the locations of the SZ fast paths relative to the UZ fast paths and the cross-unit fracture connectivity. The degree of interaction between flow in the fractures and matrix may influence groundwater travel times in the system.

Conceptual models of the saturated zone proposed by Czarnecki and Waddell (1984), Czarnecki (1985), Czarnecki (1989), Sinton (1989), and Fridrich et al. (1994) differ primarily in the processes controlling the high-gradient zone north of the site. The primary representations of the system are the diversionary and non-diversionary fault models (Fridrich et al., 1994). Fridrich et al. (1994) recommended identifying individual hydrostratigraphic units by the degree of welding, style of crystallization, fabric, secondary alteration, tectonic fracturing, and faulting. Their conceptual model predicted that zones of high hydraulic conductivity will exist in the densely welded tuffs and coarse-fabric tuffs, and parallel to faults. All the saturated zone conceptual models describe a three-dimensional flow system through a faulted, fractured porous medium.

2.3 Implementation of Conceptual Models

Implementation of a conceptual model of groundwater flow for GWTT calculation requires a numerical formulation of the relevant flow processes in the UZ. The numerical formulation of flow processes, when combined with material properties and boundary conditions, forms the basis for numerical modeling of the flow system. Numerical formulations of groundwater flow vary in complexity in relation to the flow processes represented (i.e. matrix and fracture) and the interactions between these processes in unsaturated flow. The range of numerical formulations of groundwater flow in fractured media is shown in Figure 2-5. The following discussion summarizes possible numerical formulations of flow processes and relates them to alternative conceptual models.

In the equivalent-porous-medium formulation, the medium is represented as a single continuum, for which porosity, saturated hydraulic conductivity, moisture-retention relationship, and relative-permeability relationship are defined. The equivalent-porous-medium formulation is appropriate for implementation of conceptual models in which flow occurs entirely in the matrix domain or entirely in the fracture domain.

The composite-porosity or equivalent-continuum formulation incorporates hydraulic properties of both the matrix and fractures into a single continuum representation (Klavetter and Peters, 1986). Composite values of porosity and saturated hydraulic conductivity are used in this formu-

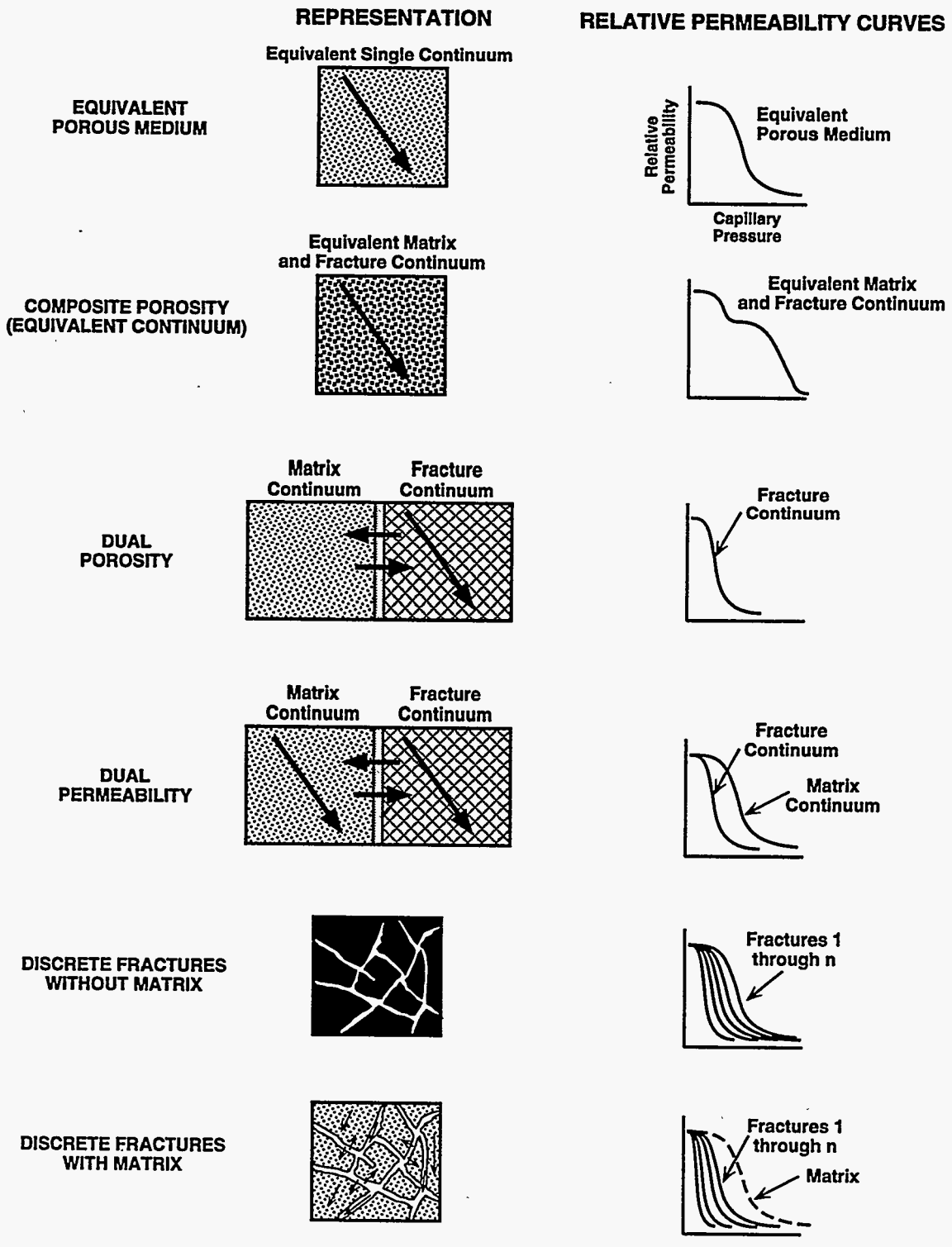

Figure 2-5. Alternative numerical formulations of flow processes in the UZ.

lation, but the relative-permeability relationship contains aspects of both matrix and fractures (see Figure 2-5). An important implication of the equivalent-continuum formulation is that capillary pressure is equal in the matrix and fracture domains. Because of the characteristics of the composite relative-permeability relationship, groundwater flow at higher (fracture) velocities only occurs under nearly saturated conditions. The composite-porosity formulation is applicable to conceptual models in which flow occurs in both the fractures and matrix. However, this formulation cannot explicitly account for groundwater flow between the fracture domain and the matrix domain nor for capillary pressure disequilibrium between them.

In the dual-porosity formulation, flow is assumed to occur only in the fracture continuum, but groundwater may be exchanged between the fracture domain and the matrix domain (Warren and Root, 1963). A separate value of porosity and moisture-retention relationship is used for the matrix and fracture continua. Other hydraulic properties only apply to the fracture continuum. Flow between the fracture continuum and matrix may be limited by a conductance term. Because the matrix serves only as storage for groundwater in this formulation, its application is limited to the conceptual model in which groundwater flows only in the fracture domain under transient conditions.

Groundwater flow occurs in both the matrix continuum and the fracture continuum in the dual-permeability formulation. Consequently, all of the hydraulic parameters have separate values in the matrix and the fracture domains. Conductance of flow between the matrix and fracture continua may be controlled by an additional parameter (see Figure 2-5). The dual-permeability formulation is the most general of the continuum numerical formulations, explicitly accounting for groundwater flow both within and between the matrix and fracture domains. This formulation is appropriate to the implementation of conceptual models in which flow occurs in both the matrix and fractures under transient or steady-state conditions.

In the discrete-fracture formulation, the fracture domain is not considered to be a continuum, but flow through individual fracture segments within the fracture network is explicitly represented (Figure 2-5). The hydraulic properties of each fracture are assigned individually. Flow within the matrix may or may not be included in the discrete-fracture formulation. Because fracture networks generally do not display continuum behavior at smaller scales (relative to fracture density) or in cases of low fracture connectivity, the discrete-fracture formulation is necessary to represent the fracture domain under these circumstances. The discrete-fracture formulation is the most general of those presented here, but is infrequently employed due to lack of specific data on the fracture network and computational limitations.

2.4 GWTT-94 Conceptual Model of the Unsaturated Zone

The modeling process in this study was based on a revised conceptual model of the site in which locally saturated flow zones occur within the unsaturated zone. This conceptual model is consistent with observations of perched water within the UZ at the site. The initiation and propagation of flow in fractures is the focus of this conceptual model to represent fast-path flow in the analysis. The conceptual model serves as a basis for the numerical modeling which is designed to

simulate UZ groundwater flow at the Yucca Mountain site in order to answer the question of whether the site meets the criterion for pre-waste-emplacement GWTT.

2.4.1 Geological Representation

Locally saturated conditions in the UZ form when groundwater flux through a region exceeds the ability of the medium to conduct water from the region under unsaturated conditions. The primary factor controlling the occurrence of perched water is the contrast in the hydraulic properties of the medium on the local scale. Thus, the geological conceptualization used in this study includes the locally heterogeneous material properties which can lead to the occurrence of locally saturated conditions. The heterogeneous distribution of material properties may also lead to the focusing of groundwater flux through some regions of the flow field. This focusing effect can only occur in a multi-dimensional medium; therefore, the conceptual model is two-dimensional. Both inter-unit and intra-unit heterogeneity of hydraulic properties were incorporated in the modeling of the geology of Yucca Mountain as explained in Chapter 3.

2.4.2 Boundary Conditions

The conceptual model of the boundary conditions at the upper surface of the UZ is steady-state, specified capillary pressure. The conceptual upper boundary is the steady-state depth at which transient infiltration becomes averaged into net infiltration, not the ground surface. This conceptualization, along with the assumption of climatic stationarity, allows the assumption of steady-state conditions throughout the UZ groundwater flow system. The upper boundary of the UZ may be conceptualized as either specified pressure or specified flux (infiltration). Pressure conditions can be inferred from measured saturation conditions and pressure-saturation relationships, whereas estimation of infiltration must also be based on relative-permeability relationships and assumptions on flow processes. In this sense, specified-pressure boundary conditions are more closely linked to observable conditions in the shallow subsurface and the conceptualization was chosen for this reason. Capillary pressure at the upper boundary was assumed to be constant within each of the hydrostratigraphic units for any given realization (i. e., there was no variability of capillary pressure as a function of topography within a unit).

The water table is the specified-pressure lower boundary of the conceptual model and the lateral fault boundaries are no-flow. The water table has fixed pressure head of zero. The faults which serve as the lateral boundaries of the model are assumed to divert any lateral groundwater flow downward. Vertical diversion of UZ flow would be expected at downdip faults if the fault zones have either high or low hydraulic conductivity.

2.4.3 Flow Processes

Unsaturated groundwater flow occurs in both the matrix and the fractures in the conceptual model employed in this study (see Figure 2-3). At lower values of saturation the flow is primarily within the rock matrix. Significant flow occurs within the fractures only at relatively high saturation. This relationship results from the assumption of capillary pressure equilibrium between matrix and fractures in this conceptualization. Implementation of this conceptual model of flow processes was accomplished using the composite-porosity (equivalent-continuum) formulation of flow. The composite-porosity formulation incorporates the flow characteristics of the matrix and fractures, but is computationally efficient (relative to the dual-permeability and discrete-fracture formulations). This conceptualization of flow processes in the UZ is consistent with the emphasis placed on simulating the initiation of fracture flow in the system by this study. The conceptual model used in this study can thus be located within scenario C in Figure 2-4.

This page intentionally left blank.

Chapter 3
Parameter and Model Development

Numerical modeling of groundwater flow in the unsaturated zone (UZ) for GWTT calculations was based on the conceptual models of Yucca Mountain geology and flow processes (Chapter 2) and included hydrogeologic parameters that have been derived from available data. Because of uncertainty and variability in both the geology and the hydrogeologic parameters, a probabilistic approach was adopted in this study. Uncertainty in the geologic interpretation of Yucca Mountain was incorporated through the use of geostatistical simulations to produce multiple, equally likely three-dimensional realizations of the hydrostratigraphic units. Variability of hydrologic properties within each unit was accounted for by the derivation of parameter probability density functions (PDFs) from which values are randomly drawn for individual locations in the system. The final model consisted of multiple realizations of heterogeneous, spatially correlated random fields of the relevant hydrogeologic parameters. Since the DUAL flow code (Chapter 4) simulates a two-dimensional domain, three cross-sections were selected for flow modeling.

3.1 Geostatistical Models of Hydrostratigraphy and Porosity

The thicknesses of hydrostratigraphic units and the locations of unit contacts can have significant effects on the results of numerical modeling of groundwater flow and particle travel times in the UZ. Though the volcanic stratigraphy of Yucca Mountain is highly layered and in many respects geologically simple, only limited drillhole data are available at and below the depth of the potential repository to confirm stratigraphic locations. Geological models of Yucca Mountain have been constructed for a variety of purposes through the subjective interpretation of lithostratigraphic and structural data (Ortiz et al., 1985; Wittwer et al., 1992; Buesch et al., 1993). Such models rely on the extrapolation or interpolation of stratigraphic and structural features based on conceptual models of the geologic processes involved in their genesis. These deterministic models of the internal geometry of the mountain do not explicitly account for geological uncertainty and variability. A stochastic approach, as implemented in this study, incorporates uncertainty and variability through the use of geostatistical techniques.

The strategy in this study was to geostatistically simulate the spatial distribution of individual hydrostratigraphic units using the indicator simulation method. A Gaussian simulation of a correlated random field was superimposed on the indicator simulation of the geologic units, and porosity values within each unit are derived from the random field in accordance with the PDF of porosity derived for that unit. All other relevant hydrologic parameters were directly or indirectly derived from the porosity values (see Section 3.2).

This approach assumes that the geostatistical description adopted for the system captures the spatial relationships of parameters that are relevant to the flow simulation and GWTT calculations. Ultimately, however, the geostatistical simulations of geology and porosity should be evaluated by comparison with subjective conceptual models of the Yucca Mountain site.

3.1.1 Indicator Simulation of Hydrostratigraphic Units

Indicator techniques are a class of non-parametric geostatistical methods that allow the incorporation of categorical data in estimation and simulation (Isaaks and Srivastava, 1989; Journel and Alabert, 1990). Categories may be a set of ranges for a continuous variable or a set of subjective discrete classes, as in the case of rock types. The indicator variable, I(x), is expressed mathematically as follows:

$$I(x) = \begin{cases} 1 \text{ if } z(x) \in category \\ 0 \text{ if } z(x) \notin category \end{cases} \quad (3\text{-}1)$$

where $z(x)$ is the categorical observation at spatial location x. Furthermore, the indicator variable may be a vector in which membership in one of multiple categories may be expressed at any spatial location. The indicator variable can be analyzed like any other spatially distributed random variable; the spatial correlation can be determined by construction of the variogram or can be assumed, based on geologic interpretation.

Once the spatial correlation of the indicator variable has been established, geostatistical simulation methods can be used to produce multiple, equiprobable realizations of the indicator field. The sequential indicator simulation (SIS) technique used in this study (Deutsch and Journel, 1992) discretizes the field into a regular grid. Initially, conditioning indicator-coded data are assigned within the grid. A random path is designated through the grid, visiting only once each grid node at which the indicator variable is unknown. At each grid node, a conditional cumulative distribution function (CDF) is calculated by indicator kriging, based on the conditioning data and any previously simulated nodes. A random number is drawn and, using the conditional CDF, an indicator value is assigned at that node. The process continues until the simulated random field is completely filled.

Detailed descriptions of the indicator simulation strategy along with a presentation of the geostatistical parameters used in this study are given in Rautman and Robey (1994) and Wilson et al. (1994). Simulations were three-dimensional, consisting of 466 east-west nodes (8.5 m in extent), 21 north-south nodes (100 m), and 775 vertical nodes (1 m). The volume simulated by the indicator method was bounded on the west by the Solitario Canyon fault and on the east by the Bow Ridge fault; the areal extent of the geostatistical simulation domain is shown in Figure 1-3. Simulations were conditioned on data from 25 drill holes and digitized data from geologic cross-sections of Scott and Bonk (1984). The model variogram consisted of two nested structures, and parameters used in the simulations are given in Table 3-1. The principal direction of anisotropy is horizontal, to the north.

All units were simulated with the same variogram model and included a dip of 6.7 degrees to the east. The horizontal/vertical anisotropy ratio is 50:1 to subjectively match the highly layered nature of the stratigraphy and to avoid (as much as possible) geologically unrealistic interfingering of welded and non-welded units. A nugget value of zero was used in all simulations (See Schenker et al.,[1] for a description of the variogram usage).

Table 3-1. Model variogram parameters

	Range (m)	Structure Weight (Sill)	Horizontal Anisotropy	Vertical Anisotropy
Structure 1	914	0.31	1.00	0.02
Structure 2	15,239	0.69	0.16	0.02

Indicator simulations were performed using the five indicator classes summarized in Table 3-2. The welded and nonwelded rocks were each subdivided into two separate categories to assist in the post-processing procedure. A search radius of 3000 m was used in the SIS algorithm, and a minimum of two conditioning data were used for each simulated node.

Table 3-2. Indicator classes

Indicator Class	Category	Hydrostratigraphic Units	Global Probability
1	general welded	TCw, TSw, BFw	0.665
2	nonwelded	PTn, PPn	0.170
3	nonwelded	CHnv, BFn	0.070
4	zeolitic	CHnz	0.068
5	welded	PPw	0.027

After the raw three-dimensional indicator simulations were performed, the indicator classes along the three cross-sections to be used in the flow simulations were extracted for post-processing. Geologically unrealistic artifacts are generated by the SIS method in regions of the simulation far from conditioning data. This occurs because in the early stages of the simulation process, the values at nodes distant from conditioning data or previously simulated points are simply selected from the global-probability CDF. Such statistically uninformed values then propagate as the simulation progresses, resulting in such geologically implausible situations as interfingering of welded and nonwelded units and older units overlying younger units. Post-processing was performed on all of the cross-sections to distinguish among the hydrostratigraphic units contained in a single indicator class (e.g., TCw, TSw, and BFw of indicator 1), remove some of the interfingering (e.g., moving TCw nodes up and TSw nodes down so the PTn is vertically contiguous), and add a continuous basal vitrophyre of constant thickness at the base of the TSw. The basal vitrophyre thickness which is constant for each particular simulation was stochastically drawn from the modeled PDF, which is based on drillhole data. An example post-processed simulation of the

hydrogeologic units is shown in Figure 3-1. Nine such simulations of hydrogeologic units were created, consisting of three realizations along each of three cross-sections.

3.1.2 Gaussian Simulation of Porosity

Unconditional simulations of the porosity field were created for each of the nine two-dimensional realizations of the hydrostratigraphic units. The resulting combined porosity and hydrostratigraphic fields were the basis for hydrologic parameter assignment and flow modeling within each cross-section.

The first step in generating the porosity field was to simulate a spatially correlated random field for each stratigraphic unit by the Sequential Gaussian Simulation (SGS) technique using the same nodal spacings as those used in the rock-type indicator simulations. The SGS method is conceptually similar to the SIS algorithm described earlier, except the simulated variable is continuous with a standard normal distribution (Deutsch and Journel, 1992). The geostatistical parameters used in the simulations were a horizontal range of 152 m, horizontal/vertical anisotropy of 4:1, and a search radius of 150 m. The horizontal range and anisotropy ratio were based on a preliminary estimate of the horizontal range of porosity from an outcrop study (Istok et al., 1991). Subsequent analysis has revealed highly deterministic vertical and horizontal trends in porosity in the PTn, indicating a much greater horizontal range than was used in the simulations in this study (Istok et al., 1994).

The second step in creating the porosity field was the back-transformation of the values generated by the SGS algorithm to convert the standard normal distribution to the beta distribution of porosity for each hydrostratigraphic unit. Development of the beta distributions of porosity for the hydrostratigraphic units is presented in Section 3.2.1. This process of back-transformation preserves the spatial correlation of porosity from the original simulation and reproduces the statistical distribution of porosity within each hydrostratigraphic unit. Simulated porosity fields for all nine simulations are shown in Figure 3-2.

3.2 Hydrological and Physical Parameters

The hydrological parameters porosity, pore-size distribution (mean and standard deviation), and saturated and unsaturated hydraulic conductivity are essential to characterize the hydrogeologic processes of Yucca Mountain. These parameters are required input data for the flow simulations (Chapter 4). As discussed in Section 3.1, probability distribution functions for porosity, using the most current data available were used to determine the porosity at each geostatistical node. From porosity, other parameters were estimated.

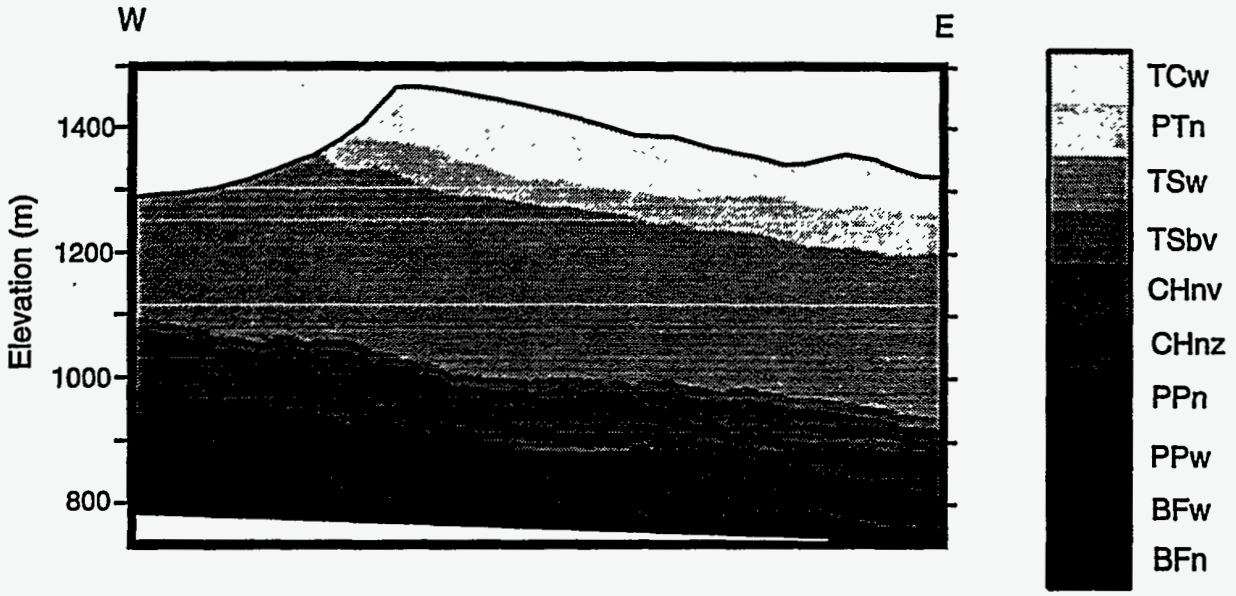

Figure 3-1. Post-processed indicator simulation of hydrostratigraphic units, cross-section 1b. The cross-section is bounded on the west by the Solitario Canyon Fault and on the east by the Ghost Dance Fault.

3.2.1 Porosity

Porosity data were obtained from drillhole cores. These data were checked to ensure the measured values were consistent with lithological logs. Where inconsistencies were observed, they were generally resolved by changing the contact points between adjacent units. If more than one porosity measurement was made at the same location, the values were averaged. Cores from which data were obtained, along with the references of the data, are listed in Table 3.3. A summary of the range of matrix porosities is presented in Figure 3-3.

A beta distribution was fit to the porosity data for each hydrological unit using a non-linear entropy-fit program. The beta distribution was chosen because it is a bounded function (in the case of porosity, between 0.0 and 1.0), and its parameters can be fitted in a manner consistent with the data available. Such a fitting procedure is consistent with the maximum-entropy formalism (Jaynes, 1957; Shannon, 1948). The beta distribution is the most flexible probability distribution for fitting data (Harr, 1989). The beta distribution parameters for each hydrogeological unit are presented in Table 3.4 and Figure 3-4. The equation for the probability

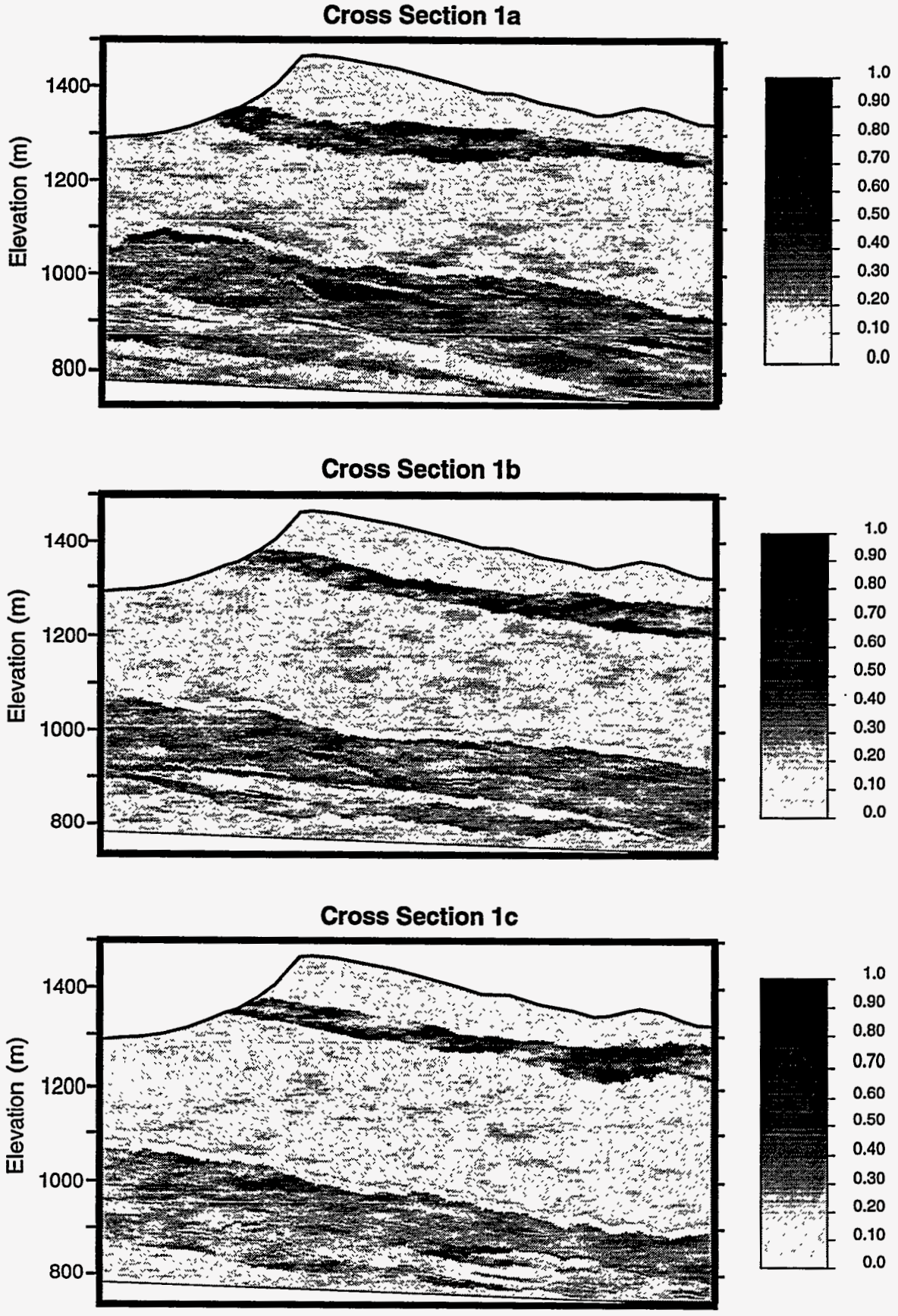

Figure 3-2. Simulated porosity fields for cross-section 1

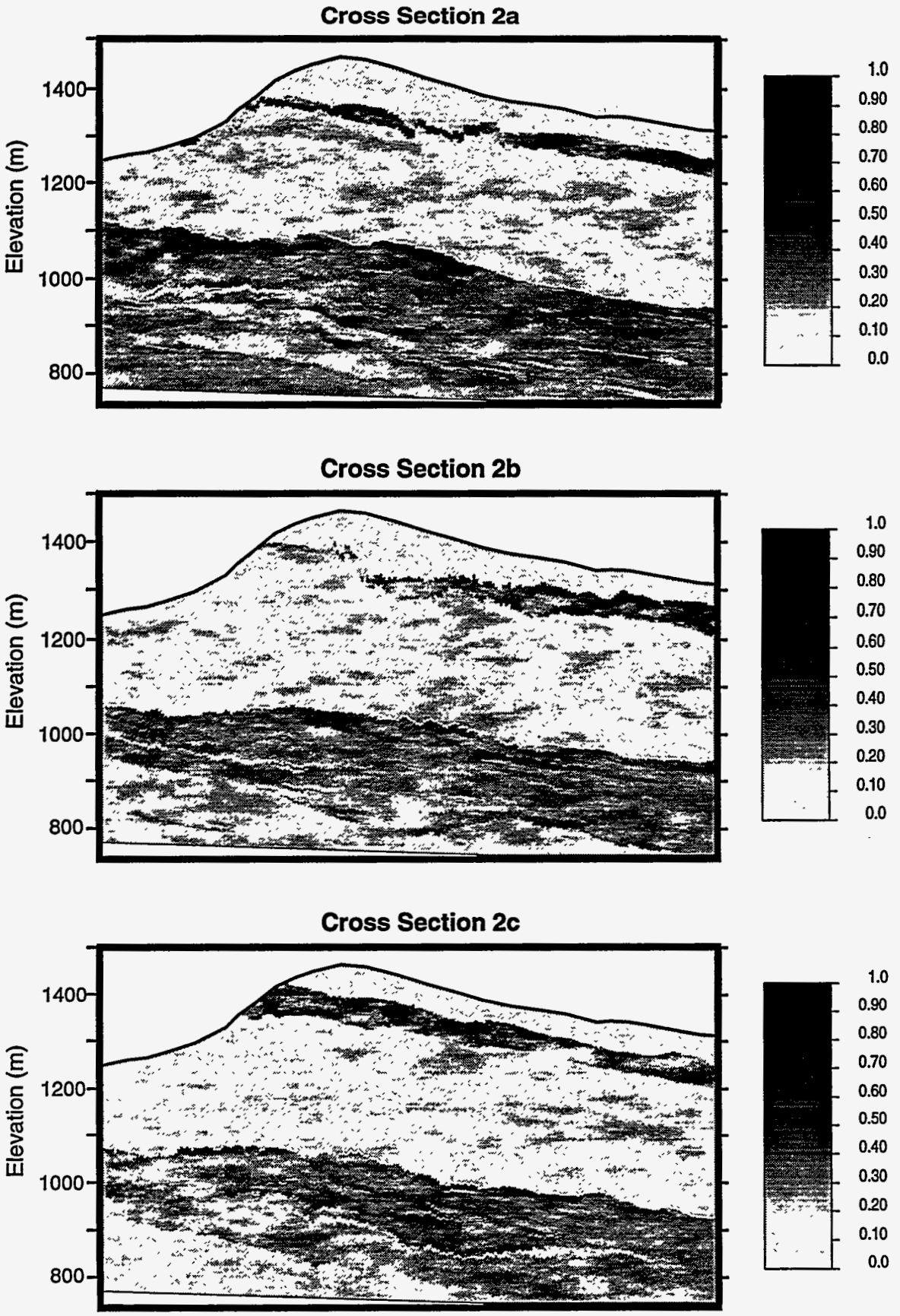

Figure 3-2 (Cont.). Simulated porosity fields for cross-section 2.

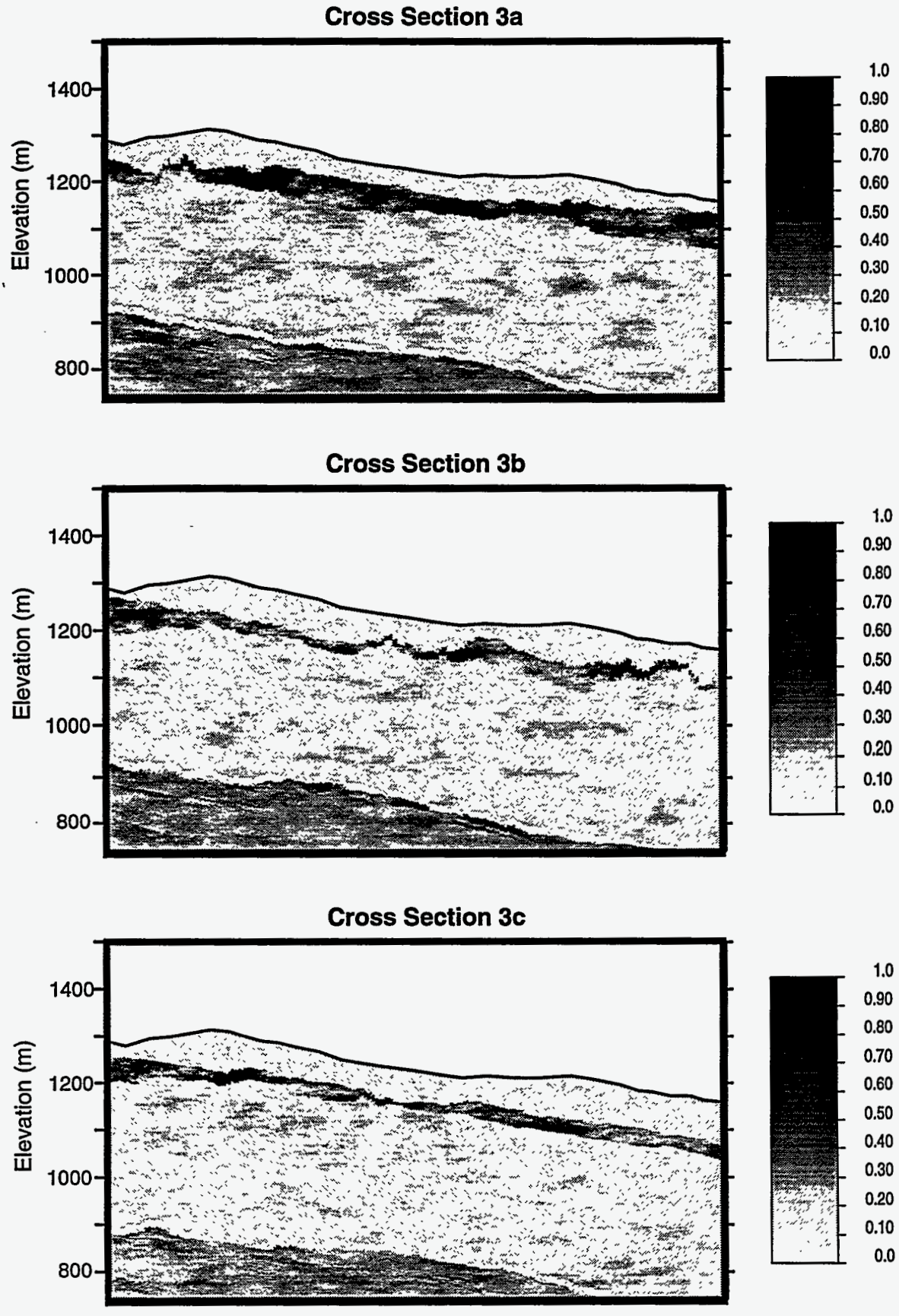

Figure 3-2 (Cont.). Simulated porosity fields for cross-section 3.

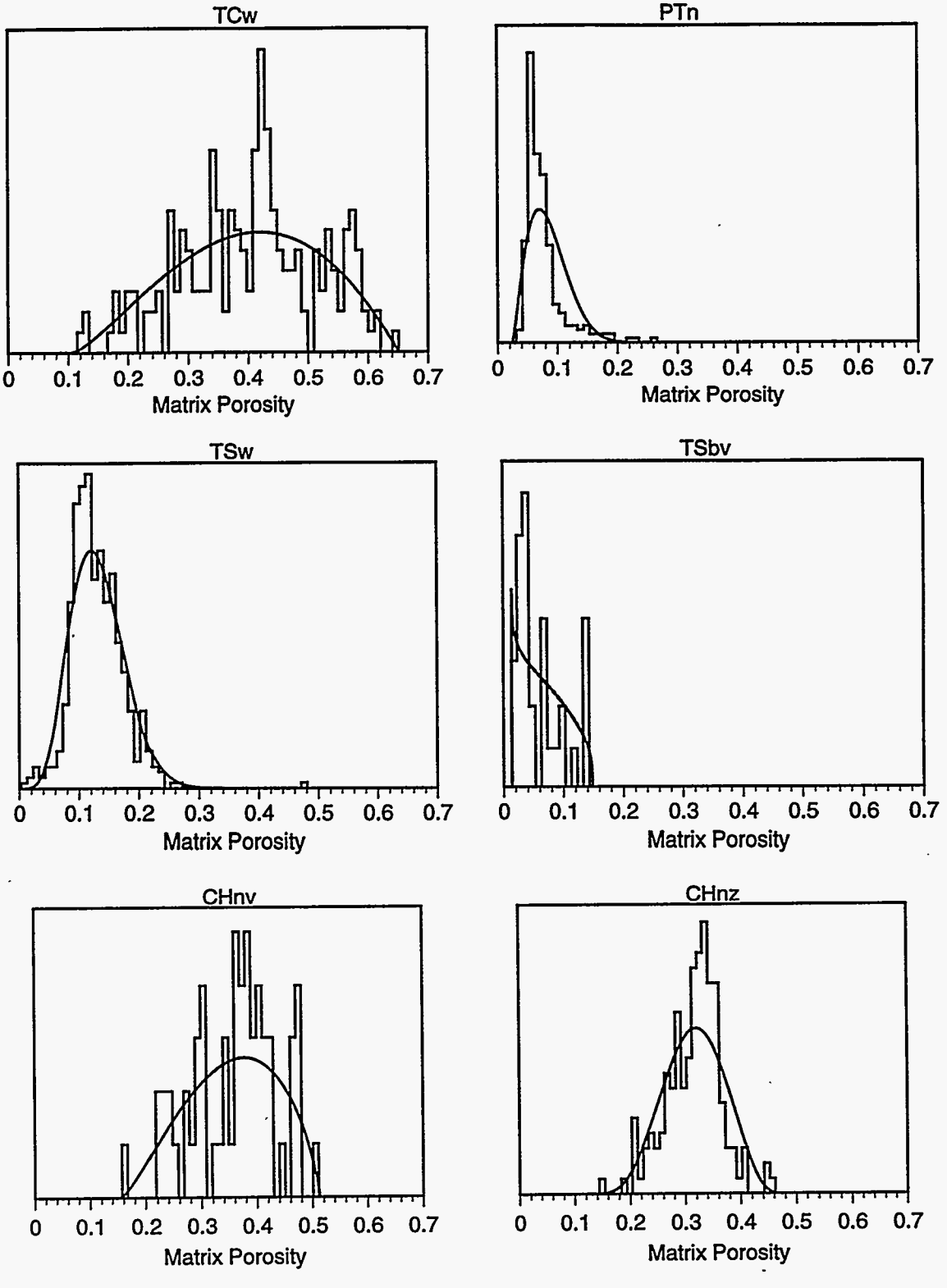

Figure 3-3: Summary of matrix porosity core data for each hydrogeological unit.

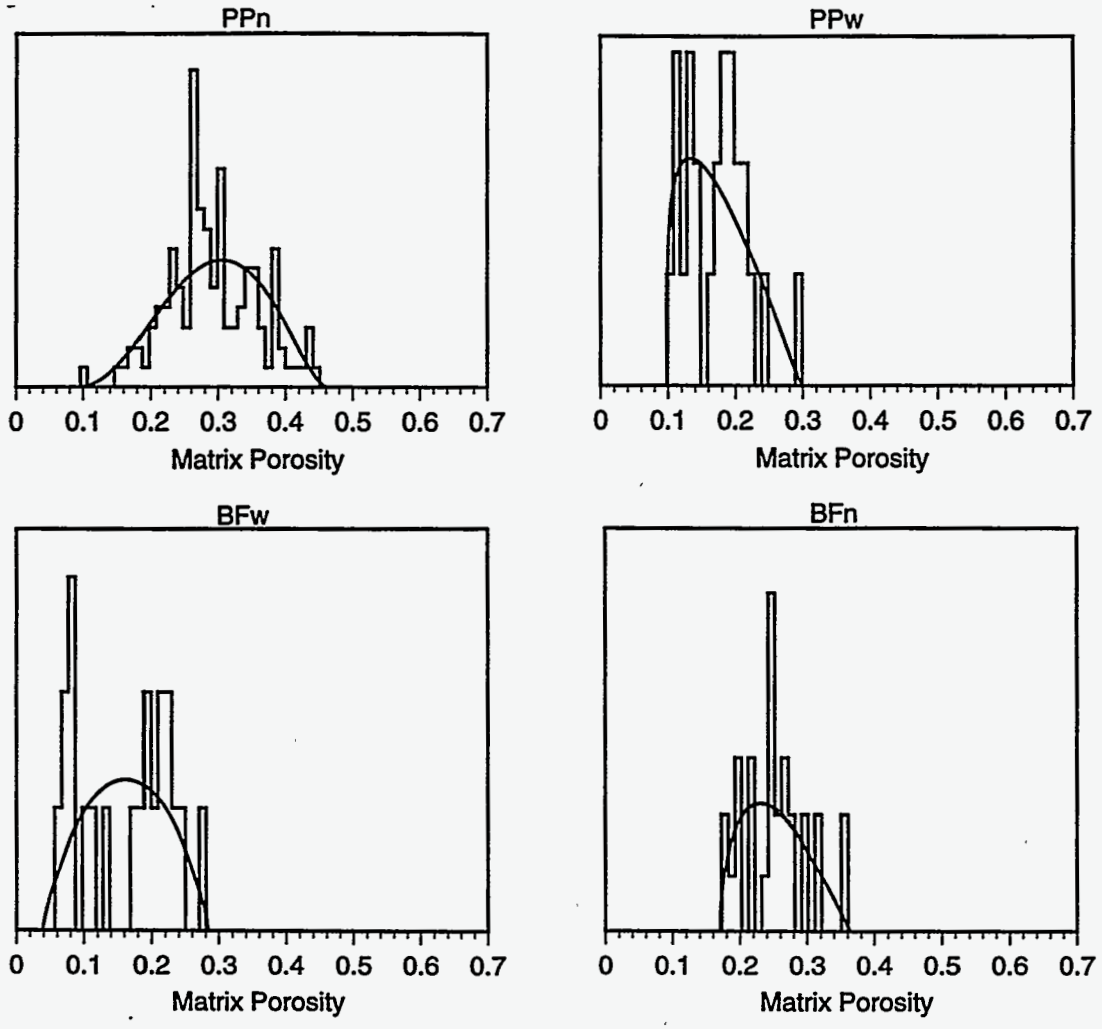

Figure 3-3 (Cont.). Summary of matrix porosity core data for each hydrogeological unit.

density function for the beta distribution used in this simulation is:

$$p(x) = \frac{1}{(b-a)^{\alpha+\beta+1}} \frac{\Gamma(\alpha+\beta+2)}{\Gamma(\alpha+1)\Gamma(\beta+1)} (x-a)^{\alpha} (b-x)^{\beta} \begin{bmatrix} \alpha > -1 \\ \beta > -1 \end{bmatrix} \qquad (3\text{-}2)$$

where a and b are the lower and upper bounds of the distribution, respectively, x is the variable of interest (e.g., porosity), α and β are fitting parameters, and Γ is the gamma function. For a discussion of the application of the beta distribution to these analyses, see Schenker et al.[1] and Wilson et al. (1994).

Table 3-3. List of cores from which porosity data were obtained.

Borehole	Reference	Borehole	Reference
UE-25 UZ #4	Flint and Flint (1990)	USW G-3	Anderson (1984)
UE-25 UZ #5	Flint and Flint (1990)	USW G-4	Anderson (1984)
UE-25a #1	Anderson (1981)		Knauss and Peifer (1986)
	Flint and Flint (1990)		Peters et al. (1984)
	Schwartz (1990)		Rush et al. (1983)
UE-25a #4	Anderson (1991)		Schwartz (1990)
	Flint and Flint (1990)	USW GU-3	Anderson (1984)
UE-25a #5	Anderson (1991)		Flint and Flint (1990)
UE-25a #6	Anderson (1991)		Peters et al. (1984)
	Flint and Flint (1990)		Schwartz (1990)
UE-25a #7	Anderson (1991)		Voss (1992a)
UE-25b #1	Lahoud et al. (1984)	USW H-1	Rush et al. (1983)
UE-25c #1	Flint and Flint (1990)		Weeks and Wilson (1984)
UE-25c #2	Flint and Flint (1990)	USW UZ-7	Kume and Hammermeister (1990)
USW G-1	Flint and Flint (1990)		
	Knauss et al., 1985	USW UZ-16	Voss (1993)
	Lin and Daily (1984)	USW UZN-53	Voss (1992c)
	Schwartz (1990)	USW UZN-54	Voss (1992b)
		USW UZN-55	Voss (1992b)

Table 3.4. Matrix Porosity Beta Distribution Parameters

Unit	a	b	α	β	mean	Average Measured Porosity
TCw	0.0236	0.269	1.56	6.67	0.0851	0.0768
PTn	0.104	0.652	1.43	1.05	0.401	0.405
TSw	0.000	0.486	5.08	15.2	0.132	0.131
TSbv	0.0140	0.148	-0.0834	0.348	0.0685	0.0602
CHnv	0.154	0.513	1.32	0.800	0.356	0.359
CHnz	0.133	0.472	3.77	3.05	0.316	0.316
PPn	0.0922	0.462	2.23	1.63	0.296	0.291
PPw	0.0990	0.298	0.216	1.05	0.173	0.173
BFw	0.0387	0.284	0.822	0.811	0.162	0.162
BFn	0.170	0.365	0.498	1.10	0.251	0.253

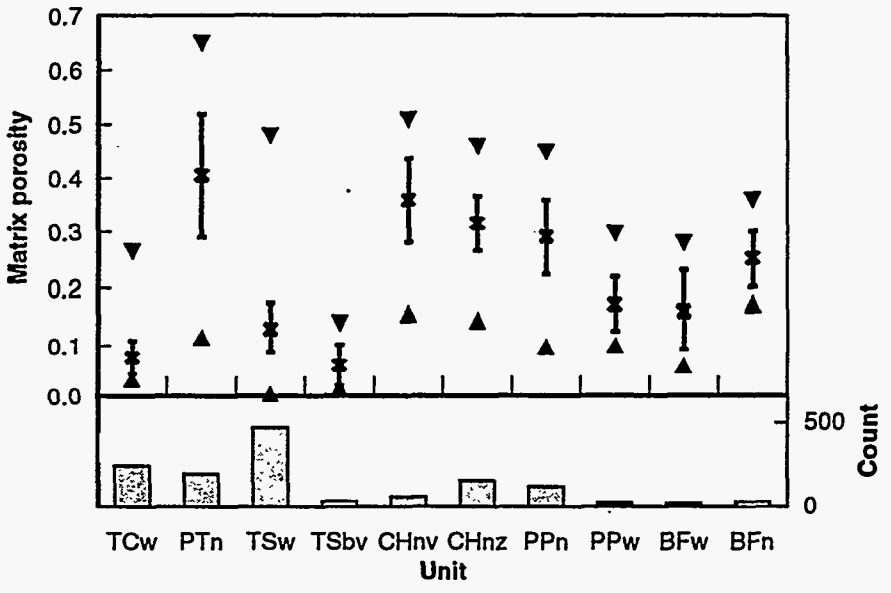

Figure 3-4: Beta distribution fit to the porosity data for each hydrogeological unit. Triangles represent the minimum and maximum values, x's the mean value, and the error bars plus and minus one standard deviation from the mean. The histogram at the bottom shows the number of data for each unit.

3.2.2 Saturated Hydraulic Conductivity

Saturated hydraulic conductivity values used in the model were directly calculated from the porosities. The relationship between saturated conductivity and porosity was determined using a semi-log regression analysis. A list of boreholes from which the data for this analysis were obtained and their references are presented in Table 3-5. The best relationships were obtained when the data were grouped, not by hydrogeological unit, but more broadly into the two groups: zeolitic units and non-zeolitic units. The relationship of the two parameters based on the regression analyses (Figure 3-5) is:

non-zeolitic	$\ln K_{sat} = -26.999 + 25.272\phi$	$r^2 = 0.81$
zeolitic	$\ln K_{sat} = -27.686 + 13.980\phi$	$r^2 = 0.31$

Beta distributions describing the error terms associated with the prediction of saturated hydraulic conductivity were also determined so that this error could be used in the calculation of saturated hydraulic conductivity from porosity. Uncertainty in the regression relationship was incorporated by adding a stochastically drawn value from the beta distribution of the error to the saturated hydraulic conductivity value derived from the regression.

Table 3.5. References for saturated hydraulic conductivity data

Borehole	Reference	Borehole	Reference
UE-25 UZ #4	Flint and Flint (1990)	UE-25c #2	Flint and Flint (1990)
UE-25 UZ #5	Flint and Flint (1990)	USW G-1	Flint and Flint (1990) Rutherford et al. (1992)
UE-25a #1	Anderson (1981) Flint and Flint (1990)	USW G-4	Peters et al. (1984) Rutherford et al. (1992)
UE-25a #4	Flint and Flint (1990)	USW GU-3	Flint and Flint (1990) Peters et al. (1984) Rutherford et al. (1992)
UE-25a #6	Flint and Flint (1990)	USW H-1	Rush et al. (1984)
UE-25b #1	Lahoud et al. (1984)	UZ-4	Yang et al. (1988)
UE-25c #1	Flint and Flint (1990)	UZ-5	Yang et al. (1988)

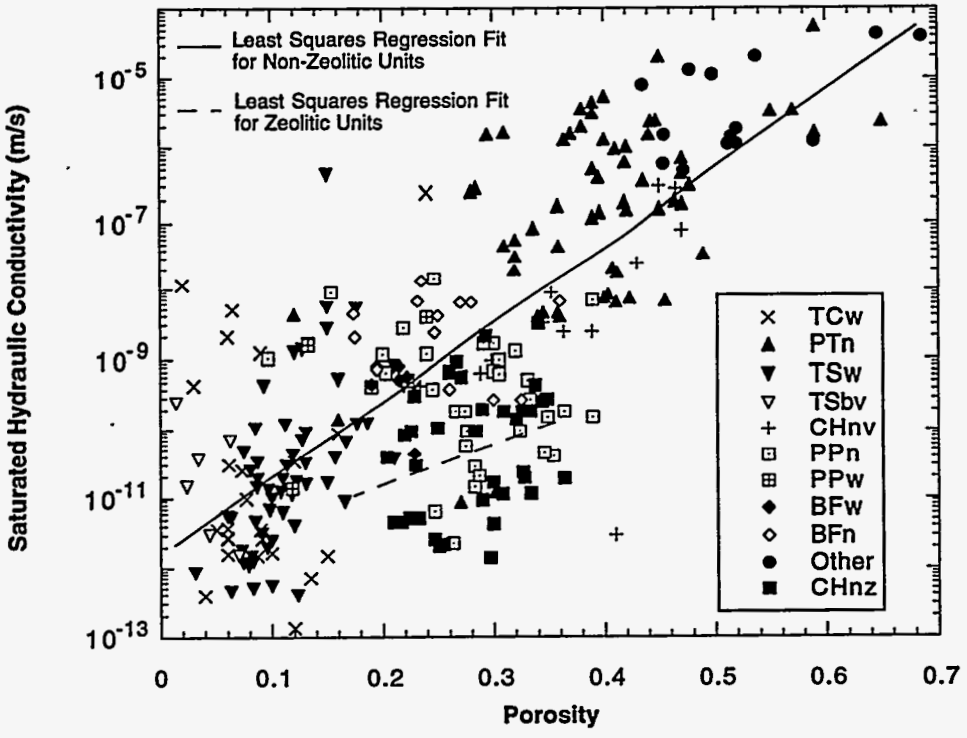

Figure 3-5: Relationship of porosity to saturated hydraulic conductivity with best fit regression lines of zeolitic and non-zeolitic materials.

3.2.3 Moisture-Retention Curves

Moisture-retention curves were modeled using the incomplete gamma function (IGF). Samples from which the IGF was fit to pressure saturation data are listed in table 3-6. The IGF was chosen over a van Genuchten fit (van Genuchten, 1978) because IGF is more readily fit to small data sets. The IGF also produces a sharper break at the beginning of desaturation in the saturation vs. pressure curve. A more mathematical discussion of the benefits of IGF over van Genuchten methodologies is presented in Robey (1994). By fitting an IGF to measured pressure-versus-saturation data, the mean and standard deviation of the pore size were obtained. The moisture retention curve fitted by the IGF is the integral of the pore-size distribution. The fitting parameters for the IGF were interpreted as average pore size (r_{avg}) and the standard deviation of the pore size (σ_r). There is a physical basis for using the pore size distribution to define the parameters in the moisture-retention relationship. Because capillary forces are related to pore diameter, the average pore size controls the average magnitude of the suction pressure. The standard deviation of pore size, as a measure of the variability, generally defines the slope of the relationship between pressure and saturation. A strong relationship exists between r_{avg} and σ_r as seen below and in Figure 3-6.

welded	$\ln\sigma_r = 0.41983 + 1.0537 \ln r_{avg}$	$r^2 = 0.98$
non-welded	$\ln\sigma_r = 0.21855 + 1.15057 \ln r_{avg}$	$r^2 = 0.92$
zeolitic	$\ln\sigma_r = 0.80519 + 1.1041 \ln r_{avg}$	$r^2 = 0.99$

Table 3-6. Samples from which the IGF was fit to pressure saturation data

Borehole	Unit	Sample Numbers	Reference
UE25 UZ#4	PTn	4-5, 4-5H, 4-6, 4-6H, 4-7, 4-7H	Flint and Flint (1990)
UE25 UZ#5	PTn	5-2	Flint and Flint (1990)
UE25 UZ#5	CHnv	5-9	Flint and Flint (1990)
UE25a#1	PTn	2A	Flint and Flint (1990)
UE25a#6	PTn	IV	Flint and Flint (1990)
UE25c #1	CHnz	3P	Flint and Flint (1990)
USW G-1	TSw	G1-1a, G1-1b, G1-2a, G1-2b, G1-3a, G1-3b, G1-4a, G1-4b, G1-6a, G1-6b	Rutherford et al. (1992)
USW G-1	TSbv	G1-5a, G1-5b	Rutherford et al. (1992)
USW G-1	CHnv	G1-7a, G1-7b	Rutherford et al. (1992)

Table 3-6. Samples from which the IGF was fit to pressure saturation data

Borehole	Unit	Sample Numbers	Reference
USW G-1	CHnz	G1-8a, G1-8b, G1-9a, G1-9b, G1-10a, G1-10b, G1-11a, G1-11b, G1-12a, G1-12b	Rutherford et al. (1992)
USW G-1	CHnz	17A, 18A	Flint and Flint (1990)
USW G-1	PPnw	G1-13a, G1-13b, G1-14a, G1-14b, G1-15a, G1-15b	Rutherford et al. (1992)
USW G-4	TCw	G4-1a, G4-1b, G4-1c	Peters et al. (1984)
USW G-4	PTn	G4-2a, G4-2b, G4-2c, G4-3a, G4-3b, G4-3c	Peters et al. (1984)
USW G-4	PTn	G4-101a, G4-101b, G4-102a, G4-102b,	Rutherford et al. (1992)
USW G-4	TSw	G4-4a, G4-4b, G4-4c, G4-5a, G4-5b, G4-5c, G4-24a, G4-24b, G4-24c, G4-6a, G4-6b, G4-6c, G4-7a, G4-7b, G4-7c, G4-8a, G4-8b, G4-8c	Peters et al. (1984)
USW G-4	TSbv	G4-9a, G4-9b, G4-9c	Peters et al. (1984)
USW G-4	CHnv	G4-10a, G4-10b, G4-10c	Peters et al. (1984)
USW G-4	CHnz	G4-11a, G4-11b, G4-11c, G4-12a, G4-12b, G4-12c, G4-13a, G4-13b, G4-13c, G4-14a, G4-14b, G4-14c	Peters et al. (1984)
USW G-4	PPnw	G4-15a, G4-15b, G4-15c, G4-16a, G4-16b, G4-16c, G4-17a, G4-17b, G4-17c, G4-19a, G4-19b, G4-19c, G4-20a, G4-20b, G4-20c	Peters et al. (1984)
USW G-4	PPw	G4-18a, G4-18b, G4-18c	Peters et al. (1984)
USW G-4	BFnw	,G4-21a, G4-21b, G4-21c, G4-22a, G4-22b, G4-22c	Peters et al. (1984)
USW GU-3	TCw	GU3-1a, GU3-1b, GU3-2a, GU3-2b, GU3-3a, GU3-3b, GU3-4a, GU3-4b, GU3-5a, GU3-5b	Peters et al. (1984)
USW GU-3	PTn	GU3-6a, GU3-6b, GU3-7a, GU3-7b, GU3-8a, GU3-8b	Peters et al. (1984)

Table 3-6. Samples from which the IGF was fit to pressure saturation data

Borehole	Unit	Sample Numbers	Reference
USW GU-3	TSw	GU3-9a, GU3-9b	Peters et al. (1984)
USW GU-3	TSw	GU3-101a, GU3-101b, GU3-102a, GU3-102b, GU3-103a, GU3-103b	Rutherford et al. (1992)
USW GU-3	TSbv	GU3-10a, GU3-10b, GU3-11a, GU3-11b	Peters et al. (1984)
USW GU-3	CHnv	GU3-12a, GU3-12b, GU3-13a, GU3-13b, GU3-14a, GU3-14b, GU3-15a, GU3-15b, GU3-16a, GU3-16b	Peters et al. (1984)
USW GU-3	CHnv	1U, 1UH	Flint and Flint (1990)
USW GU-3	PPnw	GU3-17a, GU3-17b, GU3-18a, GU3-18b, GU3-19a, GU3-19b,	Peters et al. (1984)
Outcrop Samples along Solitario Canyon	TCw	TPC9s, TPC2s, TPC5s	Flint et al. (1994)
Outcrop Samples along Solitario Canyon	PTn	BT17s, BT24Hs, BT23-1s, BT18s, BT22Hs, BT11s, BT25Hs, BT27Hs, BT26Vs	Flint et al. (1994)
Outcrop Samples along Solitario Canyon	TSw	BT1s, BT2s, BB16s, BB45s, BB68s, BB13As, TS56s, TS58s, TS26s, TS50s, TS54s, BB31s, BB64s, TS40s, TS29s, TS47s, TS32s	Flint et al. (1994)
Outcrop Samples along Solitario Canyon	TSbv	BB5s	Flint et al. (1994)
Outcrop Samples along Solitario Canyon	CHnv	BT3s	Flint et al. (1994)
Samples taken from outcrops along transects	CHnz	CH44s, CH40s, CH47s, CH60s	Flint et al. (1994)

Table 3-6. Samples from which the IGF was fit to pressure saturation data

Borehole	Unit	Sample Numbers	Reference
Samples collected from Mortendad Canyon in the Jemez Mountains, Los Alamos, New Mexico. These data were only used for nonwelded tuff data.		MCM 5.1 (53.0-54.0), MCM 5.1 (57.5-58.0), MCM 5.1 (67.0-67.5), MCM 5.1 (72.0-72.5), MCM 5.1 (82.0-82.5), MCM 5.1 (87.0-87.5), MCM 5.1 (92.5-93.0), MCM 5.1 (97.0-97.5), CM 5.1 (107.0-107.5), MCC 5.9A (85.5-86.0), MCC 5.9A (94.5-95.0), MCC 5.9A (104.5-105.0), MCC 5.9A (109.0-109.5), MCC 5.9A (119.5-120.0)	Stoker et al., 1991

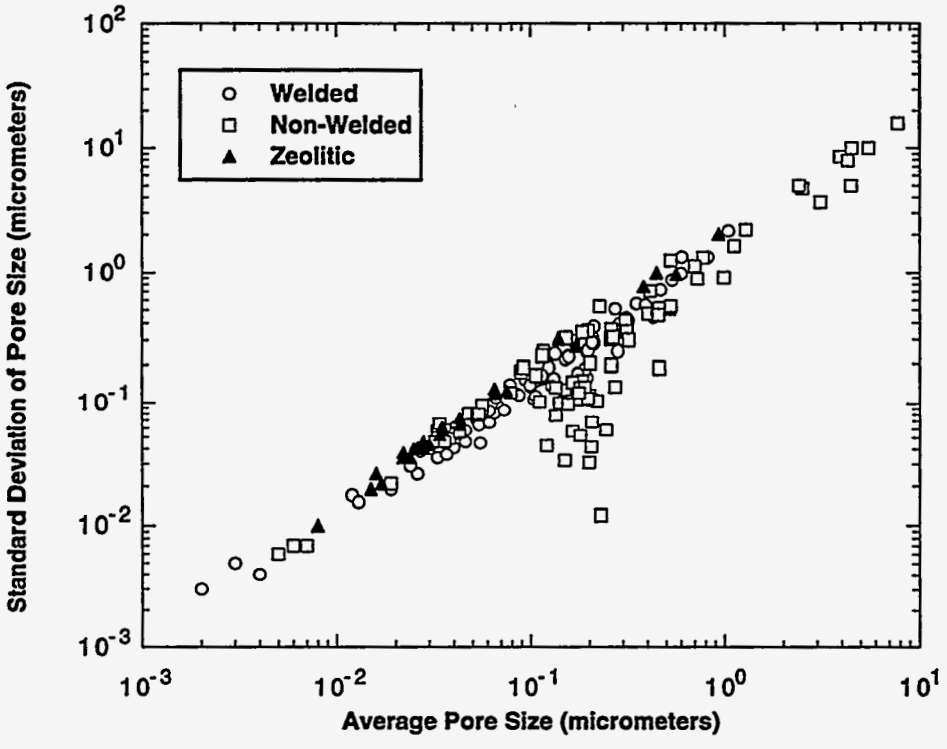

Figure 3-6: Relationship of average pore size to the standard deviation of the pore size for welded, non-welded and zeolitic materials.

While r_{avg} and porosity (ϕ) were better correlated using a logarithmic fit, a linear relationship between the two parameters was necessary in order to perform upscaling from geostatistical nodes to flow model elements. As with saturated conductivity, the errors associated

While r_{avg} and porosity (ϕ) were better correlated using a logarithmic fit, a linear relationship between the two parameters was necessary in order to perform upscaling from geostatistical nodes to flow model elements. As with saturated conductivity, the errors associated with the prediction of average pore size from porosity, then standard deviation from average pore size, were taken into account in determining the IGF fitting parameters. The linear relationship used (Figure 3-7) was:

Material	Regression Fit	Standard Deviation of the Error
welded	$r_{avg} = 0.020224 + 1.1640\ \phi$	0.12262
non-welded	$r_{avg} = 1.7269$	3.9628
zeolitic	$r_{avg} = 0.086993$	0.13959

Because a heterogeneous domain is being modeled, each element in the domain has a different pore-size distribution and therefore a different moisture-retention curve. The range of these curves based on minimum, maximum, and median pore size for three hydrogeological units (TCw, PTn, and TSw) in two simulations (cross-section 1, simulations b and c) was plotted and compared to those used in the site-scale model (Wittwer et al., 1993) (Figure 3-8). The curves used in the GWTT calculations matched fairly well with those used in the site-scale model. The curves produced in this study predict somewhat lower saturations in the lower pressure head ranges (10 - 1,000 meters of water), especially for the TCw unit.

3.2.4 Relative Permeability Curves

The Brooks-Corey model (Brooks and Corey, 1966) was used to predict relative permeability. To determine the Brooks-Corey constant (ε), the logarithms of the saturation are plotted against the logarithms of the capillary pressure. These data were obtained from the samples listed in Table 3-6. The slope of this plot is defined as $-\lambda$, where λ is the pore-size distribution index (Klavetter and Peters, 1986). The Brooks-Corey constant is defined as:

$$\varepsilon = \frac{2+3\lambda}{\lambda} \tag{3-3}$$

Relative permeability is then defined as:

$$k_r = S_e^{(2+3\lambda)/\lambda} = S_e^{\varepsilon} \tag{3-4}$$

where S_e is the effective saturation.

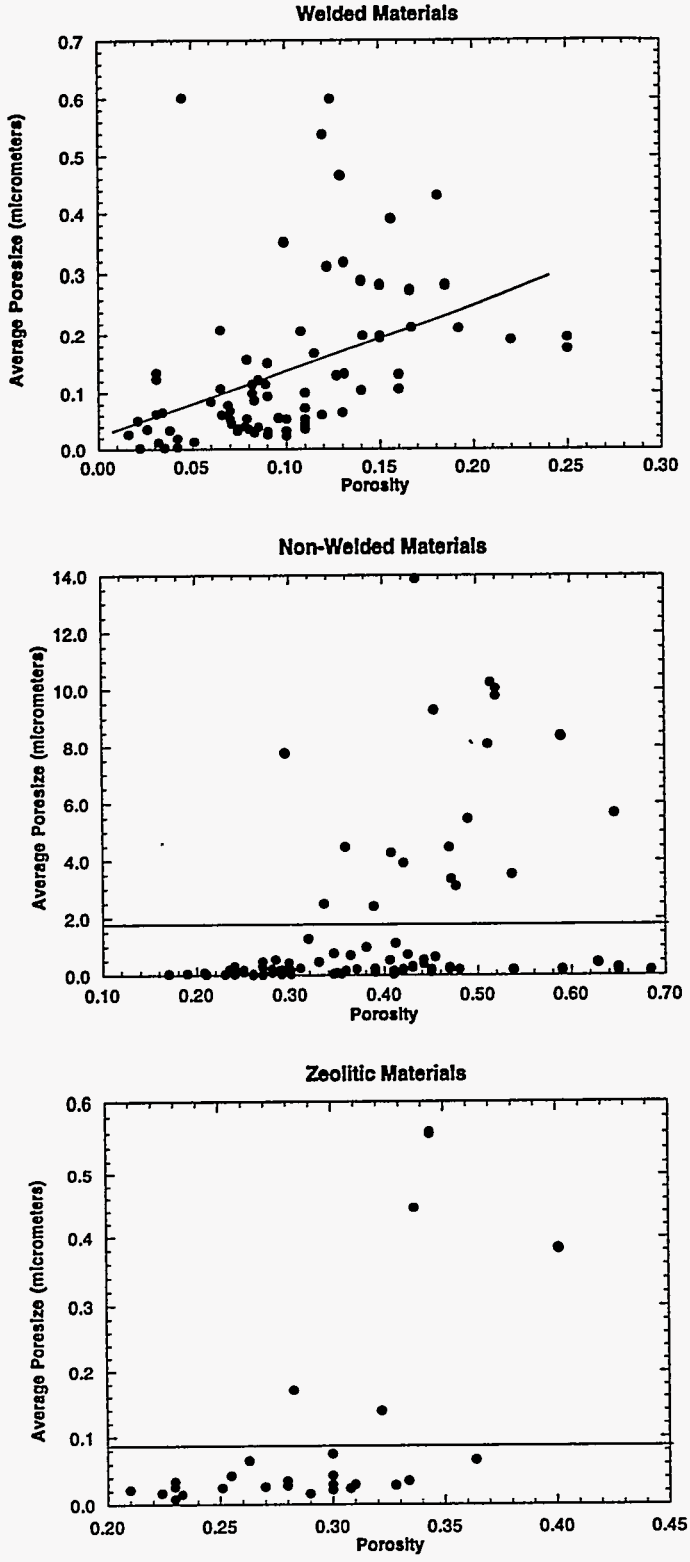

Figure 3-7: Relationship of porosity to average pore size with best fit regression lines for welded, non-welded and zeolitic materials.

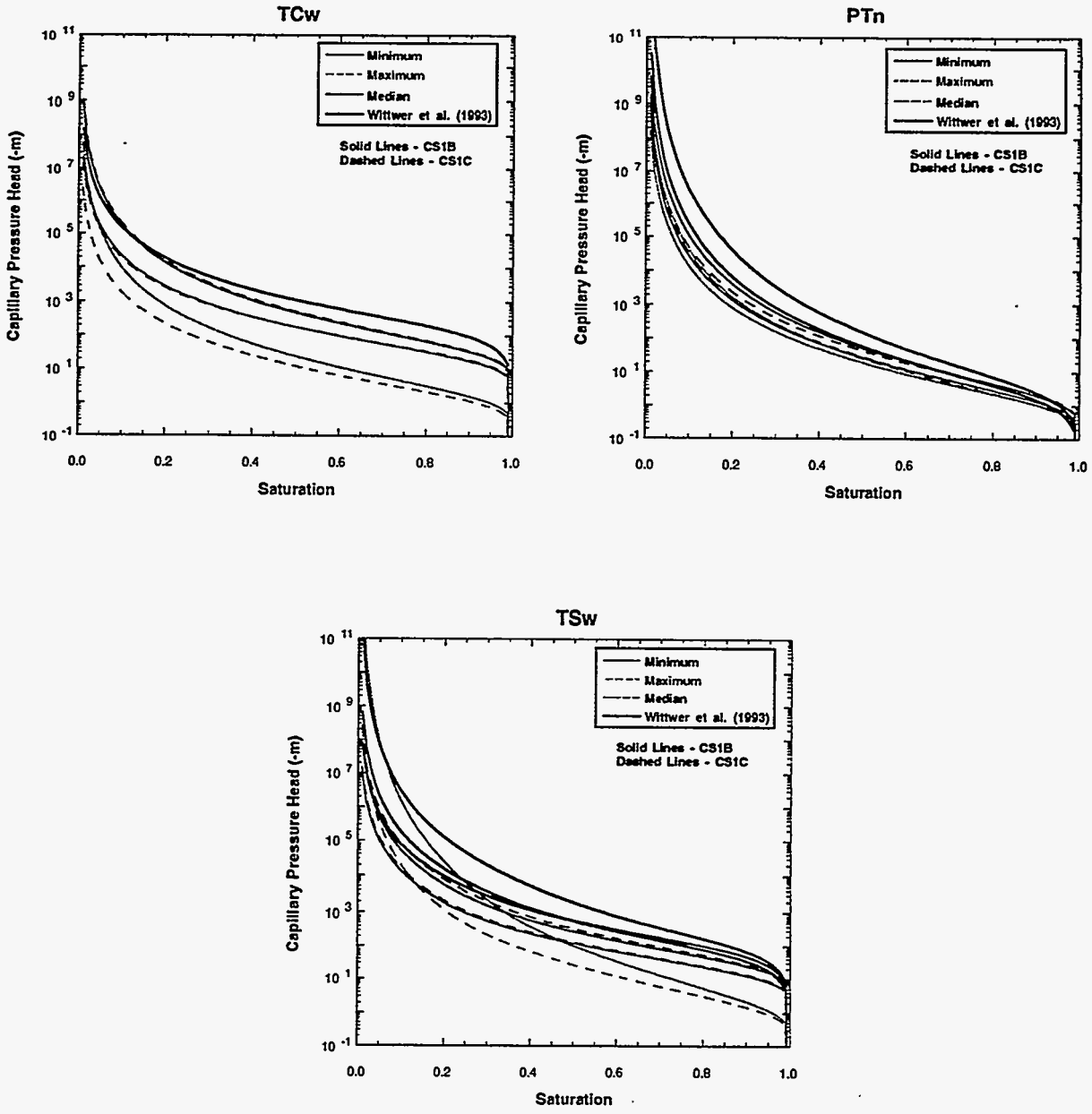

Figure 3-8: Comparison of range of moisture retention curves to those used in the site-scale model (Wittwer et al.,1993) for three hydrogeological units.

The relationships between the Brook-Corey constant (ε) and the standard deviation of pore size (σ_r) (Figure 3-9) were:

welded	$\ln\varepsilon = 2.1005 + 0.084913 \ln\sigma_r$	$r^2 = 0.23$
non-welded	$\ln\varepsilon = 2.0224 + 0.13599 \ln\sigma_r$	$r^2 = 0.40$
zeolitic	$\ln\varepsilon = 2.4865 + 0.13208 \ln\sigma_r$	$r^2 = 0.69$

Equations describing the errors associated with the prediction of the Brooks-Corey constant were determined so that the error of predicting ε from the standard deviation of pore size was incorporated, as described in Section 3.2.2.

As with the moisture-retention curves, unsaturated permeability curves were compared to those used in the site-scale model (Wittwer et al., 1993) (Figure 3-10). A range of curves used in two simulations (cross-section 1, simulations b and c) was obtained by choosing the minimum, maximum and median Brooks-Corey constant for three hydrogeological units (TCw, PTn, and TSw). The relative permeabilities were calculated and these values were multiplied by the saturated hydraulic conductivity of the element and converted to absolute permeability (assuming a temperature of 20 °C). Because there is some variation in the saturated conductivity, these curves do not necessarily represent the actual range of curves in each unit. Differences in saturated hydraulic conductivity also explain the differences of curves observed between the two simulations because the relative permeability curves were quite close when the simulations were compared. For all three units, the site-scale model (Wittwer et al., 1993) predicts slightly higher saturations at a given permeability, though the curves are relatively close, with better matches at the higher saturation range.

3.2.5 Fracture Properties

The relationships discussed above apply to matrix properties. Because the flow code employs a composite-porosity or effective-continuum model, fracture properties are also needed. Considerable uncertainty exists in the current fracture-property data set. Beta distributions of porosity and saturated hydraulic conductivity for each unit developed for TSPA-93 (Wilson et al., 1994; Schenker et al.[1]) were used. When more than one hydrogeologic unit is represented in an element, a weighted average of the fracture porosity or fracture hydraulic conductivity was calculated. Fracture porosity beta distribution parameters developed from Schenker et al.[1] are presented in Table 3.7.

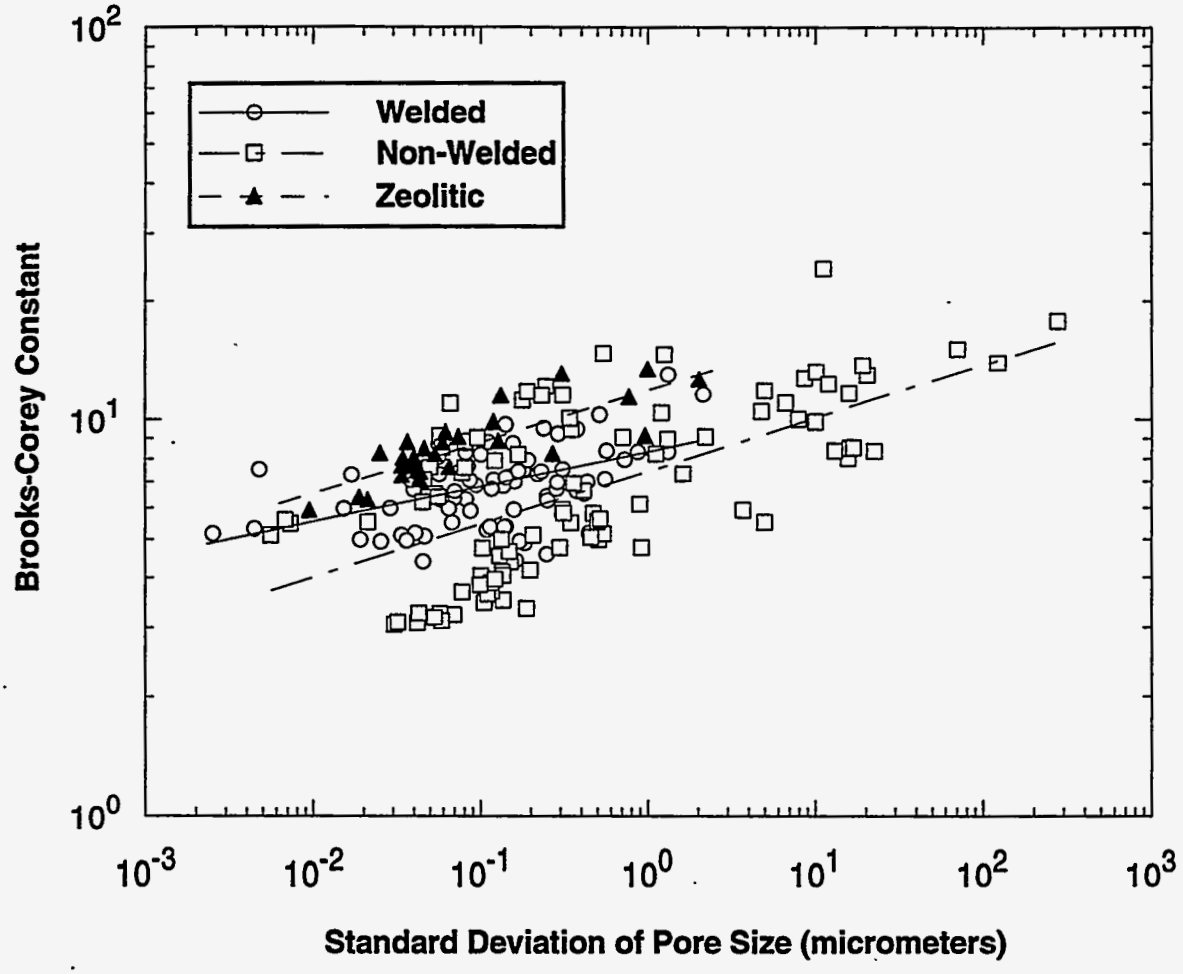

Figure 3-9: Relationship of the standard deviation of the pore size to the Brooks-Corey constant with best fit regression lines for welded, non-welded and zeolitic materials

The expected values for fracture aperture did not vary much for the first seven units, so their average was used, resulting in an r_{avg} = 178 micrometers and σ_r = 178 micrometers. Thus the IGF parameters are: $a = r_{avg}^2/\sigma_r^2 = 1.0$; and $\lambda = r_{avg}/\sigma_r^2 = 0.00562$. A Brooks-Corey constant of $\varepsilon_f = 5.08$ was calculated by determining the van Genuchten parameters from the moisture saturation curve described above and calculating the Brooks-Corey constant as described in Klavetter and Peters (1986). A combined (matrix and fracture) expected unsaturated conductivity curve for each hydrogeological unit is presented in Figure 3-11.

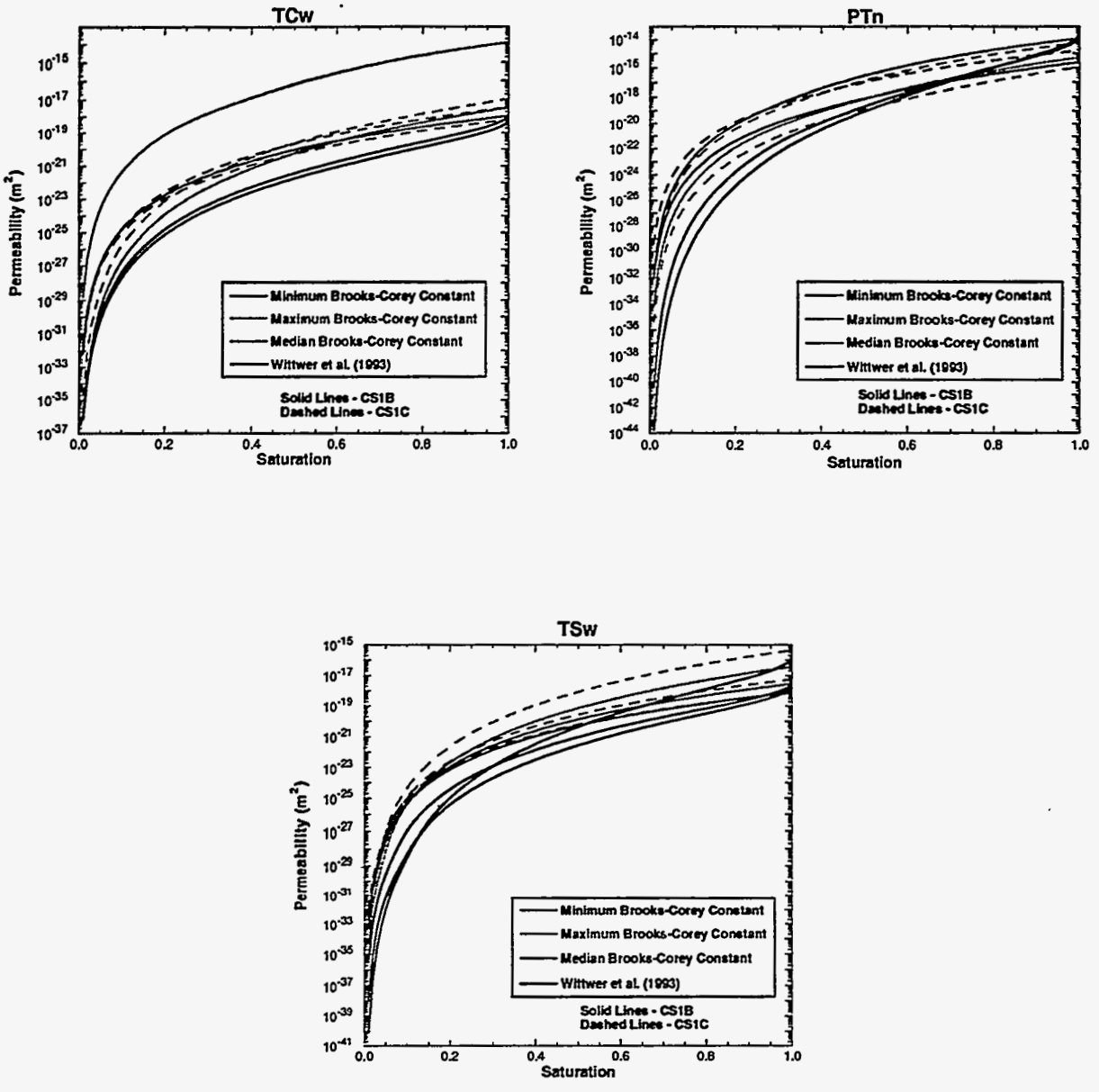

Figure 3-10: Comparison of range of unsaturated permeability curves to those used in the site-scale model (Wittwer et al., 1993) for three hydrogeological units.

Table 3.7: Fracture porosity beta distribution parameters

Unit	log(a)	log(b)	α	β	mean
TCw	-4.179	-1.966	1.815	1.805	5.45×10^{-3}
PTn	-4.825	-2.354	1.982	2.189	2.15×10^{-3}
TSw	-4.301	-1.371	1.457	2.072	1.89×10^{-2}
TSbv	-4.367	-1.427	1.483	2.072	1.67×10^{-2}
CHnv	-4.834	-1.860	1.594	1.932	6.49×10^{-3}
CHnz	-5.073	-2.174	1.608	2.001	3.12×10^{-3}
PPn	-5.073	-2.174	1.608	2.001	3.12×10^{-3}
PPw	-5.193	-2.309	1.843	2.484	2.21×10^{-3}
BFw	-4.664	-1.596	1.451	1.998	1.14×10^{-2}
BFn	-5.493	-3.160	1.811	1.794	3.49×10^{-4}

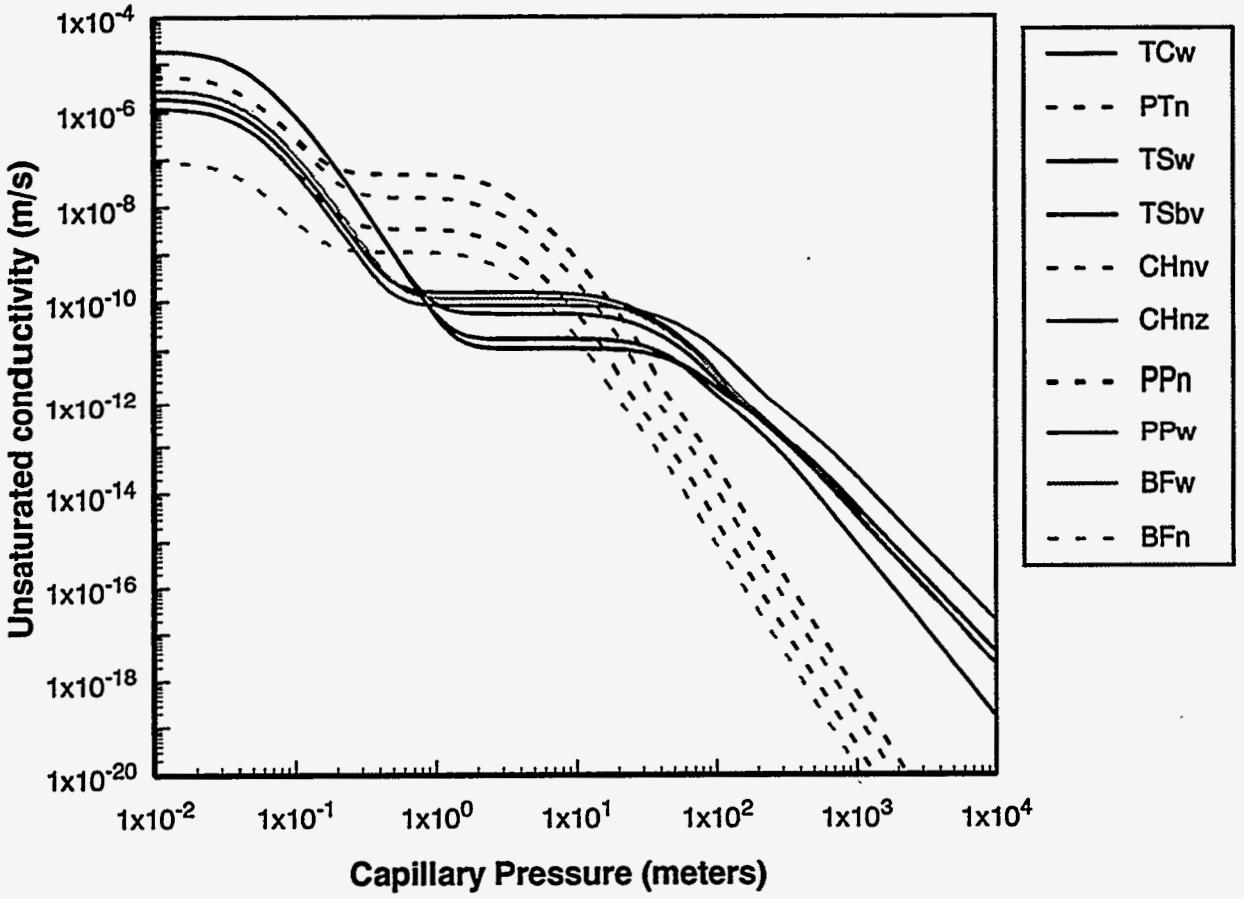

Figure 3-11: Combined matrix and fracture unsaturated conductivity characteristic curves.

This page intentionally left blank.

Chapter 4
Flow Model

Numerical modeling of groundwater flow in the UZ utilizing the geostatistical simulations of geology and hydrologic parameter distributions is needed to calculate the groundwater velocity field for particle tracking analyses, which are used to estimate the GWTT distribution in the system. Flow modeling requires the discretization of the flow domain for numerical analyses. Because of computational limitations, the numerical grid used for the flow model was much coarser than the grid system used for the geostatistical simulations. The discretized grid was adjusted to minimize intra-element variations in porosity caused by the heterogeneous nature of the simulated system. Properties assigned to an individual element of the flow grid were derived by upscaling and averaging of the properties associated with the geostatistical nodes within that element. Boundary conditions of the flow model were specified in accordance with the conceptual model. The upper boundary conditions were stochastically assigned, based on measurements of saturation in the shallow subsurface. The flow simulations used the composite-porosity model of fracture-matrix interaction. The numerical solution of steady-state unsaturated flow is reached with the finite-element method using the dual variable approach. This approach differs significantly from more classical numerical modeling techniques in that continuity of fluid flux is enforced at element boundaries, but continuity of fluid pressure is not.

4.1 Adaptive Numerical Grid

In many groundwater flow modeling applications, the numerical grid is adapted to the problem by making *a priori* assumptions regarding the flow field. The discretization is generally finer in regions of high flux (e.g., wells) or in regions of sharply convergent or divergent flow. An automated adaptive process was applied in this study because of the heterogeneous field of hydrologic parameters.

Adaptation of the numerical grid to the underlying heterogeneous porosity field causes elements of the numerical flow simulation to conform to the spatial distribution of the relevant hydrologic parameters. The adaptive grid algorithm seeks to minimize the heterogeneity of porosity within elements. This procedure reduces the range of values averaged for each element to move from the geostatistical scale to the flow model scale. Because of contrasts in porosity across contacts of hydrostratigraphic units, adaptation of the grid resulted in general coincidence of hydrostratigraphic contacts and element boundaries. A more detailed description of the adaptive gridding algorithm is presented in Robey (1994).

The initial step in the grid adaptation process was the generation of a regular grid for the problem domain. Nodes of quadrilateral elements are equally spaced in the x-direction and were equally spaced in proportion to the height of the cross-section in the y-direction. The coordinates

of nodes were adjusted in an iterative procedure to reduce the heterogeneity of porosity within elements. The objective function of the minimization procedure is expressed mathematically using the two-norm variable:

$$\|\sigma a\|_2 = \left[\sum_{i=1}^{n} (\sigma_i a_i)^2 \right]^{\frac{1}{2}} \qquad (4\text{-}1)$$

where n is the number of elements, σ_i is the standard deviation of porosity within the element, and a_i is the area of the element. Reduction of the objective function occurs either by realignment of element boundaries to reduce the variability within elements or by reduction of the area of highly heterogeneous elements.

The iterative procedure used to minimize the two-norm variable consisted of movement of individual nodes within the initial, regular grid. Nodes along the sides, lower, and upper boundaries were allowed to slide along the boundaries. The local norm for a node was calculated based on the four elements that share that node using Equation 4-1. The nodes were ranked according to their local norm, and nodal coordinates were adjusted, beginning with the node having the highest local norm. The nodal position was adjusted incrementally and the adjustment is accepted if the local norm is reduced. The increments of adjustment were the same as the discretization at the geostatistical simulation scale (i.e., 1 m vertical and 8.5 m horizontal). To avoid numerical inconsistency in the flow simulation, all elements in the grid must be convex; the adaptive grid algorithm checked to ensure that this criterion was met following nodal adjustment. After all of the nodes were adjusted, the global norm was calculated and the process of nodal adjustment is repeated. The adaptation of the grid stopped when the reduction of the two-norm variable was less than 0.5% for successive iterations.

For the nine simulations used in this study of GWTT distribution, the adaptive gridding procedure resulted in reductions in the global norm ranging from 29 to 39%. The results of the adaptive grid process for an example cross-section are shown in Figures 4-1 and 4-2; the initial grid is shown in Figure 4-1, and the final numerical flow grid is shown in Figure 4-2. Note that the element boundaries generally conform to the hydrostratigraphic contacts and that intra-element variability of porosity is lower in the adapted grid. Where the initial grid dips to the west, elements produced by the adaptive gridding procedure cross unit contacts. However, sensitivity analyses indicated that the configuration of these elements has little effect on flow simulations (Chapter 6).

The flow simulation grid used in the nine simulations was 40 elements in the vertical direction and 20 elements in the horizontal. This level of discretization corresponds to approximately two elements per correlation length of simulated porosity in the vertical and horizontal directions (for cross-section 2). The sensitivity of the flow modeling results to spatial discretization is discussed in Chapter 6.

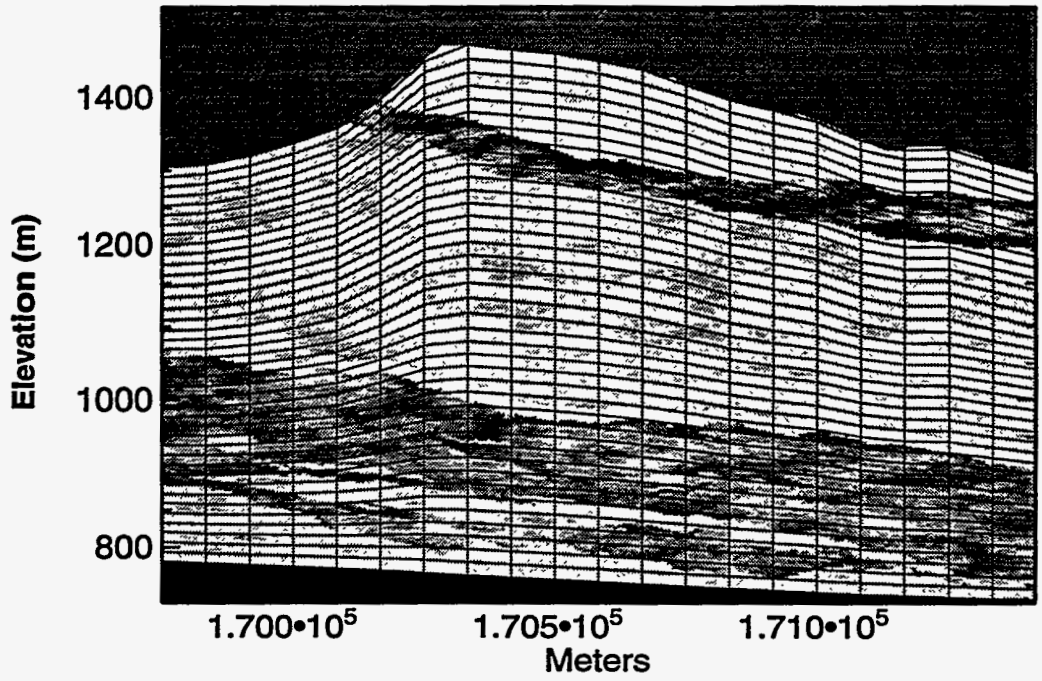

Figure 4-1. Initial flow grid prior to application of the adaptive grid algorithm.

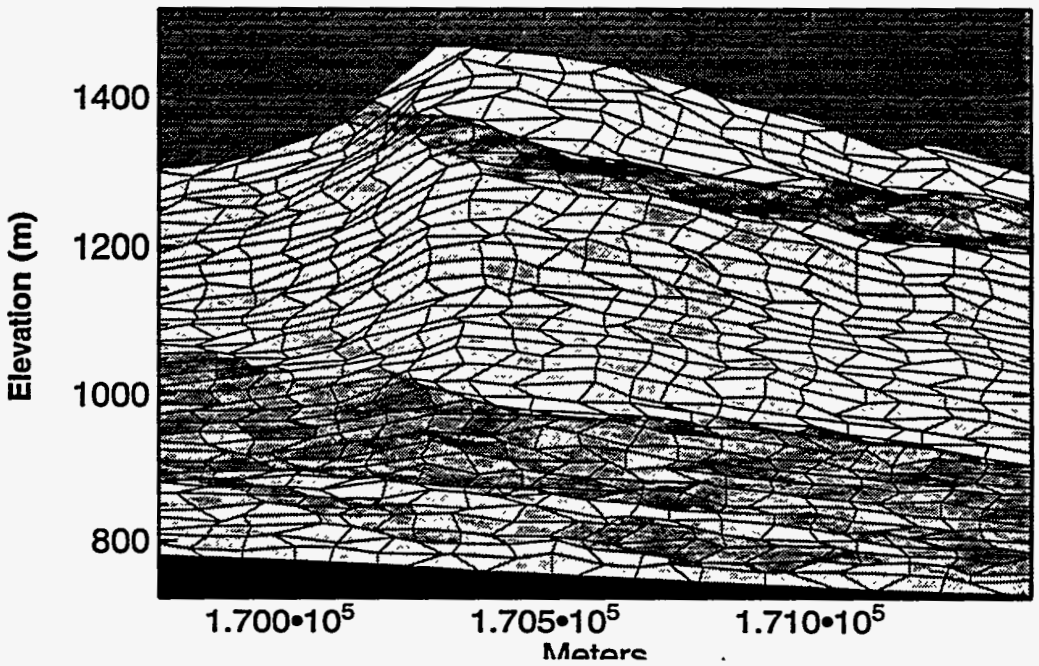

Figure 4-2. Numerical flow grid following application of the adaptive grid algorithm. The grid consists of 20 elements in the horizontal direction and 40 elements in the vertical direction. The porosity field is indicated by the shading.

4.2 Upscaling of Parameters

Although the adaptive gridding process minimized the heterogeneity of hydraulic properties within each element of the flow model, significant variability of these parameters on the geostatistical scale remained within the elements. Each of the relevant parameters was upscaled using an appropriate averaging scheme to estimate effective values at the scale of flow simulation. The same upscaling procedures were used for both matrix and fracture parameters.

The effective element porosity (ϕ^e) is estimated by the arithmetic average of porosity on the geostatistical scale:

$$\phi^e = \frac{1}{n} \sum_{i=1}^{n} \phi_i \tag{4-2}$$

where n is the number of values of porosity at the geostatistical simulation scale within the element and ϕ_i is the geostatistical simulation scale porosity value. Using an arithmetic average to calculate effective porosity is appropriate due to the relatively limited range in values of porosity expected within each flow element.

Effective saturated hydraulic conductivity at the element scale was somewhat more difficult to determine. In anisotropic or layered media, the effective saturated hydraulic conductivity not only is a function of the underlying hydraulic conductivity field, but also depends on the boundary conditions on the individual element. Theoretical analysis of isotropic random distributions of hydraulic conductivity indicates that geometric averaging of hydraulic conductivity is the appropriate method of calculating effective saturated hydraulic conductivity (Gelhar, 1993). Since intra-element parameters were assumed to be relatively unstratified, geometric averaging was used to calculate effective saturated hydraulic conductivity (K^e_{sat}):

$$K^e_{sat} = \exp\left[\frac{1}{n} \sum_{i=1}^{n} \ln K^i_{sat}\right] \tag{4-3}$$

Parameters for relative permeability and moisture-retention relationships were also upscaled to determine effective properties at the flow-model scale. The effective average pore size (r^e) is calculated using a porosity-weighted arithmetic average:

$$\bar{r}^e = \frac{1}{\phi^e n} \sum_{i=1}^{n} \bar{r}_i \, \phi_i \tag{4-4}$$

where r_i is the average pore size at the geostatistical simulation scale. The effective standard deviation of pore size ($\sigma(r)^e$) was estimated as the porosity-weighted arithmetic average with an ad-

ditional term to account for the log-linear correlation of standard deviation of pore size to average pore size:

$$\sigma(r)^e = \left[\frac{1}{\phi^e n}\sum_{i=1}^{n}\phi^i(\bar{r}^e - \bar{r}_i)^2\right]^{\frac{1}{2}} + \left[\exp\left[\frac{1}{\phi^e n}\sum_{i=1}^{n}\phi_i \ln(\sigma^2(r_i))\right]\right]^{\frac{1}{2}} \quad (4\text{-}5)$$

The effective Brooks-Corey constant (ε^e) was calculated as the porosity-weighted geometric average of values at the underlying geostatistical scale using the following relationship:

$$\varepsilon^e = \exp\left[\frac{1}{\phi^e n}\sum_{i=1}^{n}\phi_i \ln(\varepsilon_i)\right] \quad (4\text{-}6)$$

where ε_i is the Brooks-Corey constant at the geostatistical simulation scale.

4.3 Boundary Conditions

The boundary conditions applied to numerical simulations of flow in the UZ are both specified flux and specified pressure. The lateral boundaries of the three cross-sections, corresponding to the Solitario Canyon fault, Ghost Dance fault, and Bow Ridge fault, were specified as no-flow boundaries. The lower boundary was the water table and had a specified pressure head equal to 0.0 m. The upper boundary conditions were specified pressure values which were drawn from PDFs of suction pressure developed for the three outcropping hydrostratigraphic units (TCw, PTn, and TSw).

The distributions of suction pressure at the surface were derived from data on volumetric water content, porosity, and moisture retention relationships in shallow boreholes. Volumetric water content data have been monitored in boreholes by neutron probe. Direct measurements of volumetric water content, porosity, and moisture retention relationships were available on core samples from a subset of the neutron-probe boreholes. The data used in this analysis were those used in a site-scale analysis of infiltration (Flint and Flint, 1994).

Near-surface saturation at Yucca Mountain varies because of seasonal fluctuations in infiltration. The neutron probe data were analyzed to estimate the steady-state saturation of bedrock at the depth just below the transient region. This steady-state depth was chosen to be the upper boundary of the flow model. Plots were constructed of the mean water content and the coefficient of variation of water content vs. depth for each of the neutron-probe boreholes. An example plot is shown in Figure 4-3. Values of volumetric water content greater than three standard deviations from the mean were considered to be outliers and were discarded from the calculation of the coefficient of variation. The depth at which the coefficient of variation decreased to an approximately constant value was taken as the steady-state depth and the corresponding volumetric water content was noted. The steady-state water content and the porosity as measured from cores were used to

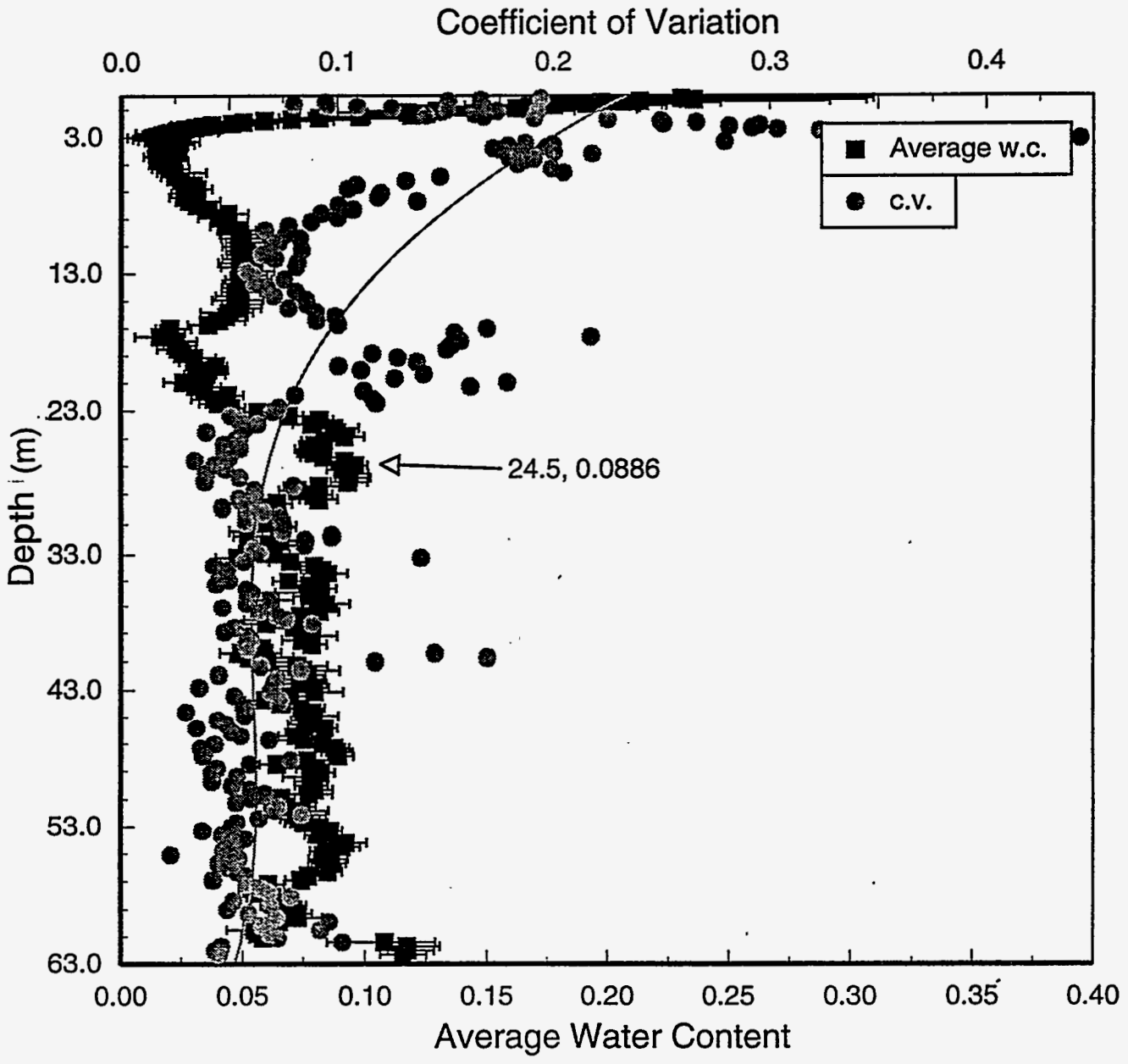

Figure 4-3. Example plot of the coefficient of variation in water content versus depth for neutron probe borehole N-27. The coefficient of variation is shown as the gray circle for each depth interval and the solid line is a polynomial fit to these values. The average water content for each depth interval is plotted as the black square with bars indicating plus and minus one standard deviation. The coefficient of variation attains a minimum value at a depth of 24.5 m, which corresponds to an average water content of 0.0886. The depth of 24.5 m is considered to be the steady-state depth at this borehole.

calculate the steady-state saturation. Finally, the saturation was converted to the steady-state pressure at that borehole location from moisture-retention curves generated as described in Chapter 3.

Data from 16 boreholes were used to derive steady-state pressures as described above. The steady-state depth derived for the boreholes ranged from 5.2 to 24.4 m and occurred from directly at the bedrock-alluvium contact to as deep as 23.6 m below the interface. These values of pressure were associated with the stratigraphic units, and a beta distribution with a lower bound of 0.0 m and an upper bound of three standard deviations above the mean was assumed for each unit. The parameters of the normal distribution used to approximate the distribution for the three outcropping units are given in Table 4-1. The PDFs of capillary pressure surface boundary conditions are shown in Figure 4-4.

Table 4-1. Distributions of surface pressure conditions

Hydrostratigraphic Unit	Mean (m)	Standard Deviation (m)
TCw	-110	35.8
PTn	-6.49	2.99
TSw	-220	66.3

Random selections of the pressure at the upper boundary were used to assign pressures for flow modeling of each realization. A single pressure for each hydrostratigraphic unit was applied for elements where that unit outcropped and the pressure for each unit was drawn independently. The values of suction pressure used in all of the simulations are given in Table 4-2 (see Figure 1-3 for cross-section locations). A moderately extreme value of -47 m for the TCw was assigned in simulation 1c, resulting in anomalous conditions calculated by the flow code (Section 4.5).

4.4 Numerical Simulation of Flow

The partial differential equations describing the flow of groundwater in unsaturated media are usually solved for complex systems using either finite-difference or finite-element techniques, both of which require spatial discretization of the problem domain. The solution technique chosen should be matched to relevant features of the problem and the goals of the analysis. Because the goal of the GWTT analysis is to model flow along the fastest pathways, the numerical simulation of flow should attempt to replicate the conditions in the conceptual model contributing to fastest flow. The conceptual model of matrix-fracture interaction in the unsaturated zone adopted in this study indicates that significant, relatively rapid flow in fractures will only occur in regions where the matrix is nearly saturated. Furthermore, heterogeneity of hydraulic parameters is the primary factor resulting in locally saturated conditions within the unsaturated zone. The numerical method used to calculate flow should be capable of simulating realistic variations in saturation on the local scale due to heterogeneous spatial distribution of hydraulic properties.

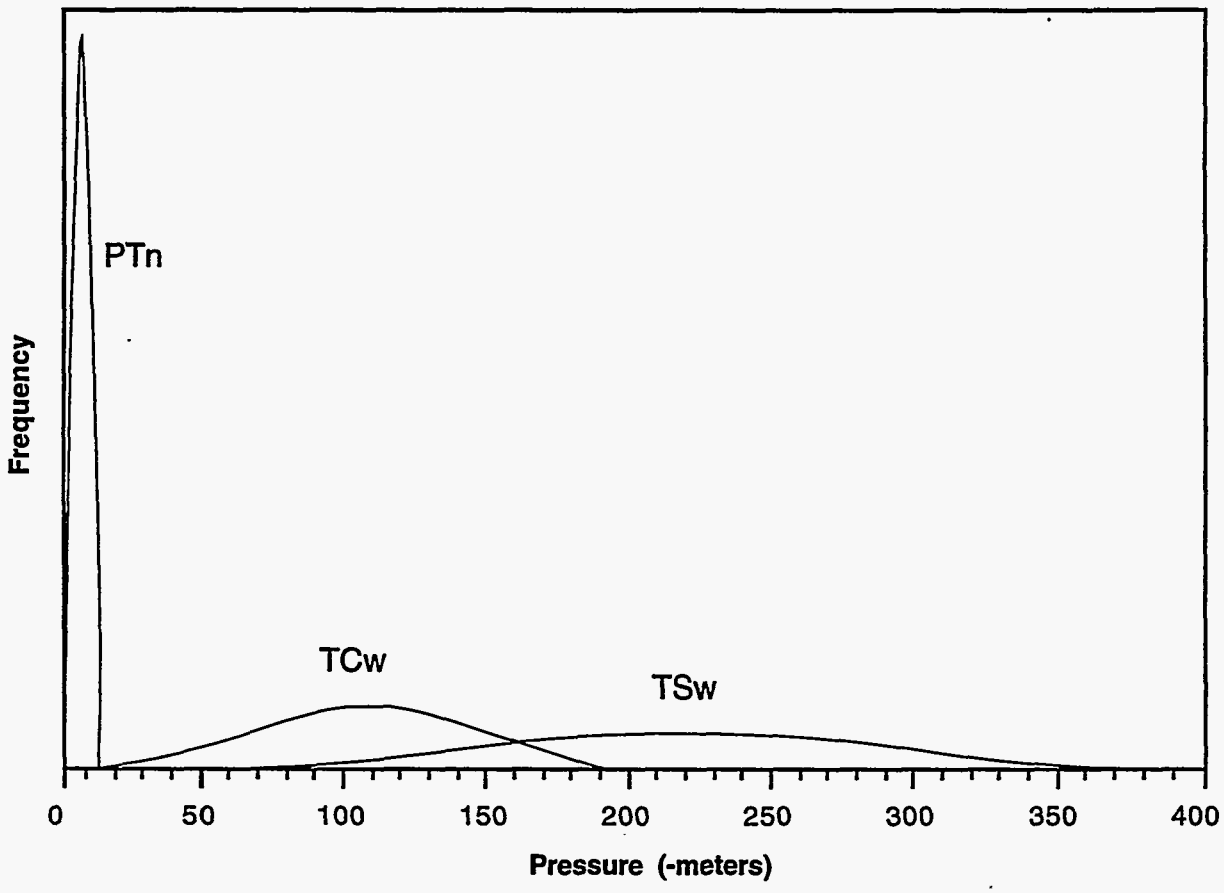

Figure 4-4. PDFs of capillary pressure for the upper boundary condition for the TCw, PTn, and TSw units.

Table 4-2. Specified pressure head conditions (m), upper boundary

cross-section	Realization	TCw	PTn	TSw
1	a	-128	-7.6	-200
1	b	-167	-5.5	-149
1	c	-47	-8.9	-164
2	a	-132	-2.0	-118
2	b	-83	n/a	-225
2	c	-115	-4.7	-302
3	a	-111	n/a	n/a
3	b	-94	n/a	n/a
3	c	-135	n/a	n/a

4.4.1 Governing Equation

The groundwater flow considered in this study is an unsaturated flow system under steady-state conditions. The medium is represented as a composite-porosity effective continuum, in which unsaturated-flow parameters for fractures and matrix are combined (Peters and Klavetter, 1988). Assuming constant liquid density and viscosity, the equations governing groundwater flow are Darcy's Law:

$$q = -K(\Psi)\nabla(\Psi + z) \tag{4-7}$$

and conservation of mass:

$$\nabla \cdot q = 0 \tag{4-8}$$

where **q** is the Darcy flux, Ψ is the capillary pressure head, $K(\Psi)$ is the hydraulic conductivity as a function of pressure, and z is the elevation. Equations 4-7 and 4-8 may be combined to produce the steady-state form of the Richards equation (Freeze and Cherry, 1979):

$$\nabla \cdot [K(\Psi)\nabla(\Psi + z)] = 0 \tag{4-9}$$

These equations are based on single-phase flow (i.e., the liquid phase) and do not explicitly model gas-phase flow in the unsaturated groundwater system. Equation 4-9 is a highly non-linear partial differential equation because of the functional relationship between unsaturated hydraulic conductivity and pressure. The extreme non-linearity of the unsaturated flow system can lead to great contrasts in fluid velocities and liquid saturations in heterogeneous media. Mathematical solution of the extremely non-linear equations can be difficult.

4.4.2 Numerical Solution

In the finite-element technique, the domain is discretized into adjacent elements that are defined by nodes. The size and shape of individual elements may vary within the problem domain, making the finite-element method well suited to problems with heterogeneous material properties or irregular boundaries. The nodes serve as points at which the dependent variable is calculated, while the value of the dependent variable can be defined within each element by an interpolation or basis function.

The classical finite-element solution technique applied to groundwater flow is to use hydraulic head or capillary pressure as the dependent variable and to solve for this quantity at the nodes. Because values of pressure at nodes are shared by adjacent elements and because of the strong dependence of conductivity on pressure, contrasts in unsaturated hydraulic conductivity are suppressed

and the effects of heterogeneity on the flow field are generally decreased. To effectively model flow in regions of contrasting material properties, it is necessary to use a relatively fine spatial discretization with this classical approach.

The dual mixed finite-element method (Robey, 1994; Robey, 1990; Roberts and Thomas, 1990) retains the effects of heterogeneity in the flow simulation at relatively coarser levels of discretization. In contrast to the classical technique, the dual method enforces continuity of normal flux at adjacent element boundaries. Because pressure is a secondary variable in the dual method, it is discontinuous across element boundaries (i.e., the pressure calculated at a given node may be different for each of the elements containing that node). Higher contrast in pressure in adjacent elements results in greater contrast in unsaturated hydraulic conductivity and greater heterogeneity in the flow field. Applications of the dual mixed finite-element method in heterogeneous, saturated groundwater flow problems associated with petroleum engineering have shown the superiority of the method in simulating streamlines in regions of highly convergent flow (Kaasschieter and Huijben, 1992; Ewing et al., 1985).

4.4.3 DUAL Flow Code

The flow code DUAL, which is based on the dual mixed finite-element method, was used in calculations of GWTT in this study. A description of the DUAL code, along with relevant derivations, is presented in Robey (1994). The code is designed to produce a steady-state solution for unsaturated groundwater flow in two dimensions. The unsaturated medium is modeled in DUAL using the composite-porosity model of Klavetter and Peters (1986), which incorporates the relative permeabilities of the matrix and fractures into a single continuum.

The composite-porosity model assumes that the medium is a single continuum in which the hydraulic properties of both the matrix and fractures are combined. In this representation, the unsaturated flow behavior of the matrix dominates at all but the highest values of bulk saturation and significant fracture flow only occurs under nearly saturated conditions. The primary limitation of the composite-porosity model is the inability to explicitly simulate flow in the separate matrix and fracture domains. Groundwater flow velocities in fractures and matrix are estimated in the particle tracking method of this study by a post-processing procedure (see Section 5-1). The composite-porosity model, however, is not capable of simulating the disequilibrium between the matrix domain and the fracture domain, in contrast to the alternative dual-permeability conceptual model.

Solution of the unsaturated flow problem is divided into nonlinear and linear iterations by the DUAL code. The initial guess used in DUAL is the saturation profile based on hydrostatic conditions. The Picard method linearizes or fixes the conductivities based on pressures from the previous nonlinear iteration. An efficient direct solution technique is used to solve the Picard equations. Use of a direct method allows fluxes of all scales to be resolved. The Newton step is approximately solved using an iterative second order stabilized biconjugate gradient solver (Sleijpen and Fokkema, 1993) with the Picard solution as the initial guess. A cubic line search method is used to adjust the Newton step where required in order to guarantee convergence of the nonlinear iterations.

A stopping criterion based on the norm of the Jacobian matrix and machine precision is used in the nonlinear iterations (Criterion 1, Barrett et al., 1993).

Input to the DUAL code consists of nodal coordinates, nodal connections defining each element, boundary fluxes and pressures, and hydraulic parameters for each element. Hydraulic parameters are entered separately for matrix and fractures and consist of the Brooks-Corey constant, the IGF parameters a and λ, saturated hydraulic conductivity, and porosity. Output from the DUAL code contains an echo of nodal geometry and input parameters, the x and y-direction components of Darcy flux at nodes, the pressure head and bilinear interpolation constants for each element, and the average conductivity, matrix saturation and fracture saturation for each element.

4.5 Results of the Flow Simulations

4.5.1 Matrix Saturation

Matrix saturations calculated by the DUAL flow code for the nine simulations are presented in Figure 4-5a (cross-section 1), b (cross-section 2), and c (cross-section 3). Most noticeable is that the matrix saturations in cross-section 1c are much higher than in the other simulations. These high saturations are clearly due to the unusually low upper surface capillary suction pressure condition of the TCw (-47 m).

Zones of higher saturations are also observed in simulations cs1a, cs1b, and cs2c, all below the PTn outcrop. This repeated pattern indicates that the PTn outcrop is a critical zone for high infiltration which leads to higher saturations beneath the outcrop. This pattern is not observed in the other simulations (cs2a2 and cs2b) because of the lower porosities of the PTn at its outcrop (see Figure 4-6 for the porosities of the elements), and where there is no PTn outcrop at all (cross-section 3, all simulations), saturations are in fact noticeably lower and more evenly distributed.

Zones of high saturation are also observed in and directly above the TSbv in all three simulations of both cross-sections 1 and 3. This is to be expected because with such low porosities, it does not take much water to saturate the unit. However, the higher saturations indicate that the TSbv might be an important unit in the initiation of fracture flow. These results also might give an explanation for the perched water in the boreholes UZ-1, UZ-14, and NRG-7/7A drilled through Drill Hole Wash and SD-9 drilled through Coyote Wash, just south of Drill Hole Wash. In UZ-14 and NRG-7/7A, the perched water was observed at the base of the Topopah Springs Tuff. In SD-9, the perched water was observed near the TSw/CHn interface only 4.6 m below the contact with the Topopah Springs Tuff The unit in which the perched water in UZ-1 was observed has not been published. High saturations are not observed in cross-section 2 because the TSbv generated by the geostatistical model was so thin that it was not captured after upscaling.

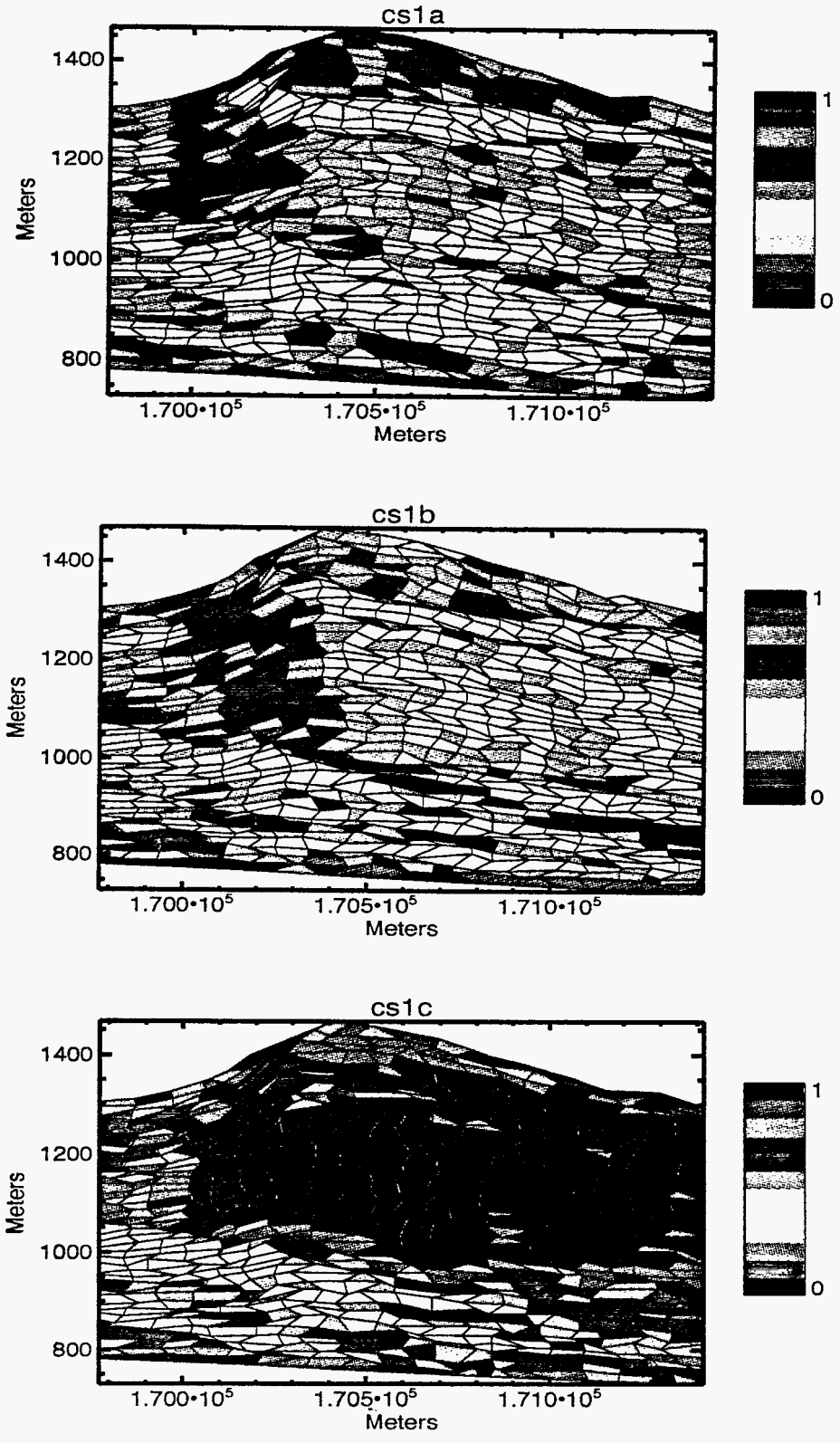

Figure 4-5a. Matrix saturation distribution of the three simulations for cross-section 1. The average matrix saturation of each element is expressed by the color scale.

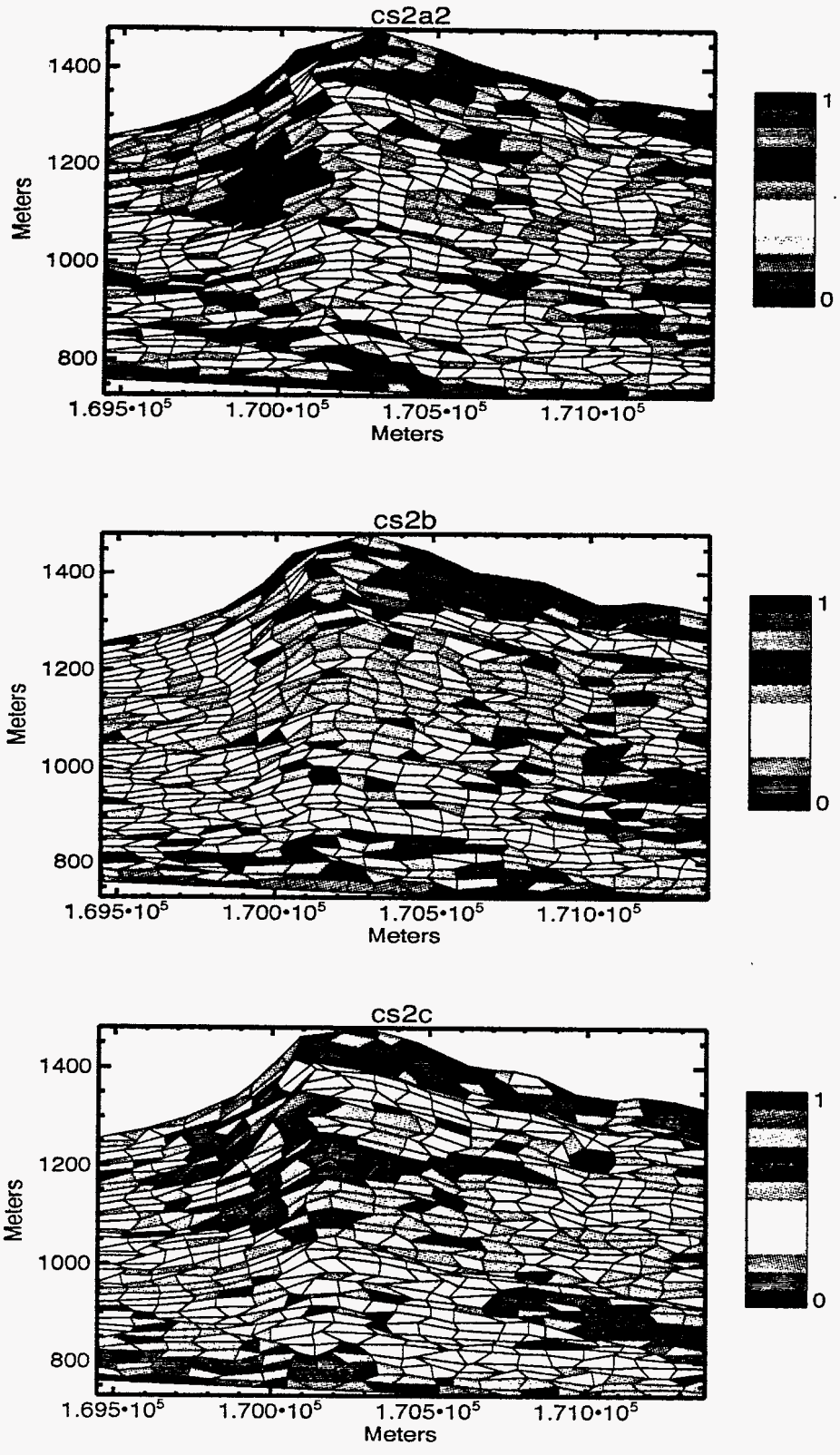

Figure 4-5b. Matrix saturation distribution of the three simulations for cross-section 2. The average matrix saturation of each element is expressed by the color scale.

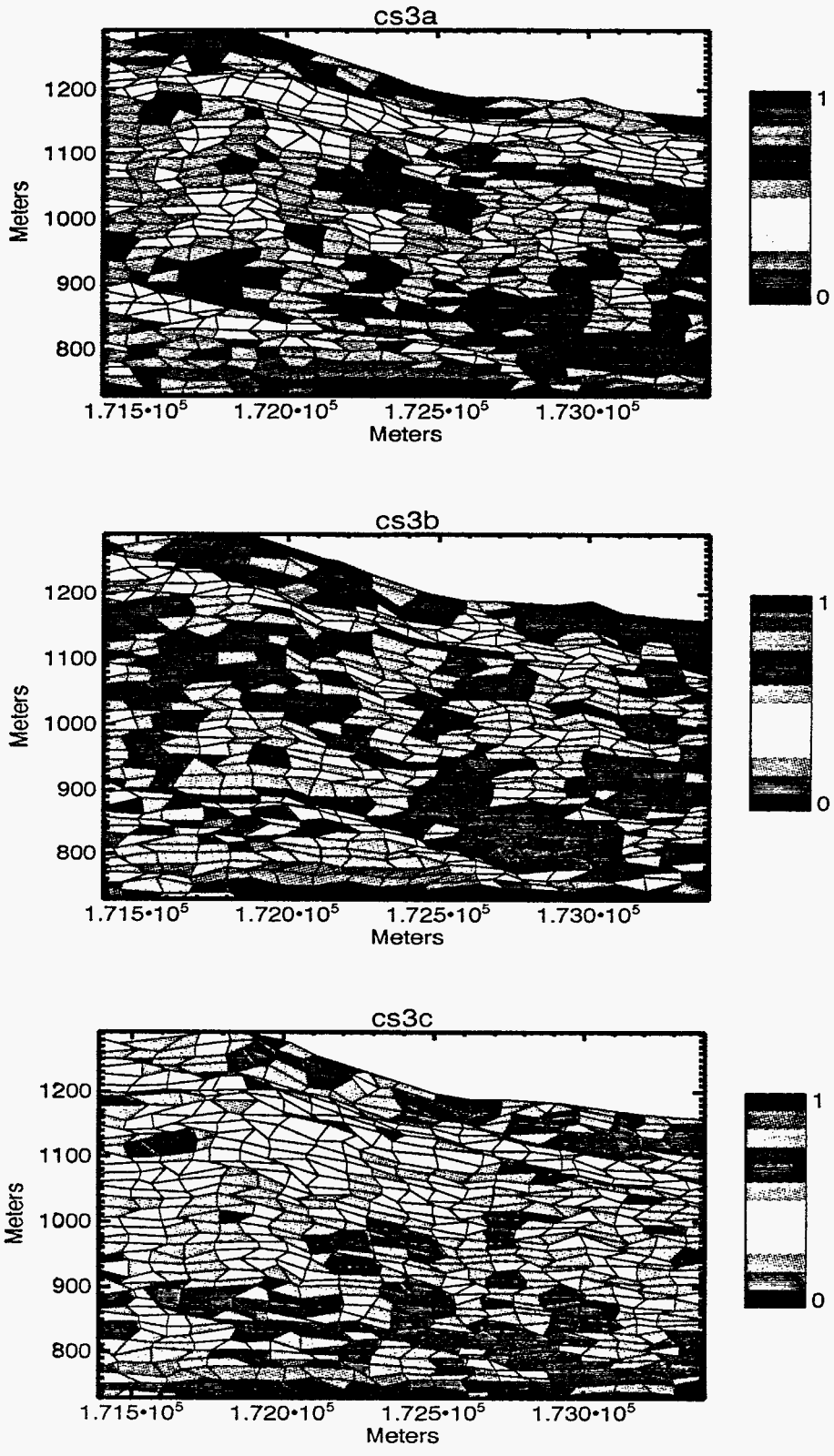

Figure 4-5c. Matrix saturation distribution of the three simulations for cross-section 3. The average matrix saturation of each element is expressed by the color scale.

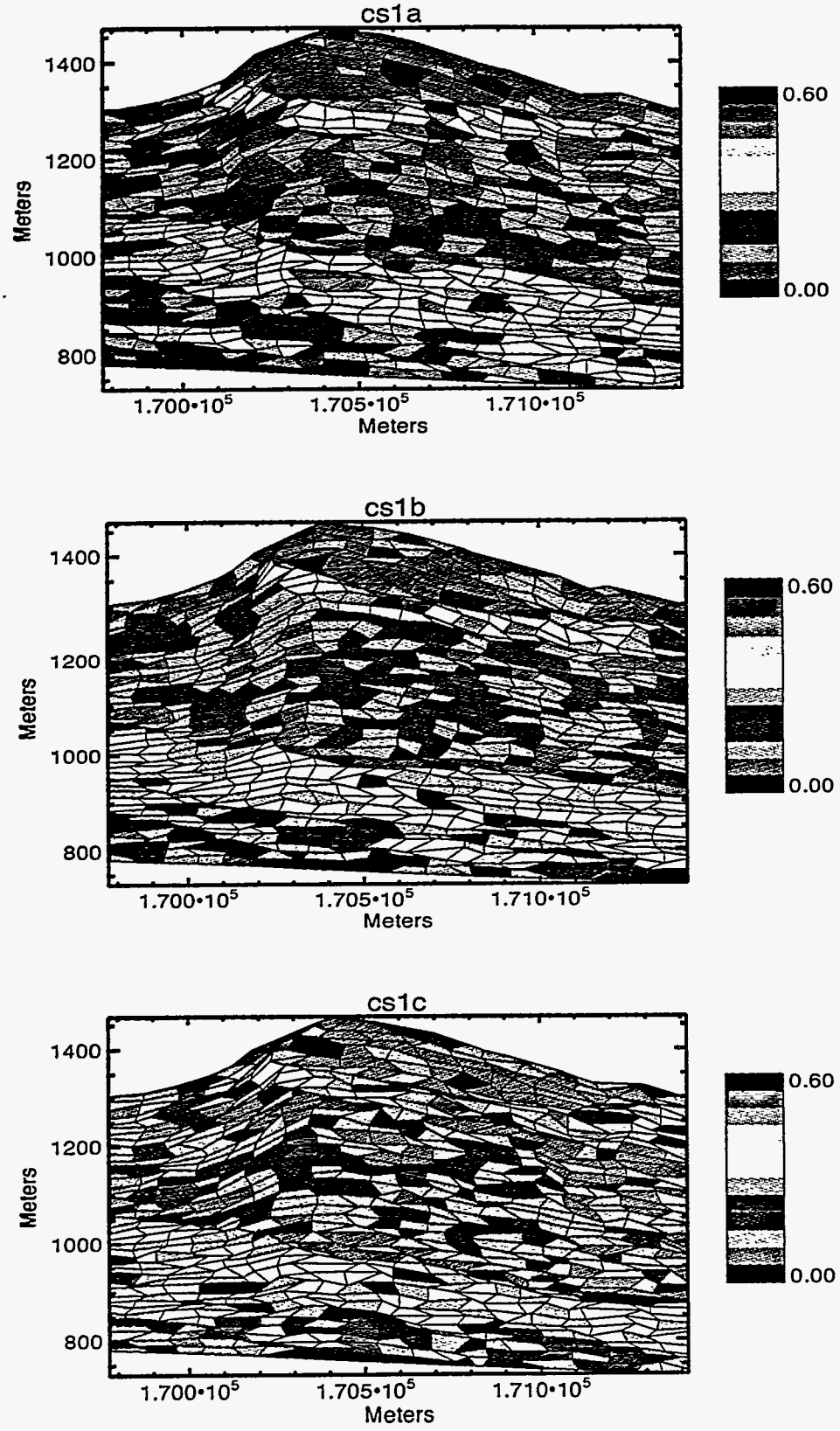

Figure 4-6a. Porosity distribution of the three simulations for cross-section 1.

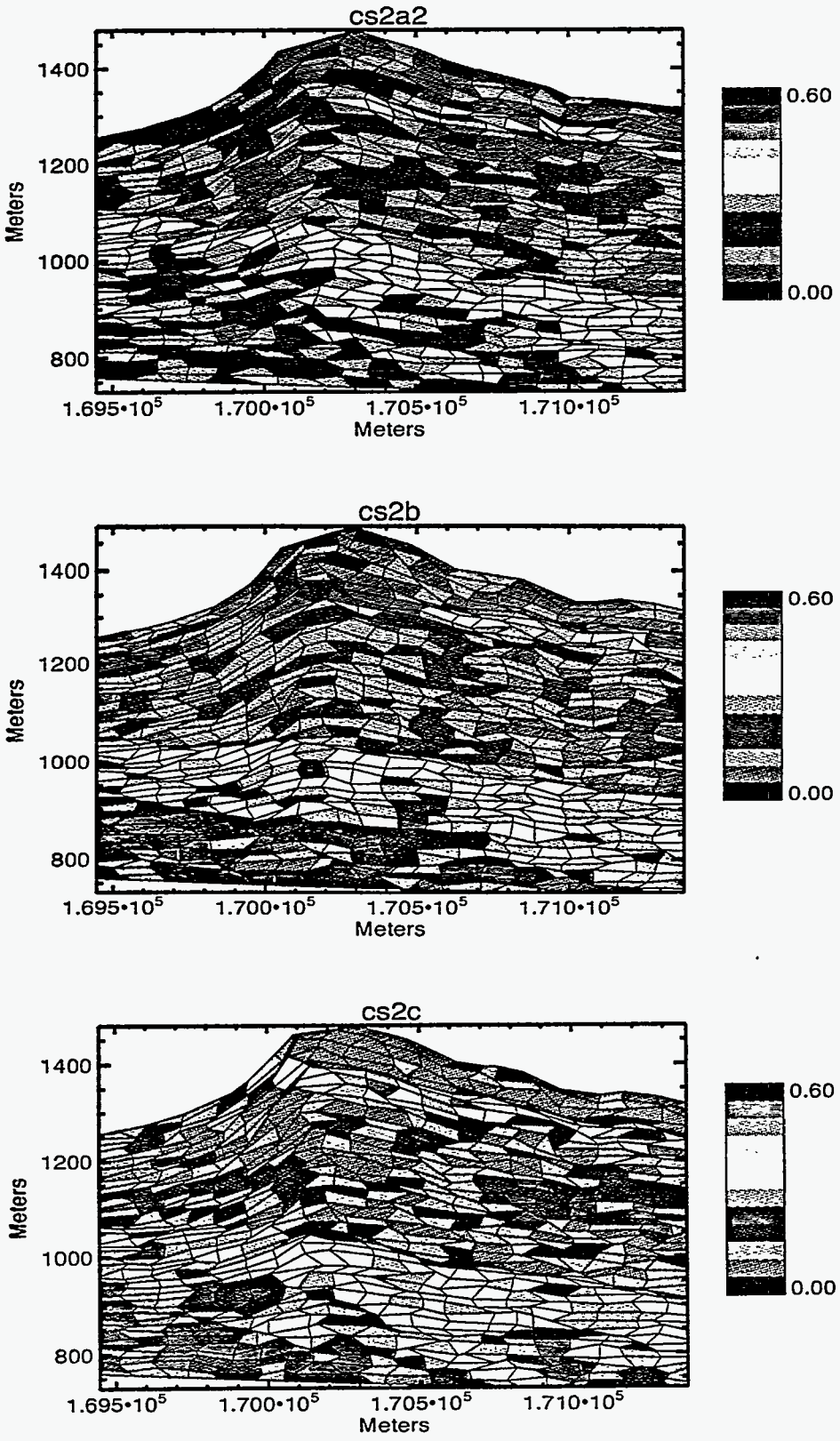

Figure 4-6b. Porosity distribution of the three simulations for cross-section 2.

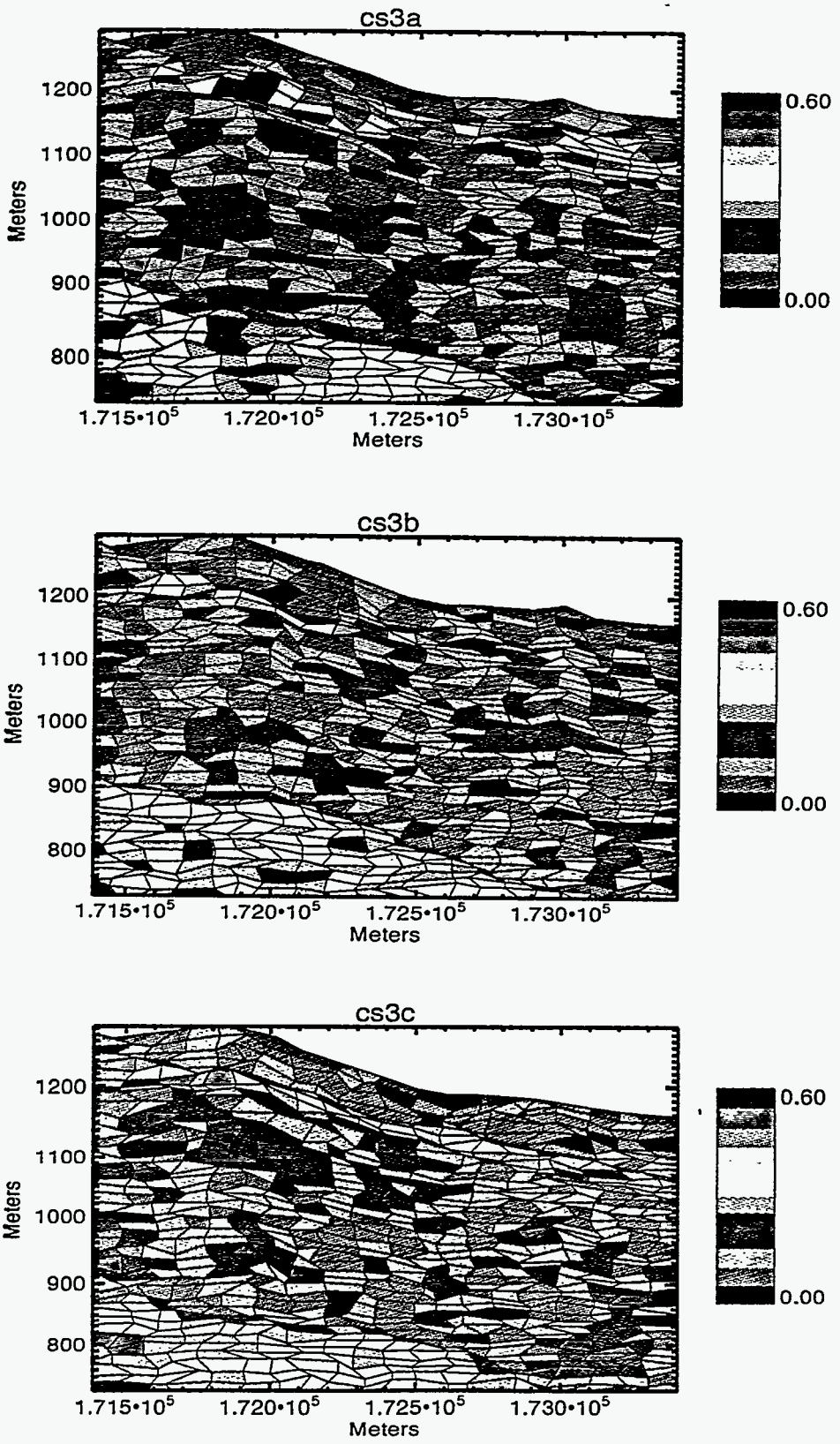

Figure 4-6c. Porosity distribution of the three simulations for cross-section 3.

It is interesting to note that neither high nor low saturation zones were observed along the Ghost Dance fault, the eastern boundary of cross-sections 1 and 2. The LBL/USGS site-scale model predicts moisture buildup along faults when they act as capillary barriers and relatively dry conditions when the faults are assumed to readily conduct water (Bodvarsson et al., 1994). In contrast, the results of these simulations indicate that heterogeneities might have a strong enough influence on the flow system to divert lateral flow downwards and thus prevent such transport of liquid to the faults where it might build up or be diverted down the fault.

4.5.2 Fracture Saturation

There is a clear correlation between matrix saturation and fracture saturation (compare Figures 4-5 and 4-7). While the fractures tend to be nearly dry for a large portion of the cross-sections (with the exception of cs1c), the areas of higher fracture saturation corresponded to areas of higher matrix saturation. These zones below the PTn outcrop and along the TSbv are observed in simulations cs1a, cs1b, and cs1c. In cs1c, the zone of higher fracture saturation extends below the TSbv because that unit was not captured during upscaling. This correlation between matrix and fracture saturation is exaggerated in simulation cs1c with very high fracture saturations throughout the system. The three simulations of cross-section 3 show the opposite extreme, containing few elements with elevated fracture saturation. There are a few elements in cs3a with higher fracture saturations along the TSbv.

There are some zones of elevated fracture saturation along the upper PTn contact in the three simulations of cross-section 3. This is a capillary barrier, documented both by data in UZ-N54 and N55 and the observation of minerals indicating water alteration in this zone. Examination of the fluxes (Figure 4-9e) shows evidence of some lateral flow. Note that, due to the low saturated conductivity, the lateral flow is of relatively small magnitude.

Fracture saturations presented in Figure 4-7 are average saturations for the whole element. When running the particle tracker (Chapter 5), fracture flow is initiated when the fracture velocity exceeds the matrix velocity. Fracture saturation is related to fracture velocity through the permeability characteristic curves (Section 3.2.4) and Darcy's law. The comparison of velocities in the particle tracker are made at the point where the particle is located, not for a whole element. Figure 4-8 presents those geostatistical nodes in cs1a where the fractures are saturated. Comparison of this figure to Figure 4-7, cs1a shows how much more localized the zones of higher fracture saturation are than when viewed at the flow-element scale.

4.5.3 Darcy Flux

Fluxes presented in Figure 4-9 are averages for the elements. The scale of fluxes shown in eight of the nine cases are identical. The ninth case, cs1c, had much larger fluxes than the other cases and therefore was not scaled to the others. Excluding cs1c, the fluxes are the largest in the

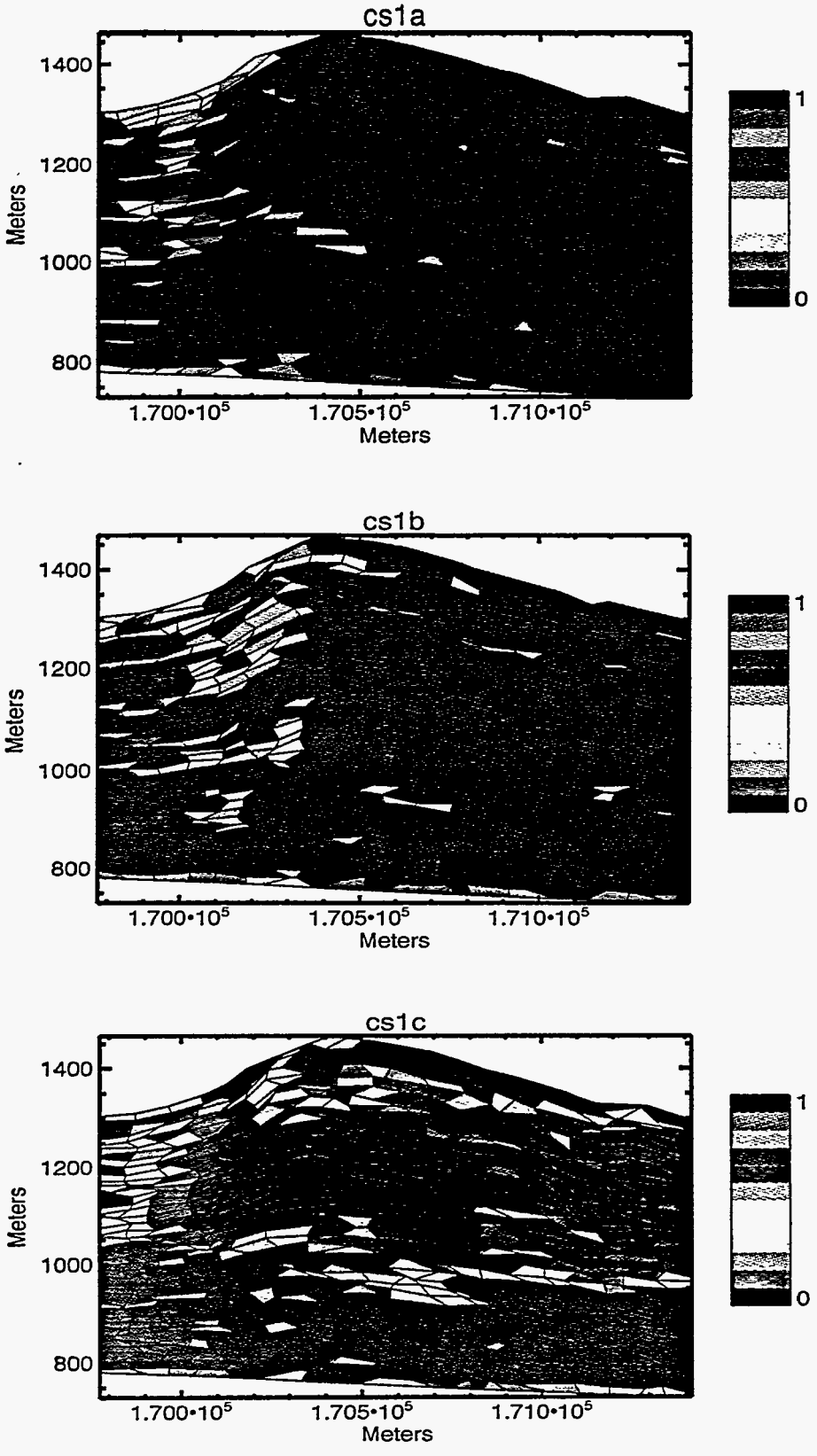

Figure 4-7a. Fracture saturation distribution of the three simulations for cross-section 1. The average fracture saturation of each element is expressed by the color scale.

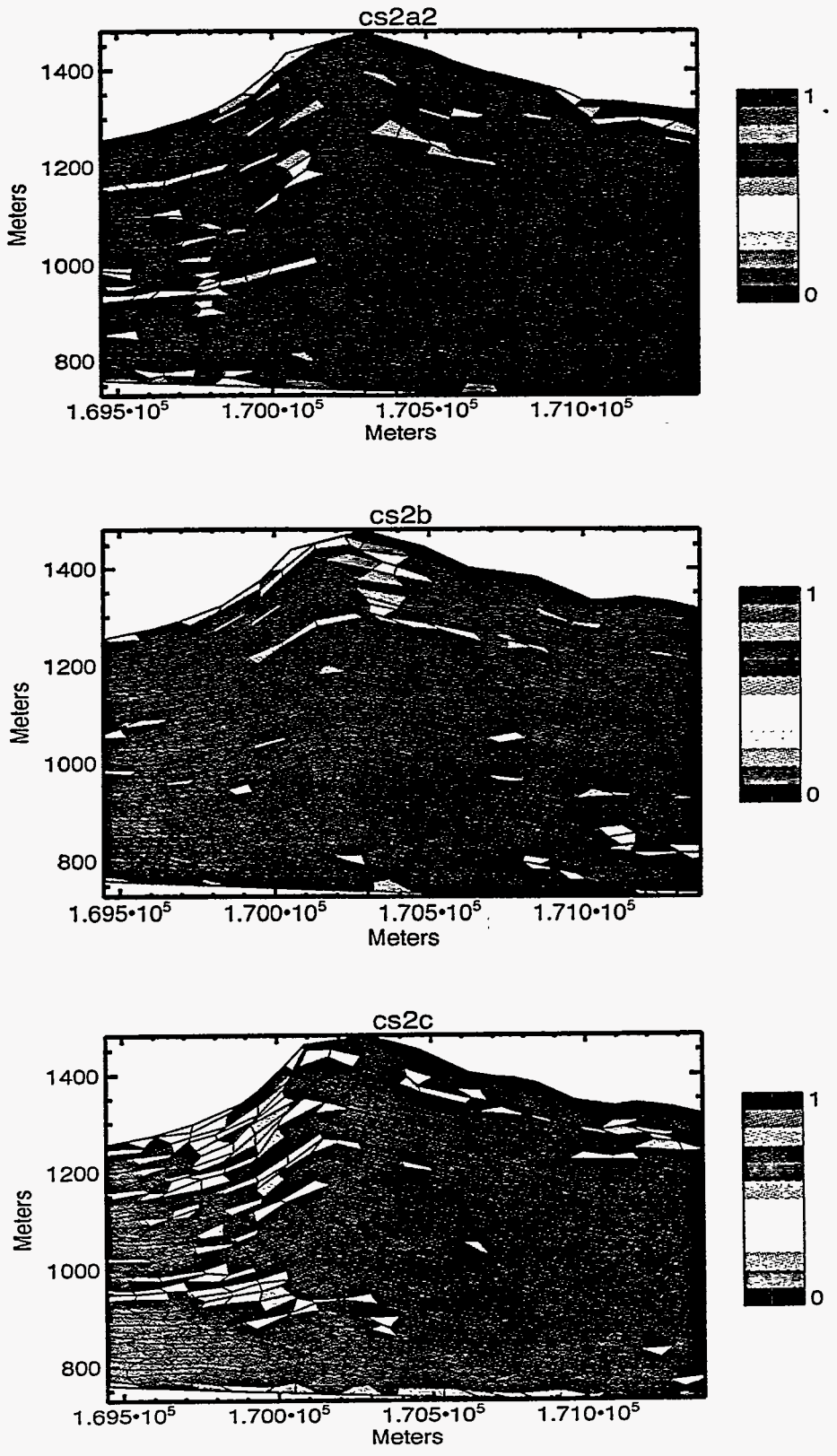

Figure 4-7b. Fracture saturation distribution of the three simulations for cross-section 2. The average fracture saturation of each element is expressed by the color scale.

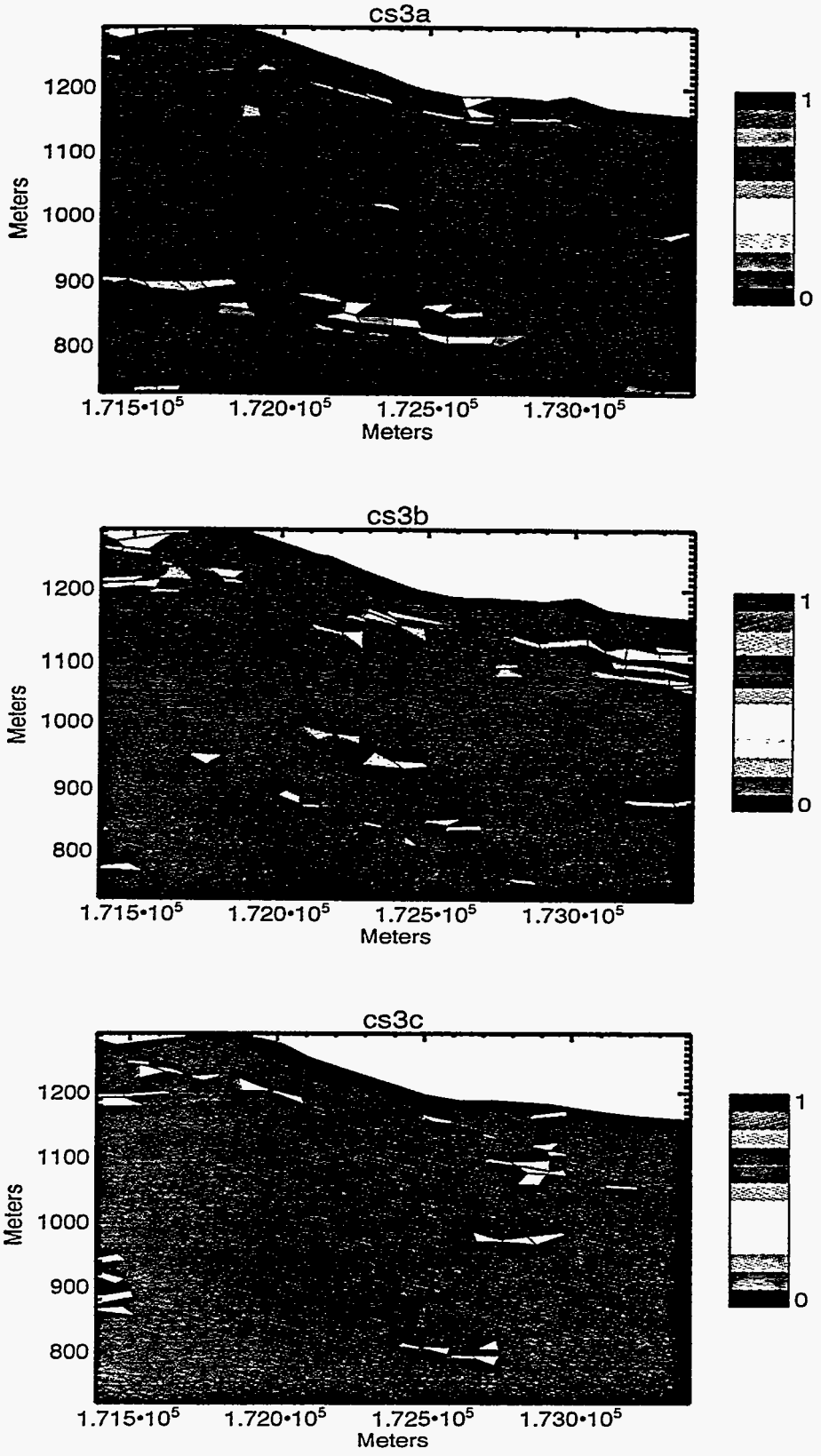

Figure 4-7c. Fracture saturation distribution of the three simulations for cross-section 3. The average fracture saturation of each element is expressed by the color scale.

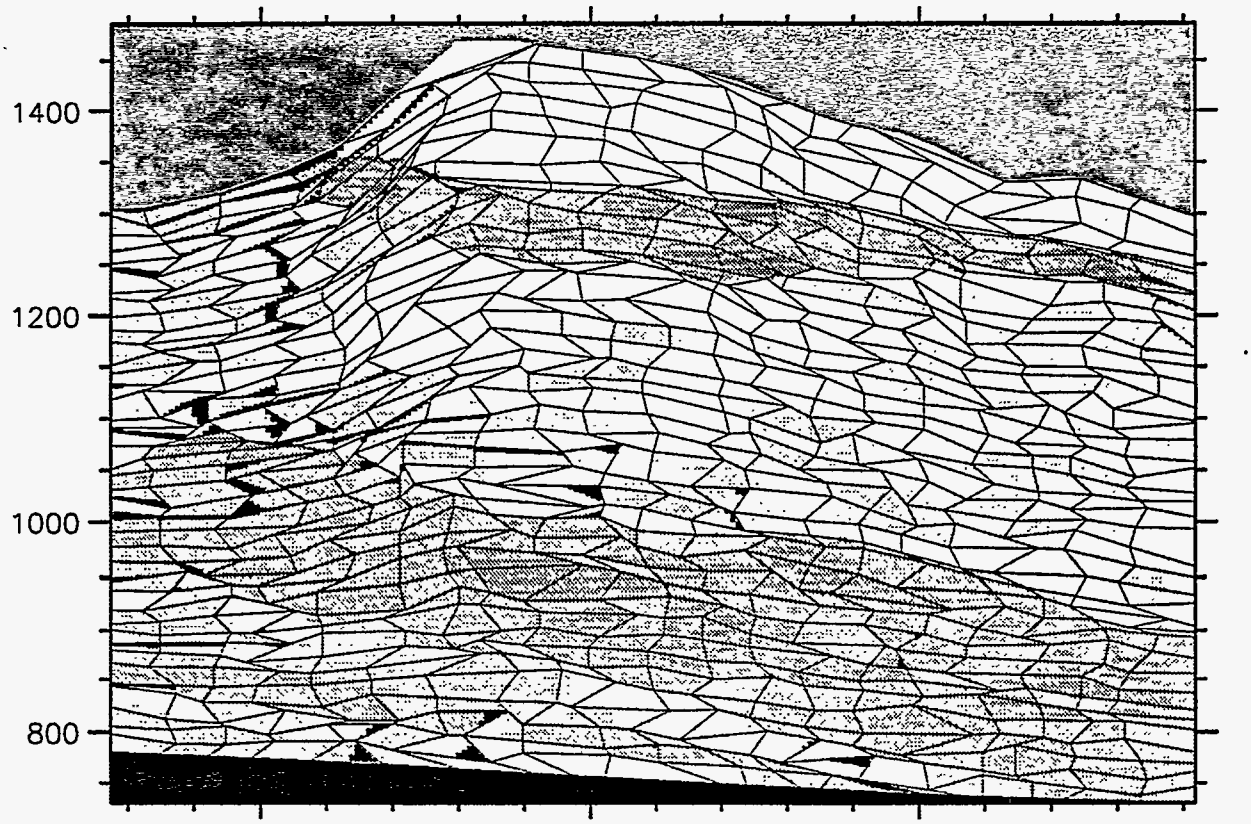

Figure 4-8. Comparison of matrix to fracture velocity for cross-section 1a. Green areas represent geostatistical nodes where the fracture velocity exceeds the matrix velocity and thus fracture flow is assumed to occur. Brown shading represents the porosity of the cross-section (darker shading indicates higher porosity).

cases with infiltration at the PTn outcrop (cs1a, cs1b, and cs2c). In almost all of the cases, the dominant fluxes are vertical. Lateral flow is observed in the PTn in cs1b, cs2c, cs3a, as well as a little in the western portions of cs3b and cs3c. The flow is diverted downwards in the last two cases when the thickness of the PTn decreases and the porosity of the elements in the PTn decrease slightly. The lateral flow in cs1c and cs2c is small relative to the vertical flow. Case cs1c is so saturated that lateral flow is not only observed in the PTn, but halfway down the TSw. Some vertical flow is also observed below the TSbv in cases cs1a and cs2a.

Fluxes were also examined through the upper and lower sides of the upper row of elements to determine the infiltration along the upper boundary for cs1c, in which the capillary suction pressure along the TCw was an unusually low -47 m, and cs1b, where the capillary pressure was -167 m (Figure 4-10). Average fluxes are generally lower than those predicted by Flint and Flint (1994) but within the same order of magnitude for the TCw. It is known (Flint et al., 1994) that infiltration is strongly dependent on location, being higher at ridge tops and side slopes than in valleys. The approach of using a sampled value for capillary pressure over the entire outcrop was recognized as being conservative; work by the USGS is being planned to examine more detailed variation in infiltration with unit and location instead of taking an average for a unit. The results of this work might lead to more closely matched infiltrations, and extremes such as cs1c would not persist.

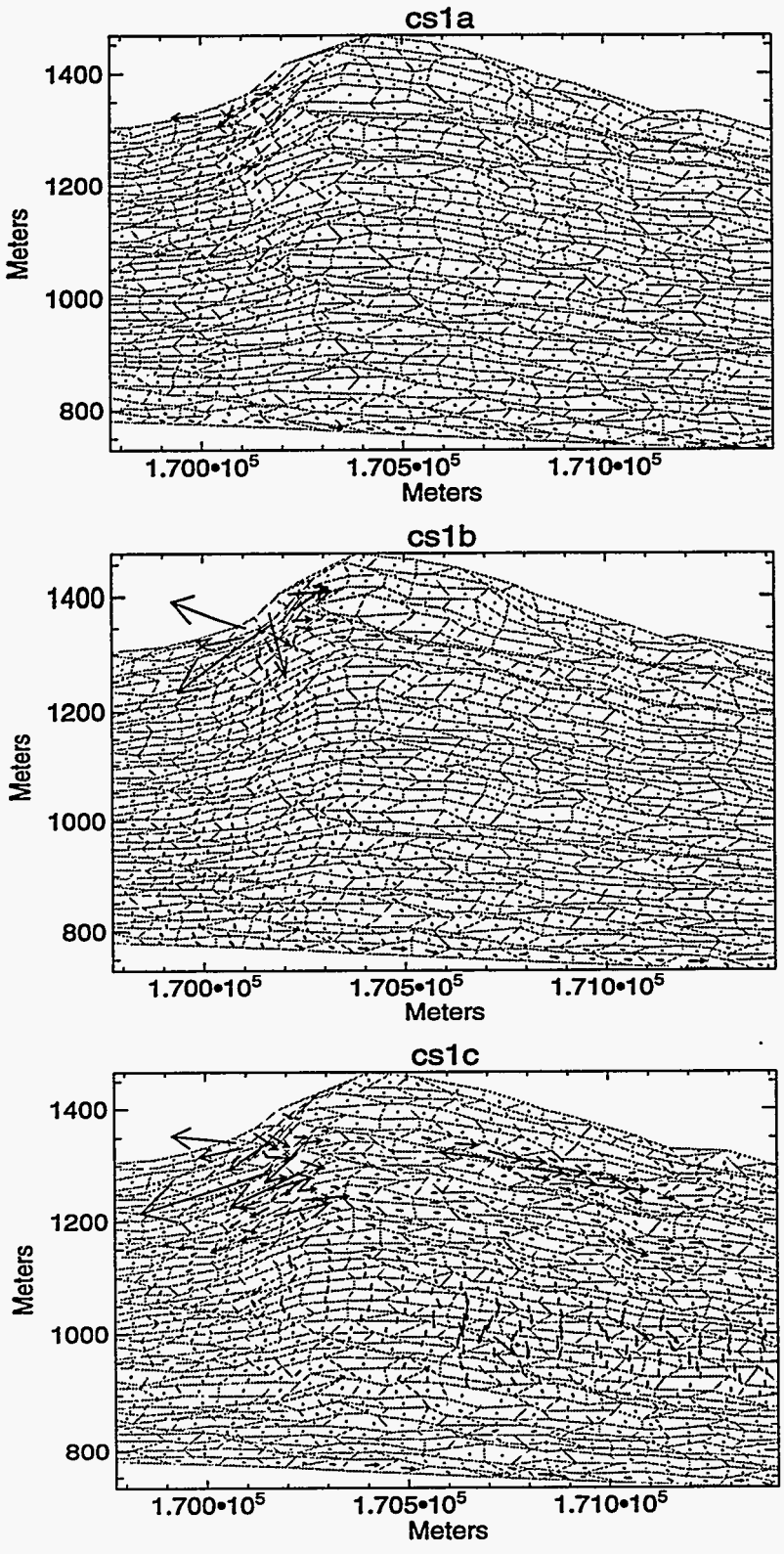

Figure 4-9a. Darcy flux distribution of the three simulations for cross-section 1.

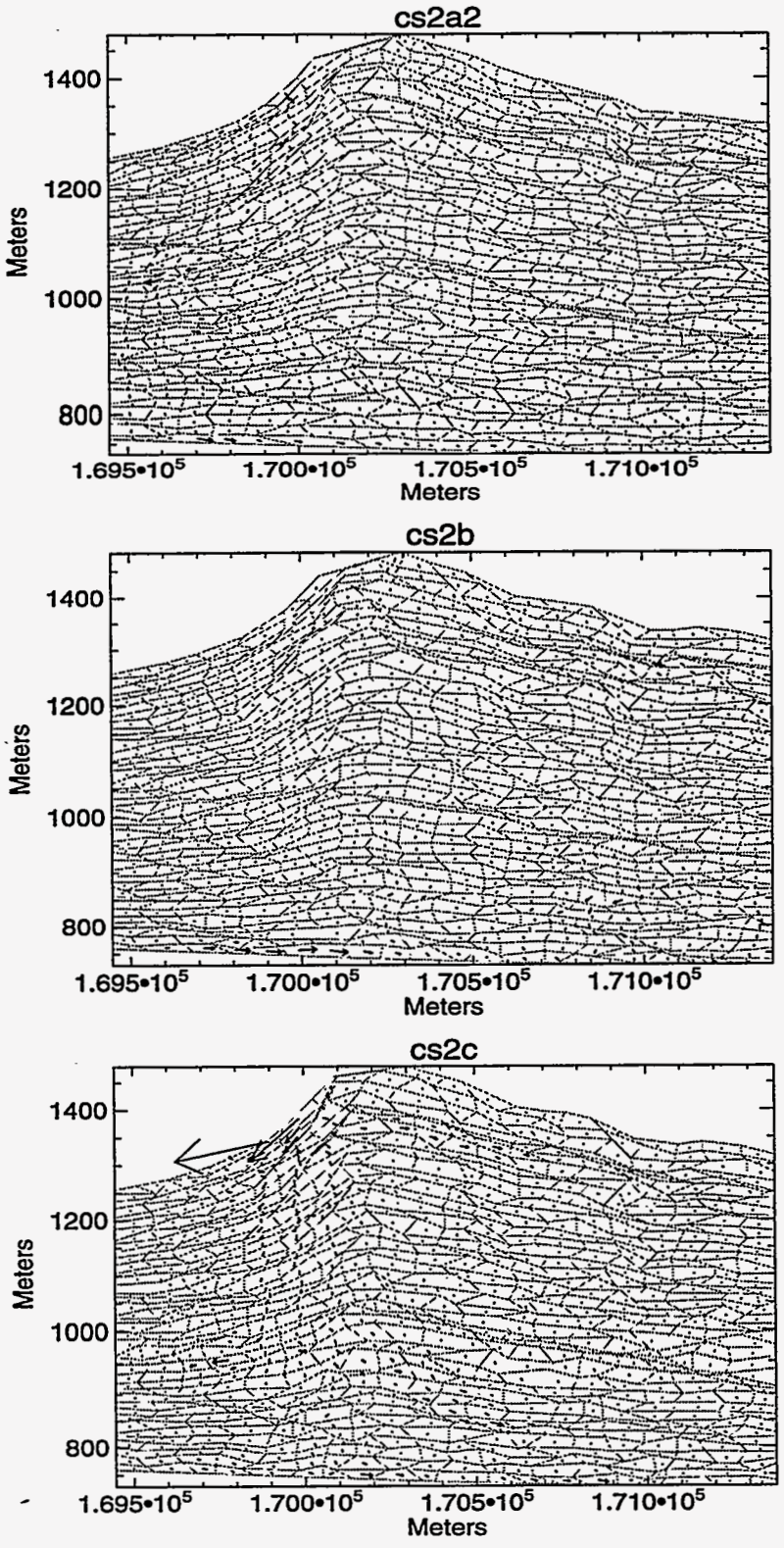

Figure 4-9b. Darcy flux distribution of the three simulations for cross-section 2.

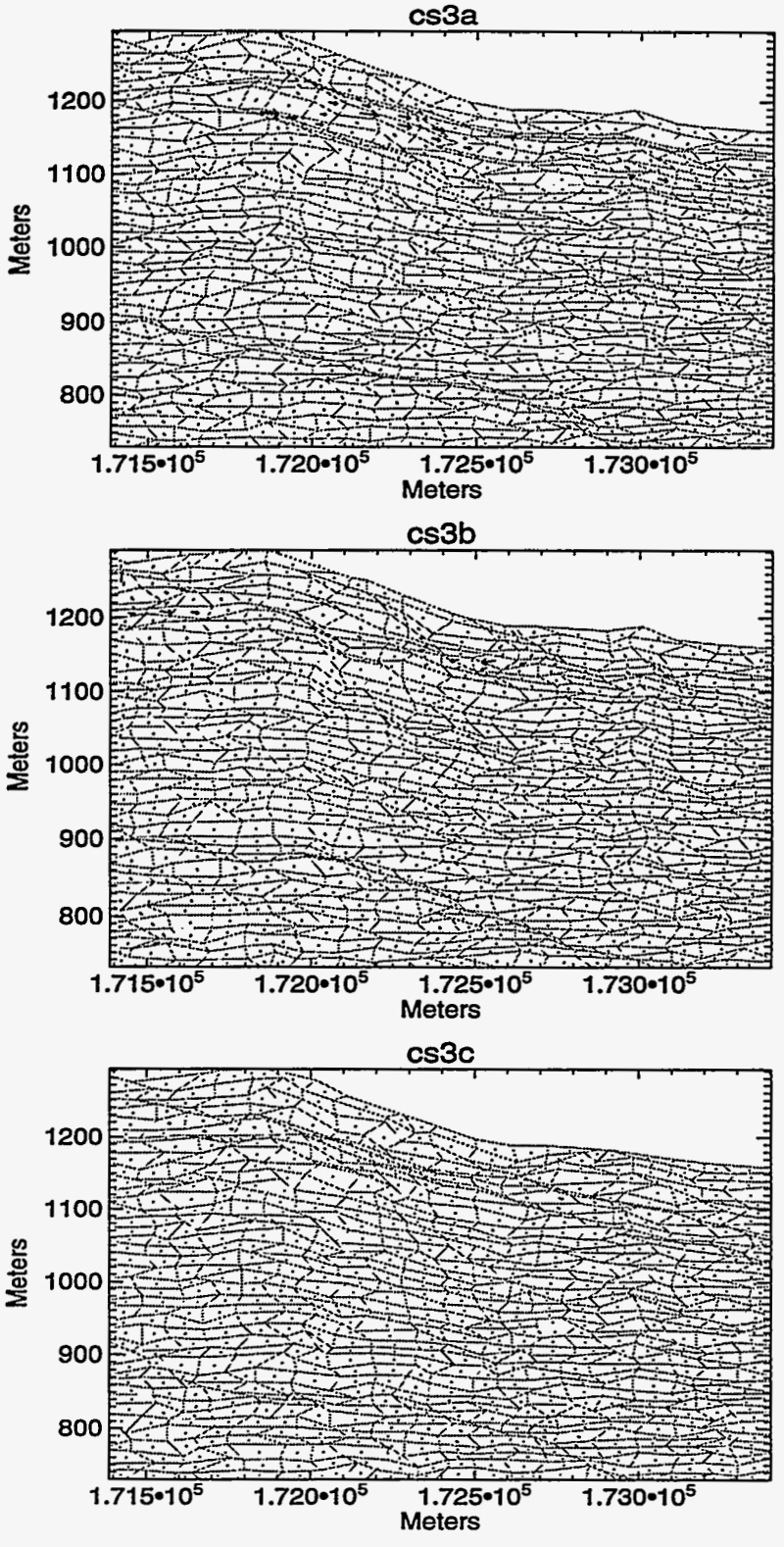

Figure 4-9c. Darcy flux distribution of the three simulations for cross-section 3.

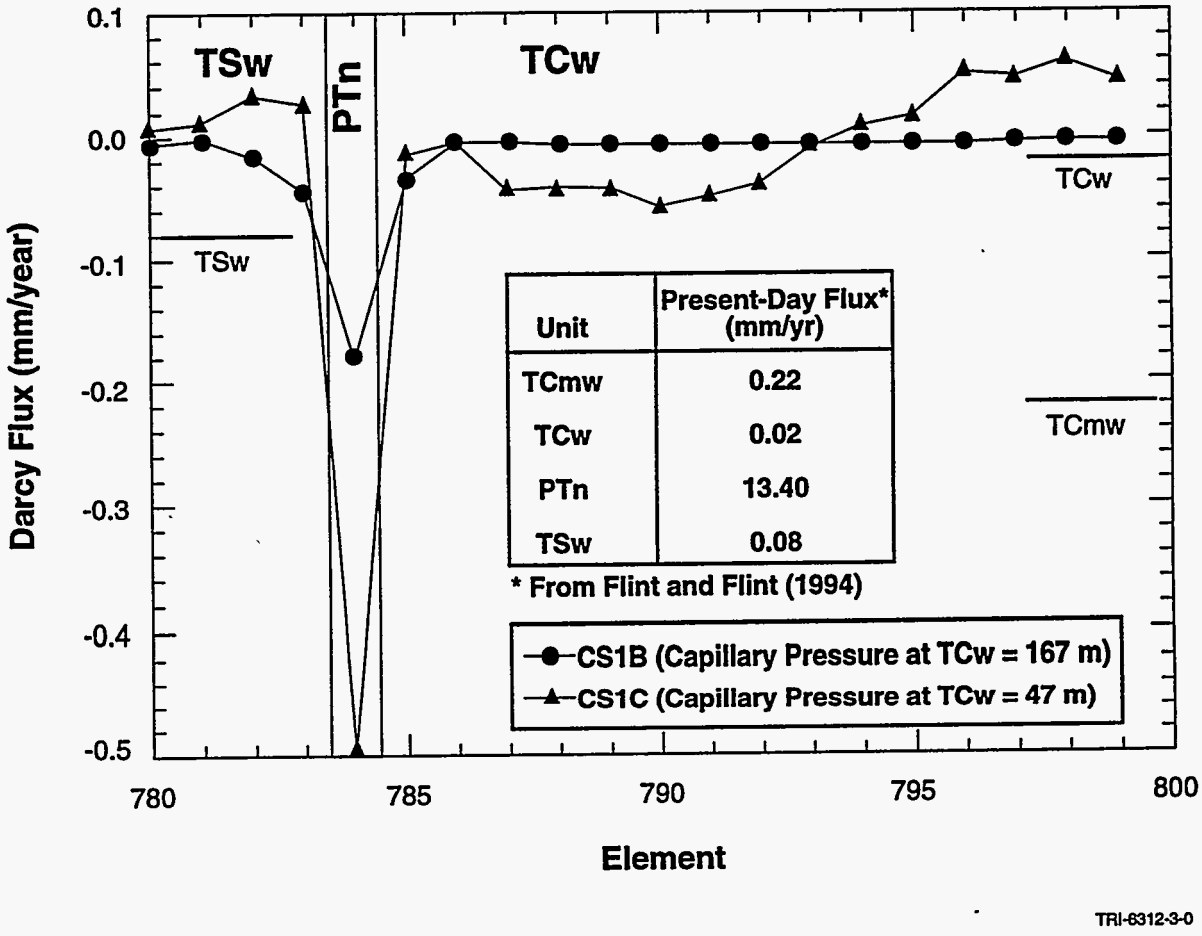

Figure 4-10. Infiltration through the lower side of the upper row of elements for simulations of cs1b and cs1c and comparison to fluxes estimated by Flint and Flint (1994).

4.5.4 Unsaturated Hydraulic Conductivity and Pressure

Unsaturated hydraulic conductivity and capillary pressure are also calculated by the flow code. Examination of trends in these two parameters does not provide any more insight into the flow system than described in the preceding sections. Both hydraulic conductivity and water pressure are closely linked with matrix saturation (Figure 4-11).

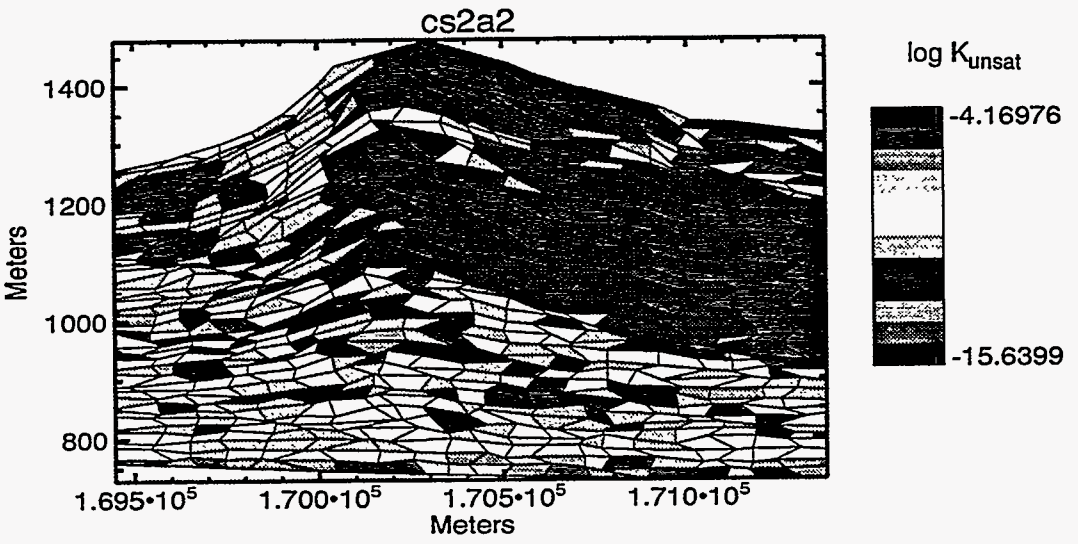

(a)

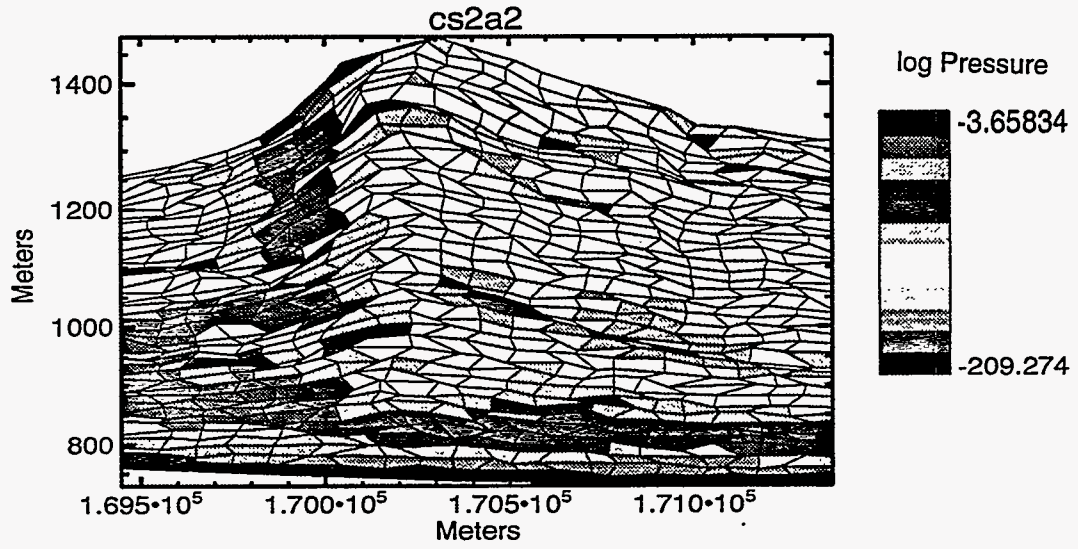

(b)

Figure 4-11. Unsaturated hydraulic conductivity (a) and capillary pressure (b) distributions for cross-section 2a2

Chapter 5
Particle Tracking

The particle tracker is a post-processing procedure that simulates the movement of individual water particles within the two-dimensional steady-state groundwater velocity field calculated by the DUAL flow code (Robey, 1994), providing the means to estimate a GWTT. Water particles move within the simulation by advection and molecular diffusion. Advection may occur at either matrix or fracture-flow velocities, depending on the local saturation determined by the flow model. By allowing particles to experience advective transport at fracture-flow velocities, the fastest groundwater pathways within the flow system can be simulated. The use of numerous particles in multiple realizations of the unsaturated zone flow system provides a probabilistic representation of GWTT.

5.1 Particle Transport Processes

Particle transport occurs in the particle-tracking code by advection at the local fluid velocity for each time step of the transport simulation. Particle tracking is accomplished using an interpolation of the velocity vector within each element and a numerical estimate of the new particle position following each time step.

Because groundwater velocities are calculated by the flow code at the nodes of the quadrilateral elements of the problem domain, it is necessary to estimate the local fluid velocity for particles within each element. The bilinear interpolation scheme, as described in Anderson and Woessner (1992) and Istok (1989), is used to estimate groundwater velocities. The bilinear interpolation method results in a fully continuous flow field and is the same as the basis functions used in the finite-element formulation of the DUAL flow code.

Particles are tracked along flowlines by numerical integration of fluid velocity using the first-order Euler technique (Cheney and Kincaid, 1985). Accuracy of the Euler technique is highly dependent on the length of the time step, relative to the magnitude and variations in the velocity field. Because large time steps were used in the GWTT analysis, accurate results were probably obtained for particle tracking only at the very low matrix velocities predominant over most of the domain. Accurate particle tracking at fracture flow velocities in future analysis may require utilization of a higher order technique (e.g., fourth-order Runge-Kutta), especially in regions of strongly divergent or convergent flow.

Molecular diffusion of water particles is modeled as a random process in the particle tracking code. The standard deviation of the Gaussian distribution of the diffusion length is defined as follows (Fetter, 1992):

$$\sigma = \sqrt{2D\Delta t} \tag{5-1}$$

where D is the effective diffusion coefficient and t is the time step. A value of 93.0×10^{-6} cm^2/s was used as the effective diffusion coefficient. Particles are moved a random distance as described by this Gaussian distribution in a uniformly distributed random direction for each time step in the simulation. Although molecular diffusion is a relatively slow process, especially in porous media, it can be significant relative to the very low matrix velocities in the unsaturated zone and at the long time periods of the simulation (Anderson, 1979).

Because molecular diffusion is a process generally associated with solute transport and seen to be "driven" by solute concentration gradient, it may not be intuitively obvious why molecular diffusion of water particles is included in the particle-tracking algorithm. The driving force in molecular diffusion is the temperature-dependent random motion of molecules or ions due to Brownian movement. The result of such random motion is the net movement from areas of high concentration to areas of low concentration. However, the random movement process continues, even in the absence of a concentration gradient, but with no net change in concentration.

Hydrodynamic dispersion is not explicitly included as a transport process in the particle tracking code. However, heterogeneity of hydraulic parameters in the flow model results in significant variability in the magnitude and direction of groundwater velocities in the simulated flow field. The physical interpretation of hydrodynamic dispersion in other codes is the variability of the hydrologic properties, so this treatment is essentially the same. Additional dispersion occurs at the subelement scale and could be included in future particle tracking as an additional random component of particle transport.

Because the DUAL flow code is based on the composite-porosity formulation of groundwater flow, a single fluid flux is calculated for the unsaturated medium. Although the flow code does not explicitly simulate fluid-flow interaction between the matrix and fractures, the particle tracker, as a postprocessing procedure, approximates the groundwater velocities in the matrix and fracture domains at particle locations for each time step. The relative components of fluid flux for each domain are calculated based on the hydraulic conductivities of the fractures and the matrix at the element scale and above. Using the fracture fluid flux, the matrix fluid flux, and values of porosity for each domain, the relative velocities in both the fractures and the matrix are determined. Figure 5-1 illustrates the relationships between pore velocity and pressure in the two domains for the Topopah Spring welded (TSw) unit as an example. If the fracture pore velocity is greater than the matrix pore velocity at the particle location, or if the pressure head is greater than or equal to zero, then the particle is assumed to be advected by fracture flow and advection of the particle

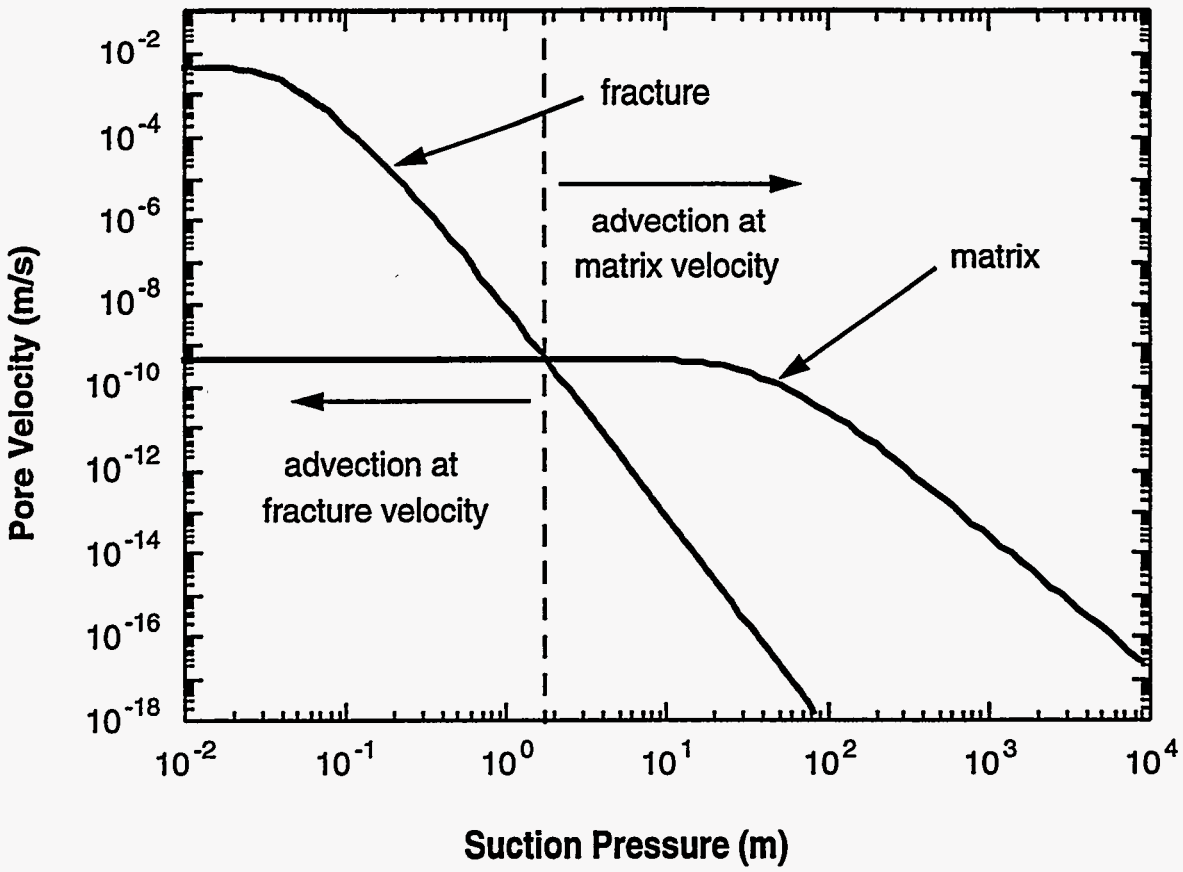

Figure 5-1. Example showing the relative pore velocities in the matrix and fracture domains in the Topopah Spring welded unit based on a unit hydraulic gradient.

occurs at the fracture-flow velocity. The general implication is that advective transport at lower saturations occurs in conjunction with matrix flow at relatively low velocities, and that only at very high saturations does advective transport occur at relatively high fracture flow velocities.

5.2 Assumptions and Limitations

The particle tracking procedure used in the GWTT analysis is implicitly based on the assumptions and limitations of the flow model. The results are subject to the assumptions regarding the boundary conditions and the composite-porosity formulation of the model, as well as the pressure equilibrium implied from the steady-state conditions of the flow solution. Processes not considered in the flow model and particle tracking, but which may have significant influence on groundwater travel times, include transient response of the system, vapor-phase transport of water particles, the natural geothermal gradient, and transport in the third dimension.

The interaction between matrix flow and fracture flow is approximated by the particle tracking code in a conservative manner. In regions where fracture pore velocity exceeds matrix pore velocity, water particles are immediately transferred to the fracture domain in spite of the fact that a significant portion of the groundwater may flow in the matrix. Also, because of the relatively high fracture velocities and large time steps, particles in fractures are moved large distances without reimbibition into the matrix. In most of the preliminary simulations, particles were advectively transported to the water table in a single time step following transfer to the fracture flow domain. While reimbibition into the matrix would be expected in zones of lower saturation after the initiation of fracture flow in the unsaturated zone, this process is generally excluded from the particle-tracking scheme due to the large time steps. The combination of allowing the initiation of fracture-flow transport (but limiting the reimbibition of water particles into the matrix) is very conservative. The planned dual-permeability formulation of the flow code will refine the matrix-fracture interaction, in terms of both the initiation and propagation of fracture flow in the model.

5.3 Implementation of Particle Tracking

The particle tracking was performed in a graphical computing environment that facilitates the interpretation of results. Computation of particle movement and visual representation of the process was performed using the PV-WAVE[3] command language and visualization software package. Individual screens display the positions of particles superimposed on a cross-section which shows the porosity distribution, numerical grid, and flow velocity vectors; an example screen is shown in Figure 5-2. Animation of the particle-tracking simulation may be produced with a series of frames. During the simulation, the times at which particles exit the system are tabulated for use in the construction of cumulative distributions of particle travel times in the unsaturated zone.

A weighted random distribution of particles along a line at the repository horizon was used in all of the simulations performed for this preliminary analysis. The weighting of the particle distribution reflects the mass of waste within the repository in the third dimension, perpendicular to the cross-section. For a complete GWTT analysis, initial placement of the particles may depend on the definition of the disturbed zone for the GWTT analysis; alternative initial positioning can be considered to evaluate other delineations of the disturbed zone. Since the definition of the disturbed zone may not be precise, the ability to use alternative positioning allows sensitivity analyses to be conducted.

The distribution of the GWTTs calculated by the particle-tracking code was reported as a cumulative probability distribution function (CDF) plot of particle travel times. The cumulative number of particles leaving the system was plotted against the travel time in the CDF plot. An

3. Precision-Visuals, Incorporated. 1992. *PV-WAVE.* Boulder, CO.

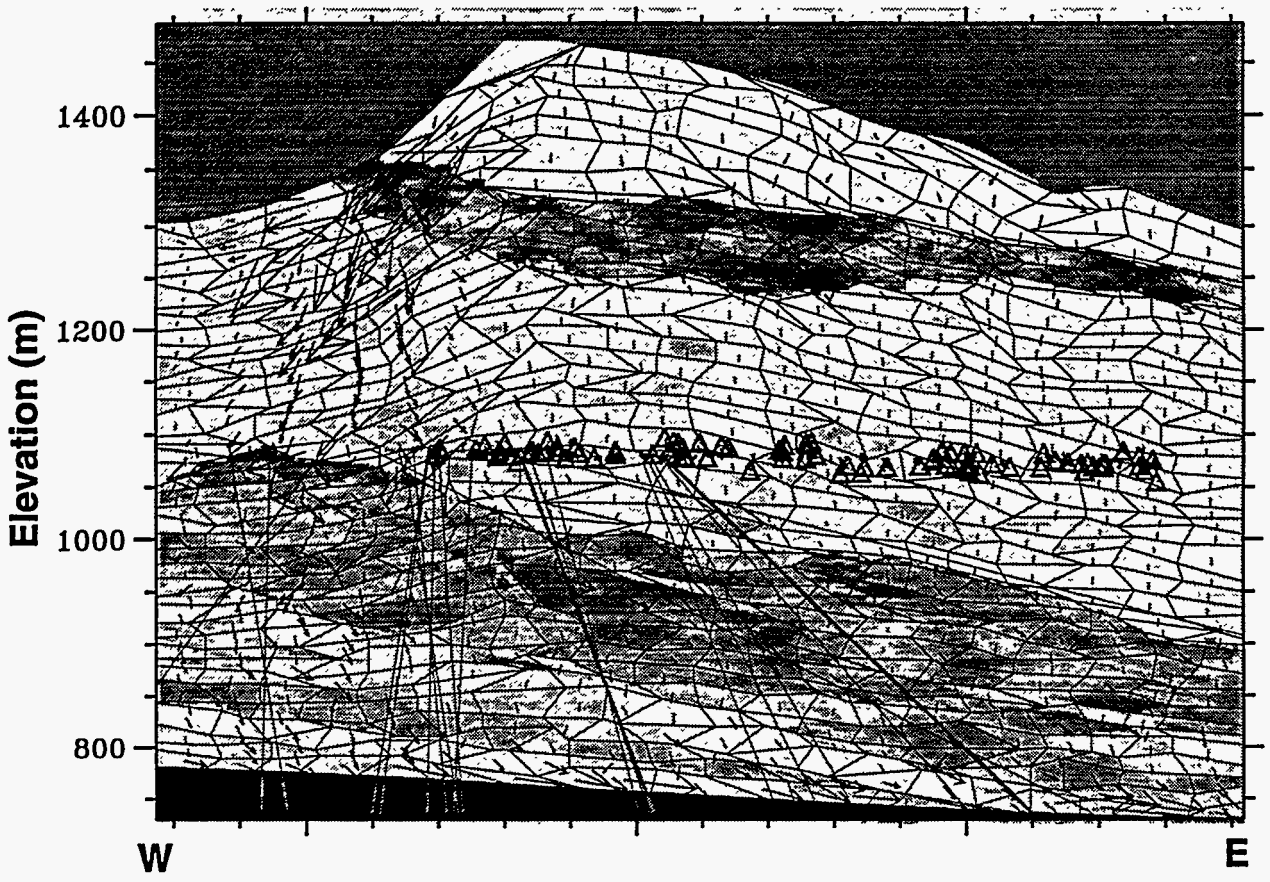

Figure 5-2. Example particle tracking screen showing topographic relief along the cross-section, numerical grid, composite flow velocity vectors, porosity distribution (as shading), particle positions, and particle exit paths. The cross-section is bounded on the west by the Solitario Canyon fault and on the east by the Ghost Dance fault. The duration of the simulation is 600,000 years.

example CDF plot for a single simulation along one of the modeled cross-sections is shown in Figure 5-3. Because 100 particles were used in each simulation, 1% of the cumulative probability corresponds to one particle.

5.4 Results

Particle tracking simulations were performed for each of the nine realizations described previously. Although these simulations are preliminary in nature, some tentative conclusions are made from these realizations of the flow system. However, it should also be noted that it is not

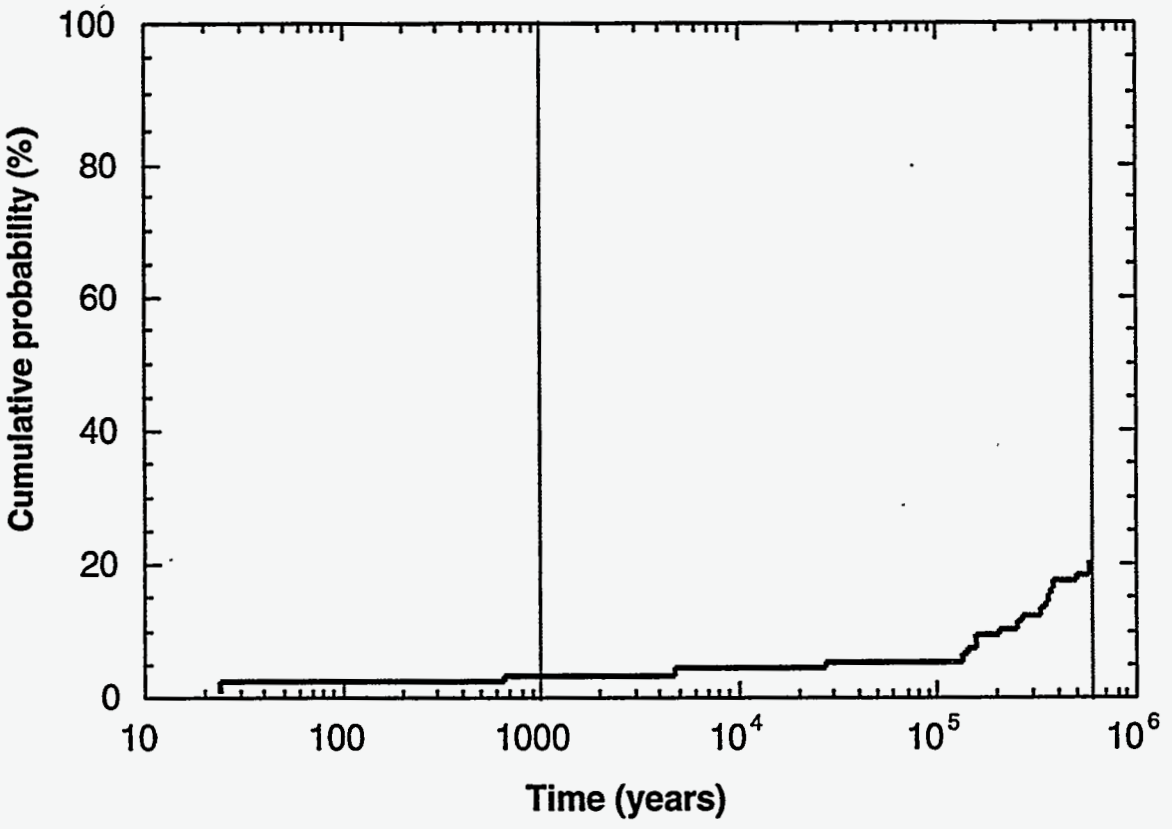

Figure 5-3. Example of CDF plot of particle travel times for a single realization along cross-section 1.

appropriate to infer anything about the conformance of the site to the GWTT regulations from the limited number of realizations and particles used in this study.

The results of the particle-tracking simulations for travel times of up to 1,000 years are summarized in Table 5-1. In each realization, 100 particles were introduced at the repository horizon. The relatively high percentage of particles being transported out of the UZ in realization cs1c is due to the very high saturations in the region of the repository in the steady-state flow simulation (see Chapter 4). In realizations other than cs1c, the maximum percentage of the particles exiting the UZ system within 1,000 years is 3%.

A pattern to the spatial distribution of particles that experience fracture flow and are removed from the unsaturated zone is apparent in these preliminary simulations. In most realizations, the particles that exit the system originate from the western part of the repository, beneath the outcrop of the PTn. Along cs3, in which there is no outcrop of the PTn, none of the particles is trans-

Table 5-1. Number of particles exiting the UZ

	Before 1,000 years	Before 600,000 years
cs1a	3	4
cs1b	2	3
cs1c	35	42
cs2a2	0	0
cs2b	0	1
cs2c	1	1
cs3a	0	0
cs3b	0	0
cs3c	0	0

ported to the water table within the 600,000-year duration of the simulation. Groundwater flow is primarily vertical, with only minor lateral diversion of flow within the PTn and some lateral flow at the basal vitrophyre of the TSw (Section 4.5). The generally higher saturation of the upper boundary conditions at the outcrop of the PTn, combined with the dominance of vertical flow, results in high local saturation below the PTn outcrop and the consequent mobilization of particles at fracture-flow velocities in this region of the model.

The surface capillary-pressure boundary conditions exert a strong influence on the number and spatial distribution of particles transported from the unsaturated zone. Because the capillary pressure boundary conditions applied at the surface of the cross-sections vary among the simulations according to the PDF defined for each unit, the saturation at the upper surface and the resulting steady-state groundwater fluxes and saturation conditions within the model domain vary considerably among the realizations. For example, in cs1c, the pressure assigned to the outcrop of the TCw unit, -47 m, was from the upper tail of the PDF. The resulting simulation of the flow field contained numerous regions of local saturation, causing about 35% of the particles throughout the area of the repository to exit the system within 1,000 years. The imposition of uniform pressure boundary conditions for the entire outcrop of a unit, especially from an extreme of the distribution, is probably not realistic. The effects of spatially heterogeneous outcrop pressure boundary conditions for each unit will be examined in future sensitivity analyses.

The stratigraphic position of the TSw basal vitrophyre relative to the elevation of the western part of the potential repository has a significant effect on the number of particles exiting the system during the simulation. In several of the realizations along cross-sections 1 and 2, high saturations are simulated at the basal vitrophyre, especially beneath the outcrop of the PTn. The

movement of particles at matrix-flow velocities in moderately saturated elements near the repository horizon is quite slow, even dominated by molecular diffusion in most cases. The vertical separation of the initial particle positions and the zones of higher saturation at the basal vitrophyre is thus a controlling feature of the groundwater travel time calculated by the model. Because of the uncertainty in the vertical position of the TSw basal vitrophyre, as introduced to the realizations by indicator geostatistical simulation, the distribution of particle travel times varies among simulations, demonstrating the importance of including uncertainty in the geologic model used for the GWTT analyses.

Chapter 6
Sensitivity Studies

In order to have confidence in the GWTT estimates, it is important to identify the aquifer properties that have the most significant effect on fast-path flow. By conducting sensitivity analyses, these critical parameters and their effect on the flow system can be determined. Sensitivity analyses are beneficial because they help to understand the limitations of a model, the effects of boundary conditions (location and type), and the interaction between the matrix and fracture system (e.g., composite-porosity vs. dual-permeability). In addition, they help to optimize data acquisition and computer use.

The sensitivity analyses reported here concentrated on understanding the effects of intra-unit heterogeneities versus homogeneous units, and deterministically versus geostatistically assigned unit contacts. The extent of the zeolitic region in the Calico Hills was also examined. In addition, the capabilities of the unsaturated-flow code DUAL were examined by varying grid sizing, using a finer grid along the PTn outcrop, and changing the upper boundary condition from specified pressure to specified flux.

6.1 Introduction

Preliminary sensitivity analyses were conducted on cross-section cs1b, located along the northern portion of Yucca Mountain. In choosing a cross-section, cs3a, b, and c were eliminated because of small fluxes and low velocities of particles in each simulation. Simulation *c* in cross-section 1 was also eliminated because of the extreme upper boundary condition. Otherwise, the selection of a cross-section was somewhat arbitrary, and the investigation of only one cross-section was primarily due to limited resources.

A number of specific sensitivity analyses were conducted (Table 6-1). The effects of hydrologic heterogeneities were evaluated by comparing the base case (*cs1b2*) with a case in which the hydrologic parameters remained uniform within a unit (*ihm*). The effects of deterministically assigned unit contacts, as would be done based on subjective interpretation of lithostratigraphic and structural data, were examined. This was accomplished by setting the thickness of PTn (*uht5* and *uht*) to its mean and comparing it with the base case, which has geostatistically generated unit contacts (*cs1b2* and *cs1b5*). The sensitivity of the model to grid size was examined by relating results of the 20 by 40 base case (*cs1b2*), a coarser grid (*cs1b8*), and three finer grids (*cs1b6*, *cs1b7*, and *cs1b9*). A comparison of the specified pressure upper boundary condition (*cs1b2*) to a specified flux boundary calculated from the base case was attempted, but the model did not converge. Instead, comparisons to other specified pressures along the upper boundary were made (*cs1b2a* and *ihma*). Finally, a porosity anisotropy ratio and spatial-correlation length based on recent thermal conductivity modeling (*ratio*) were compared with those used in the base case (*cs1b2*). The sensitivity of the groundwater saturation and flux to

Table 6-1: Descriptions of runs simulated for the sensitivity analyses

Run Name	Run Description
cs1b2 **Base Case**	Heterogeneous units and geostatistically determined unit thickness (PTn of variable thickness). Grid: 20 by 40 elements. This case differs from *cs1b* used in the original 9 simulations only in that elements were adjusted so they would only lie within one unit.
ihm	Similar to *cs1b2* except each unit is homogeneous. PTn of variable thickness. Grid: 20 by 40. The porosity of each unit was set to the mean porosity of that unit based on the beta distribution of porosity for that unit.
uht	PTn thickness set to the mean thickness of the PTn from *cs1b2*. Each unit is heterogeneous. Grid: 20 by 40.
uht5	Identical to *uht* except the porosities for each element were set to match those of *cs1b2*. Grid: 20 by 40.
cs1b5	This case is identical to *cs1b2* except that the porosities of each element were adjusted to match those of *uht*. Grid: 20 by 40.
cs1b6	Similar to *cs1b2*. Grid: 20 by 60. Porosity values assigned to elements after upscaling could therefore differ.
cs1b7	Similar to *cs1b2*. Grid: 25 by 40. Porosity values assigned to elements after upscaling could therefore differ.
cs1b7a	Similarl to *cs1b2*. Grid: 30 by 60. Porosity values assigned to elements after upscaling could therefore differ. The flow code did not converge in running this case, thus discussion in the text is minimal.
cs1b7b	Similar to *cs1b2*. Grid: 30 by 40. Porosity values assigned to elements after upscaling could therefore differ. The flow code did not converge in running this case, thus discussion in the text is minimal.
cs1b8	Similar to *cs1b2*. Grid: 10 by 20. Porosity values assigned to elements after upscaling could therefore differ.
cs1b9	Similar to *cs1b2*. Grid: 24 by 60. Porosity values assigned to elements after upscaling could therefore differ. The four extra elements added in the x-direction were weighted so that they underlay the PTn outcrop.
ihma	Identical to *ihm* except for the upper boundary condition exerted on the system.
cs1b2a	Identical to *cs1b2* except for the upper boundary condition exerted on the system.
ratio	Similar to *cs1b2* except the anisotropy ratio of the porosity distribution within a layer is set at 50:1 instead of 4:1 and a correlation length of 500 m instead of approximately 150 m.
ch1b (base case), *ch1b1*, *ch1b2*, and *ch1b3*	Identical to the base case except new indicator simulations were run only for TSbv, CHnz, and CHnv units.
ch1bf	Identical to ch1b except heterogeneity has been added to the fracture moisture retention curves.

the amount of vitric versus zeolitic tuffs in the Calico Hills unit (CHnv vs. CHnz) was analyzed by running additional indicator simulations that only varied the CHnz, CHnv, and TSbv. Finally, the sensitivity of the model to fracture heterogeneities was evaluated by varying the fracture moisture retention curves. The methodologies of setting up all of these simulations are described in more detail in Section 6.3.

Flow simulations were run with DUAL (Robey, 1994). To date, the code has been effective in modeling flow at Yucca Mountain because of its capability of preserving heterogeneities throughout the model domain and within a hydrogeological unit.

East and west fault boundaries were simulated using no-flow conditions. The lower boundary at the water table and the upper boundary were modeled as specified pressures. In all the cases, except where noted, the capillary pressure heads along the upper boundary of the TSw, PTn and TCw were set at -149 m, -5.5 m, and -167 m respectively. Because of the constant-pressure upper boundary, infiltration rates along this boundary were not uniform and must be examined separately. Node locations for some elements for runs *cs1b2*, *ihm*, and *uht* (Table 6-1) required adjustment so that the elements did not cross hydrogeological boundaries between the PTn and TCw or TSw.

6.2 Methodology, Results, and Discussion

6.2.1 Intra-Unit Heterogeneity vs. Intra-Unit Homogeneity

Sensitivity analyses were performed to compare the base case (*cs1b2*) in which unit thicknesses and element porosities were geostatistically determined, producing a cross-section with units of variable thickness having intra-unit heterogeneities, to a cross-section also having units of variable thickness but with homogeneous hydrologic parameters (*ihm*). To generate a system with homogeneous layers, the matrix porosity of the units were assigned their mean values, based on beta distribution of the available data: TCw = 0.09; PTn = 0.40; TSw = 0.13; TSbv = 0.07; CHnv = 0.36; CHnz = 0.32; PPn = 0.30; PPw = 0.17; BFn = 0.25; and BFw = 0.16. See Figure 6-1 for a comparison of the porosities for the two systems.

As Figure 6-2 shows, the matrix saturation is clearly much higher in *cs1b2* (intra-unit heterogeneities), especially under the PTn outcrop. In the case with homogeneous units, a layer of high saturation is present above and within the basal vitrophyre. Comparing the Darcy fluxes in each unit (Figure 6-3), the fluxes are also much greater in *cs1b2*. Much of the infiltration is diverted downwards under the PTn outcrop in both cases, though some lateral diversion is observed through the PTn in *cs1b2*. For the case with homogeneous units, there is lateral diversion of water on top of the basal vitrophyre, but not through the PTn where the water is flowing vertically. Infiltration was two orders of magnitude higher into the PTn and one order of magnitude higher into the TSw for the case with heterogeneous units (Figure 6-4 and Table 6-2). In both case *cs1b2* and *ihm*, a small percentage of particles leave the system after 1,000 years (2% and 0%, respectively) and 600,000 years (4% and 1%, respectively) (Table 6-2).

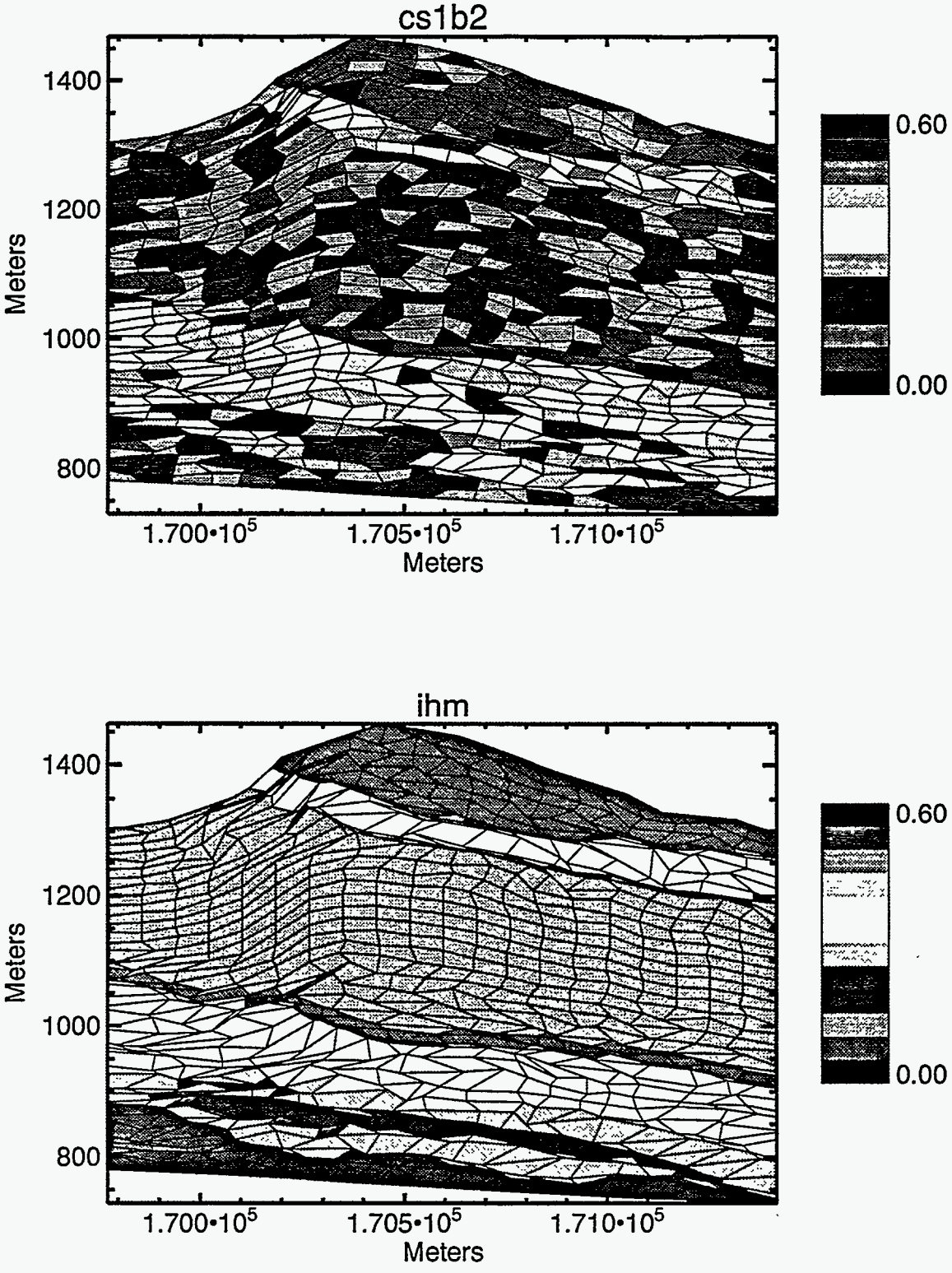

Figure 6-1. Comparison of porosity distributions for simulations with (*cs1b2*) and without (*ihm*) intra-unit heterogeneities.

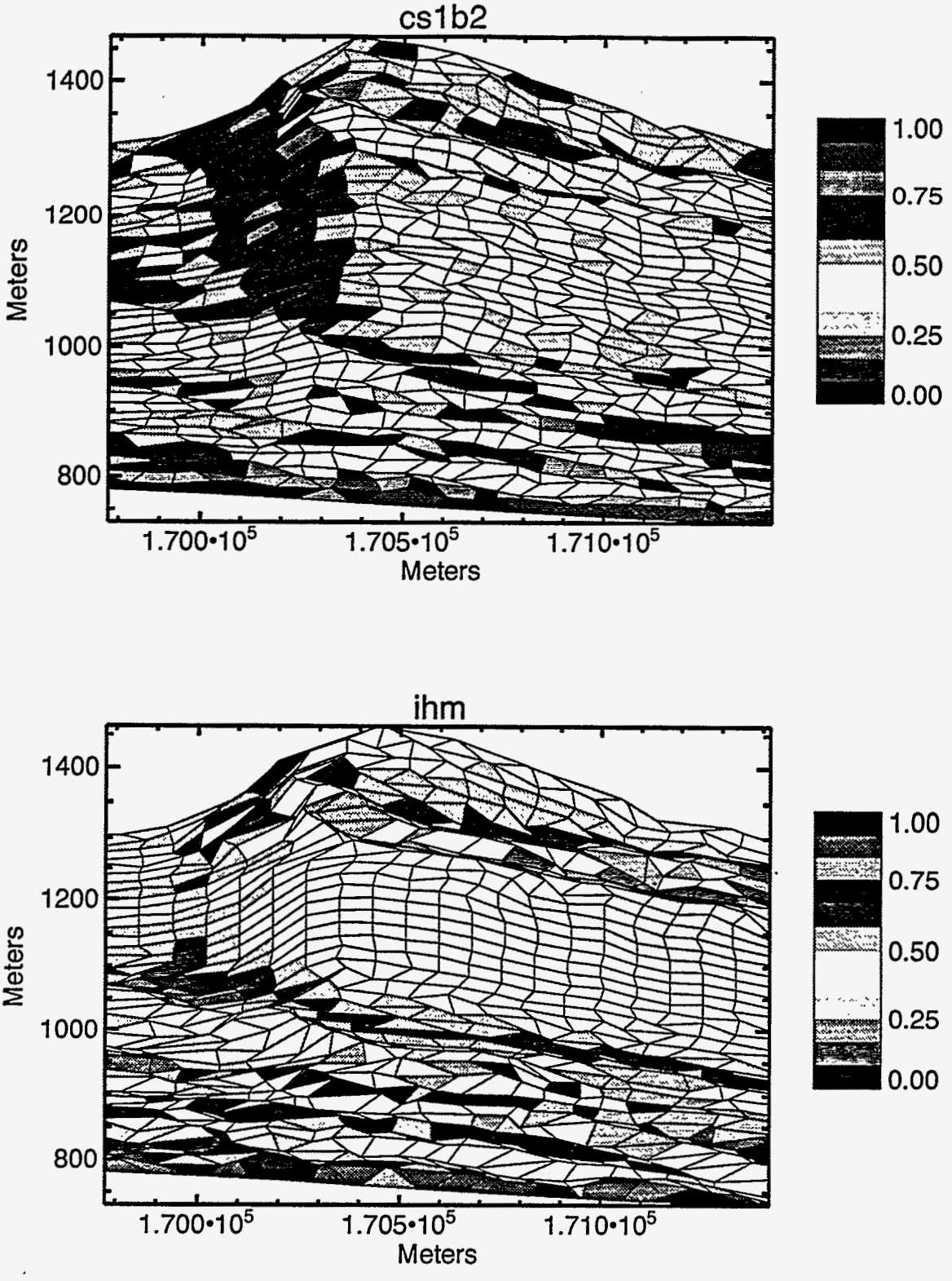

Figure 6-2. Comparison of matrix saturations for simulations with (*cs1b2*) and without (*ihm*) intra-unit heterogeneities.

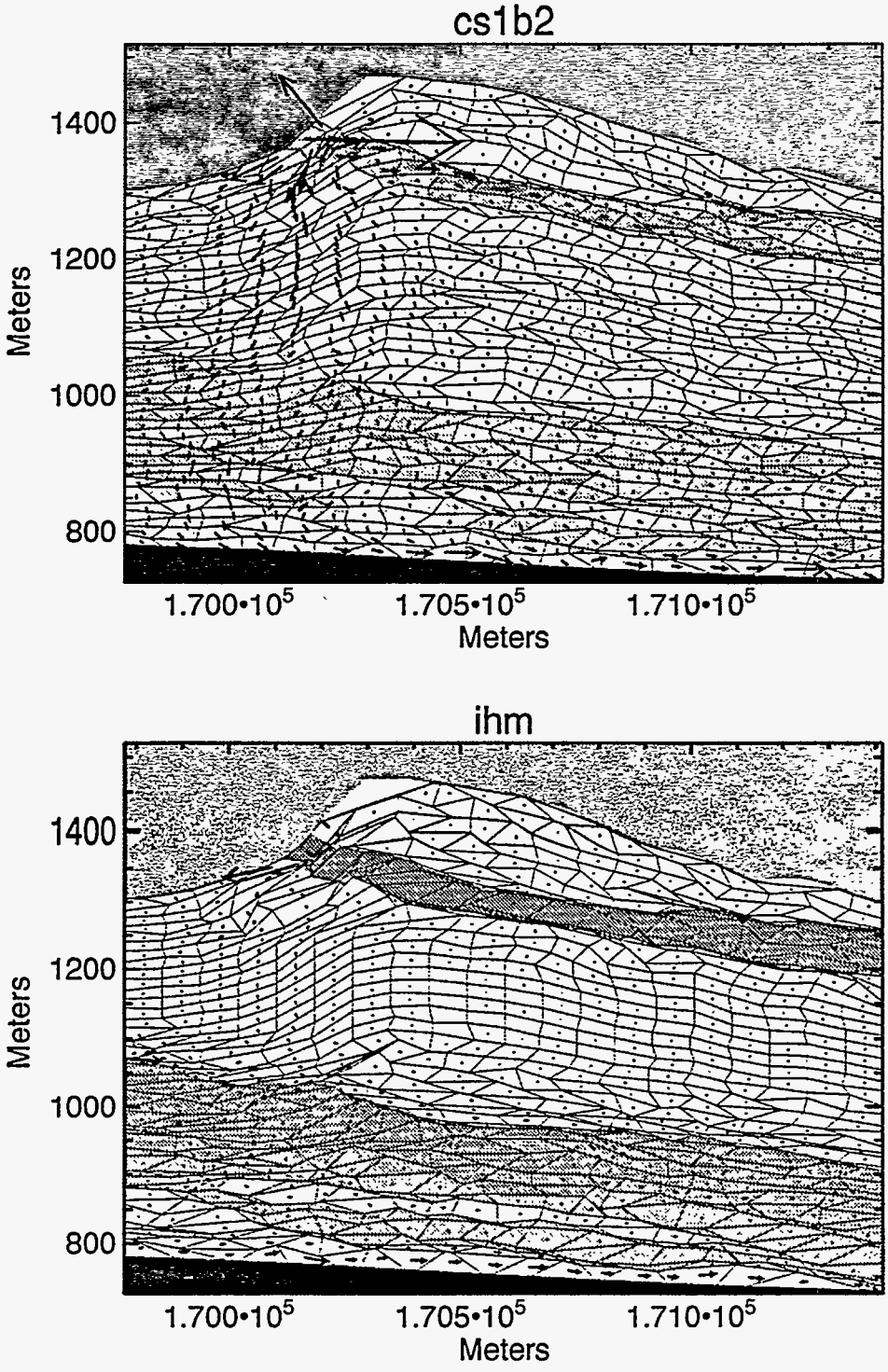

Figure 6-3. Comparison of Darcy fluxes for simulations with (*cs1b2*) and without (*ihm*) intra-unit heterogeneities. The brown scale represents the porosities assigned to the geostatistical nodes. The flux out of the system just above the PTn outcrop in *cs1b2* represents only a small outflow because of the small cross-sectional area of the element. The fluxes shown in this figure are only scaled to each other and those in Figure 6-17.

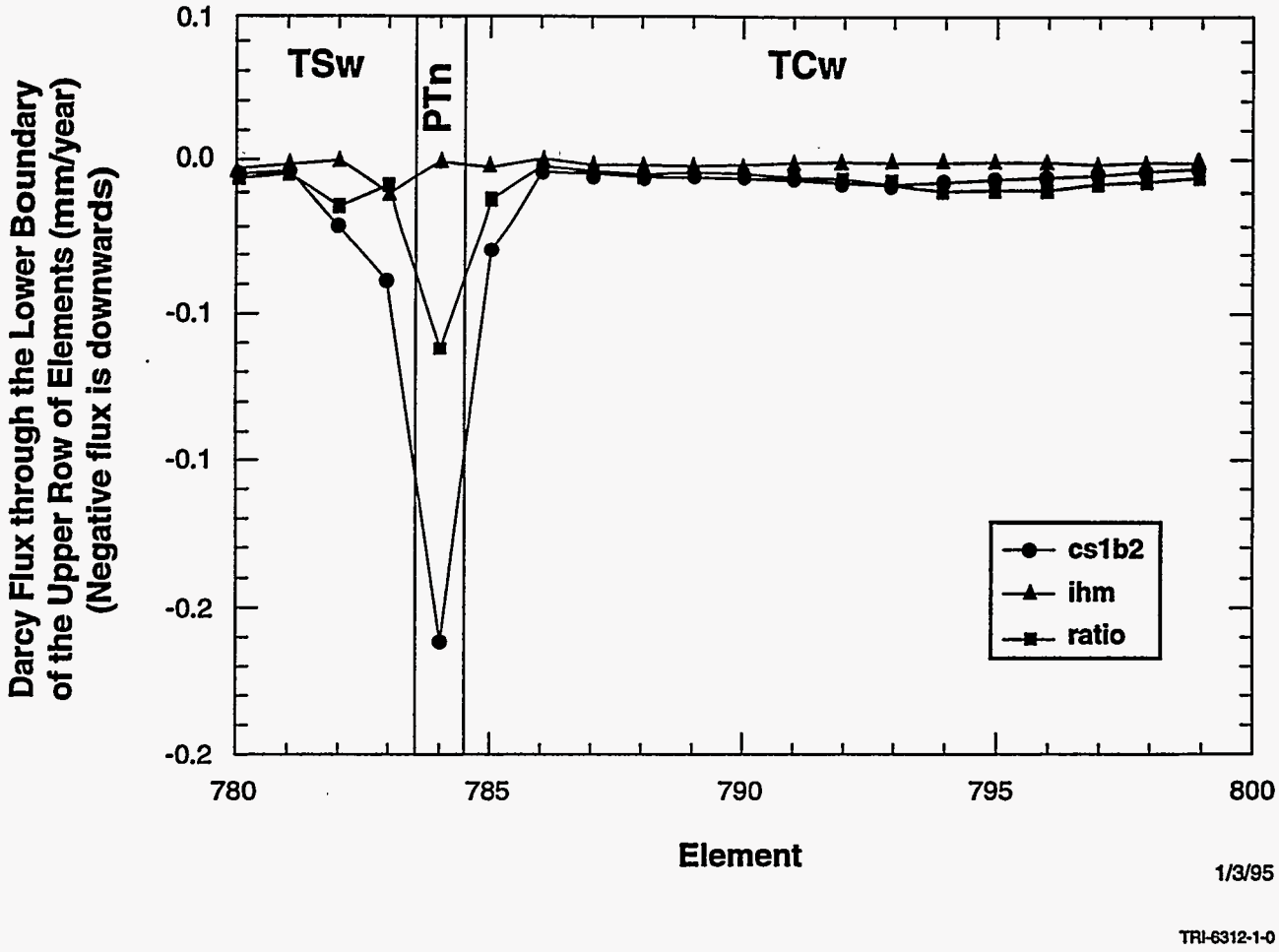

Figure 6-4. Comparison of Darcy flux through the lower side of the upper row of elements for comparisons between heterogeneous (*cs1b2*) and homogeneous (*ihm*) units. Case *ratio* also has relatively homogeneous units which were created by increasing the anisotropy ratio.

Most noticeable in comparing the fluxes of the two simulations is how much larger the fluxes are in *cs1b2* (Figure 6-3). In a system with small-scale heterogeneities, the fluxes are expected to be concentrated in certain areas, whereas in a system with homogeneous layers, they should be more evenly distributed. Because this flow system is unsaturated (and thus the equations describing the flow are non-linear), the concentration of fluxes leads to areas of higher saturation and higher unsaturated conductivity. Since the upper boundary was set at a specified pressure (and thus non-uniform infiltration) and because the model was run to steady state, a positive feedback was created. Thus, higher saturations led to higher conductivities which in turn led to higher fluxes, thus creating more zones with higher saturation. In a system without these small scale heterogeneities, where saturations are more evenly distributed, this positive feedback is less likely to be perpetuated. This is clearly illustrated by comparing the Darcy flux through the PTn along the upper boundary (Figure 6-4 and Table 6-2).

Table 6-2: Comparisons of infiltrations and particles exiting system for sensitivity analyses excluding grid size comparison

Run Name	Infiltration through the Upper Boundary			Particles Exiting Before	
	TCw (mm/yr)	PTn (mm/yr)	TSw (mm/yr)	1,000 yrs	600,000 yrs
cs1b2	0.005	0.16	0.005	2	4
ihm	0.001*	0.0007	0.0006	0	1
cs1b5	0.01*	0.88	0.004	7	14
uht	0.1*	2.13	0.004	3	21
cs1b2	0.005	0.16	0.005	2	4
uht5	0.005	0.48	0.004	6	11
cs1b2	0.005	0.16	0.005	2	4
ratio	0.006	0.061	0.005	3	6

* Numbers are order-of-magnitude estimates.

6.2.2 PTn with Uniform Thickness versus PTn with Variable Thickness

To generate a system with deterministically assigned unit contacts, the thickness of the PTn was uniformly set to the mean vertical thickness of the geostatistically generated unit. Comparing the two simulations turned out not to be straightforward because of differences in porosities from the two simulations and therefore different element configurations after using the adaptive gridding technique. To standardize the porosities as much as possible, four different simulations were run. There were two different element configurations, one for *cs1b2* and the other for *uht*. After upscaling, each element configuration had a different porosity distribution which proved to have a strong effect on the flow system. The porosities assigned to each element in *cs1b2* were therefore re-assigned to the element configuration of *uht* forming *uht5*. Likewise, the porosities assigned to the elements in the original *uht* were re-assigned to the element configuration of *cs1b2* making *cs1b5*. Therefore, comparison of *cs1b2* to *uht5* (Figure 6-5) and *uht* to *cs1b5* (Figure 6-6) should minimize the effects of inconsistencies in porosity. Some of the porosities had to be adjusted because the PTn had a different number of elements in the two different cases. Thus, where the PTn was thin in *cs1b2*, a TCw element might have been assigned a PTn porosity. This element porosity was then changed to a value more typical of the TCw based on the adjoining elements. Refer to Table 6-1 for a description of each run.

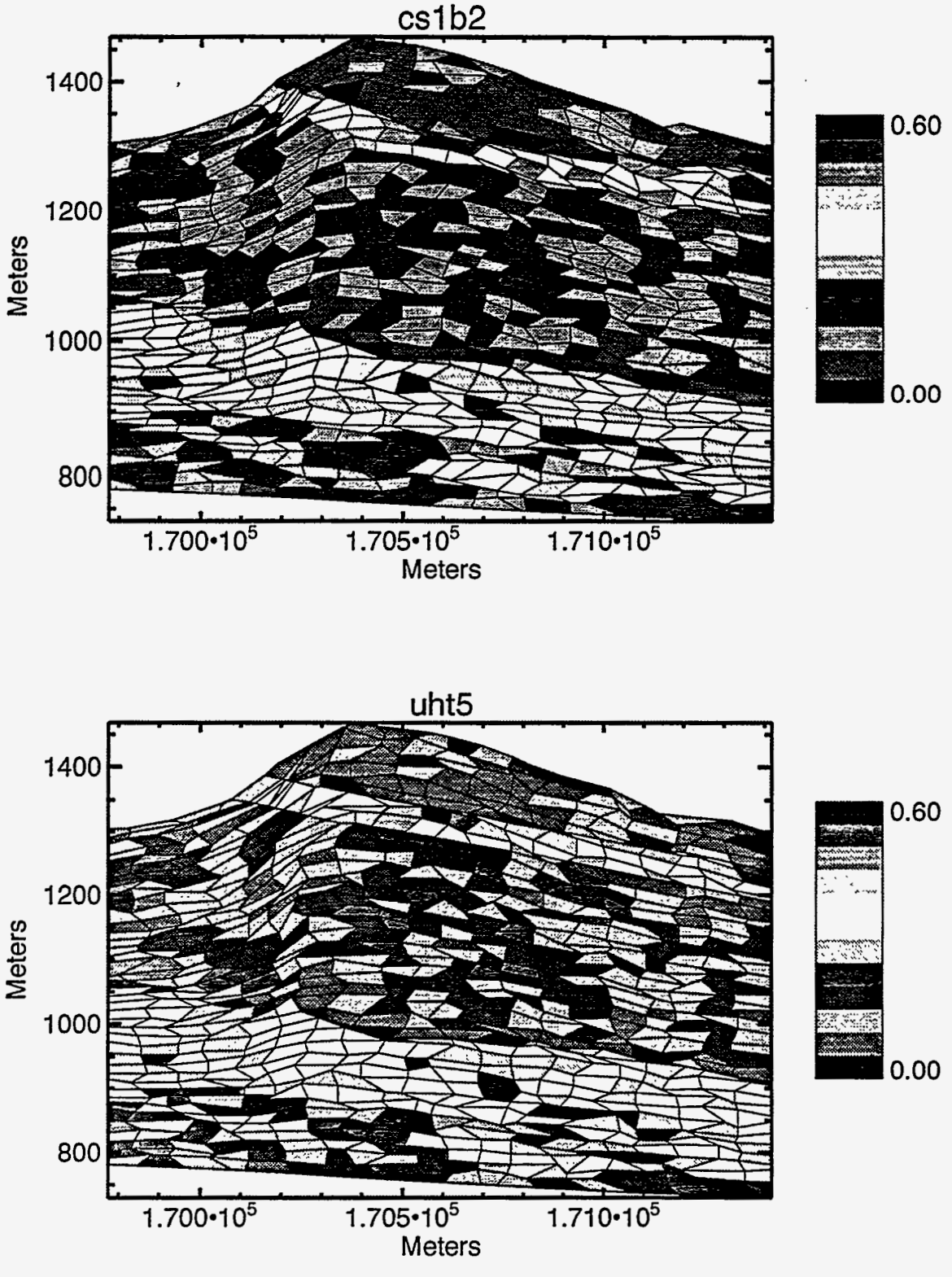

Figure 6-5. Comparison of porosity distributions generated in the upscaling of *cs1b2* for simulations with variably (*csib2*) and uniformly (*uht5*) thick PTn.

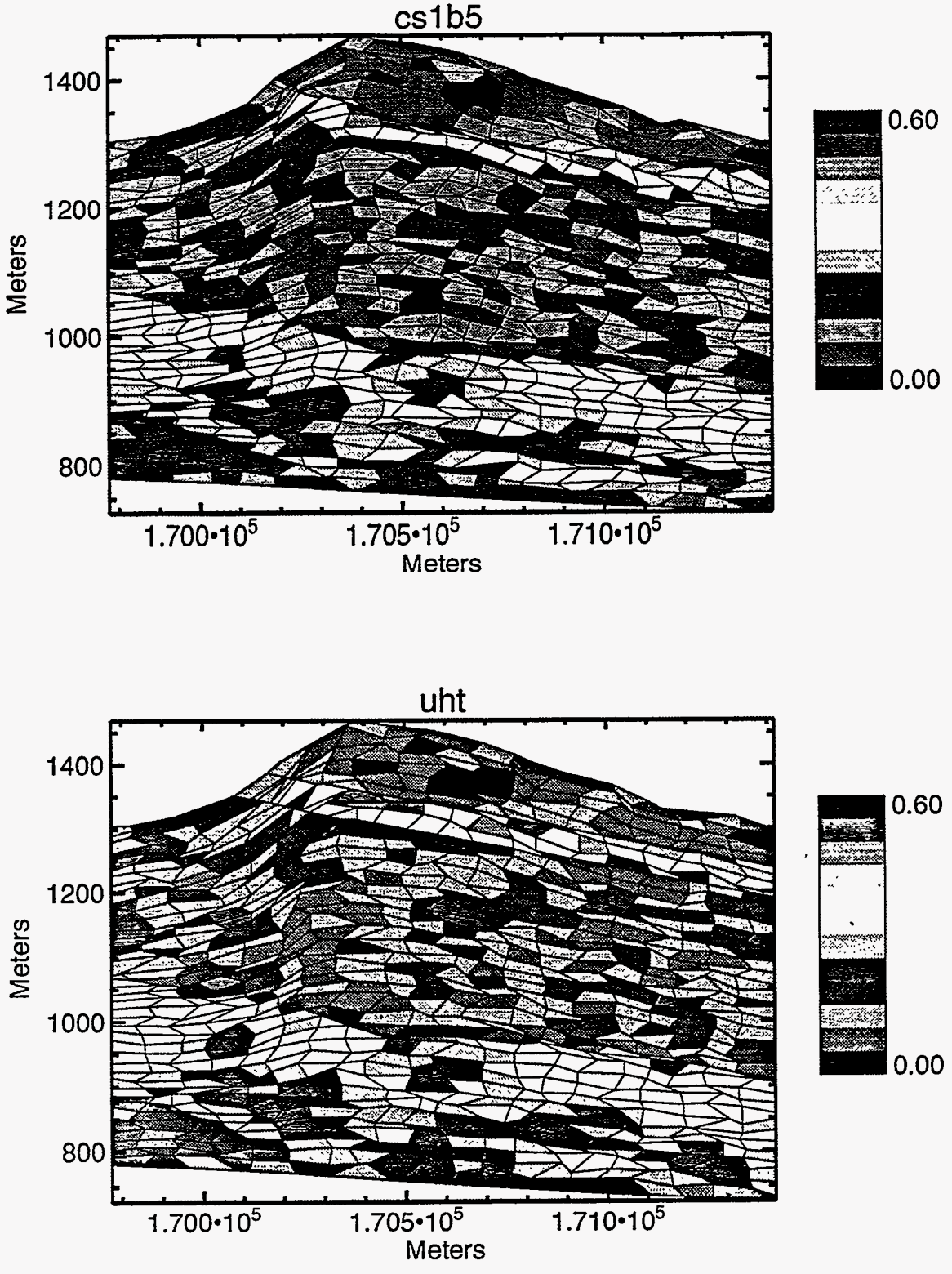

Figure 6-6. Comparison of porosity distributions generated in the upscaling of *uht* for simulations with variably (*csib5*) and uniformly (*uht*) thick PTn.

6.2.2.1 Comparison of *cs1b5* to *uht*

Matrix and fracture saturations are similar, though slightly higher in the case with uniform PTn thickness (*uht*) (see Figure 6-7 for a comparison of matrix saturations). As with the other simulations discussed, the areas of highest saturations are below the PTn outcrop. The Darcy flux distributions seem similar with much vertical flow below the PTn outcrop and some lateral flow in the PTn (Figure 6-8). The magnitude of the fluxes are generally higher for *uht*. There is more pronounced vertical flow near the basal vitrophyre in the case with a uniformly thick PTn. Examination of infiltration along the upper boundary shows the fluxes through the TCw and PTn are an order of magnitude higher for the case with the uniformly thick PTn (Table 6-2, Figure 6-9). The fluxes through the TSw are similar for the two cases. After 1,000 years the particle tracker shows that 7% of the particles exit the system in the case with non-uniformly thick PTn (*cs1b5*), whereas only 3% particles leave in the case with the uniformly thick PTn (*uht*). This is surprising because of the higher saturations in the second case. However, after 600,000 years a higher percentage of particles leave the system in the case with the PTn of uniform thickness (21% as compared to 14%). A probable explanation for fewer particles leaving after 1,000 years for case *uht* is that the location of areas of high saturations is slightly different for cases *uht* and *cs1b5* relative to the repository location so that few particles just happen to be in areas of high saturation in case *uht* after 1,000 years.

6.2.2.2 Comparison of *cs1b2* to *uht5*

The porosity distributions of these two cases differ from the previous two in that the porosities of the PTn at the outcrop are lower (compare Figures 6-5 and 6-6). In these two cases there is a much more pronounced difference in the results of running the flow code between the uniformly thick PTn (*uht5*) and the variably thick PTn (*cs1b2*). Matrix and fracture saturations are noticeably higher in *uht5* and more similar to *cs1b5* and *uht* (see Figure 6-10 for matrix saturations). The Darcy flux distributions are similar to each other and to the two cases discussed above, though the fluxes are higher in *uht5* than *cs1b2* (Figure 6-11). The flux through the PTn along the upper boundary is larger when the thickness of the PTn is uniform, though the fluxes are within the same order of magnitude, unlike the previously discussed case. Fluxes through the TCw and TSw along the upper boundary are similar for the two cases (Figure 6-9 and Table 6-2). A higher percentage of particles leave the system in case *uht5* both after 1,000 years (6% as opposed to 2%) and 600,000 years (11% as opposed to 4%).

6.2.3 Effects of Grid Size

Four different grid-sizes were compared to the base case of a 20 by 40 grid (*cs1b2*). The grid was refined vertically to a 20 by 60 grid (*cs1b6*) and horizontally to a 25 by 40 grid (*cs1b7*). When the grid was refined in both directions (30 by 60) the flow code did not converge. A coarser, 10 by 20, grid was also examined (*cs1b8*). The finest grid run successfully was 24 by 60 in which the extra four elements along the x-axis were weighted so that finer gridding would

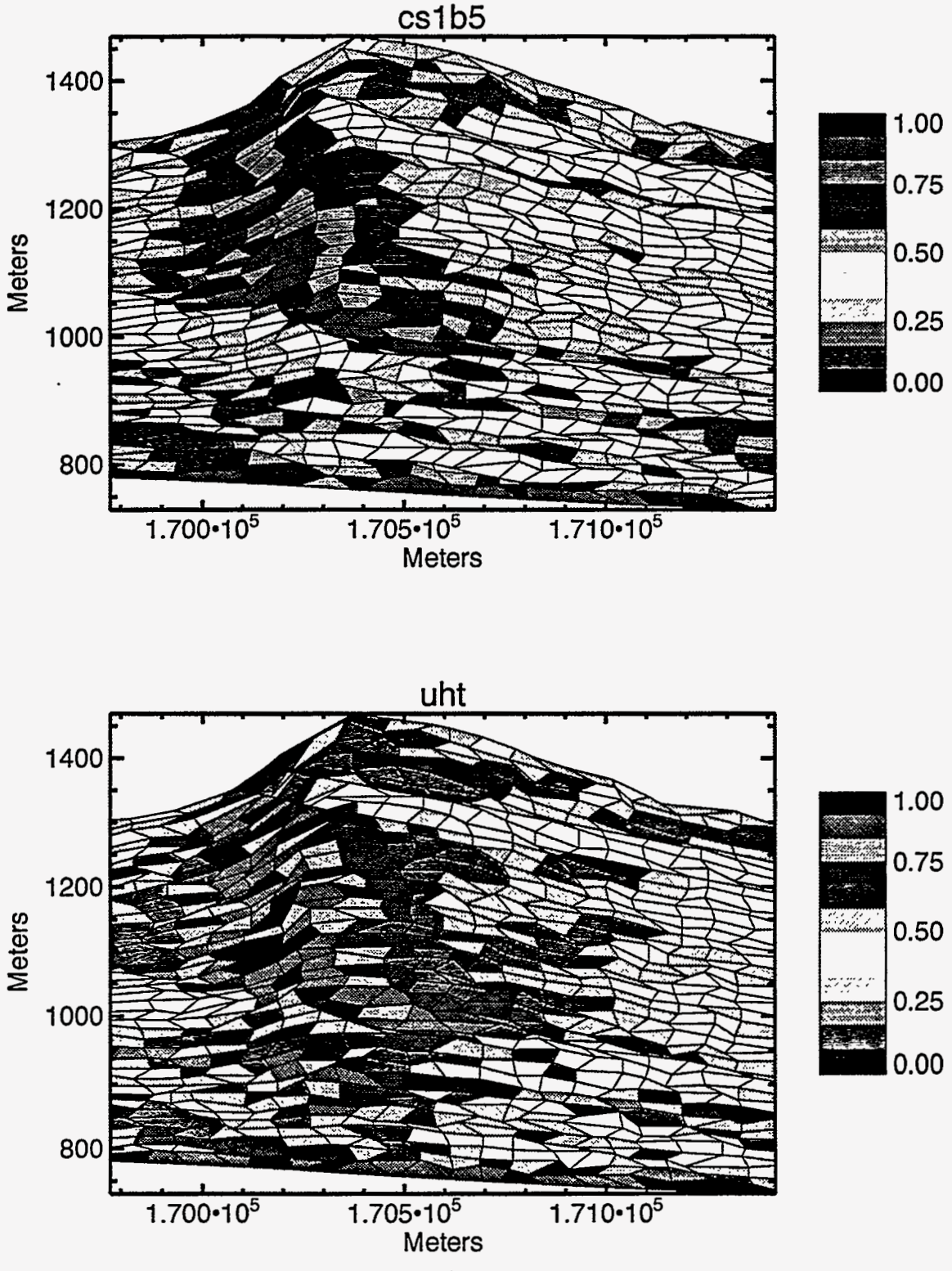

Figure 6-7. Comparison of matrix saturation distribution for simulations with variably (*cs1b5*) and uniformly (*uht*) thick PTn for the simulations with the higher porosities at the PTn outcrop.

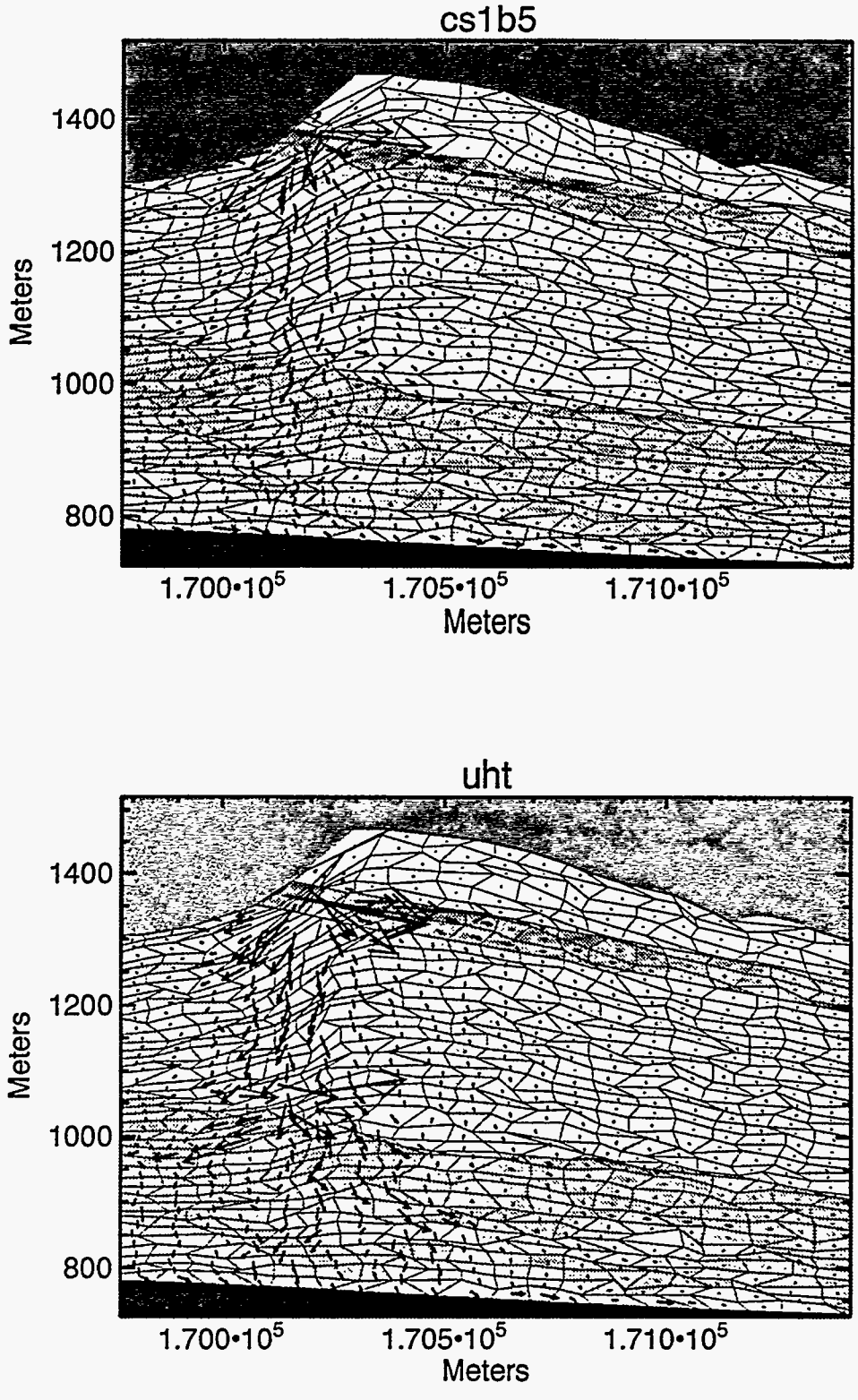

Figure 6-8. Comparison of Darcy fluxes for simulations with variably (*cs1b5*) and uniformly (*uht*) thick PTn for the simulations with the higher porosities at the PTn outcrop. The brown scale represents the porosities assigned to the geostatistical nodes. Fluxes shown in this figure are scaled only to each other and those in Figure 6-11.

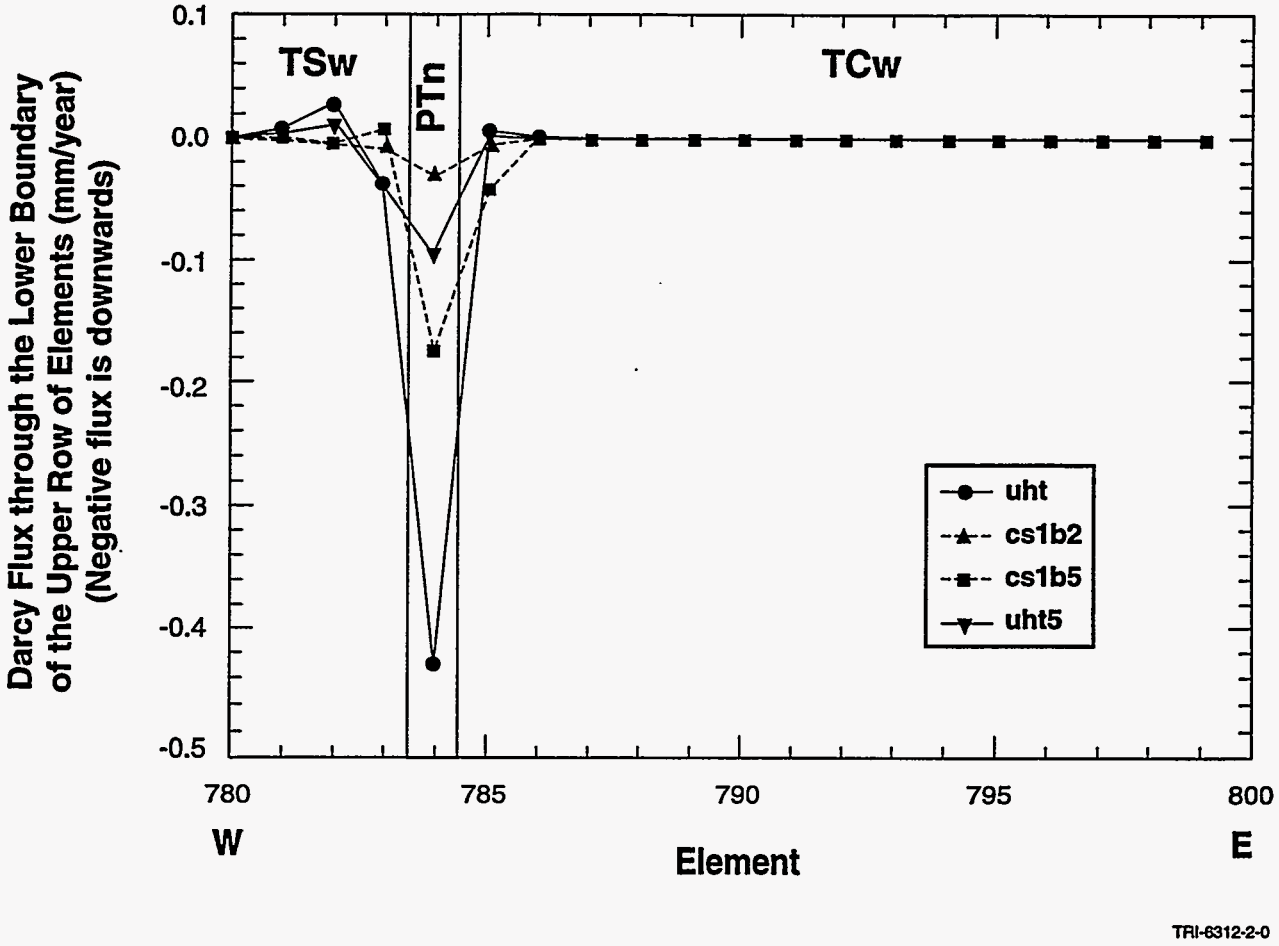

Figure 6-9. Comparison of Darcy flux through the lower side of the upper row of elements for comparisons of uniformly (*uht* and *uht2*) and variably (*cs1b2* and *cs1b5*) thick PTn. Comparisons should be made between *cs1b5* and *uht* and between *cs1b2* and *uht5* in order to match similar porosity distributions.

be present under the PTn outcrop (*cs1b9*). Each case started with the same original porosity distribution, but upscaling was conducted after the adaptive grid program was used on the individual cases. Therefore, slight discrepancies in the porosities assigned to elements for the individual cases could exist (Figure 6-12).

There are not clear trends in infiltration, fluxes or saturation with the refinement of the grid. In all cases, areas of higher matrix saturation are present below the PTn outcrop (Figure 6-13). The only case with noticeably lower saturations is *cs1b6*, where the grid is refined in the vertical. Because DUAL is a flux-based model it tends to produce higher saturations for coarser meshes. For GWTT calculations, this implies that DUAL will tend to produce conservative approximations, thus tending to produce higher fluxes (and saturations) for coarser grids. Where fracture flow occurs in only a portion of an element (such as below the PTn outcrop) refining the grid may either produce lower fluxes and no fracture flow or result with one element with a greater degree of fracture flow and another element with only matrix flow. The first case is due to the conservative approximations inherent in DUAL while the second indicates there is fracture flow

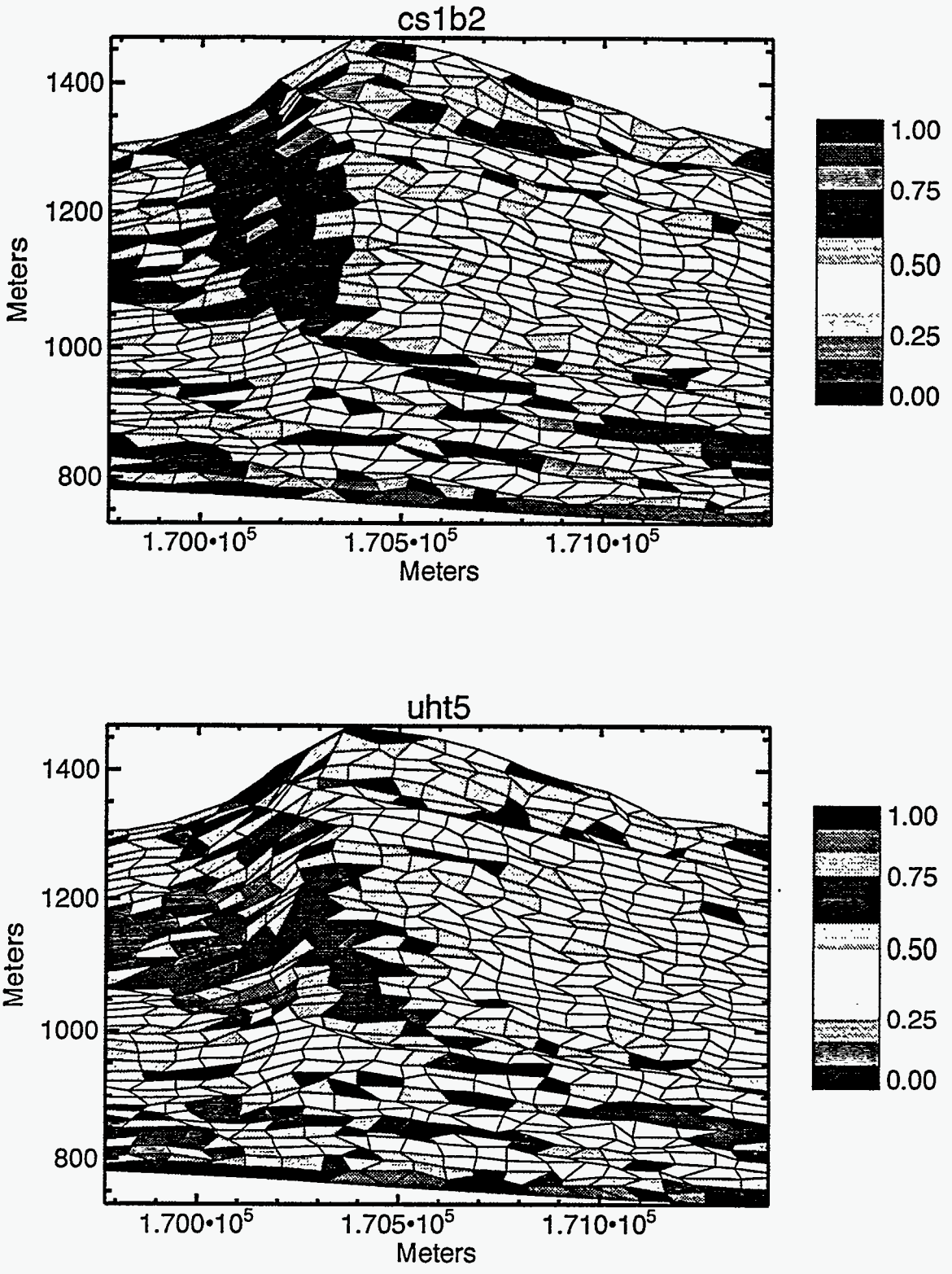

Figure 6-10. Comparison of matrix saturation for simulations with variably (*cs1b2*) and uniformly (*uht5*) thick PTn for the simulations with the lower porosities at the PTn outcrop.

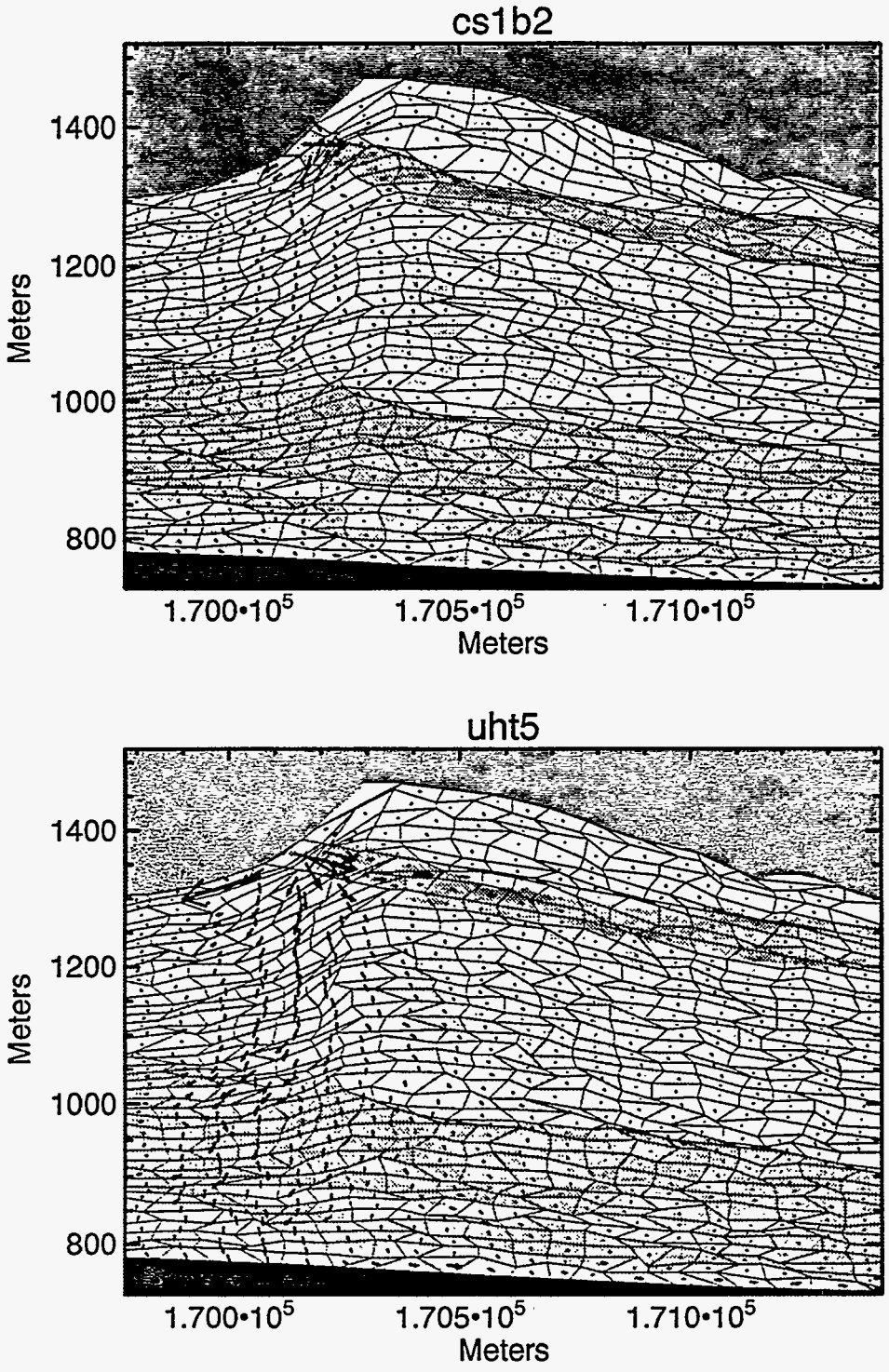

Figure 6-11. Comparison of Darcy fluxes for simulations with variably (*cs1b2*) and uniformly (*uht5*) thick PTn for the simulations with the lower porosities at the PTn outcrop. The brown scale represents the porosities assigned to the geostatistical nodes. The flux out of the system just above the PTn outcrop in *cs1b2* represents only a small outflow because of the small cross-sectional area of the element. Fluxes shown in this figure are scaled only to each other and those in Figure 6-8.

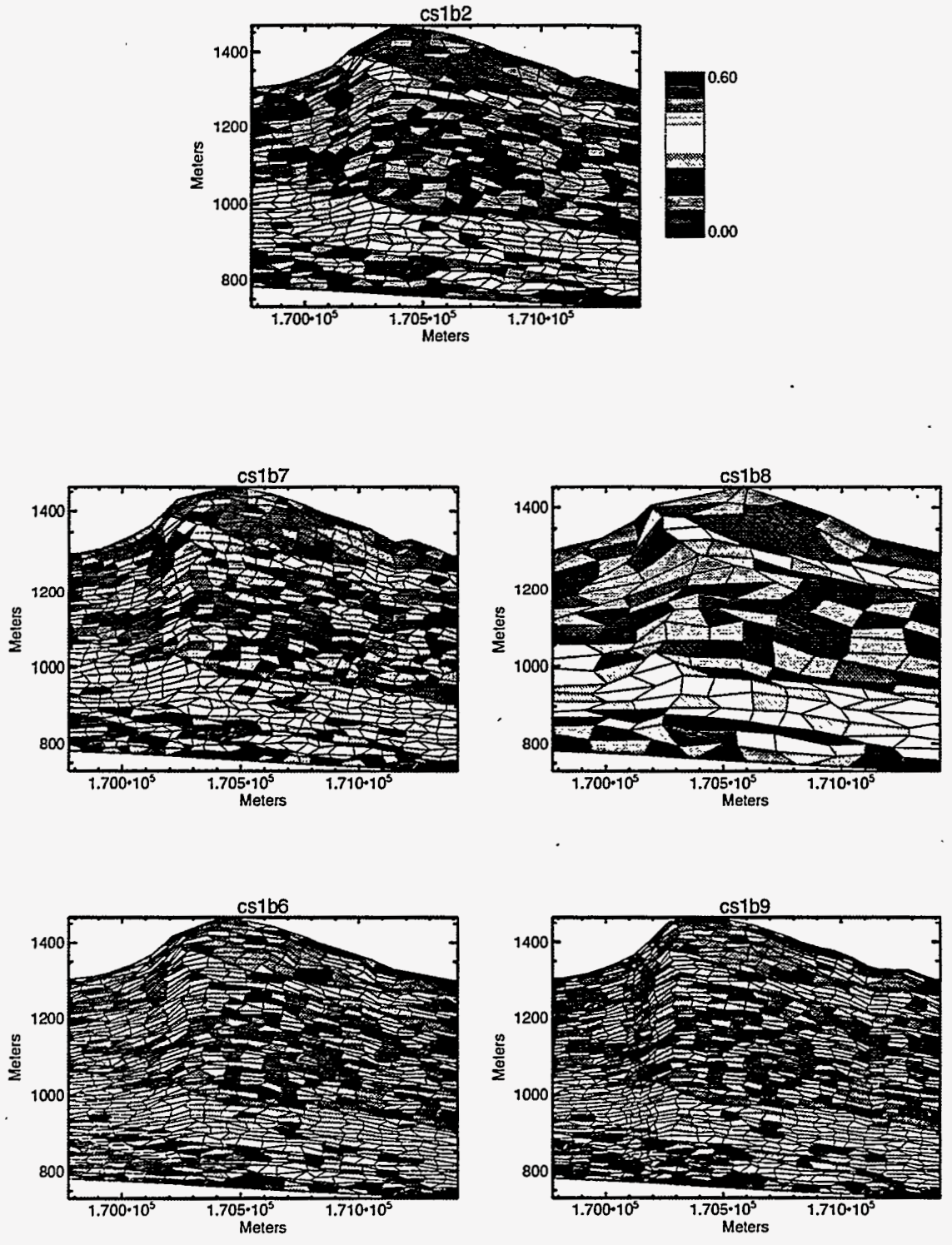

Figure 6-12. Comparison of porosity distributions after upscaling in grid size comparisons.

occurring in the system. Splitting an element with partial fracture flow into an element completely in fracture flow and another in matrix flow results in two elements with hydraulic conductivities that differ by many orders of magnitude. This can be expected to cause numerical problems due to limited precision of computer arithmetic, therefore explaining the cases that did not converge (Table 6-3). The refinement of the grid might therefore explain the lower saturations observed in *cs1b6*. However, the case with the most refined grid (*cs1b9*) does show more localized saturation underneath the PTn outcrop. Another explanation for the lower saturations in *cs1b6* is that because each case is upscaled individually, the porosity distributions after upscaling will be slightly different for each case. Differences in porosities, especially at the PTn outcrop, as observed in the comparison between a variably thick and uniformly thick PTn (Section 6.3.2), could have a strong effect on the flow system (Section 3.2). Examination of the porosities after upscaling (Figure 6-12), however, do not show strong differences. It is still possible that even small differences can affect the flow system. Infiltration through the upper boundary of the PTn ranged from 0.05 mm/year (*cs1b6*) to 0.35 mm/year (*cs1b8*) (Figure 6-14, Table 6-3). The highest infiltrations are for the cases with the least and most refined grid, indicating grid size does not have a consistent effect on infiltration. With the exception of *cs1b6*, the infiltrations are within 0.29 mm/year. The pattern of fluxes throughout the system (not shown) is similar in all cases. Lateral flow through the PTn is most pronounced (relative to the fluxes within the one system) in cases *cs1b6* and *cs1b7*, the first having a vertically refined grid, and the second having a horizontally refined grid. In three of the five cases no particles left the system after 1,000 years. In the two cases where particles leave the system, a higher percentage of particles leave in the case with the coarser grid, as should be expected. The same trend of fewer particles exiting with the refinement of the grid is also observed after 600,000 years. The highest percentage of particles that leave the system is 4% after 1,000 years and 17% after 600,000 years for *cs1b8*, the case with the least refined grid (Table 6-3).

Table 6-3: Effects of grid size

Run Title	# of elements		Converged?	Infiltration through the PTn (mm/yr)	Particles Exiting Before	
	X	Y			1,000 yrs	600,000 yrs
cs1b2	20	40	Yes	0.16	2	4
cs1b6	20	60	Yes	0.05	0	1
cs1b7a	30	60	No	---	---	---
cs1b7b	30	40	No	---	---	---
cs1b7	25	40	Yes	0.14	0	0
cs1b8	10	20	Yes	0.35	4	17
cs1b9	24*	60	Yes	0.31	0	1

* weighting applied to the extra elements added so that they would be located vertically below the PTn outcrop.

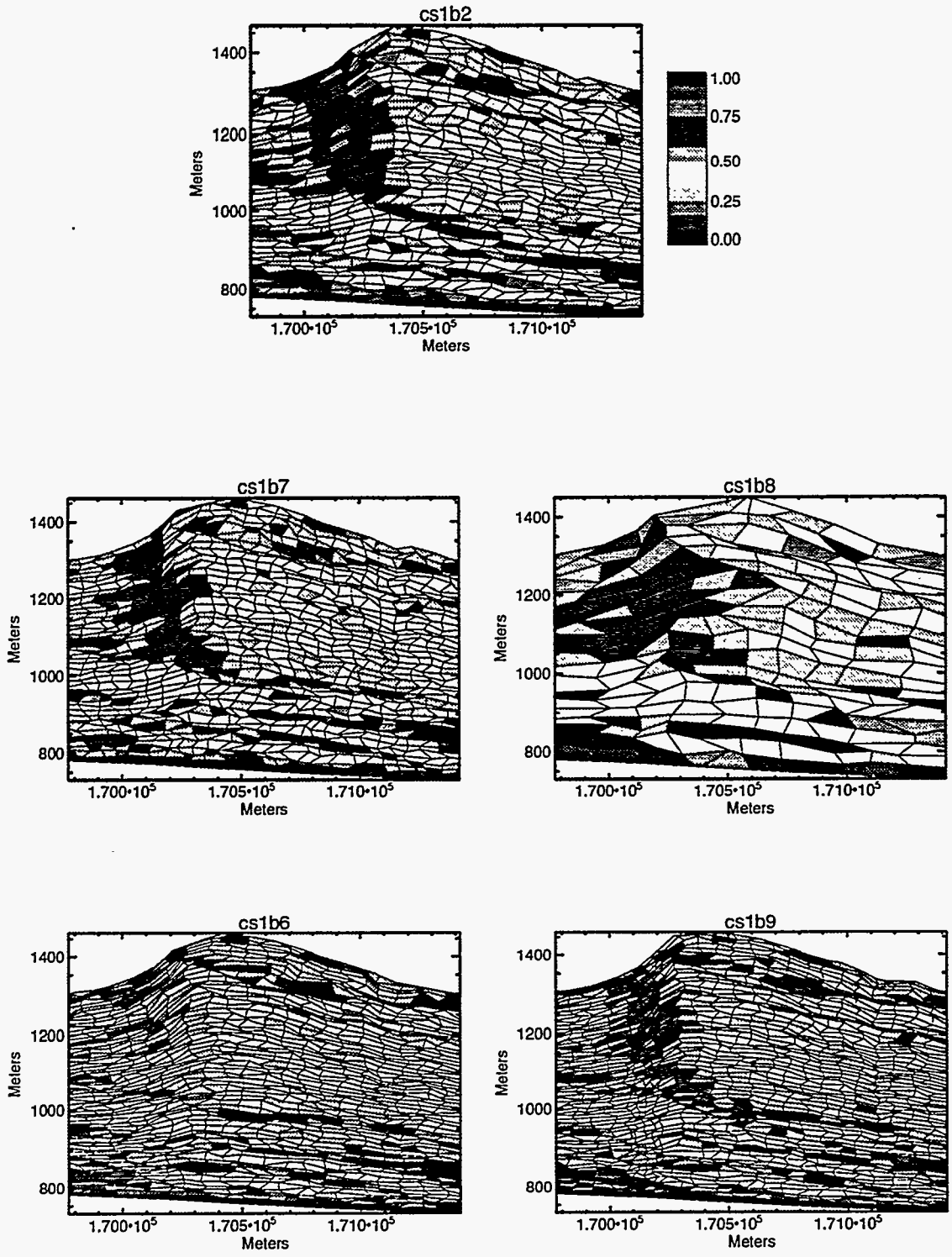

Figure 6-13. Comparison of matrix saturation distribution in grid size comparisons.

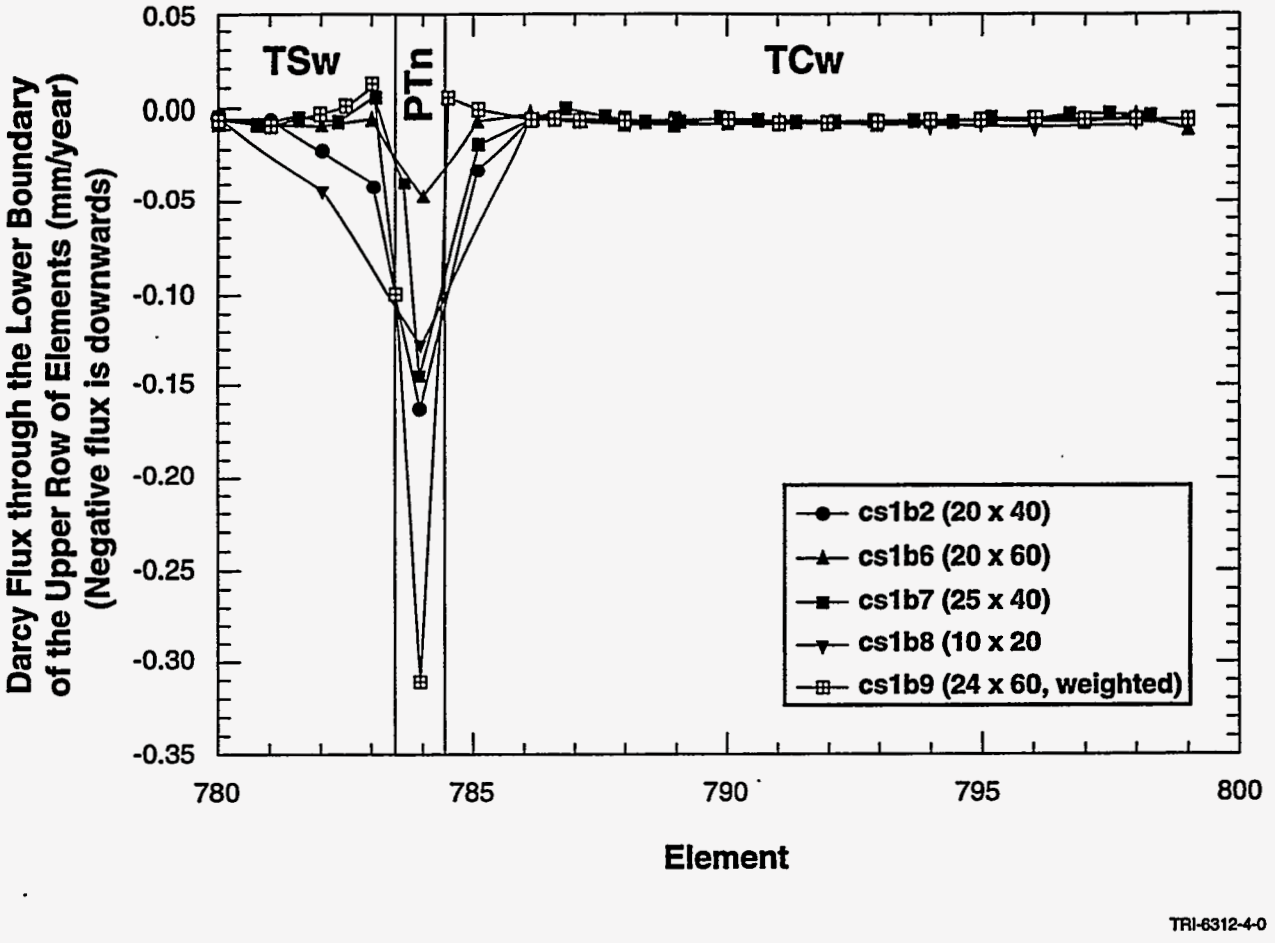

Figure 6-14. Comparison of Darcy flux through the lower side of the upper row of elements for grid size comparisons.

6.2.4 Effects of Changing Boundary Conditions

The effects of the types of boundary conditions (specified pressure versus specified flux) on the flow simulation *cs1b2* were examined. The boundary conditions set along the upper boundary were changed to the fluxes determined from the base case (*cs1b2*); therefore, similar results to the original run were anticipated. The effects of the magnitude of the boundary conditions were also examined for *cs1b2* and *ihm* using different pressures along the upper boundary. In this case the capillary pressure head along the upper boundary of the TSw, PTn and TCw were set at -164m, -8.9m, and -47 m respectively. Note that the most noticeable difference in these boundary conditions from the base case is the much lower capillary suction pressure in the TCw. Thus, greater saturations should be expected.

Unfortunately, DUAL was not able to converge when the pressure boundary condition was changed to a flux boundary. This complicated the sensitivity analyses because in many of the cases, having a constant flux along the upper boundary would have facilitated the comparison of

the parameter that was varied. Instead, the sensitivity analyses are more a measure of how the change in the parameter affected the flux into the system.

Changing pressure of the upper boundary conditions did, however, have a strong effect on the flow system. This can be seen in examining the matrix saturations of the cases with the modified pressure conditions (Figure 6-15) to those of the original pressures (Figure 6-2). Notice that with the low capillary suction pressure along the upper boundary of the TCw the effects of the intra-unit heterogeneities of the system are exaggerated with much greater relative increase in matrix saturation for *cs1b2* than *ihm*.

6.2.5 Effects of Changing Porosity Anisotropy Ratio

The anisotropy ratio of porosity set for the original run (*cs1b2*) was set at 4:1 and the spatial correlation length was set at approximately 150 m. Explanation for use of these values is discussed in Section 3.1. Rautman (in review) examined effective anisotropy ratios for Yucca Mountain in more depth in modeling the thermal conductivity of the mountain. Spatial correlation lengths used by Rautman[4] (in review) were based on transect-sampling and geostatistical modeling done on the mountain. Based on his work, the spatial correlation length and the anisotropy ratio were re-set to 2,000 m and 20:1. The porosity distribution for the new simulation was generated, upscaled and the flow code was re-run (case *ratio*).

The resultant porosity distribution with the new anisotropy ratio and correlation length led to a cross-section with almost homogeneous layers (see Figure 6-16 for porosity distribution before (a) and after (b) upscaling). The porosity of the PTn of this system is generally higher than the case where the mean porosity is assigned to each unit (*ihm*). As could be expected the matrix saturation (Figure 6-17a) resembled that of run *ihm* more than *cs1b2* (Figure 6-2). Saturations are slightly higher in *ratio* than *ihm*, which can be explained by the higher porosity of the PTn. Case *ratio* showed much more lateral flow through the PTn, through there still is a strong component of vertical flow underneath the PTn outcrop (Figure 6-17b). Infiltration through the PTn upper boundary proved to be intermediary to *cs1b2* and *ihm* (Figure 6-4, Table 6-2). The percentage of particles that exit the system are similar in both cases (Table 6-2).

6.2.6 Vitric versus Zeolitic Calico Hills

The Calico Hills is divided into two distinct types of tuff for modeling purposes: vitric and zeolitic. The CHnv represents unaltered tuff, whereas the CHnz represents tuff that has undergone mineral alteration in part caused by exposure to high saturations. The alteration typically causes a slight reduction in porosity and a much larger reduction in matrix saturated hydraulic conductivity (Figure 3-5). Because of the smaller pore size, the zeolitic region will tend to exhibit higher saturations than the vitric region of the Calico Hills at similar capillary pressures.

4. Rautman, C.A. (in review). *Preliminary Geostatistical Modeling of Thermal Conductivity for a Cross Section of Yucca Mountain, Nevada.* SAND94-2283. Albuquerque, NM: Sandia National Laboratories.

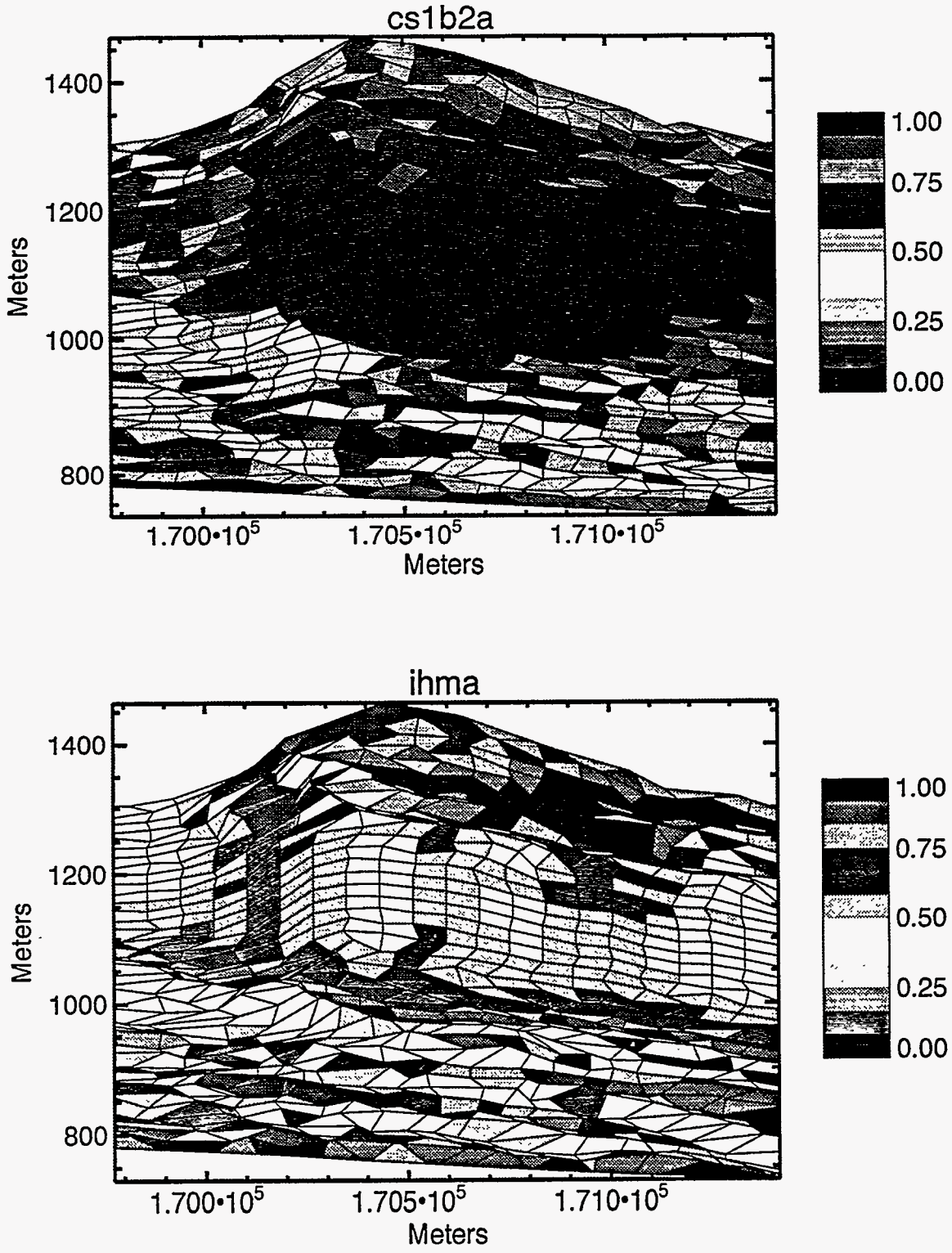

Figure 6-15. Comparison of matrix saturation distributions for two cases similar to those presented in Figure 6-2 except for a modified capillary pressure upper boundary condition.

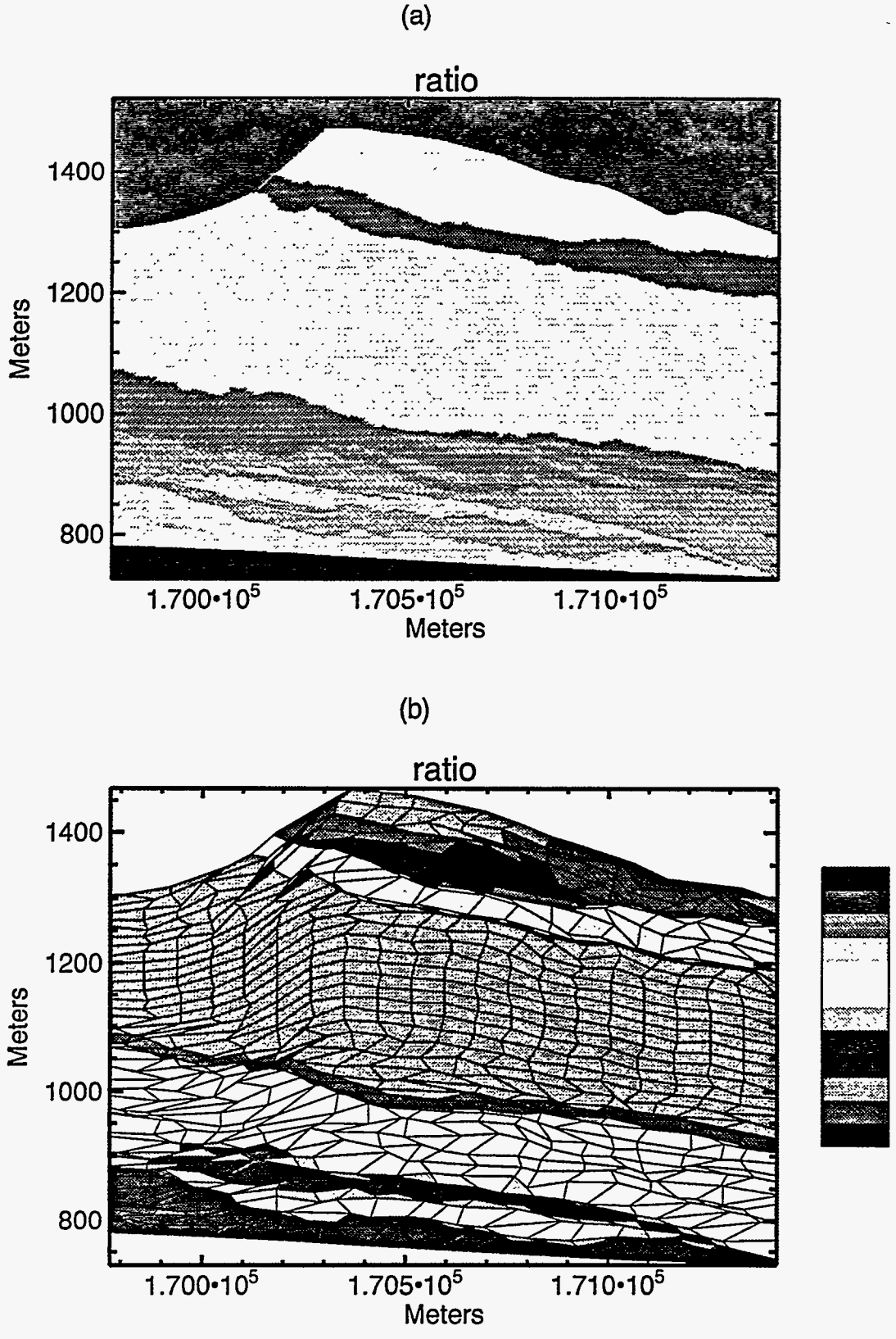

Figure 6-16. Porosity distribution before (a) and after (b) upscaling of new anisotropy ratio. Porosity increases with darker shading.

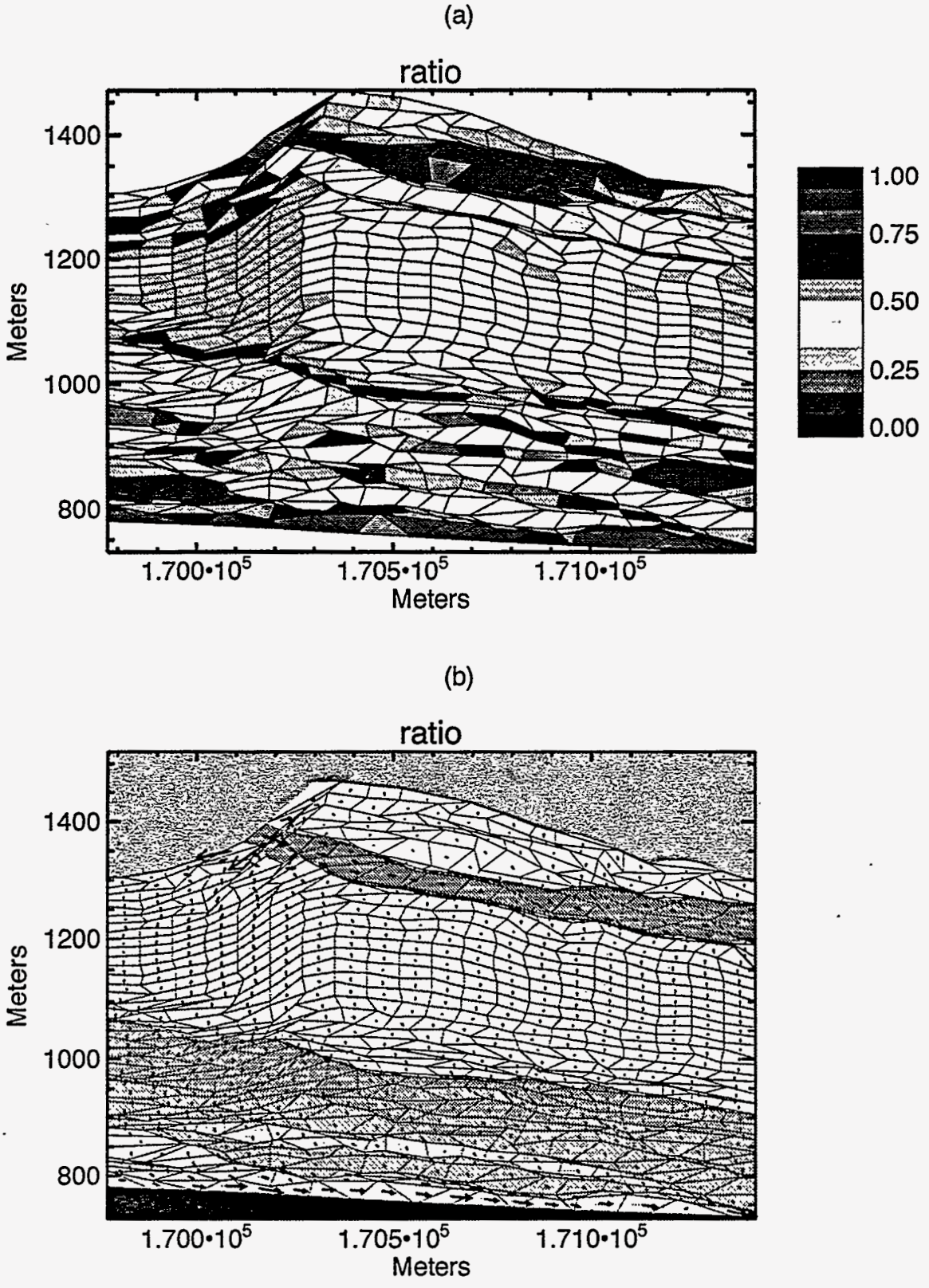

Figure 6-17. Matrix saturation (a) and Darcy flux (b) with revised anisotropy ratio. Fluxes shown are scaled only to those shown in Figure 6-3.

In order to evaluate the effect on the analyses of the variation in amounts of the vitric versus zeolitic Calico Hills tuffs, new indicator simulations were run on cross-section 1b. No dip was used in this indicator simulation for the zeolitic Calico Hills since its position is thought to be primarily controlled by paleo-water table positions which are generally horizontal. Different random number files from the original simulations were used to generate the CHnv, CHnz, and TSbv hydrogeological units only. Therefore, the porosity distribution for the other units should be similar to those of the original simulations. There are only conditioning data from two boreholes in the vicinity of the cross-section which should affect the indicator simulations. Drill hole H-5 is located 258.7 meters north of the western portion of the cross-section. The majority of the Calico Hills unit has been recorded as being vitric with 68.6 meters as CHnv and 19.8 m as CHnz. Borehole G-4 is located 201.4 meters east of the eastern end of the cross-section. The zeolitic Calico Hills has been recorded as being dominant in this borehole with 108 m CHnz and 13 m CHnv.

The results of the indicator simulations show varying amounts of zeolitic Calico Hills with the least amount in ch1b3 and the most in ch1b2 (Figure 6-18). As expected from the conditioning data, more CHnz is present on the eastern side of the cross-section and more CHnv is present on the western section south of boring H-5. These results can be seen after upscaling by comparing the saturated hydraulic conductivities in these units (Figure 6-19). Saturated conductivity in the Calico Hills is much higher in ch1b3 than ch1b2, intermediate in ch1b1 and lowest in ch1b (the base case).

All four simulations exhibit the same plume of water below the PTn outcrop as expected since the properties of the upper units (TCw, PTn, and TSw) have not been altered (Figure 6-20). Matrix saturation in this plume is highest for ch1b2, the cross-section with the most zeolitic Calico Hills, and lowest for ch1b3. Fracture saturations generally mirror matrix saturations (Figure 6-21). Higher fracture saturations are not observed in the eastern part of the Calico Hills in any of the simulations where there is more CHnz. There are some elements with higher fracture saturation underneath the PTn outcrop in ch1b1. The extent of zeolitic units does appear to affect how far down the areas of higher fracture saturation will extend, as can be seen by comparing ch1b2 to ch1b3. Lateral flow is more prominent in the CHnv unit than the CHnz and the elements with lateral flow correspond with high saturated conductivity regions of the vitric region of the Calico Hills (Figure 6-22 and Figure 6-19).

Overall, there appears to be little sensitivity of the flow model to the extent of the zeolitic portion of the Calico Hills, even though the presence of the CHnv was important for channeling of water. Although this study only looked at the qualitative flow behavior, it is unlikely that the travel times through zeolitic material could change appreciably. In running the particle tracker, most of the particles left the UZ from units above the Calico Hills; therefore, particle tracker results should not be greatly affected by these sensitivity studies.

6.2.7 Sensitivity to Fracture Properties

There is very little information on the fractures at depth. It is unknown whether the zeolitic alteration extends into the fractures. The GWTT-94 models were based on heterogeneity

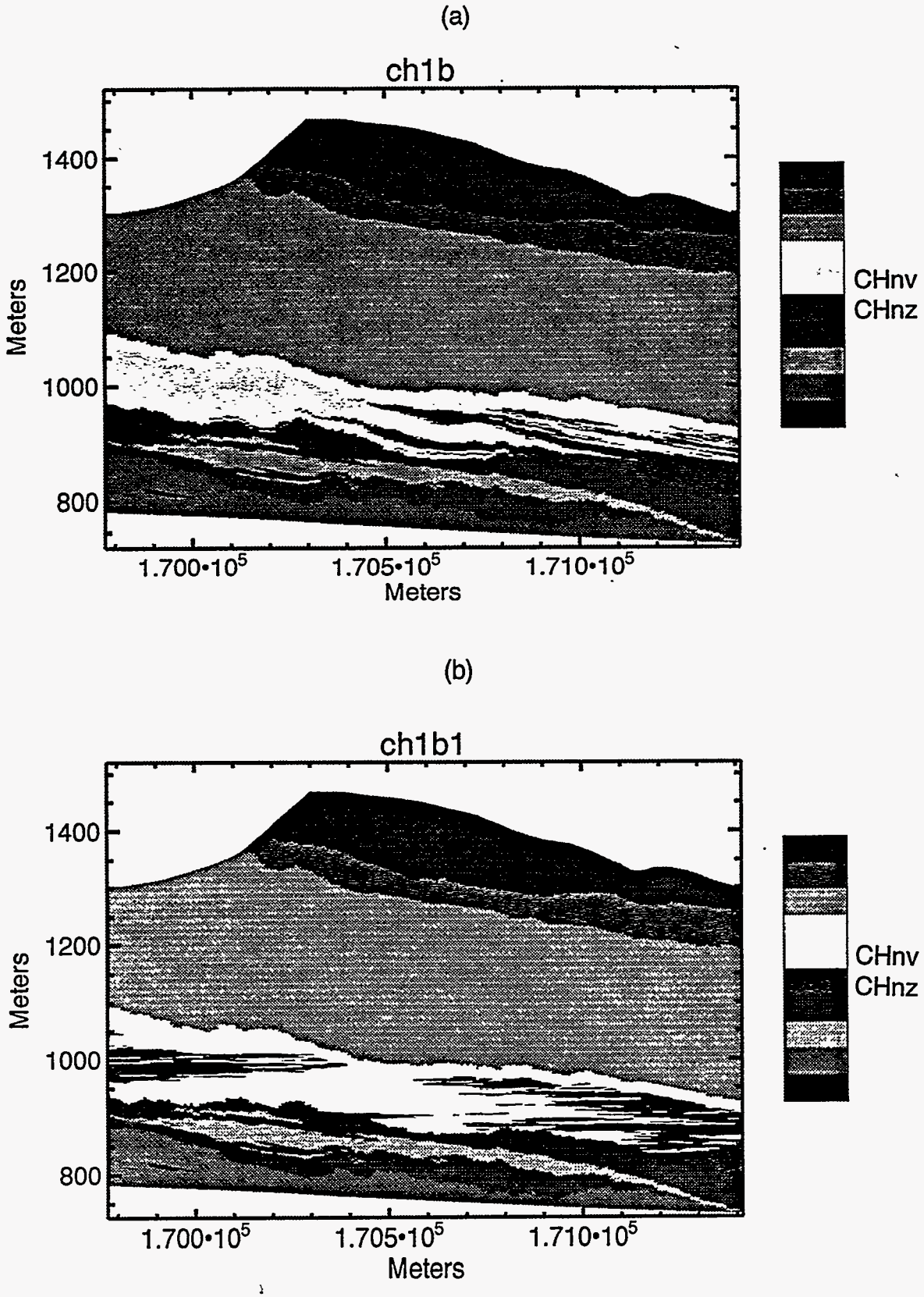

Figure 6-18. Results of indicator simulations varying only the TSbv, CHnv, and CHnz units: (a) base case; (b) one realization with horizontal CHnv and CHnz.

(c)

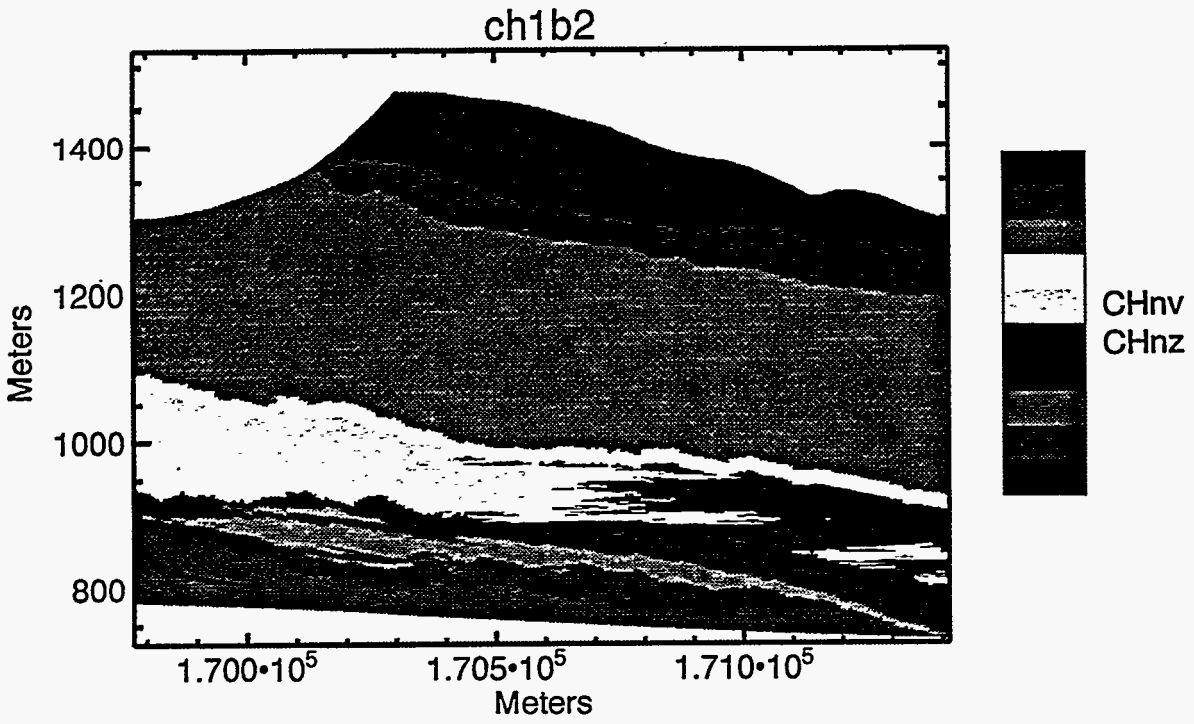

(d)

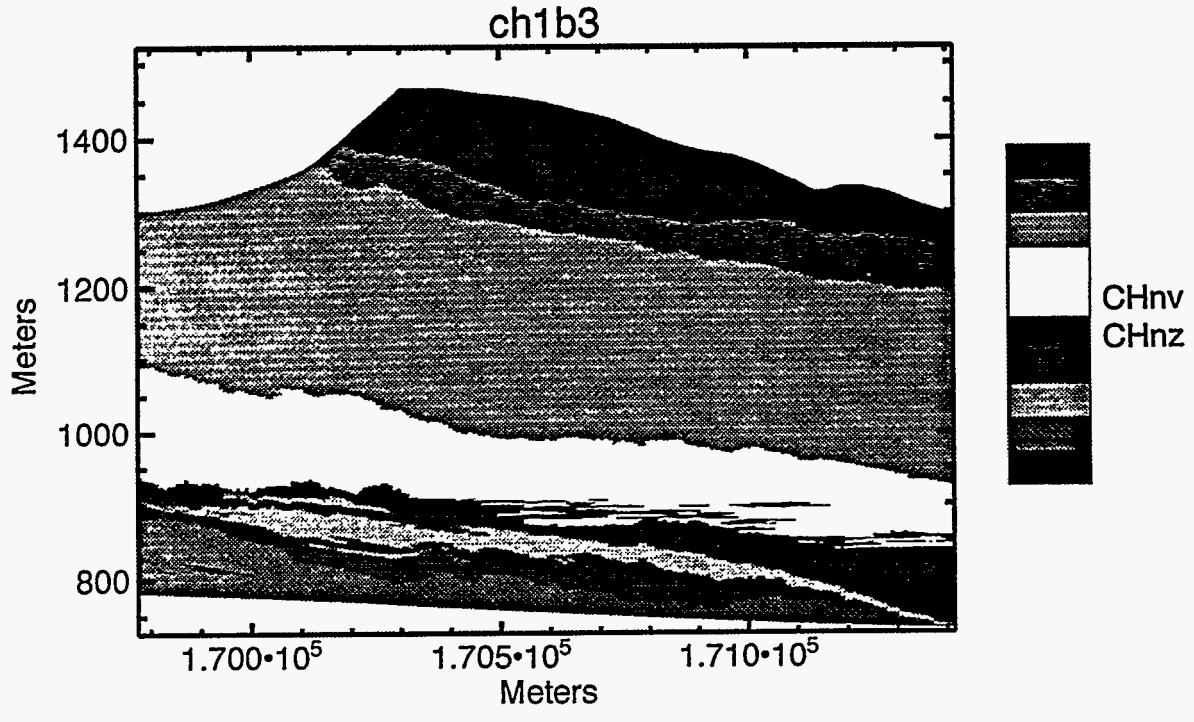

Figure 6-18 (Continued). Results of indicator simulations varying only the TSbv, CHnv, and CHnz units: (c) & (d); other realizations with horizontal CHnz and CHnv.

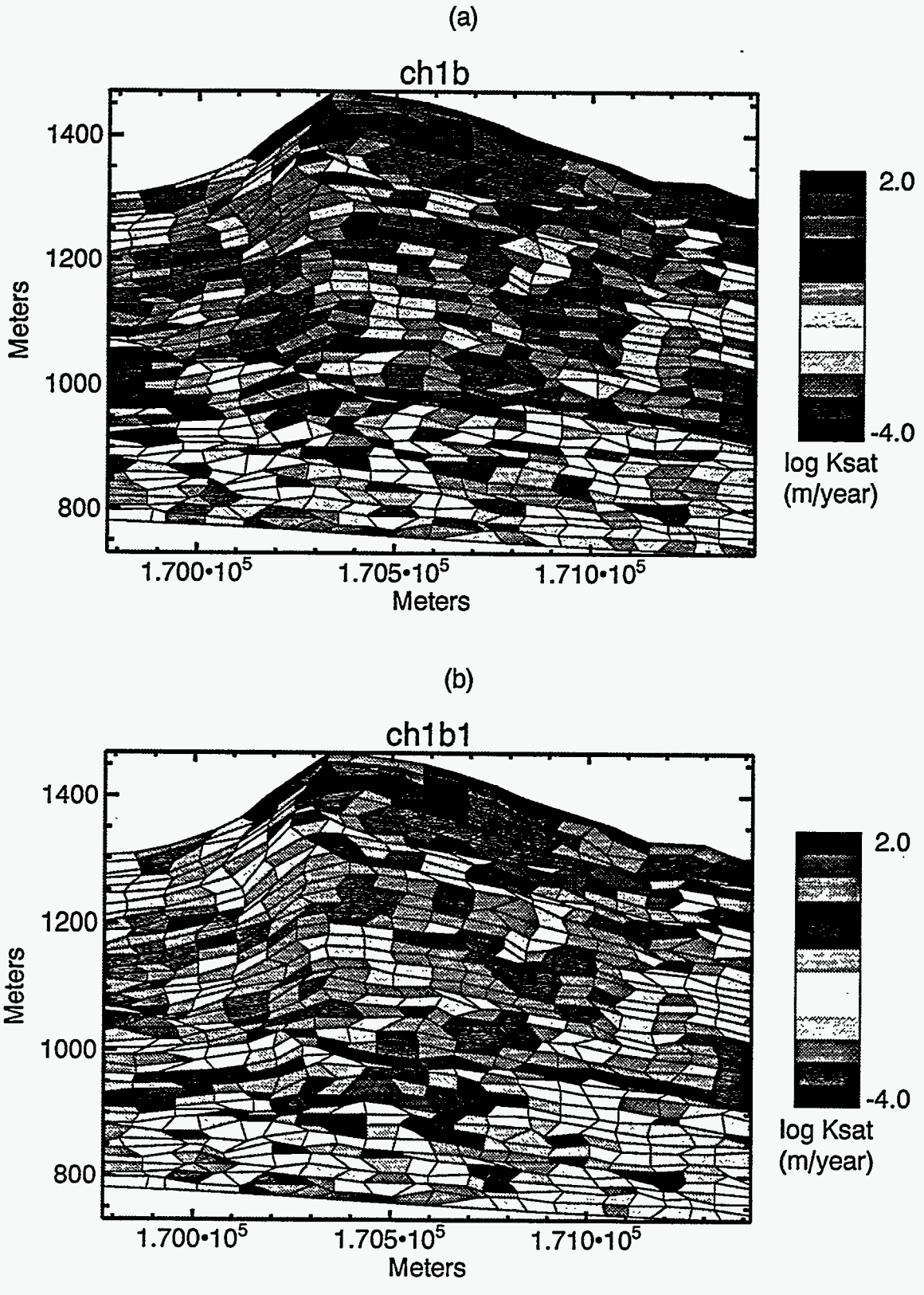

Figure 6-19. Saturated hydraulic conductivity comparisons when varying the indicator simulations for the TSbv, CHnv, and CHnz: (a) base case; (b) one realization with horizontal CHnv and CHnz.

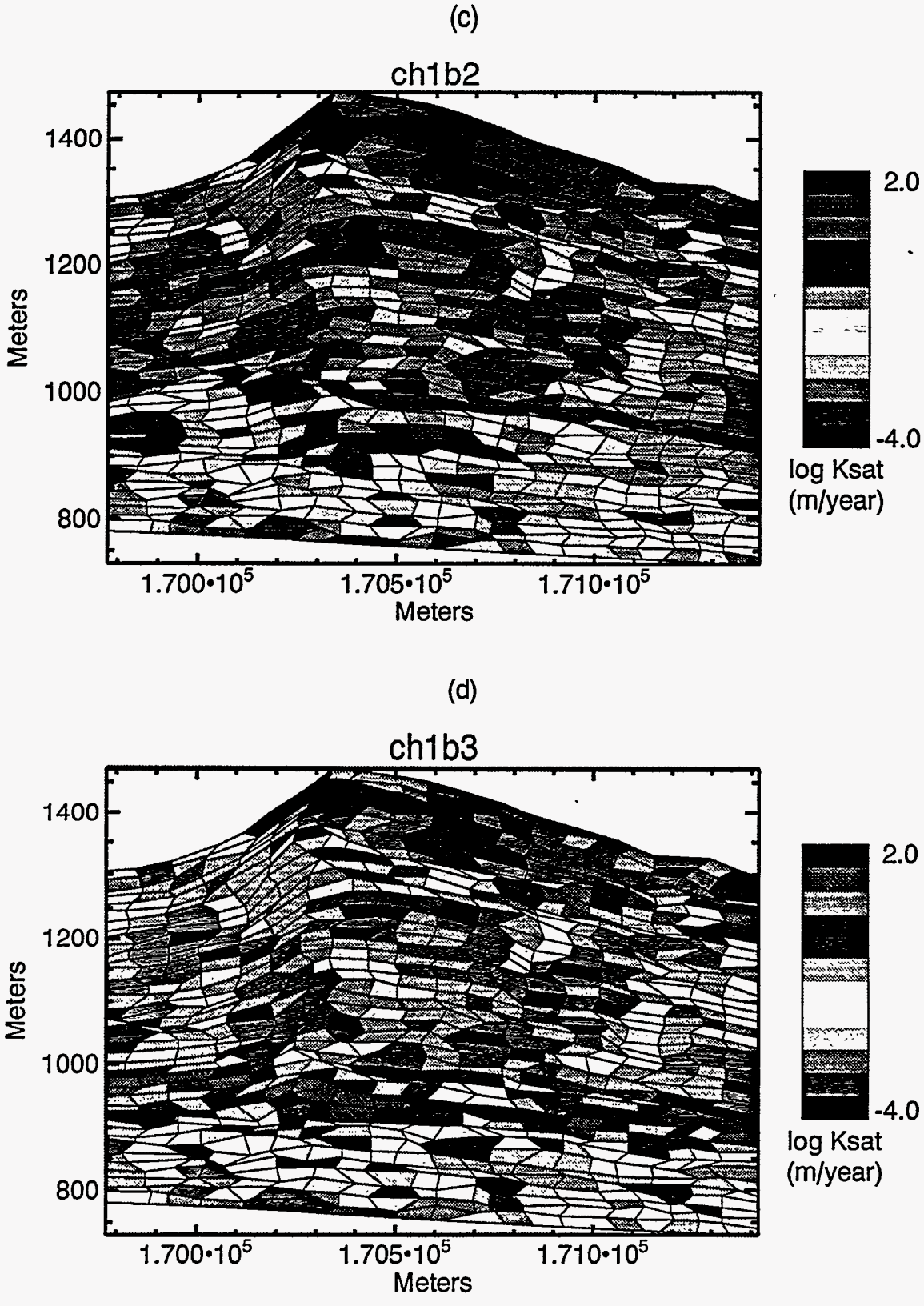

Figure 6-19 (Continued). Saturated hydraulic conductivity comparisons when varying the indicator simulations for the TSbv, CHnv, and CHnz: (c) & (d); other realizations with horizontal CHnz and CHnv.

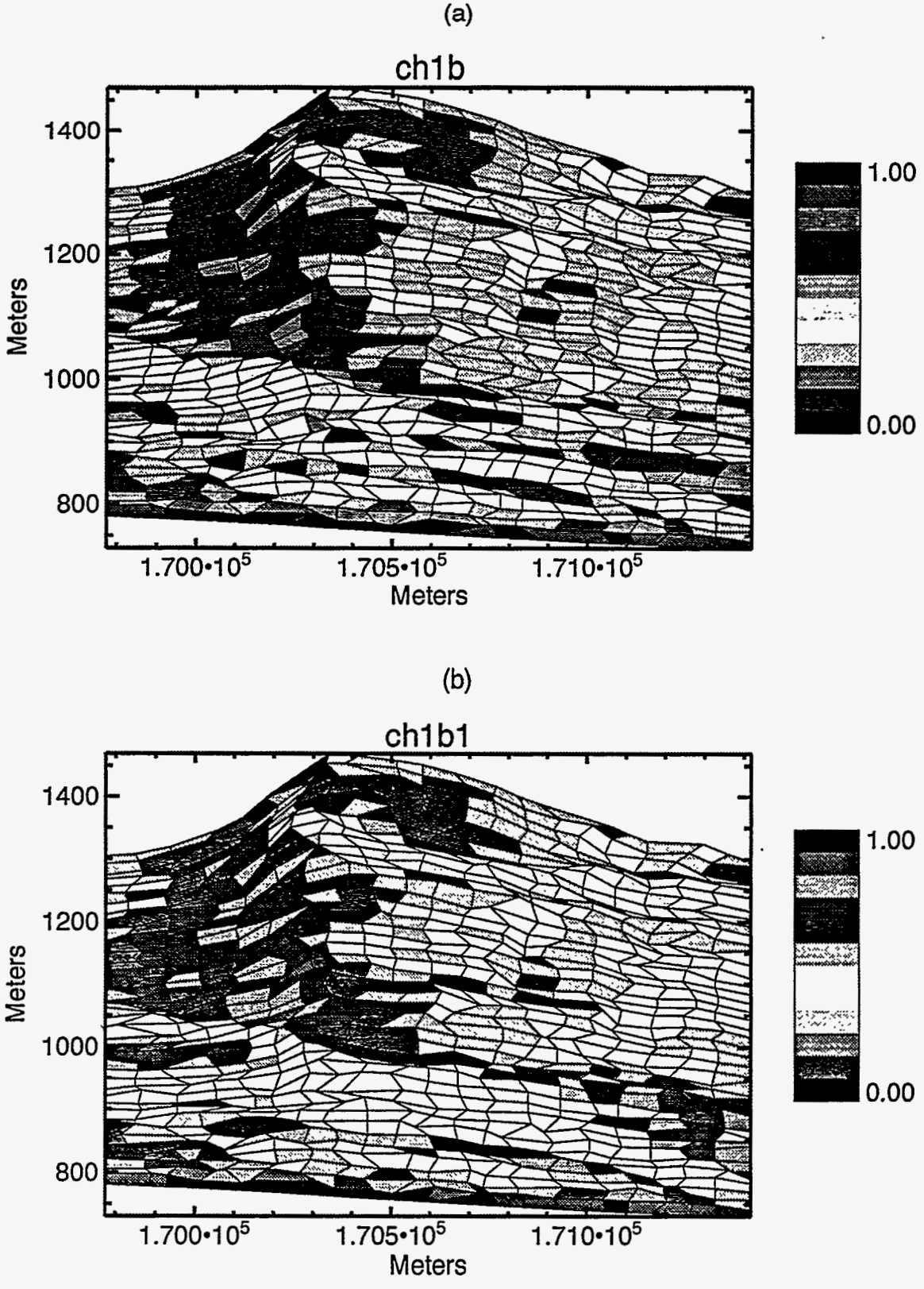

Figure 6-20. Matrix saturation comparison when varying the indicator simulations for the TSbv, CHnv, and CHnz units: (a) base case; (b) one realization with horizontal CHnv and CHnz.

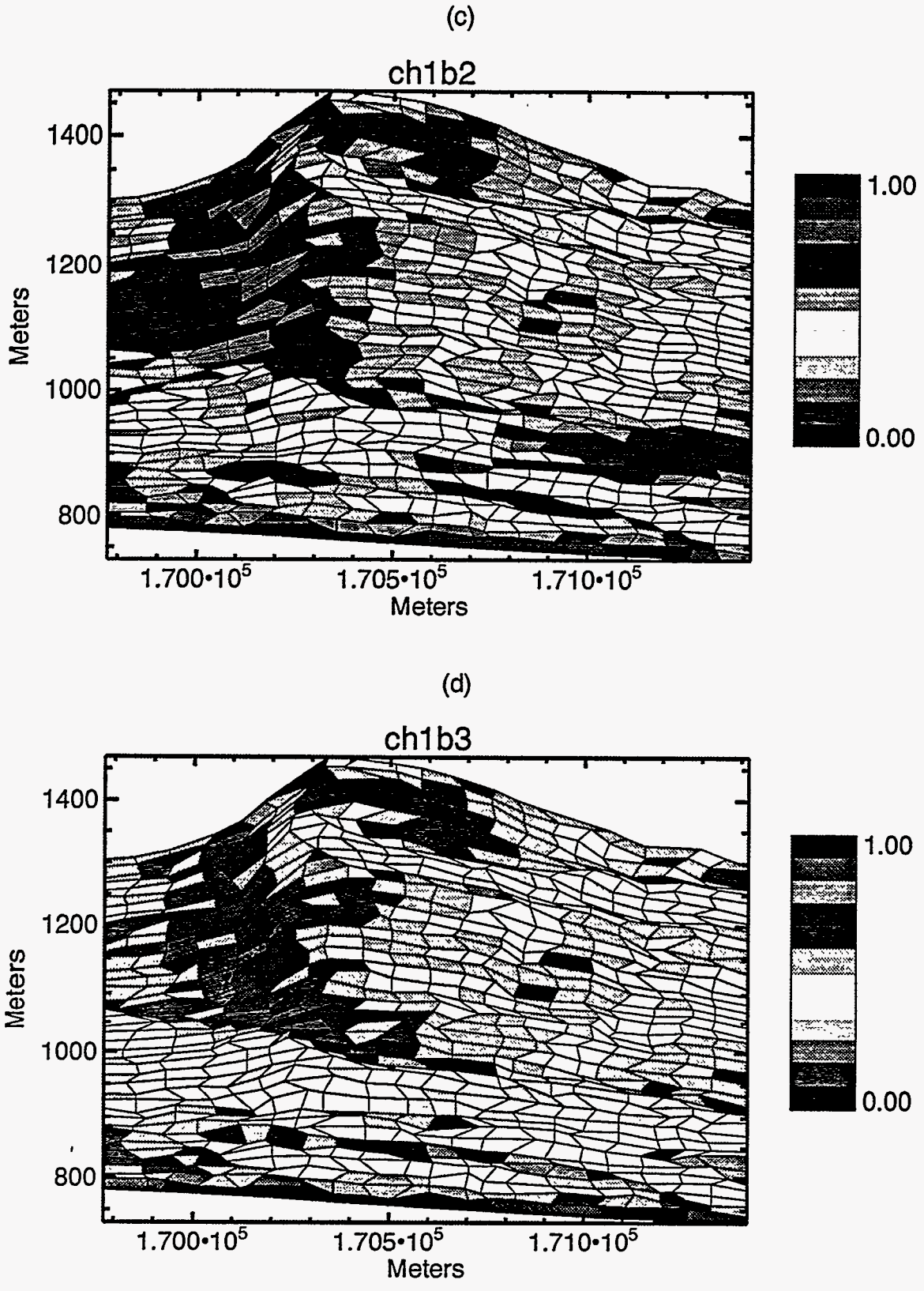

Figure 6-20 (Continued). Matrix saturation comparison when varying the indicator simulations for the TSbv, CHnv, and CHnz units: (c) & (d); other realizations with horizontal CHnz and CHnv.

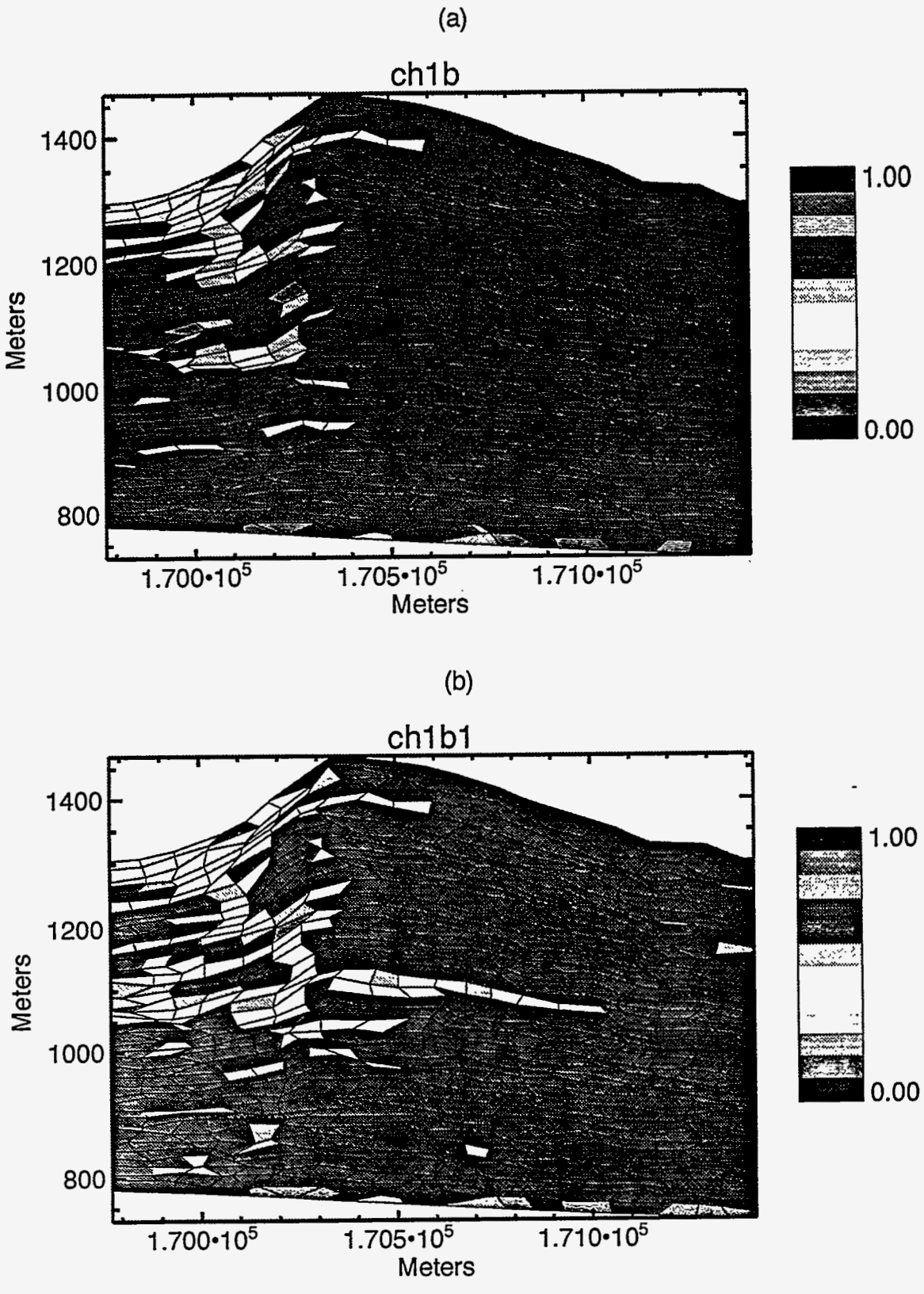

Figure 6-21. Fracture saturation comparisons when varying the indicator simulations for the TSbv, CHnv, and CHnz units: (a) base case; (b) one realization with horizontal CHnv and CHnz.

(c)

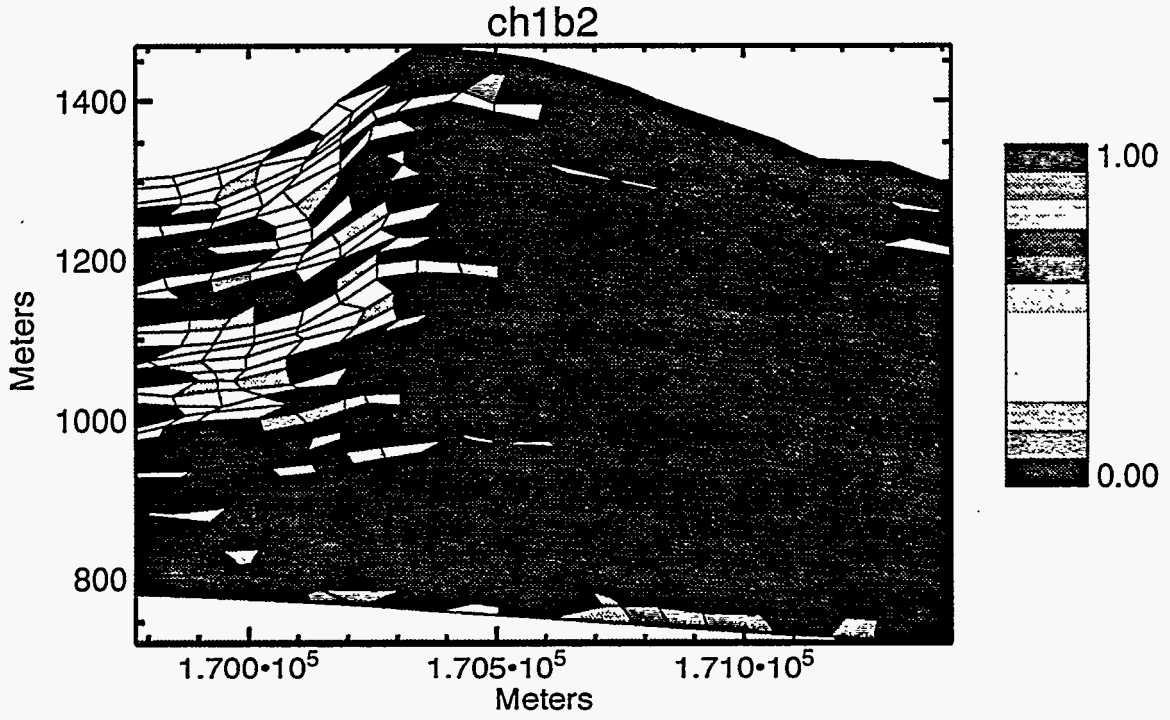

(d)

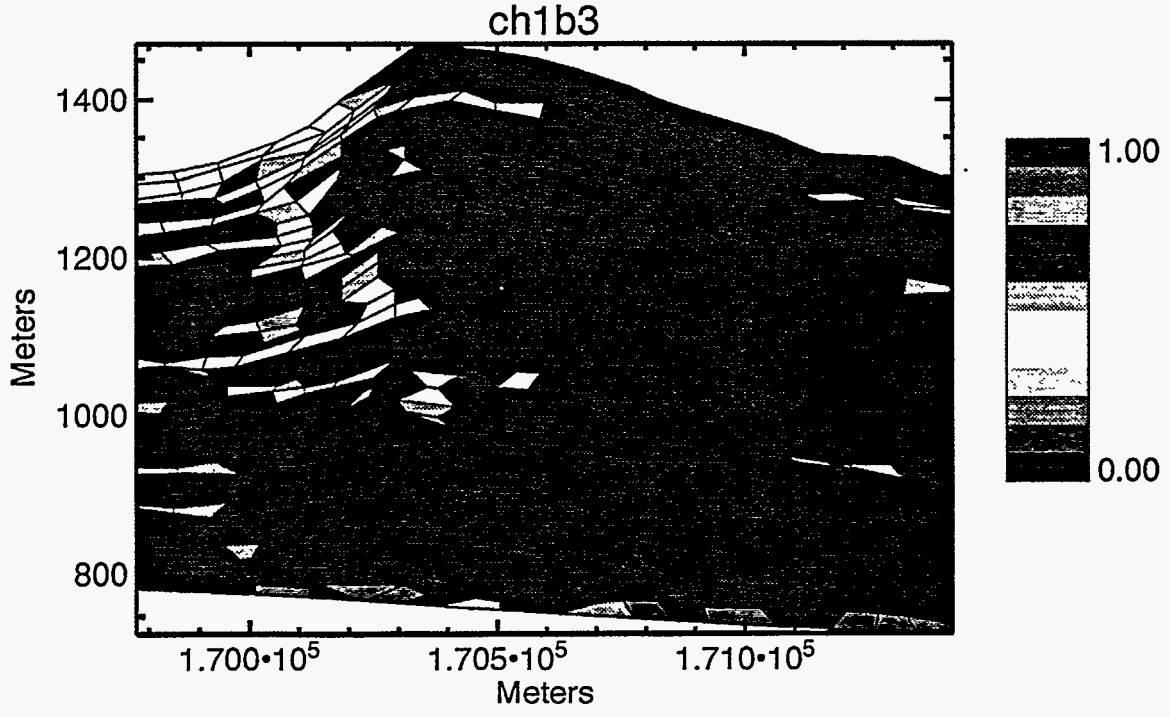

Figure 6-21 (Continued). Fracture saturation comparisons when varying the indicator simulations for the TSbv, CHnv, and CHnz units: (c) & (d); other realizations with horizontal CHnz and CHnv.

(a)

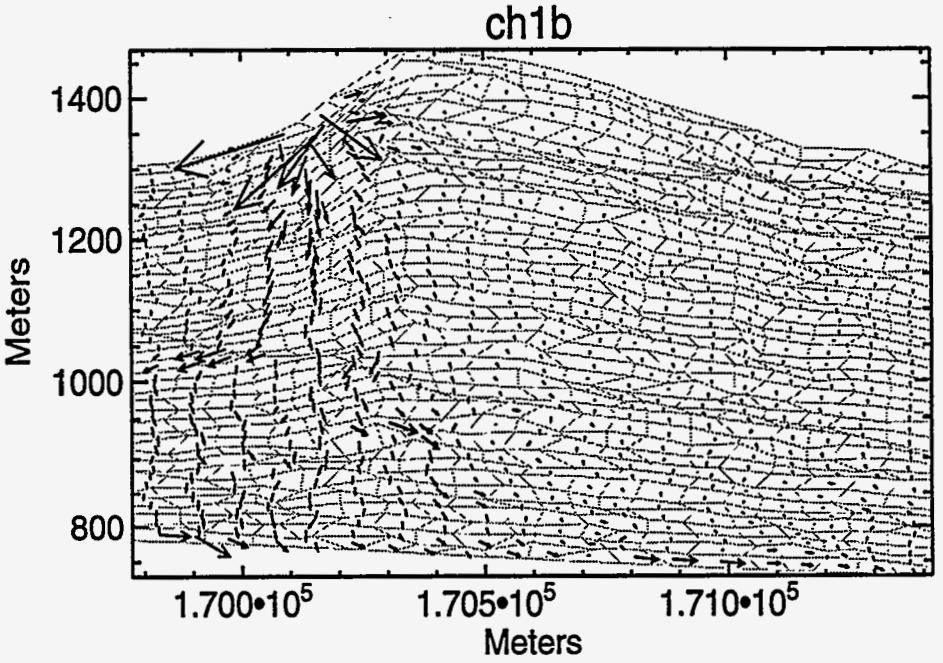

(b)

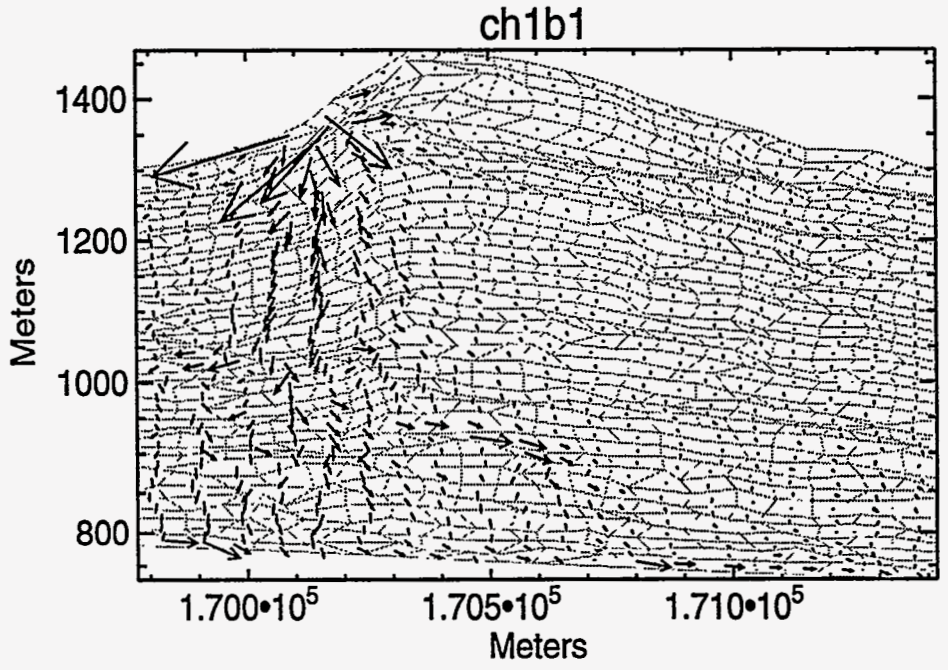

Figure 6-22. Darcy flux comparisons when varying the indicator simulations for the TSbv, CHnv, and CHnz: (a) base case; (b) one realization with horizontal CHnv and CHnz.

(c)

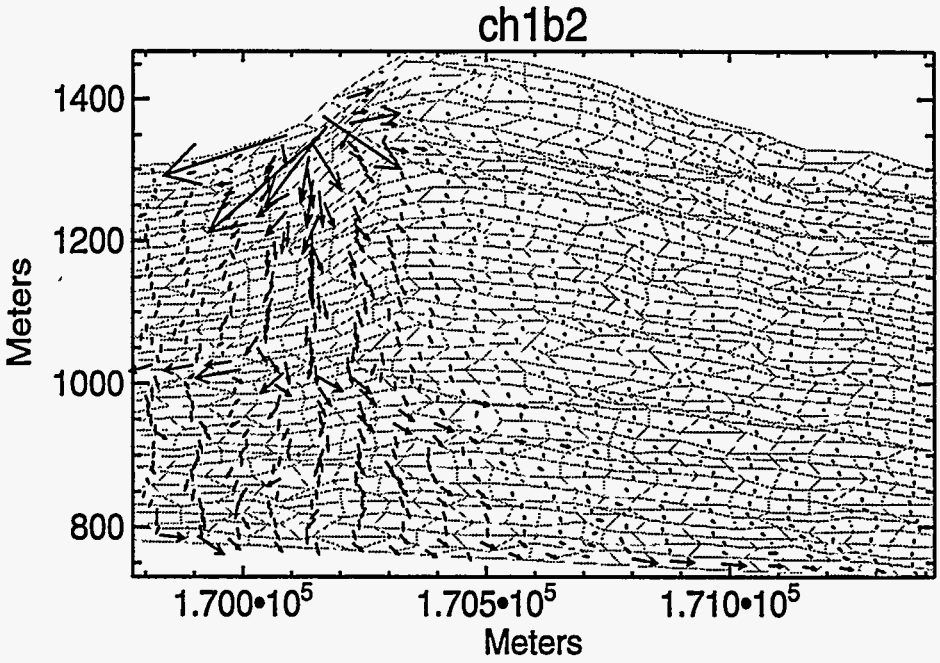

(d)

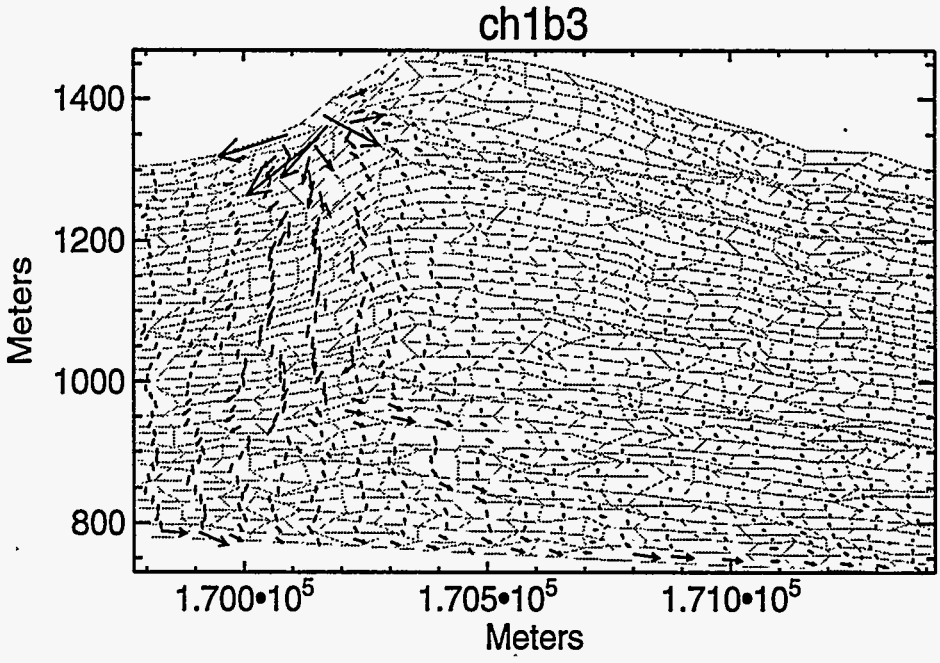

Figure 6-22 (Continued). Darcy flux comparisons when varying the indicator simulations for the TSbv, CHnv, and CHnz: (c) & (d); other realizations with horizontal CHnz and CHnv.

in the fracture porosity and saturated hydraulic conductivity. Fracture moisture retention curves were identical for all of the elements regardless of their hydrogeological units. In order to assess the sensitivity of the flow field to heterogeneities in the fracture moisture retention curves, the mean half-aperture was sampled from an exponential distribution with a mean half-aperture of 178 μm instead of remaining constant at 178 μm. The mean and standard deviation of the fracture pore size was assumed to be exponential. The fracture saturated conductivity and fracture porosity were calculated as described in Section 3.2.5.

The resulting matrix saturation, fracture saturations and fluxes as compared to the base case are shown in Figure 6-23, 6-24, and 6-25, respectively. In general, the saturations are lower in the simulation with variable moisture retention curves (*ch1bf*); however, no distinct trends emerged. Overall, matrix saturation appeared to have a greater effect on fracture flow than the moisture retention curves used for fractures. More simulations need to be performed in order to sufficiently answer question about the effects of fracture properties on the flow field.

6.3 Summary and Conclusions

The sensitivity analyses are useful in that they have shown how certain hydrogeologic properties affect simulation of the flow system and also some of the limitations of DUAL. Including intra-unit heterogeneities has been shown to be critical to modeling groundwater-flow fast paths. It is the heterogeneities that can concentrate flow, forming areas of higher saturation and therefore higher unsaturated hydraulic conductivity and groundwater velocities. With the composite-porosity conceptual model, a zone of higher matrix saturation could lead to fracture flow and thus significant fast-path flow. These results are not surprising, but should emphasize the importance of understanding the heterogeneities of a system.

The effects of using deterministic boundaries between units (in this case a uniformly thick PTn) were not as straightforward. These analyses showed that small differences in porosity, especially at the PTn outcrop, can have a strong control on the flow system. When these differences were minimized as much as possible, there was some evidence that the system with the uniformly thick PTn was more likely to have fast paths. However, the effect of the deterministic versus geostatistically simulated unit boundaries was small compared to the effects of small changes in porosities. These analyses again show the importance of complexities in the system (porosity distribution) in controlling fast paths.

Many of the sensitivity analyses conducted have shown a great deal of variability in the infiltration is through the upper boundary in response to small changes in the system. Changes in infiltration in turn led to changes (in some cases quite large) in saturations and Darcy fluxes. Infiltration, therefore, appears to be an important factor in controlling groundwater flow.

The capabilities of DUAL in its present state were also tested by changing boundary conditions and grid sizing. DUAL was shown to be unable to converge when a flux condition was specified along the upper boundary. It would have facilitated the sensitivity analyses to be able to hold flux into the system constant. However, there is not a direct method for determining flux. On

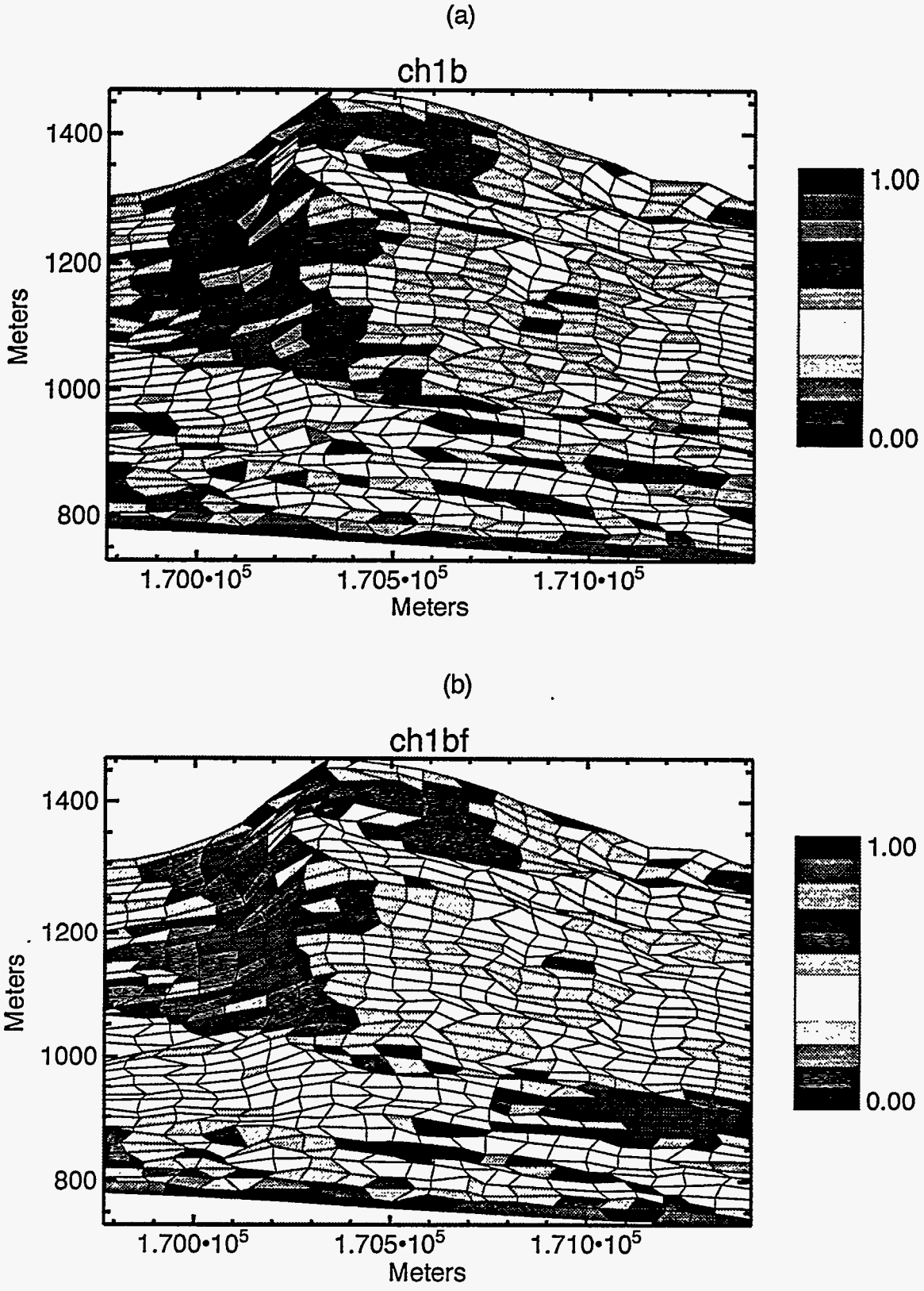

Figure 6-23. Matrix saturation comparisons with constant (a) and variable (b) fracture moisture retention curves.

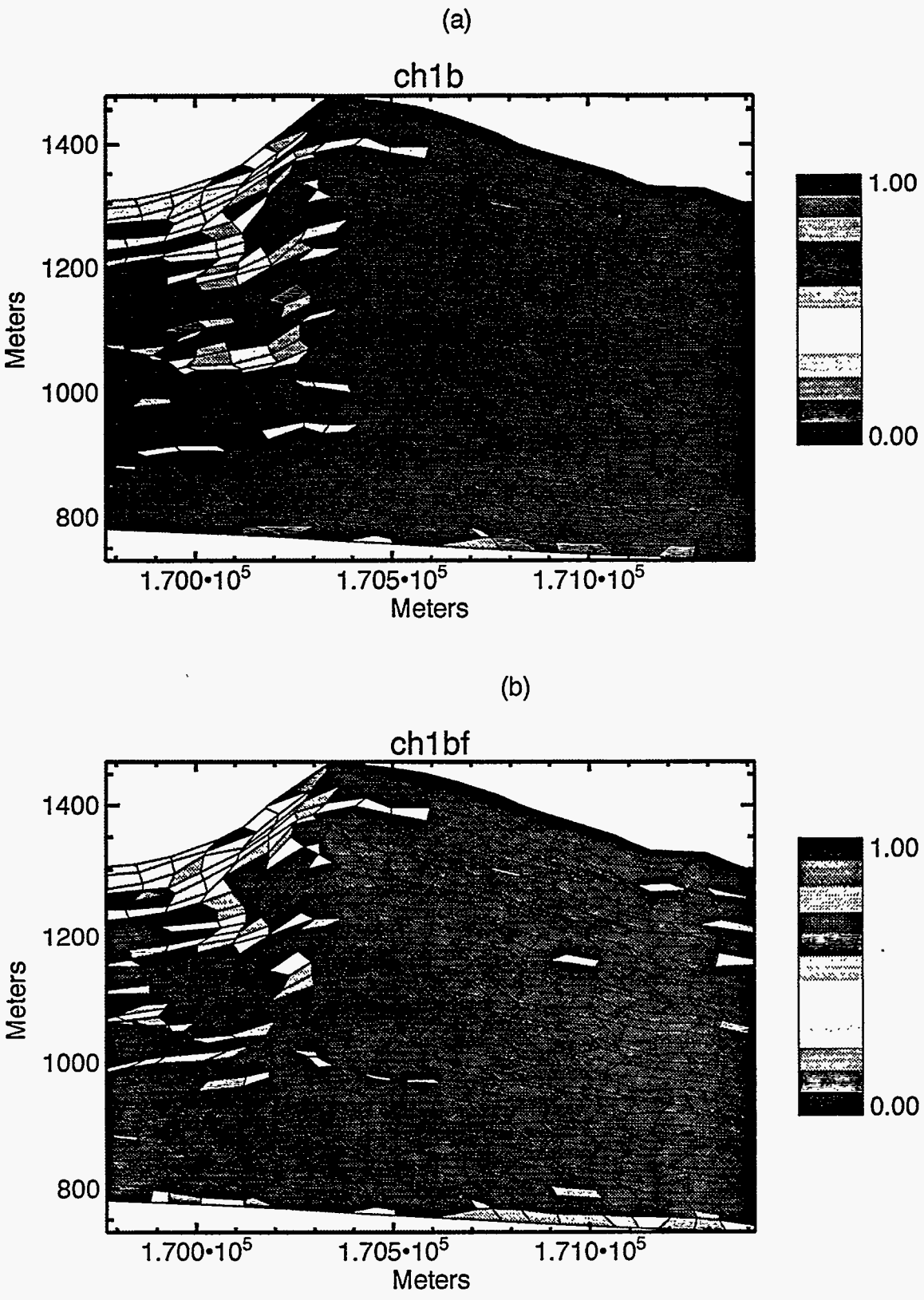

Figure 6-24. Fracture saturation comparisons with constant (a) and variable (b) fracture moisture retention curves.

(a)

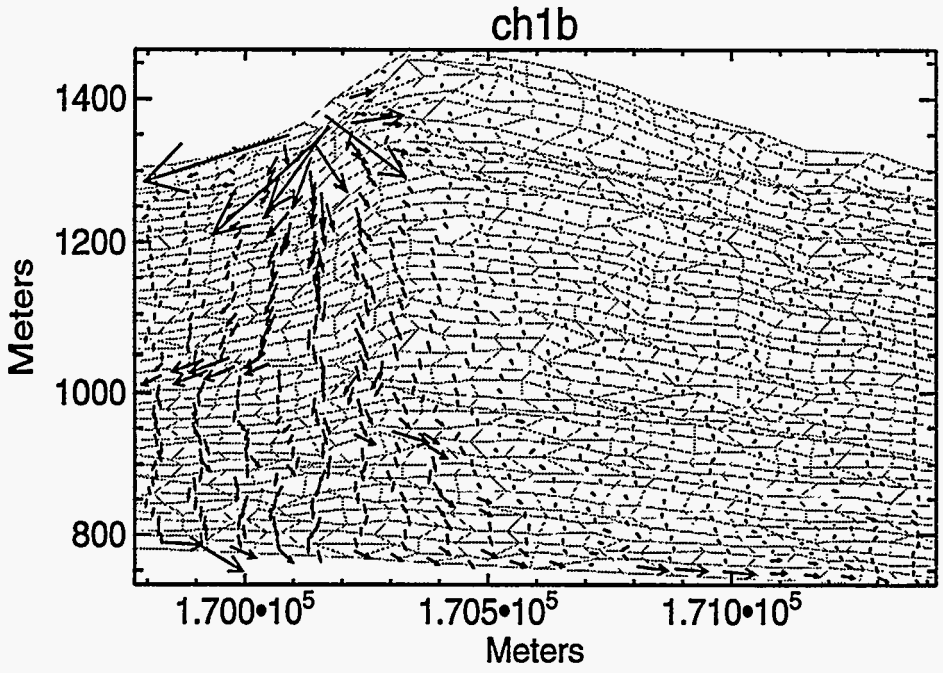

(b)

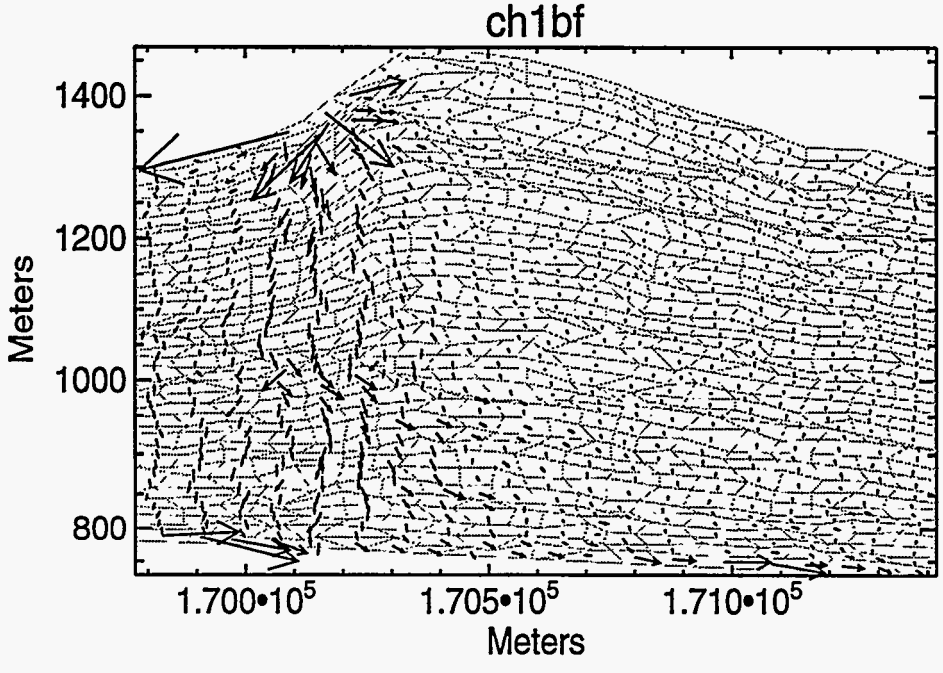

Figure 6-25. Darcy flux comparison with constant (a) and variable (b) fracture moisture retention curves.

the other hand, pressure can be directly inferred from field measurements of saturation. Thus a pressure boundary condition is more closely linked to the available data.

The limitations of DUAL were also tested by refining the grid size. Simulations were able to be conducted with finer grids than used in the base case; however, if too fine a grid was used the code did not converge. This is most likely due to high contrasts in saturations between adjoining elements. For the cases that did converge, while there were slight variations, in general the results were consistent and independent of grid size.

It has been recognized that the correlation length and anisotropy ratio used in GWTT-94 might not best reflect the data to date (Istok et al., 1994) (see section 3.1). However, it can be seen that in using alternative ratios leads to generating a system with more homogeneous hydrogeological units. Because heterogeneities in a system are critical for the initiation of fast-path flow, it is important to preserve intra-unit heterogeneities in conducting future GWTT calculations.

Channeling in the vitric Calico Hills unit became apparent when the amount of vitric versus zeolitic Calico Hills was geostatistically varied. These findings indicate that fast-path flow is more likely to occur in the CHnz. This finding is not surprising due to its higher saturated hydraulic conductivity of the CHnz. Addition boreholes drilled to the depth of the Calico Hills would assist finding potential in fast-paths.

Chapter 7
Conclusions and Recommendations

7.1 Findings

The GWTT-94 work was intended to identify and evaluate the processes and conditions that initiate fast-path flow in the unsaturated zone, a necessary step in the ultimate calculation of groundwater travel time. The conclusions presented reflect our success at evaluating these preliminary, limited aspects of the problem. Our findings are:

- The flow modeling simulations produced only a few areas of locally high groundwater saturation in the unsaturated-zone in the nine two-dimensional realizations. The factors that cause locally saturated conditions are: infiltration at the PTn outcrop, low upper-boundary capillary suction pressures, and low porosities in the TSbv.

- The particle-tracking modeling indicates particles that remain in matrix-flow conditions move very small distances over the duration of the simulations even when large time steps were used. Only when particles move at fracture-flow velocities is it possible for them to exit the system, demonstrating the importance of understanding the mechanisms causing locally saturated conditions or any other conditions that can initiate and sustain fracture flow (Table 5-1). Because of the large time steps used in the particle tracker, and the assumptions made regarding imbibition of particles from fractures into the matrix, the reported travel-time results are quite conservative.

- Zones of higher saturation below the PTn outcrop are observed in simulations of the cross-sections between the Solitario Canyon and Ghost Dance faults (Figures 4-5a and 4-5b), suggesting that the PTn outcrop is a critical zone for high infiltration. This pattern is not observed in the other simulations where there are lower porosities of the PTn at its outcrop in Solitario Canyon, or where there is no PTn outcrop at all (Figure 4-5c).

- In most realizations, the zones of localized high saturation occur in the western part of the repository, beneath the outcrop of the PTn. The generally higher saturation of the upper boundary at the outcrop of the PTn (Figure 4-5a), combined with predominantly vertical flow (Figure 4-9a), results in high local saturation below the outcrop and the consequent mobilization of particles at fracture-flow velocities in this region of the model.

- The surface capillary pressure boundary conditions exert a strong influence on the saturations and flow fields observed in the flow simulations which in turn affect the travel time of particles. In one simulation, cs1bc (Figure 4-5a), an unusually high-magnitude capillary suction pressure produced high matrix saturations which consequently resulted in a large number of particles experiencing fast-path fracture flow.

- Low porosities in the TSbv result in zones of high saturation in all three simulations of both cross-sections 1 and 3 (Figure 4-5a and c), suggesting that the TSbv might be an important unit in the initiation of fracture flow. The stratigraphic position of the basal vitrophyre relative to the western part of the repository has a significant impact on the number of particles exiting the system. If the disturbed zone boundary caused particles to start from below the repository in the vicinity of the TSbv, travel times would be faster than the difference in path lengths would predict. The vertical separation of the initial particle positions and the zones of higher saturation at the basal vitrophyre is therefore a controlling feature of the groundwater travel time calculated by the model.

- The LBL/USGS site-scale model predicts that moisture would build up along faults when they act as capillary barriers, while relatively dry conditions would prevail when the faults are assumed to readily conduct water (Bodvarsson et al., 1994). However, the results of the simulations performed for this study show that neither high nor low saturation zones were observed along the Ghost Dance Fault at the eastern boundary of cross-sections 1 and 2 (Figures 4-5a and b), suggesting instead that heterogeneities or irregularities of unit contacts may have a strong enough influence on the flow system to minimize lateral flow (Figure 4-9a and b) and thus prevent such transport of liquid to the faults where it would either build up or be diverted down the fault.

- The sensitivity analyses demonstrated how certain hydrologic properties affect simulation of the flow system. Inclusion of intra-unit heterogeneities of porosity is critical to modeling groundwater-flow fast paths because they concentrate flow, forming areas of higher saturation, unsaturated hydraulic conductivity, and groundwater velocities (Figure 6-2, 6-3, 6-4). The effects of the deterministic versus geostatistically simulated unit boundaries were also tested; these effects were minor, however, compared to the effects of small changes in porosities at the outcrop of the PTn (Figures 6-7, 6-8, 6-9, 6-10, 6-11). Many of the sensitivity analyses conducted showed that small changes in the system resulted in significant variation in infiltration through the upper boundary which in turn led to changes in saturations and Darcy fluxes, suggesting that infiltration is an important factor in controlling groundwater flow.

- The capabilities of DUAL in its present state were tested by changing boundary conditions and refining grid size. When specified-pressure upper boundaries of the model were changed to the specified fluxes, DUAL failed to converge. If too fine a grid was used (e.g., 30 by 60), the code also did not converge, most likely due to high contrasts in saturations between adjoining elements. Otherwise, the results of alternative simulations were consistent and independent of grid size, demonstrating that grid size is not a sensitive factor when using DUAL to the extent it was varied (Figure 6-13, 6-14).

- Because the assumptions regarding water-particle travel are quite conservative, the travel-time results have not been emphasized here. Once fracture flow was initiated for a particle, it was almost always transported to the water table and thus out of the system. Overall, with one exception, a small percentage of particles (less than 3%) exited the system by these pro-

cesses. Had a mechanism for reimbibition of fracture water into the matrix been implemented, the number of particles moving to the water table by fracture flow may have been significantly less.

7.2 Future Directions

Despite the conservative assumptions regarding mechanisms which propagate fracture-flow as indicated by water-particle movement, the modeling done for the GWTT-94 study has given positive indications that the Yucca Mountain site might meet the GWTT regulations. However, these calculations are preliminary and do not account for important factors specified in the criteria (saturated zone and disturbed zone). The modeling has identified sensitive factors and demonstrated areas needing further investigation. Several areas of future work can be proposed at this time:

- The geostatistically determined geometry of hydrostratigraphic units and distributions of porosity should be compared with alternative geological conceptualizations of the site, especially as new hydrogeological data become available.

- Infiltration appears to be an important factor controlling groundwater flow. The imposition of uniform pressure upper boundary conditions for the entire outcrop of a unit as was done in this study is probably not realistic. Thus more detailed and accurate data (spatially varying within a unit) about infiltration or pressure boundary conditions, in-situ saturations and shallow-water content along PTn outcrop are needed.

- All numerical simulations of groundwater flow in the GWTT-94 study were for steady-state conditions. Numerical modeling of transient flow in response to high-infiltration events may delineate fast flow paths in response to temporarily non-uniform distribution of infiltration. Transient groundwater flow modeling will provide a more realistic simulation of fast flow in the unsaturated zone.

- To incorporate outcrop data effectively into the model, it will be necessary to use finer grid patterns along the outcrop of the PTn.

- Understanding water flow in PTn will increase our confidence in our predictions of UZ flow behavior. If lateral diversion occurs, flow may drain toward Ghost Dance fault, where it may either drain into the fault zone or accumulate, depending on the permeability of the fault zone. If, however, vertical flow predominates, perched-water zones may develop, particularly in western portion of site.

- The particle tracker used in GWTT-94 incorporated large time steps, allowing the initiation of transport at fracture-flow velocities when matrix saturation occurs, but essentially prohibiting reimbibition of particles. The particle tracker therefore is likely to underestimate

the travel time of the particles exiting the system by fracture flow. A dual-permeability formulation of the code that simulates reimbibition of groundwater into areas with low matrix saturation will provide more realistic estimates of travel times.

- The sensitivity analyses demonstrated that infiltration, matrix saturation, and Darcy fluxes were all higher in simulations of a heterogeneous system; more realistic investigation of the effects of the heterogeneities is essential.

- Refinements are needed in the flow code to provide for simulation of the heterogeneity in the fracture system, thereby refining the matrix-fracture interaction in terms of both the initiation and propagation of fracture flow in the model. Fracture-system heterogeneities, like those of the matrix, will be geostatistically simulated.

- Future modeling should include an estimate of the effect of disturbances by the repository on surrounding rock to more accurately predict travel times to the water table.

- Additional investigation and data collection will eliminate uncertainties about hydrogeological parameters; nevertheless, multiple-realization numerical modeling will continue to be performed to account for uncertainties which remain about the conceptual model.

7.3 Plans for GWTT-95 Work

Plans for improving the modeling done as part of the 1995 GWTT calculations include:

- Selecting additional cross-sections, based on information gained from the site-scale modeling effort and available site-characterization data. One cross-section will be oriented roughly north-south. Another will trend northwest to southeast, approximately through Drill Hole wash. The east-west cross-sections will extend from the Solitario Canyon fault to the Bow Ridge fault, thus incorporating the Ghost Dance fault as an interior feature.

- Co-simulating matrix porosity and saturated conductivity in the geostatistical simulations. Although there are more abundant porosity data, saturated conductivity is a more effective hydrological parameter for flow calculations because it accounts for the interconnection between pore space. The future geostatistical simulations will use saturated conductivity data where available. Where only porosity data are available, a correlation between porosity and saturated hydraulic conductivity will be used, similar to what was done for the 1994 GWTT calculations.

- Using a dual-permeability conceptual model in addition to modeling an equivalent continuum. This model allows for capillary-pressure disequilibrium between fractures and the

matrix. With this model it is possible to propagate fracture flow under less saturated conditions than is needed for an composite-porosity model. This model will allow for more realistic reimbibition of water from fractures into the matrix.

- Using the currently available data for infiltration or pressure along the upper boundary, including if possible spatial variation within units.

7.4 Implications for Other YMP Activities

This work is a precursor to the complete evaluations of GWTT for the Technical Site Suitability report due in 1997. The complete GWTT evaluations require analyses in the unsaturated and saturated zones, and that the effects of repository-induced thermal disturbances to the hydrologic flow field be defined. It is expected that the future analyses will be able to build on the current geostatistical unsaturated-zone model domains. This work will be used for both future GWTT analyses and other performance-assessment activities, such as upcoming total-system performance assessments. Furthermore, the conceptual model of the groundwater flow (i.e., the composite-porosity model) used here is expected to represent one of the alternative conceptual models that must be considered in the complete GWTT evaluation.

The geostatistically simulated model domain used in this work can also be applied to other investigations, such as the evaluation of the importance of a more complete characterization of the Calico Hills unit beneath the potential repository.

The observations that the fast-path flow times are not linearly related to the distance from the point of initiation to the water table is of importance to the design and systems-engineering activities. Because of the presence of areas of high local saturation beneath the potential repository horizon, design and construction practices that result in a disturbed-zone that extends to these saturated areas might imply a relatively high percentage of fast-flow paths.

This page intentionally left blank.

Chapter 8
References

Anderson, L.A. 1981. *Rock Property Analysis of Core Samples from the Yucca Mountain UE25a-1 Borehole, Nevada Test Side, Nevada.* Open-File Report 81-1338. Denver, CO: US Geological Survey. (NNA.870406.0031)

Anderson, L.A. 1984. *Rock Property Measurements on Large-Volume Core Samples from Yucca Mountain USW GU-3/G-3 and USW G-4 Boreholes, Nevada Test Site, Nevada.* Open-File Report 84-552. Denver, CO: US Geological Survey. (NNA.870323.0195)

Anderson, L.A. 1991. *Results of Rock Property Measurements Made on Core Samples from Yucca Mountain Boreholes, Nevada Test Site, Nevada. Part 1: Boreholes UE25A-4, -5, -6, and -7; Part 2: Borehole UE25p#1.* Open-File Report 90-474. Denver, CO: US Geological Survey. (NNA. 910411.0081)

Anderson, M.P. 1979. "Using Models to Simulate the Movement of Contaminant Through Groundwater Flow Systems," *CRC Critical Reviews in Environmental Control.* 97-156. (NNA.920505.0056)

Anderson, M.P., and W.W. Woessner. 1992. *Applied Groundwater Modeling, Simulation of Flow and Advective Transport.* San Diego, CA: Academic Press, Inc.

Barnard, R.W., M.L. Wilson, H.A. Dockery, J.H. Gauthier, P.G. Kaplan, R.R. Eaton, F.W. Bingham, and T.H. Robey. 1992. *TSPA 1991: An Initial Total-System Performance Assessment for Yucca Mountain.* SAND91-2795. Albuquerque, NM: Sandia National Laboratories. (NNA.920630.0033)

Barr, G.E., and S.A. Shannon. 1994. "Constraining Local 3-D Models of the Saturated-Zone, Yucca Mountain, Nevada," *High Level Radioactive Waste Management: Proceedings of the Fifth Annual Conference, Las Vegas, Nevada, May 22-26, 1994.* La Grange Park, IL: American Nuclear Society. Vol. 4, p. 1814-1821.

Barrett, R., M. Berry, T. Chan, J. Demmel, J. Donato, J. Dongarra, V. Eijkhout, R. Pozo, C. Romine, and H. van der Vorst. 1993. *Templates for the Solution of Linear Systems: Building Blocks for Iterative Methods.* Philadelphia, PA: Society for Industrial and Applied Mathematics.

Bloomsburg, G., R.E. Williams, and J.L. Osiensky. 1989. "Distribution of Downward Flux in Unsaturated Heterogeneous Hydrologic Environments," *Geological Society of America Bulletin.* Vol. 101, 1623-1630. (NNA.901228.0257)

Bodvarsson, G., G. Chen, and C.S. Wittwer. 1994. "Preliminary Analysis of Three-Dimensional Moisture Flow within Yucca Mountain, Nevada," *High Level Radioactive Waste Management, Proceedings of the Fifth Annual International Conference, Las Vegas, Nevada, May 22-26, 1994.* La Grange Park, IL: American Nuclear Society. 2038-2047. (MOL.19950419.0116)

Brooks, R.H., and A.T. Corey. 1966. "Properties of Porous Media Affecting Fluid Flow," *Journal of the Irrigation and Drainage Division, Proceedings of the American Society of Civil Engineers.* Vol. 92, no. IR2, 61-88. (NNA.870407.0356)

Buesch, D.C., J.E. Nelson, R.P. Dickerson, and R.W. Spengler. 1993. "Development of 3-D Lithostratigraphic and Confidence Models at Yucca Mountain, Nevada," *High-Level Radioactive Waste Management, Proceedings of the Fifth Annual International Conference, Las Vegas, Nevada, April 26-30, 1993.* La Grange Park, IL: American Nuclear Society. 943-948. (NNA.931214.0104)

Buscheck, T.A., and J.J. Nitao. 1988. *Preliminary Scoping Calculations of Hydrothermal Flow in Variably Saturated, Fractured, Welded Tuff During the Engineered Barrier Design Test at the Yucca Mountain Exploratory Shaft Test Site.* UCID-21571. Livermore, CA: Lawrence Livermore National Laboratory. (NNA.890224.0009)

Byers, F.M., Jr., W.J. Carr, and P.P. Orkild. 1989. "Volcanic Centers of Southwestern Nevada: Evolution of Understanding, 1960-1988," *Journal of Geophysical Research.* Vol. 94, no. B5, 5908-5924. (NNA.900403.0407)

Carr, W. J. 1988. "Volcano-Tectonic Setting of Yucca Mountain and Crater Flat, Southwestern Nevada," *Geologic and Hydrologic Investigations of a Potential Nuclear Waste Disposal Site at Yucca Mountain, Southern Nevada.* Eds. M.D. Carr and J.C. Yount. USGS Bulletin 1790. (NNA.891114.0346)

Cheney, W., and D. Kincaid. 1985. *Numerical Mathematics and Computing.* 2nd ed. Pacific Grove, CA: Brooks-Cole Publishing.

Czarnecki, J.B. 1985. *Simulated Effects of Increased Recharge on the Ground-Water Flow System of Yucca Mountain and Vicinity, Nevada-California.* WRI-84-4344. Denver, CO: US Geological Survey. (NNA.870407.0008)

Czarnecki, J.B. 1989. "Preliminary Simulations Related to a Large Horizontal Hydraulic Gradient at the North End of Yucca Mountain, Nevada," *EOS, Transactions of the American Geophysical Union.* Vol. 70, no. 15, 321. (NNA.891218.0142)

Czarnecki, J.B., and R.R. Luckey. 1989. "Regional and Local Flow Systems near Yucca Mountain Site, Nevada," *Geological Society of America 1989 Field Trip Guidebook.* Comps. J.D. Vineyard and W.K. Wedge. Special Publication No. 5. Rolla, MO: Missouri Department of Natural Resources. 32-33. (NNA.890523.0124)

Czarnecki, J.B., and R.K. Waddell. 1984. *Finite-Element Simulation of Ground-Water Flow in the Vicinity of Yucca Mountain, Nevada-California.* Water Resources Investigations Report 84-4349. Denver, CO: US Geological Survey. (NNA.870407.0173)

Department of Energy (DOE). 1984. "Nuclear Waste Policy Act of 1982; General Guidelines for the Recommendation of Sites for the Nuclear Waste Repositories; Final Siting Guidelines," *Code of Federal Regulations, Title 10, Part 960.* Washington, DC: US Government Printing Office. (NNA.870506.0140)

Department of Energy (DOE). 1993. *The Yucca Mountain Site Characterization Project -- Reference Information Base, Version 4, Revision 7.* YMO/CC-0002. Las Vegas, NV: U.S. Department of Energy. (NNA.930517.0092)

Deutsch, C.V., and A.G. Journel. 1992. *GSLIB Geostatistical Software Library and User's Guide.* New York, NY: Oxford University Press. (NNA.930507.0081)

Dudley, A.L., R.R. Peters, J.H. Gauthier, M.L. Wilson, M.S. Tierney and E.A. Klavetter. 1988. *Total System Performance Assessment Code (TOSPAC) Vol. 1 Physical and Mathematical Basis.* SAND85-0002. Albuquerque, NM: Sandia National Laboratories. (NNA.881202.0211)

Eslinger, P.W., L.A. Doremus, D.W. Engel, T.B. Miley, M.T. Murphy, W.E. Nichols, M.D. White, D.W. Langford, and S.J. Ouderkirk. 1993. *Preliminary Total-System Analysis of a Potential High-Level Nuclear Waste Repository at Yucca Mountain.* PNL-8444. Richland, WA: Pacific Northwest Laboratory

Ewing, R.E., J.V. Koebbe, R. Gonzalez, and M.F. Wheeler. 1985. "Mixed Finite Element Methods for Accurate Fluid Velocities," *Finite Elements in Fluids, Volume 6: Finite Elements and Flow Problems.* Eds. R.H. Gallagher, G.F. Carey, J.T. Oden, and O.C. Zienkiewicz. New York, NY: Wiley Publishing Co. 233-249.

Fetter, C.W. 1992. *Contaminant Hydrogeology.* New York, NY: Macmillan Publishing. 43-47.

Flint, A.L., and L.E. Flint. 1994. "Spatial Distribution of Potential Near Surface Moisture Flux at Yucca Mountain," *High-Level Radioactive Waste Management, Proceedings of the Fifth Annual International Conference, Las Vegas, Nevada, May 22-26, 1994.* La Grange Park, IL: American Nuclear Society. Vol. 4, 2352-2358. (MOL.19950419.0111)

Flint, L.E., and A.L. Flint. 1990. *Preliminary Permeability and Water-Retention Data for Nonwelded and Bedded Tuff Samples, Yucca Mountain Area, Nye County, Nevada.* Open-File Report 90-569. Denver, CO: US Geological Survey. (NNA.920225.0002)

Flint, L.E., A.L. Flint, and J.A. Hevesi. 1994. "Shallow Infiltration Processes in Arid Watersheds at Yucca Mountain, Nevada." *High Level Radioactive Waste Management, Proceedings of the Fifth Annual International Conference, Las Vegas, Nevada, May 22-26, 1994.* La Grange Park, IL: American Nuclear Society. Vol. 4, 2315-2322. (MOL.19950419.0114)

Freeze, R.A., and J.A. Cherry. 1979. *Groundwater.* Englewood Cliffs, NJ: Prentice-Hall, Inc. (NNA.870406.0444)

Fridrich, C.J., W.W. Dudley, Jr., and J.S. Stuckless. 1994. "Hydrogeologic Analysis of the Saturated-Zone Ground-Water System Under Yucca Mountain, Nevada," *Journal of Hydrology.* Vol. 154, 133-168. (MOL.19940811.0102)

Gelhar, L.W. 1993. *Stochastic Subsurface Hydrology.* Englewood Cliffs, NJ: Prentice-Hall, Inc. (NNA.940509.0030)

Harr, M.E. 1989. *Reliability-Based Design in Civil Engineering.* New York, NY: McGraw-Hill, Inc. (NNA.890713.0149)

Hevesi, J.A., and A.L. Flint. 1993. "The Influence of Seasonal Climatic Variability on Shallow Infiltration at Yucca Mountain," *High Level Radioactive Waste Management, Proceedings of the Fourth Annual International Conference, Las Vegas, Nevada, April 26-30, 1993.* La Grange Park, IL: American Nuclear Society. 122-131. (NNA.931022.0070)

Hevesi, J.A., A.L. Flint, and J.D. Istok. 1992. "Precipitation Estimation in Mountainous Terrain Using Multivariate Geostatistics. Part II: Isohyetal Maps," *Journal of Applied Meteorology.* Vol. 31, no. 7, 677-688. (NNA.930427.0173)

Hevesi, J.A., A.L. Flint, and L.E. Flint. 1994a. "Verification of a 1-Dimensional Model for Predicting Shallow Infiltration at Yucca Mountain," *High Level Radioactive Waste Management, Proceedings of the Fifth Annual International Conference, Las Vegas, Nevada, May 22-26, 1994.* La Grange Park, IL: American Nuclear Society. Vol. 4, 2323-2332.

Hevesi, J.A., D.S. Ambos, and A.L. Flint. 1994b. "A Preliminary Characterization of the Spatial Variability of Precipitation at Yucca Mountain," *High Level Radioactive Waste Management, Proceedings of the Fifth Annual International Conference, Las Vegas, Nevada, May 22-26, 1994.* La Grange Park, IL: American Nuclear Society. 2520-2529. (MOL.19941128.0063)

Isaaks, E.H., and R.M. Srivastava. 1989. *Applied Geostatistics.* New York, NY: Oxford University Press. (NNA.900420.0087)

Istok, J.D., ed. 1989. *Groundwater Modeling by the Finite Element Method.* Water Resources Monograph 13. Washington, DC: American Geophysical Union. 101-109.

Istok, J.D., A.L. Flint, and L.E. Flint. 1991. "Spatial Variability in Rock Matrix Properties from Surface Outcrop Sampling," *Agronomy Abstracts, 1991 Annual Meeting, Denver, Colorado, October 27-November 1, 1991.* American Society of Agronomy. (NNA.920707.0067)

Istok, J.D., C.A. Rautman, L.E. Flint, and A.L. Flint. 1994. "Spatial Variability in Hydrologic Properties of a Volcanic Tuff," *Groundwater.* Vol. 32, no. 5, 751-760. (MOL.19941128.0061)

Jaynes, E.T. 1957. "Information Theory and Statistical Mechanic, II," *Physics Review.* Vol. 108, no. 2 , 171-190. (NNA.910306.0127)

Journel, A.G., and F.G. Alabert. 1990. "New Method for Reservoir Mapping," *JPT, Journal of Petroleum Technology.* SPE 18324. Vol. 42, no. 2, 212-219. (MOL.19950502.0010)

Kaasschieter, E.F., and A.J.M. Huijben. 1992. "Mixed-Hybrid Finite Elements and Streamline Computations for the Potential Flow Problem," *Numerical Methods for Partial Differential Equations.* Vol. 8, no. 3, 221-266. (NNA.930125.0073)

Kaplan, P.G. 1993. *Pre-Waste Emplacement Ground-Water Travel Time Sensitivity and Uncertainty Analyses for Yucca Mountain, Nevada.* SAND92-0461. Albuquerque, NM: Sandia National Laboratories. (NNA.921216.0009)

Klavetter, E.A., and R.R. Peters. 1986. *Estimation of Hydrologic Properties of an Unsaturated, Fractured Rock Mass.* SAND84-2642. Albuquerque, NM: Sandia National Laboratories. (NNA.870317.0738)

Knauss, K.G., and D.W. Peifer. 1986. *Reaction of Vitric Topopah Spring Tuff and J-13 Ground Water Under Hydrothermal Conditions Using Dickson-type Gold-bag Rocking Autoclaves.* UCRL-53795. Livermore, CA: Lawrence Livermore National Laboratory. (NNA.891102.0117)

Knauss, K.G., W.J. Beiriger, D.W. Peifer, and A.J. Piwinskii. 1985. *Hydrothermal Interaction of Solid Wafers of Topopah Spring Tuff with J-13 Water and Distilled Water at 90, 150, and 250° C, Using Dickson-type, Gold-bag Rocking Autoclave.* UCRL-53645. Livermore, CA: Lawrence Livermore National Laboratory. (NNA.900207.0282)

Kume, J., and D.P. Hammermeister. 1990. *Geohydrologic Data from Test Hole USW UZ-7, Yucca Mountain Area, Nye County, Nevada.* Open-File Report 88-465. Denver, CO: US Geological Survey. (NNA.900312.0300)

Kume, J., and J.P. Rousseau. 1994. "A Borehole Instrumentation Program for Characterization of Unsaturated-Zone Percolation," *High Level Radioactive Waste Management, Proceedings of the Fifth Annual International Conference, Las Vegas, Nevada, May 22-26, 1994.* La Grange Park, IL: American Nuclear Society. 2076-2083. (MOL.19950419.0115)

Lahoud, R.G., D.H. Lobmeyer, and M.S. Whitfield, Jr. 1984. *Geohydrology of Volcanic Tuff Penetrated by Test Well UE-25b#1, Yucca Mountain, Nye County, Nevada.* Water Resources Investigations Report 84-4253. Denver, CO: U.S. Geological Survey (NNA.890511.0117)

LeCain, G.D., and J.N. Walker. 1994. "Results of Air-Permeability Testing in a Vertical Borehole at Yucca Mountain, Nevada," *High Level Radioactive Waste Management, Proceedings of the Fifth Annual International Conference, Las Vegas, Nevada, May 22-26, 1994.* La Grange Park, IL: American Nuclear Society. 2782-2788. (NNA.940527.0013)

Lin, W., and W. Daily. 1984. *Transport Properties of Topopah Spring Tuff.* UCRL-53602. Livermore, CA: Lawrence Livermore National Laboratory. (NNA.891026.0025)

Lin, Y.T., and M.S. Tierney. 1986. *Preliminary Estimates of Groundwater Travel Time and Radionuclide Transport at the Yucca Mountain Repository Site.* SAND85-2701. Albuquerque, NM: Sandia National Laboratories. (NNA.891129.0550)

Lin, Y.T., M.S. Tierney, and S. Sinnock. 1986. *Preliminary Estimates of Groundwater Travel Time and Radionuclide Transport at the Yucca Mountain Repository Site.* SAND85-2701. Albuquerque, NM: Sandia National Laboratories. (NNA.891129.0550)

Montazer, P., and W.E. Wilson. 1985. "Hydrogeology of the Unsaturated Zone, Yucca Mountain, Nevada," *Proceedings of the NWWA Conference on Characterization and Monitoring of the Vadose (Unsaturated) Zone, Denver, Colorado, November 19-21, 1985.* 396-412. (SRX.861119.0160)

Nitao, J.J., and T.A. Buscheck. 1991. "Infiltration of a Liquid Front in an Unsaturated Fractured Porous Medium," *Water Resources Research.* Vol. 27, no. 8, 2099-2112. (NNA.920817.0138)

Nuclear Regulatory Commission (NRC). 1983. "Disposal of High-Level Radioactive Wastes in Geologic Repositories," *Code of Federal Regulations, Title 10, Part 60.* Washington, DC: US Government Printing Office. (NNA.900727.0307)

Nuclear Regulatory Commission (NRC). 1989. *NRC Staff Site Characterization Analysis of the Department of Energy's Site Characterization Plan, Yucca Mountain Site, Nevada.* NUREG-1347. Washington, DC: Nuclear Regulatory Commission. (NNA.891020.0161)

Ortiz, T.S., R.L. Williams, F.B. Nimick, B.C. Whittet, and D.L. South. 1985. *A Three-Dimensional Model of Thermal/Mechanical and Hydrologic Stratigraphy at Yucca Mountain, Southern Nevada.* SAND84-1076. Albuquerque, NM: Sandia National Laboratories. (NNA.890315.0013)

Peters, R.R., E.A. Klavetter, I.J. Hall, S.C. Blair, P.R. Heller, and G.W. Gee. 1984. *Fracture and Matrix Hydrogeologic Characteristic of Tuffaceous Materials from Yucca Mountain, Nye County, Nevada.* SAND84-1471. Albuquerque, NM: Sandia National Laboratories. (NNA.870407.0036) (DTN: SNSAND84147100.000)

Peters, R.R., and E.A. Klavetter. 1988. "A Continuum Model for Water Movement in an Unsaturated Fractured Rock Mass," *Water Resources Research.* Vol. 24, no. 3, 416-430. (NNA.890523.0139)

Prindle, R.W., and P.L. Hopkins. 1990. *On Conditions and Parameters Important to Model Sensitivity for Unsaturated Flow Through Layered, Fractured Tuff: Results of Analyses for HYDROCOIN Level 3 Case 2.* SAND89-0652. Albuquerque, NM: Sandia National Laboratories. (NNA.900523.0211)

Rautman, C.A., and T.H. Robey. 1994. "Development of Stochastic Indicator Models of Lithology, Yucca Mountain, Nevada," *High-Level Radioactive Waste Management, Proceedings of the Fifth Annual International Conference, Las Vegas, Nevada, May 22-26, 1994.* La Grange Park, IL: American Nuclear Society. Vol. 4, 510-2519. (NNA.940629.0015)

Roberts, J.E., and J.M. Thomas. 1990. "Mixed and Hybrid Methods," *Handbook of Numerical Analysis, Volume II: Finite Element Methods.* Eds. P.G. Ciarlet and J.L. Lions. Amsterdam: North-Holland. 523-639. (NNA.940303.0055)

Robey, T.H. 1990. *The Mixed Finite Element Method.* Ph.D. Dissertation. Albuquerque, NM: University of New Mexico. (NNA.930125.0074)

Robey, T.H. 1994. *Development of Models for Fast Fluid Pathways Through Unsaturated Heterogeneous Porous Media.* SAND93-7109. Albuquerque, NM: Sandia National Laboratories. (MOL.19941025.0001)

Robison, J.H. 1984. *Ground-Water Level Data and Preliminary Potentiometric Surface Maps, Yucca Mountain and Vicinity, Nye County, Nevada.* U. S. Geological Survey Water Resources Investigations Report 84-4197. Denver, CO: US Geological Survey. (NNA.870519.0096)

Rush, F.E., W. Thordarson, and L. Bruckheimer. 1983. *Geohydrologic and Drillhole Data for Test Well USW H-1, Adjacent to the Nevada Test Site, Nye County, Nevada.* Open-File Report 83-141. Reston, VA: US Geological Survey. (NNA.870519.0103)

Rush, F.E., W. Thordarson, and D.G. Pyles. 1984. *Geohydrology of Test Well USW H-1, Yucca Mountain, Nye County, Nevada.* Water Resources Investigation Report 84-4032. Denver, CO: U.S. Geological Survey. (NNA.870518.0067)

Rutherford, B.M., I.J. Hall, R.R. Peters, R.G. Easterling, and E.A. Klavetter. 1992. *Statistical Analysis of Hydrologic Data for Yucca Mountain.* SAND87-2380. Albuquerque, NM: Sandia National Laboratories. (NNA.910822.001)

Sass, J.H., A.H. Lachenbruch, W.W. Dudley, Jr., S.S. Priest, and R.J. Munroe. 1988. *Temperature, Thermal Conductivity, and Heat Flow Near Yucca Mountain, Nevada: Some Tectonic and Hydrologic Implications.* US Geological Survey Open-File Report 87-649. Denver, CO: U.S. Geological Survey. (NNA.890123.0010)

Schwartz, B.M. 1990. *SNL Yucca Mountain Data Report: Density and Porosity Data for Tuffs from the Unsaturated Zone at Yucca Mountain, Nevada.* SAND88-0811. Albuquerque, NM: Sandia National Laboratories. (NNA.900108.0028)

Scott, R.B. 1990. "Tectonic Setting of Yucca Mountain, Southwest Nevada," *Basin and Range Extensional Tectonic Near the Latitude of Las Vegas, Nevada.* Ed. B.P. Wernicke. Geological Society of America Memoir 176. Boulder, CO: Geological Society of America. 251-282. (NNA.920131.0325)

Scott, R.B., and J. Bonk. 1984. *Preliminary Geologic Map of Yucca Mountain, Nye County, Nevada, with Geologic Cross-Sections.* Open-File Report 84-494. Denver, CO: U. S. Geological Survey. (HQS.880517.1443)

Shannon, C.E. 1948. "A Mathematical Theory of Communication," *Bell System Technology Journal.* Vol. 27, no. 3, 379-423. (NNA.910306.0126)

Sinnock, S., Y.T. Lin, and J.P. Brannen. 1984. *Preliminary Bounds on the Expected Postclosure Performance of the Yucca Mountain Repository Site, Southern Nevada.* SAND84-1492. Albuquerque, NM: Sandia National Laboratories. (NNA.870519.0076)

Sinton, P.O. 1989. "Characterization of the Large Hydraulic Gradient Beneath the North End of Yucca Mountain, Nevada," *EOS Transactions, American Geophysical Union.* Vol. 70, no. 15, 321. (NNA.890204.0065)

Sleijpen, G. L.G., and D.R. Fokkema. 1993. "BICGSTAB(L) for Linear Equations Involving Unsymmetric Matrices with Complex Spectrum," *Electronic Transactions on Numerical Analysis.* Vol. 1, 11-32.

Snow, D.T. 1970. "The Frequency and Apertures of Fractures in Rock," *International Journal of Rock Mechanics and Mining Science.* Vol. 7, 23-40. (NNA.891222.0003)

Spengler, R.W., C.A. Braun, R.M. Linden, L.G. Martin, D.M. Ross-Brown, and R.L. Blackburn. 1993. "Structural Character of the Ghost Dance Fault, Yucca Mountain, Nevada," *High Level Radioactive Waste Management, Proceedings of the Fourth Annual International Conference, Las Vegas, Nevada, April 26-30, 1993.* La Grange Park, IL: American Nuclear Society. 653-659. (NNA.931025.0026)

Spengler, R.W., C.A. Braun, L.G. Martin, and C.W. Weisenberg. 1994. "The Sundance Fault: a Newly Recognized Shear Zone at Yucca Mountain, Nevada," *High Level Radioactive Waste Management, Proceedings of the Fifth Annual International Conference, Las Vegas, Nevada, May 22-26, 1994.* La Grange Park, IL: American Nuclear Society. 2359-2366. (MOL.19950105.0018))

Stoker, A.K., W.D. Purtymun, S.G. McLin, and M.N. Maes. 1991. *Extent of Saturation in Mortandad Canyon.* LA-UR-91-1160. Los Alamos, NM: Los Alamos National Laboratory. (NNA.930125.0076)

van Genuchten, R. 1978. *Calculating the Unsaturated Hydraulic Conductivity with a New Closed Form Analytical Model.* Water Resources Bulletin. Princeton, NJ: Princeton University Press, Princeton University. (HQS.880517.1859)

Voss, C., 1992a, Letter to P. Kaplan, Subject: Transfer of Test Case Data - Attachment B: USW GU-3 Core Analyses, 69 Samples from Topopah Spring Shardy Base (1263.8 ft) to Prow Pass Partially Welded (1883.5 ft), with Measurements of Porosity, Bulk Density, Sorptivity, And Saturated Conductivity, dated June 15, 1992, Golder Associates, Inc., Redmond, WA. (MOL.19941021.0001)

Voss, C., 1992b, Letter to P. Kaplan, Subject: Transfer of Test Case Data - Attachment C: USW UZN-54 and USW UZN-55 Core Analyses: Bulk Density, Porosity, Particle Density and 'In Situ' Saturation, dated June 15, 1992, Golder Associates, Inc., Redmond, WA. (MOL.19941021.0001)

Voss, C., 1992c, Letter to T. Robey, Subject: Additional Data for Yucca Mountain test case - Attachment 3: Porosity, Density, Water Content, and Percent Saturation For Core from USW UZN-53, dated October 30, 1992, Golder Associates, Inc., Redmond, WA. (MOL.19941021.0002)

Voss, C., 1993, Letter to T. Robey, Subject: YMP Data for INTRAVAL Participants - Core Data for USW UZ-16, dated June 23, 1993, Golder Associates, Inc., Redmond, WA. (MOL.19941021.0003)

Wang, J.S.Y., and T.N. Narasimhan. 1985. "Hydrologic Mechanisms Governing Fluid Flow in a Partially Saturated Fractured Porous Medium," *Water Resources Research.* Vol. 21, no. 12, 1861-1874. (NNA.891109.0050)

Wang, J.S.Y., and T.N. Narasimhan. 1986. *Hydrologic Mechanisms Governing Partially Saturated Fluid Flow in Fractured, Welded Units and Porous, Nonwelded Units at Yucca Mountain.* SAND85-7114. Albuquerque, NM: Sandia National Laboratories. (NNA.870806.0063)

Wang, J.S.Y., and T.N. Narasimhan. 1988. *Hydrologic Modeling of Vertical and Lateral Movement of Partially Saturated Fluid Flow Near a Fault Zone at Yucca Mountain.* SAND87-7070. Albuquerque, NM: Sandia National Laboratories. (NNA.871109.0057)

Warren, J. E., and P. J. Root. 1963. "The Behavior of Naturally Fractured Reservoirs, "*Society of Petroleum Engineers Journal.* Vol.3, no. 5, 245-255. (NNA.890522.0276)

Weeks, E.P., and W.E. Wilson. 1984. *Preliminary Evaluation of Hydrologic Properties of Cores of Unsaturated Tuff, Test Well USW H-1, Yucca Mountain, Nevada.* Water Resources Investigation 84-4193. Denver, CO: US Geological Survey. (NNA.870417.0037)

Wilson, M. L., J. H. Gauthier, R.W. Barnard, G.E. Barr, H.A. Dockery, E. Dunn, R.R. Eaton, D.C. Guerin, N. Lu, M.J. Martinez, R. Nilson, C.A. Rautmen, T.H. Robey, B. Ross, E.E. Ryder, A.R. Schenker, S.A. Shannon, L.H. Skinner, W.G. Halsey, J.D. Gansemer, L.C. Lewis, A.D. Lamont, I.R. Triay, A. Meijer, and D.E. Morris. 1994. *Total-System Performance Assessment for Yucca Mountain - SNL Second Iteration (TSPA-1993).* SAND93-2675. Albuquerque, NM: Sandia National Laboratories. (NNA.940112.0123)

Winograd, I.J., and W. Thordarson. 1975. *Hydrogeologic and Hydrochemical Framework, South-Central Great Basin, Nevada-California, with Special Reference to the Nevada Test Site.* Professional Paper 712-C. Denver, CO: US Geological Survey. (NNA.870406.0201)

Wittwer, C.S., G.S. Bodvarsson, M.P. Chornack, A.L. Flint, L.E. Flint, B.D. Lewis, R.W. Spegler, and C.A. Rautman. 1992. "Design of a Three-Dimensional Site-Scale Model for the Unsaturated Zone at Yucca Mountain, Nevada," *High-Level Radioactive Waste Management, Proceedings of the Third International Conference, Las Vegas, Nevada, April 12-16, 1992.* La Grange Park, IL: American Nuclear Society. Vol. 1, 263-271. (NNA.930125.0071)

Wittwer, C.S., G. Chen, and G.S. Bodvarsson. 1993. "Studies of the Role of Fault Zones on Fluid Flow Using the Site-Scale Numerical Model of Yucca Mountain," *High Level Radioactive Waste Management, Proceedings of the Fourth Annual International Conference, Las Vegas, Nevada, April 26-30, 1993.* La Grange Park, IL: American Nuclear Society. 667-674. (NNA.931214.0104)

Yang, I.C., A.K. Turner, T.M. Sayre, and P. Montazer. 1988. "Comparison of Pore-Water Extraction by Triaxial Compression Methods and High Speed Centrifugation Methods," *Proceedings of Conference on Minimizing Risk to the Environment, American Institute of Hydrology, 1990.* 250-259. (NNA.900123.0079)

YUCCA MOUNTAIN SITE CHARACTERIZATION PROJECT

UC814 - DISTRIBUTION LIST

1 D. A. Dreyfus (RW-1)
Director
OCRWM
US Department of Energy
1000 Independence Avenue SW
Washington, DC 20585

1 L. H. Barrett (RW-2)
Acting Deputy Director
OCRWM
US Department of Energy
1000 Independence Avenue SW
Washington, DC 20585

1 S. Rousso (RW-40)
Office of Storage and Transportation
OCRWM
US Department of Energy
1000 Independence Avenue SW
Washington, DC 20585

1 R. A. Milner (RW-30)
Office of Program Management
and Integration
OCRWM
US Department of Energy
1000 Independence Avenue SW
Washington, DC 20585

1 D. R. Elle, Director
Environmental Protection Division
DOE Nevada Field Office
US Department of Energy
P.O. Box 98518
Las Vegas, NV 89193-8518

1 T. Wood (RW-14)
Contract Management Division
OCRWM
US Department of Energy
1000 Independence Avenue SW
Washington, DC 20585

4 Victoria F. Reich, Librarian
Nuclear Waste Technical Review Board
1100 Wilson Blvd., Suite 910
Arlington, VA 22209

5 Wesley Barnes, Project Manager
Yucca Mountain Site Characterization
Office
US Department of Energy
P.O. Box 98608--MS 523
Las Vegas, NV 89193-8608

1 Director
Office of Public Affairs
DOE Nevada Operations Office
US Department of Energy
P.O. Box 98518
Las Vegas, NV 89193-8518

8 Technical Information Officer
DOE Nevada Operations Office
US Department of Energy
P.O. Box 98518
Las Vegas, NV 89193-8518

1 P. K. Fitzsimmons, Technical Advisor
Office of Assistant Manager for
Environmental Safety and Health
DOE Nevada Operations Office
US Department of Energy
P.O. Box 98518
Las Vegas, NV 89193-8518

1 J. A. Blink
Deputy Project Leader
Lawrence Livermore National Laboratory
101 Convention Center Drive
Suite 820, MS 527
Las Vegas, NV 89109

2 J. A. Canepa
Technical Project Officer - YMP
N-5, Mail Stop J521
Los Alamos National Laboratory
P.O. Box 1663
Los Alamos, NM 87545

1 Repository Licensing & Quality
Assurance
Project Directorate
Division of Waste Management
US NRC
Washington, DC 20555

1 Senior Project Manager for Yucca
Mountain
Repository Project Branch
Division of Waste Management
US NRC
Washington, DC 20555

1 NRC Document Control Desk
Division of Waste Management
US NRC
Washington, DC 20555

1 Chad Glenn
NRC Site Representative
301 E Stewart Avenue, Room 203
Las Vegas, NV 89101

1 E. P. Binnall
Field Systems Group Leader
Building 50B/4235
Lawrence Berkeley Laboratory
Berkeley, CA 94720

1 Center for Nuclear Waste
Regulatory Analyses
6220 Culebra Road
Drawer 28510
San Antonio, TX 78284

2 W. L. Clarke
Technical Project Officer - YMP
Attn: YMP/LRC
Lawrence Livermore National Laboratory
P.O. Box 5514
Livermore, CA 94551

1 V. R. Schneider
Asst. Chief Hydrologist -- MS 414
Office of Program Coordination
and Technical Support
US Geological Survey
12201 Sunrise Valley Drive
Reston, VA 22092

1 J. S. Stuckless, Chief
Geologic Studies Program
MS 425
Yucca Mountain Project Branch
US Geological Survey
P.O. Box 25046
Denver, CO 80225

1 N. Z. Elkins
Deputy Technical Project Officer
Los Alamos National Laboratory
Mail Stop 527
101 Convention Center Drive, #820
Las Vegas, NV 89109

2 Michaele C. Brady
Technical Project Officer - YMP
Sandia National Laboratories
Organization 6302, MS 1399
101 Convention Center Drive, Suite 880
Las Vegas, NV 89109

1 Ray Wallace
US Geological Survey
106 National Center
12201 Sunrise Valley Drive

1 L. R. Hayes
Technical Project Officer
Yucca Mountain Project Branch
MS 425
US Geological Survey
P.O. Box 25046
Denver, CO 80225

1 A. L. Flint
US Geological Survey
MS 721
P.O. Box 327
Mercury, NV 89023

1 R. E. Lewis
Yucca Mountain Project Branch
MS 425
US Geological Survey
P.O. Box 25046
Denver, CO 80225

1 D. Zesiger
US Geological Survey
101 Convention Center Drive
Suite 860, MS 509
Las Vegas, NV 89109

2 L. D. Foust
Nevada Site Manager
TRW Environmental Safety Systems
101 Convention Center Drive
Suite P-110, MS 423
Las Vegas, NV 89109

1 C. E. Ezra
YMP Support Office Manager
EG&G Energy Measurements Inc.
MS V-02
P.O. Box 1912
Las Vegas, NV 89125

1 E. L. Snow, Program Manager
Roy F. Weston, Inc.
955 L'Enfant Plaza SW
Washington, DC 20024

1 Technical Information Center
Roy F. Weston, Inc.
955 L'Enfant Plaza SW
Washington, DC 20024

1 Technical Project Officer - YMP
US Bureau of Reclamation
Code D-3790
P.O. Box 25007
Denver, CO 80225

1 B. T. Brady
Records Specialist
US Geological Survey
MS 421
P.O. Box 25046
Denver, CO 80225

1 M. D. Voegele
Technical Project Officer - YMP
M&O/SAIC
101 Convention Center Drive
Suite 407
Las Vegas, NV 89109

1 Paul Eslinger, Manager
PASS Program
Pacific Northwest Laboratories
P.O. Box 999
Richland, WA 99352

1 A. T. Tamura
Science and Technology Division
OSTI
US Department of Energy
P.O. Box 62
Oak Ridge, TN 37831

1 P. J. Weeden, Acting Director
Nuclear Radiation Assessment Div.
US EPA
Environmental Monitoring Sys. Lab
P.O. Box 93478
Las Vegas, NV 89193-3478

1 ONWI Library
Battelle Columbus Laboratory
Office of Nuclear Waste Isolation
505 King Avenue
Columbus, OH 43201

1 C. H. Johnson
Technical Program Manager
Agency for Nuclear Projects
State of Nevada
Evergreen Center, Suite 252
1802 N. Carson Street
Carson City, NV 89710

1 John Fordham, Deputy Director
Water Resources Center
Desert Research Institute
P.O. Box 60220
Reno, NV 89506

1 The Honorable Cyril Schank
Chairman
Churchill County Board of
Commissioners
190 W. First Street
Fallon, NV 89406

1 T. Hay, Executive Assistant
Office of the Governor
State of Nevada
Capitol Complex
Carson City, NV 89710

3 R. R. Loux
Executive Director
Agency for Nuclear Projects
State of Nevada
Evergreen Center, Suite 252
1802 N. Carson Street
Carson City, NV 89710

1 Brad R. Mettam
Inyo County Yucca Mountain
Repository Assessment Office
P. O. Drawer L
Independence, CA 93526

1 Lander County Board of Commissioners
315 South Humbolt Street
Battle Mountain, NV 89820

1 Vernon E. Poe
Office of Nuclear Projects
Mineral County
P.O. Box 1600
Hawthorne, NV 89415

1 Les W. Bradshaw
Program Manager
Nye County Nuclear Waste Repository
Project Office
P.O. Box 1767
Tonopah, NV 89049

1 Florindo Mariani
White Pine County Coordinator
P. O. Box 135
Ely, NV 89301

1 Judy Foremaster
City of Caliente Nuclear Waste
Project Office
P.O. Box 158
Caliente, NV 89008

1 Philip A. Niedzielski-Eichner
Nye County Nuclear Waste
Repository Project Office
P.O. Box 221274
Chantilly, VA 22022-1274

1 Dennis Bechtel, Coordinator
Nuclear Waste Division
Clark County Department of
Comprehensive Planning
301 E. Clark Avenue, Suite 570
Las Vegas, NV 89101

1 Juanita D. Hoffman
Nuclear Waste Repository
Oversight Program
Esmeralda County
P.O. Box 490
Goldfield, NV 89013

1 Eureka County Board of Commissioners
Yucca Mountain Information Office
P.O. Box 714
Eureka, NV 89316

1 Economic Development Dept.
City of Las Vegas
400 E. Stewart Avenue
Las Vegas, NV 89101

1 Community Planning & Development
City of North Las Vegas
P.O. Box 4086
North Las Vegas, NV 89030

1 Community Development & Planning
City of Boulder City
P.O. Box 61350
Boulder City, NV 89006

1 Commission of European Communities
200 Rue de la Loi
B-1049 Brussels
BELGIUM

2 Librarian
YMP Research & Study Center
MS 407
P.O. Box 98521
Las Vegas, NV 89193-8521

1 Amy Anderson
Argonne National Laboratory
Building 362
9700 S. Cass Avenue
Argonne, IL 60439

1 Glenn Van Roekel
Director of Community Development
City of Caliente
P.O. Box 158
Caliente, NV 89008

1 G. S. Bodvarsson
Head, Nuclear Waste Department
Lawrence Berkeley Laboratory
1 Cyclotron Road, MS 50E
Berkeley, CA 94720

1 Michael L. Baughman
Intertech Services Corp.
P.O. Box 93537
Las Vegas, NV 89193

1 Eric Smistad
DOE
101 Convention Center Drive
P200-216
Las Vegas, NV 89109

1 Lester Berkowitz
TRW ESS
600 Maryland Avenue SW
TES2 / 601F
Washington, DC 20024

1 Abe Van Luik
DOE
101 Convention Center Drive
P200-219
Las Vegas, NV 89109

1 Richard Codell
NRC
MS T7D13
Washington, DC 20555

1 Jeffrey Pohle
NRC
MS T7D13
Washington, DC 20555

1 George Zyvoloski
Lawrence Livemore National Laboratories
J521
Los Alamos, NM 87545

1 J. Fabryka-Martin
Lawrence Livermore National Laboratories
P. O. Box 1663
Group CST-7, MS J514
Los Alamos, NM 87545

1 Yvonne Tsang
Lawrence Berkeley Laboratories
MS 50-A-1149
1 Cyclotron Road
Berkeley, CA 94720

1 Joe Wang
Lawrence Berkeley Laboratories
MS 50-A-1149
1 Cyclotron Road
Berkeley, CA 94720

1 Benjamin Ross
Disposal Safety, Inc.
1660 L Street NW
Washington, DC 20036

1 Charles Voss
Golder Associates
4044 148th Avenue NE
Redwood, WA 98052

1 Lorri Flint
USGS
MS 721
P. O. Box 327
Mercury, NV 89023

1 Dwight Hoxie
USGS
101 Convention Center Drive
Suite 860
Las Vegas, NV 89109

1 Ed Kwicklis
USGS
P. O. Box 25046
MS 421
Lakewood, CO 80225

1 Bill Nelson
M&O / INTERA
101 Convention Center Drive
MS 423
Las Vegas, NV 89109

1 James Duguid
INTERA
101 Convention Center Drive
TES1 / 89564
Las Vegas, NV 89109

1 Ronald Green
SWRI
Center for Nuclear Waste Regulatory Analyses
6220 Culebra Road
San Antonio, TX 78238

1 Gordon Wittmeyer
Center for Nuclear Waste Regulatory Analyses
6220 Culebra Road
San Antonio, TX 78238

1 Amvrossios Bagtzoglour
SWRI
Center for Nuclear Waste Regulatory Analyses
6220 Culebra Road
San Antonio, TX 78238

1 Julie Linn
USGS
P. O. Box 327, MS 743
Mercury, NV 89023

1 S. David Sevougian
INTERA
101 Convention Center Drive
Suite P-110
Las Vegas, NV 89109

1 Ed Taylor
TRW
2650 Park Tower Drive
Suite 800
Vienna, Virginia 22180

1 Linda Lehman
L. Lehman & Associates
1103 W. Burnsville Parkway
Suite 209
Minneapolis, MN 55337

	MS	
2	1330	C. B. Michaels, 6352 100/1.2.5.4.4/SAND95-0857/QA
20	1330	WMT Library, 6352
20	1326	B. W. Arnold, 6312
5	1326	S. J. Altman, 6312
10	1326	T. H. Robey, 6312
5	1326	R. W. Barnard, 6312
2	1345	T. J. Brown, 6331
1	1326	H. A. Dockery, 6312
1	1326	S. A. Shannon, 6312
1	1326	L. H. Skinner, 6312, MS-
1	1326	A. L. Schenker, 6312, LATA
1	1326	M. L. Wilson, 6312
1	1326	J. H. Gauthier, 6312
1	1326	G. E. Barr, 6312
1	1326	N. D. Francis, 6312
1	1324	P. B. Davies, 6115
1	1324	C. K. Ho, 6115c
1	1324	C. A. Rautman, 6115
1	1324	R. J. Glass, 6115
1	9018	Central Technical Files, 8523-2
5	0899	Technical Library, 13414
1	0619	Print Media, 12615
2	0100	Document Processing, 7613-2 for DOE/OSTI